

# Appendix

Appendix A  
**VLSI Fabrication Technology** A-1

Appendix B  
**NEW-SPICE appendix** B-1

Appendix C  
**Two-Port Network Theorems** C-1

Appendix D  
**Some Useful Network Theorems** D-1

Appendix E  
**Single-Time-Constant Circuits** E-1

**Appendix F  
Bibliography**   F-1

**Appendix G  
Standard Resistance Values and Unit Prefixes**   G-1

**Appendix H  
All NEW from ISM answers**   H-1

**Appendix CD  
Domain Analysis: Poles, Zeros, and Bode Plots**   CD-1

## APPENDIX A

# VLSI FABRICATION TECHNOLOGY

### Introduction

Since the first edition of this text, we have witnessed a fantastic evolution in **VLSI** (very-large-scale integrated circuits) technology. In the late 1970s, non-self-aligned metal gate MOSFETs with gate lengths in the order of 10  $\mu\text{m}$  were the norm. Current VLSI fabrication technology is already at the physical scaling limit with gate lengths in the 20-nm regime. This represents a reduction in device size of almost 1000 $\times$ , along with an even more impressive increase in the number of devices per VLSI chip. Future development in VLSI technology must rely on new device concepts and new materials, taking quantum effects into account. While this is a very exciting time for researchers to explore new technology, we can also be assured that the “traditional” **CMOS** and **BiCMOS** (bipolar CMOS) fabrication technology will continue to be the workhorse of the microelectronic industry for many more years to come.

The purpose of this appendix is to familiarize the reader with VLSI fabrication technology. Brief explanations of standard VLSI processing steps are given. The variety of devices available in CMOS and BiCMOS fabrication technologies are also presented. In particular, the availability of components in the **IC** (integrated circuit) environment that are distinct from discrete circuit design will be discussed. In order to enjoy the economics of integrated circuits, designers have to overcome some serious device limitations (such as poor device tolerances) while exploiting device advantages (such as good component matching). An understanding of device characteristics is therefore essential in designing high-performance custom VLSIs.

This appendix will consider only silicon-based (Si) technologies. Although other compound materials in groups III through V, such as gallium arsenide (GaAs) and aluminum gallium nitride (AlGaN), are also used to implement VLSI chips, silicon is still the most popular material, with excellent cost–performance trade-off. Recent development in SiGe and strained-silicon technologies will further strengthen the position of Si-based fabrication processes in the microelectronic industry for many more years to come.

Silicon is an abundant element and occurs naturally in the form of sand. It can be refined using well-established purification and crystal growth techniques. It also exhibits suitable physical properties for fabricating active devices with good electrical characteristics. In addition, silicon can be easily oxidized to form an excellent insulator,  $\text{SiO}_2$  (glass). This native oxide is useful for constructing capacitors and MOSFETs. It also serves as a diffusion barrier that can mask against unwanted impurities from diffusing into the high-purity silicon material. This masking property allows the electrical properties of the silicon to be altered in predefined areas. Therefore, active and passive elements can be built on the same piece of material (substrate). The components can then be interconnected using metal layers (similar to those used in printed-circuit boards) to form a monolithic IC.

## A.1 IC Fabrication Steps

The basic IC fabrication steps will be described in the following sections. Some of these steps may be carried out many times, in different combinations and/or processing conditions during a complete fabrication run.

### A.1.1 Silicon Wafers

The starting material for modern integrated circuits is very-high-purity, single-crystal silicon. The material is initially grown as a single crystal ingot. It takes the shape of a steel-gray solid cylinder 10 cm to 30 cm in diameter and can be one to two meters in length. This crystal is then sawed (like a loaf of bread) to produce circular **wafers** that are 400  $\mu\text{m}$  to 600  $\mu\text{m}$  thick (a micrometer, or micron,  $\mu\text{m}$ , is a millionth of a meter). The surface of the wafer is then polished to a mirror finish using chemical and mechanical polishing (CMP) techniques. Semiconductor manufacturers usually purchase ready-made silicon wafers from a supplier and rarely start their fabrication process in ingot form.

The basic electrical and mechanical properties of the wafer depend on the orientation of the crystalline structure, the impurity concentrations, and the type of impurities present. These variables are strictly controlled during crystal growth. A specific amount of impurities can be added to the pure silicon in a process known as doping. This allows the alteration of the electrical properties of the silicon, in particular its resistivity. Depending on the types of impurity, either holes (in **p-type** silicon) or electrons (in **n-type** silicon) can be responsible for electrical conduction. If a large number of impurity atoms is added, the silicon will be heavily doped (e.g., concentration  $> \sim 10^{18} \text{ atoms/cm}^{-3}$ ). When designating the relative doping concentrations in semiconductor material, it is common to use the + and – symbols. A heavily doped (low-resistivity) *n*-type silicon wafer is referred to as *n+* material, while a lightly doped material (e.g., concentration  $< \sim 10^{16} \text{ atoms/cm}^{-3}$ ) is referred to as *n-*. Similarly, *p+* and *p-* designations refer to the heavily doped and lightly doped *p*-type regions, respectively. The ability to control the type of impurities and the doping concentration in the silicon permits the formation of diodes, transistors, and resistors in integrated circuits.

### A.1.2 Oxidation

In **oxidation**, silicon reacts with oxygen to form silicon dioxide ( $\text{SiO}_2$ ). To speed up this chemical reaction, it is necessary to carry out the oxidation at high temperatures (e.g., 1000–1200°C) and inside ultraclean furnaces. To avoid the introduction of even small quantities of contaminants (which could significantly alter the electrical properties of the silicon), it is necessary to operate in a **clean room**. Particle filters are used to ensure that the airflow in the processing area is free from dust. All personnel must protect the clean-room environment by wearing special lint-free clothing that covers a person from head to toe.

The oxygen used in the reaction can be introduced either as a high-purity gas (referred to as a “**dry oxidation**”) or as steam (forming a “**wet oxidation**”). In general, wet oxidation has a faster growth rate, but dry oxidation gives better electrical characteristics. The thermally grown oxide layer has excellent electrical insulation properties. The dielectric strength for  $\text{SiO}_2$  is approximately  $10^7 \text{ V/cm}$ . It has a dielectric constant of about 3.9, and it can be used to form excellent MOS capacitors. Silicon dioxide can also serve as an effective mask against many impurities, allowing the introduction of dopants into the silicon only in regions that are not covered with oxide.

Silicon dioxide is a transparent film, and the silicon surface is highly reflective. If white light is shone on an oxidized wafer, constructive and destructive interference will cause

certain colors to be reflected. The wavelengths of the reflected light depend on the thickness of the oxide layer. In fact, by categorizing the color of the wafer surface, one can deduce the thickness of the oxide layer. The same principle is used by more sophisticated optical interferometers to measure film thickness. On a processed wafer, there will be regions with different oxide thicknesses. The colors can be quite vivid and are immediately obvious when a finished wafer is viewed with the naked eye.

### A.1.3 Photolithography

Mass production with economy of scale is the primary reason for the tremendous impact VLSI has had on our society. The surface patterns of the various integrated-circuit components can be defined repeatedly using photolithography. The sequence of photolithographic steps is as illustrated in Fig. A.1.

The wafer surface is coated with a photosensitive layer called photoresist, using a spin-on technique. After this, a photographic plate with drawn patterns (e.g., a quartz plate with chromium layer for patterning) will be used to selectively expose the photoresist under a deep ultra-violet illumination (UV). The exposed areas will become softened (for positive photoresist). The exposed layer can then be removed using a chemical developer, causing the mask pattern to be duplicated on the wafer. Very fine surface geometries can be reproduced accurately by this technique. Furthermore, the patterns can be projected directly onto the wafer, or by using a separate photomask produced by a 10x “step and repeat” reduction technique as shown in Fig. A.2.

The patterned photoresist layer can be used as an effective masking layer to protect materials below from wet chemical **etching** or **reactive ion etching** (RIE). Silicon dioxide, silicon nitride, polysilicon, and metal layers can be selectively removed using the appropriate etching methods (see next section). After the etching step(s), the photoresist is stripped away, leaving behind a permanent pattern of the photomask on the wafer surface.

To make this process even more challenging, multiple masking layers (which can number more than 20 in advanced VLSI fabrication processes) must be aligned precisely on top of

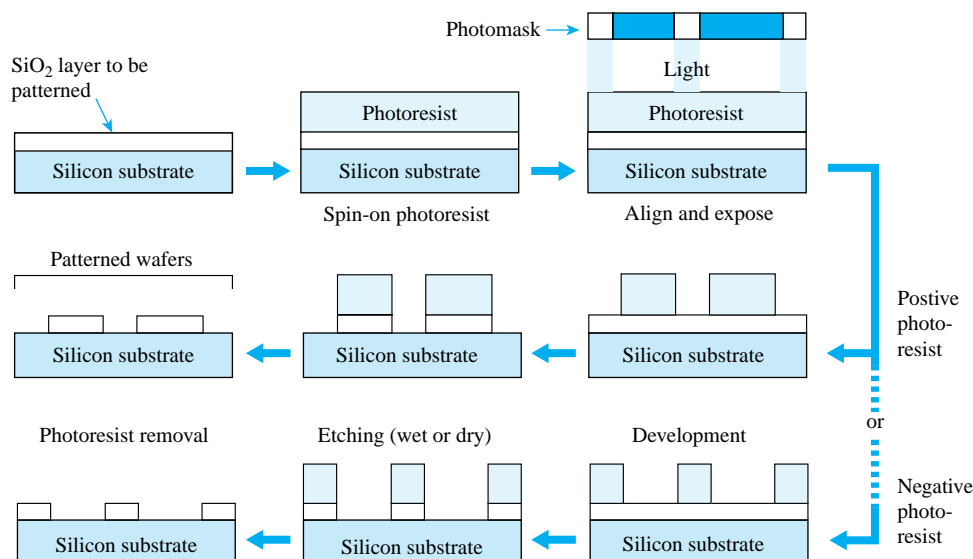
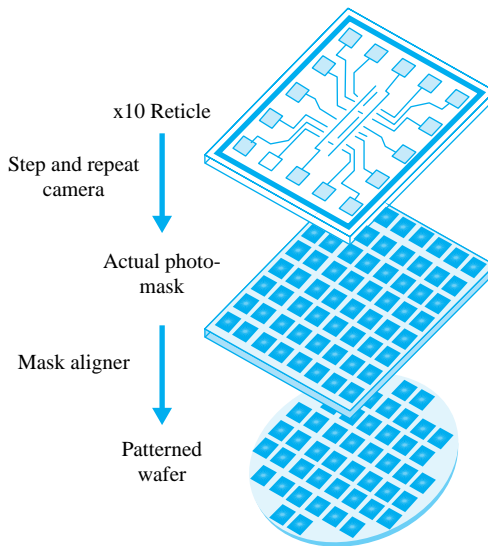


Figure A.1 Photolithography using positive or negative photoresist.



**Figure A.2** Conceptual illustration of a step-and-repeat reduction technique to facilitate the mass production of integrated circuits.

previous layers. This must be done with even finer precision than the minimum geometry size of the masking patterns. This requirement imposes very critical mechanical and optical constraints on the photolithography equipment.

#### A.1.4 Etching

To permanently imprint the photographic patterns onto the wafer, chemical (**wet**) etching or RIE **dry etching** procedures can be used. Chemical etching is usually referred to as **wet etching**. Different chemical solutions can be used to remove different layers. For example, hydrofluoric (HF) acid can be used to etch  $\text{SiO}_2$ , potassium hydroxide (KOH) for silicon, phosphoric acid for aluminum, and so on. In wet etching, the chemical usually attacks the exposed regions that are not protected by the photoresist layer in all directions (**isotropic etching**). Depending on the thickness of the layer to be etched, a certain amount of undercut will occur. Therefore, the dimension of the actual pattern will differ slightly from the original pattern. If exact dimension is critical, RIE **dry etching** can be used. This method is essentially a directional bombardment of the exposed surface using a corrosive gas (or ions). The cross section of the etched layer is usually highly directional (**anisotropic etching**) and has the same dimension as the photoresist pattern. A comparison between isotropic and anisotropic etching is given in Fig. A.3.

#### A.1.5 Diffusion

**Diffusion** is a process by which atoms move from a high-concentration region to a low-concentration region. This is very much like a drop of ink dispersing through a glass of water except that it occurs much more slowly in solids. In VLSI fabrication, this is a method to introduce impurity atoms (dopants) into silicon to change its resistivity. The rate at which dopants diffuse in silicon is a strong function of temperature. Diffusion of impurities is usually carried out at high temperatures (1000–1200°C) to obtain the desired doping profile. When the wafer is cooled to room temperature, the impurities are essentially “frozen” in

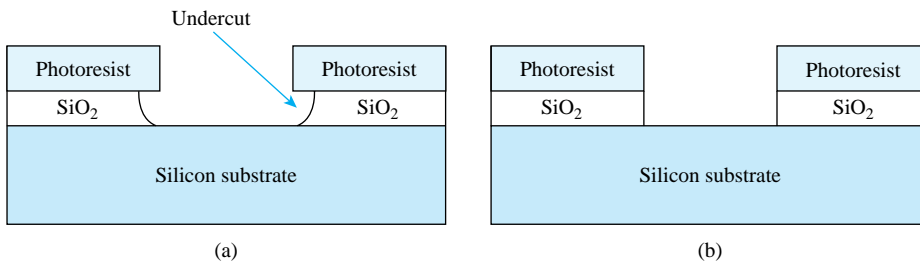


**Figure A.3** (a) Cross-sectional view of an isotropic oxide etch with severe undercut beneath the photoresist layer. (b) Anisotropic etching, which usually produces a cross section with no undercut.

position. The diffusion process is performed in furnaces similar to those used for oxidation. The depth to which the impurities diffuse depends on both the temperature and the processing time.

The most common impurities used as **dopants** are boron, phosphorus, and arsenic. Boron is a *p*-type dopant, while phosphorus and arsenic are *n*-type dopants. These dopants can be effectively masked by thin silicon dioxide layers. By diffusing boron into an *n*-type substrate, a *pn* junction is formed (diode). If the doping concentration is heavy, the diffused layer can also be used as a conducting layer with very low resistivity.

### A.1.6 Ion Implantation

**Ion implantation** is another method used to introduce impurities into the semiconductor crystal. An ion implanter produces ions of the desired dopant, accelerates them by an electric field, and allows them to strike the semiconductor surface. The ions become embedded in the crystal lattice. The depth of penetration is related to the energy of the ion beam, which can be controlled by the accelerating-field voltage. The quantity of ions implanted can be controlled by varying the beam current (flow of ions). Since both voltage and current can be accurately measured and controlled, ion implantation results in impurity profiles that are much more accurate and reproducible than can be obtained by diffusion. In addition, ion implantation can be performed at room temperature. Ion implantation normally is used when accurate control of the doping profile is essential for device operation.

### A.1.7 Chemical Vapor Deposition

**Chemical vapor deposition** (CVD) is a process by which gases or vapors are chemically reacted, leading to the formation of solids on a substrate. CVD can be used to deposit various materials on a silicon substrate including SiO<sub>2</sub>, Si<sub>3</sub>N<sub>4</sub>, polysilicon, and so on. For instance, if silane gas and oxygen are allowed to react above a silicon substrate, the end product, silicon dioxide, will be deposited as a solid film on the silicon wafer surface. The properties of the CVD oxide layer are not as good as those of a thermally grown oxide, but they are sufficient to allow the layer to act as an electrical insulator. The advantage of a CVD layer is that the oxide deposits at a faster rate and a lower temperature (below 500°C).

If silane gas alone is used, then a silicon layer will be deposited on the wafer. If the reaction temperature is high enough (above 1000°C), the layer deposited will be a crystalline layer (assuming that there is an exposed crystalline silicon substrate). Such a layer is called an **epitaxial** layer, and the deposition process is referred to as **epitaxy** instead of CVD. At lower temperatures, or if the substrate surface is not single-crystal silicon, the atoms will not be able to align along the same crystalline direction. Such a layer is called polycrystalline

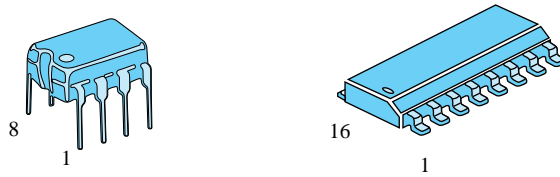


**Figure A.4** Examples of an 8-pin plastic dual-in-line IC package and a 16-pin surface-mount package.

silicon (**poly Si**), since it consists of many small crystals of silicon aligned in random fashion. Polysilicon layers are normally doped very heavily to form highly conductive regions that can be used for electrical interconnections.

### A.1.8 Metallization

The purpose of metallization is to interconnect the various components (transistors, capacitors, etc.) to form the desired integrated circuit. Metallization involves the deposition of a metal over the entire surface of the silicon. The required interconnection pattern is then selectively etched. The metal layer is normally deposited via a sputtering process. A pure metal disk (e.g., 99.99% aluminum target) is placed under an Ar (argon) ion gun inside a vacuum chamber. The wafers are also mounted inside the chamber above the target. The Ar ions will not react with the metal, since argon is a noble gas. However, the ions are made to physically bombard the target and literally knock metal atoms out of the target. These metal atoms will then coat all the surface inside the chamber, including the wafers. The thickness of the metal film can be controlled by the length of the sputtering time, which is normally in the range of 1 to 2 minutes. The metal interconnects can then be defined using photolithography and etching steps.

### A.1.9 Packaging

A finished silicon wafer may contain several hundreds of finished circuits or chips. A chip may contain from 10 to more than  $10^8$  transistors; each chip is rectangular and can be up to tens of millimeters on a side. The circuits are first tested electrically (while still in wafer form) using an automatic probing station. Bad circuits are marked for later identification. The circuits are then separated from each other (by dicing), and the good circuits (dies) are mounted in packages (headers). Examples of such IC packages are given in Fig. A.4. Fine gold wires are normally used to interconnect the pins of the package to the metallization pattern on the die. Finally, the package is sealed using plastic or epoxy under vacuum or in an inert atmosphere.

## A.2 VLSI Processes

Integrated-circuit fabrication technology was originally dominated by bipolar technology. By the late 1970s, metal oxide semiconductor (MOS) technology became more promising for VLSI implementation with higher packing density and lower power consumption. Since the early 1980s, complementary MOS (CMOS) technology has almost completely dominated the VLSI scene, leaving bipolar technology to fill specialized functions such as

high-speed analog and RF circuits. CMOS technologies continue to evolve, and in the late 1980s, the incorporation of bipolar devices led to the emergence of high-performance bipolar-CMOS (BiCMOS) fabrication processes that provided the best of both technologies. However, BiCMOS processes are often very complicated and costly, since they require upwards of 15 to 20 masking levels per implementation—standard CMOS processes by comparison require only 10 to 12 masking levels.

The performance of CMOS and BiCMOS processes continues to improve with finer lithography resolution. However, fundamental limitations on processing techniques and semiconductor properties have prompted the need to explore alternate materials. Newly emerged SiGe and strained-Si technologies are good compromises to improve performance while maintaining manufacturing compatibility (hence low cost) with existing silicon-based CMOS fabrication equipment.

In the subsection that follows, we will examine a typical CMOS process flow, the performance of the available components, and the inclusion of bipolar devices to form a BiCMOS process.

### A.2.1 Twin-Well CMOS Process

Depending on the choice of starting material (substrate), CMOS processes can be identified as ***n*-well**, ***p*-well**, or **twin-well** processes. The latter is the most complicated but most flexible in the optimization of both the *n* and *p*-channel MOSFETs. In addition, many advanced CMOS processes may make use of trench isolation and silicon-on-insulator (SOI) technology to reduce parasitic capacitance (hence higher speed) and to improve packing density.

A modern twin-well CMOS process flow is shown in Fig. A.5. A minimum of 10 masking layers is required. In practice, most CMOS processes will also require additional layers such as *n*- and *p*-guards for better latchup immunity, a second polysilicon layer for capacitors, and multilayer metals for high-density interconnections. The inclusion of these layers would increase the total number of 15 to 20 masking layers.

The starting material for the twin-well CMOS is a *p*-type substrate. The process begins with the formation of the *p*-well and the *n*-well (Fig. A.5a). The *n*-well is required wherever *p*-channel MOSFETs are to be placed, while the *p*-well is used to house the *n*-channel MOSFETs. The well-formation procedures are similar. A thick photoresist layer is etched to expose the regions for *n*-well diffusion. The unexposed regions will be protected from the *n*-type phosphorus impurity. Phosphorus implantation is usually used for deep diffusions, since it has a large diffusion coefficient and can diffuse faster than arsenic into the substrate.

The second step is to define the active regions (region where transistors are to be placed) using a technique called **shallow trench isolation** (STI). To reduce the chance of unwanted latchup (a serious issue in CMOS technology), dry etching is used to produce trenches approximately 0.3 μm deep on the silicon surface. These trenches are then refilled using CVD oxide, followed by a planarization procedure. This results in a cross section with flat surface topology (Fig. A.5b). An alternate isolation technique is called **local oxidation of silicon** (LOCOS). This older technology uses silicon nitride ( $\text{Si}_3\text{N}_4$ ) patterns to protect the penetration of oxygen during oxidation. This allows selective regions of the wafer surface to be oxidized. After a long wet-oxidation step, thick field oxide will appear in regions between transistors. This effectively produces an effect similar to that obtained in the STI process, but at the expense of large area overhead.

The next step is the formation of the polysilicon gate (Fig. A.5c). This is one of the most critical steps in the CMOS process. The thin oxide layer in the active region is first removed using wet etching followed by the growth of a high-quality thin gate oxide. Current deep-submicron CMOS processes routinely make use of oxide thicknesses as thin as 20 Å to 50 Å (1 angstrom =

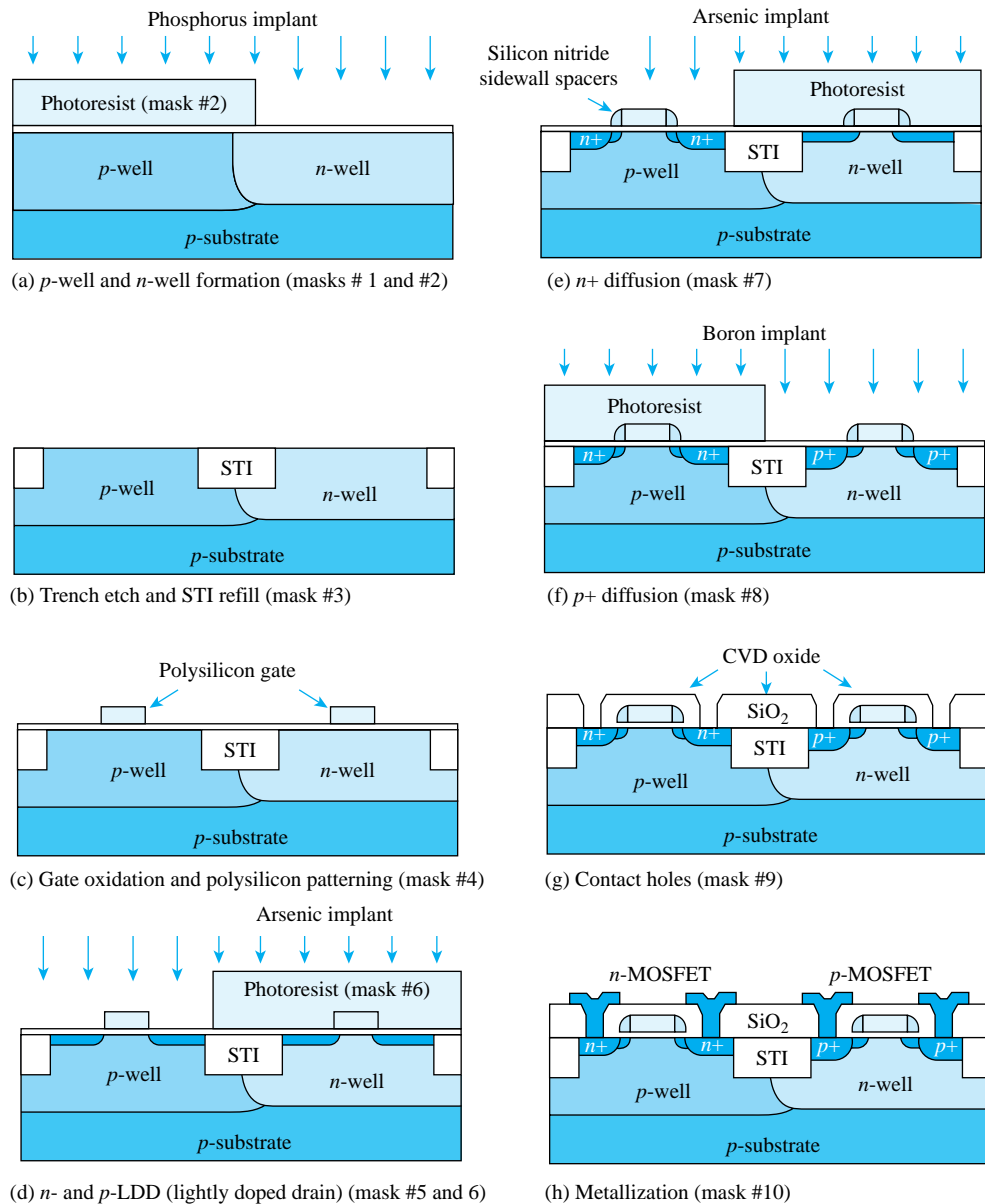


**Figure A.5** A modern twin-well CMOS process flow with shallow trench isolation (STI).

$10^{-8}$  cm). A polysilicon layer, usually arsenic doped ( $n$ -type), is then deposited and patterned. The photolithography is most demanding in this step since the finest resolution is required to produce the shortest possible MOS channel length.

The polysilicon gate is a self-aligned structure and is preferred over the older type of metal gate structure. This is normally accompanied by the formation of **lightly doped drain** (LDD) regions for MOSFETs of both types to suppress the generation of **hot electrons** that

might affect the reliability of the transistors. A noncritical mask, together with the polysilicon gates, is used to form the self-aligned LDD regions (Fig. A.5d).

Prior to the  $n+$  and  $p+$  drain region implant, a sidewall spacer step is performed. A thick layer of silicon nitride is deposited uniformly on the wafer. Due to the conformal nature of the deposition, the thickness of the silicon nitride layer at all layer edges (i.e., at both ends of the polysilicon gate electrode) will be thicker than those deposited over a flat surface. After a timed RIE dry etch to remove all the silicon nitride layer, pockets of silicon nitride will remain at the edge of the polysilicon gate electrode (Fig. A.5e). Such pockets of silicon nitride are called sidewall spacers. They are used to block subsequent  $n+$  or  $p+$  source/drain implants, protecting the LDD regions.

A heavy arsenic implant can be used to form the  $n+$  source and drain regions of the  $n$ -MOSFETs. The polysilicon gate also acts as a barrier for this implant to protect the channel region. A layer of photoresist can be used to block the regions where  $p$ -MOSFETs are to be formed (Fig. A.5e). The thick field oxide stops the implant and prevents  $n+$  regions from forming outside the active regions. A reversed photolithography step can be used to protect the  $n$ -MOSFETs during the  $p+$  boron source and drain implant for the  $p$ -MOSFETs (Fig. A.5f). Note that in both cases the separation between the source and drain diffusions—channel length—is defined by the polysilicon gate mask alone, hence the self-aligned property.

Before contact holes are opened, a thick layer of CVD oxide is deposited over the entire wafer. A photomask is used to define the contact window opening (Fig. A.5g), followed by a wet or dry oxide etch. A thin aluminum layer is then evaporated or sputtered onto the wafer. A final masking and etching step is used to pattern the interconnection (Fig. A.5h).

Not shown in the process flow is the final passivation step prior to packaging and wire bonding. A thick CVD oxide or pyrox glass is usually deposited on the wafer to serve as a protective layer.

## A.2.2 Integrated Devices

Besides the obvious  $n$  and  $p$ -channel MOSFETs, other devices can be obtained by appropriate masking patterns. These include  $pn$  junction diodes, MOS capacitors, and resistors.

## A.2.3 MOSFETs

The  $n$ -channel MOSFET is the preferred device in comparison to the  $p$ -MOSFET (Fig. A.6). The electron surface mobility is two to three times higher than that for holes. Therefore, with the same device size ( $W$  and  $L$ ), the  $n$ -MOSFET offers higher current drive (or lower on-resistance) and higher transconductance.

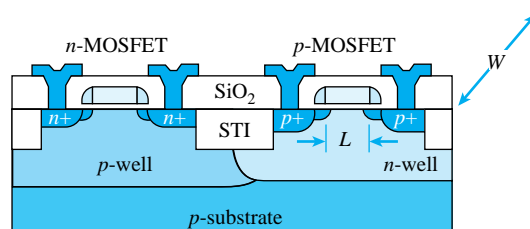


**Figure A.6** Cross-sectional diagram of  $n$ - and  $p$ -MOSFETs.

In an integrated-circuit design environment, MOSFETs are characterized by their threshold voltage and by their device sizes. Usually the  $n$ - and  $p$ -channel MOSFETs are designed to have threshold voltages of similar magnitude for a particular process. The transconductance can be adjusted by changing the device surface dimensions ( $W$  and  $L$ ). This feature is not available for bipolar transistor, making the design of integrated MOSFET circuits much more flexible.

### A.2.4 Resistors

Resistors in integrated form are not very precise. They can be made from various diffusion regions as shown in Fig. A.7. Different diffusion regions have different resistivity. The  $n$  well is usually used for medium-value resistors, while the  $n+$  and  $p+$  diffusions are useful for low-value resistors. The actual resistance value can be defined by changing the length and width of diffused regions. The tolerance of the resistor value is very poor (20–50%), but the matching of two similar resistor values is quite good (5%). Thus circuit designers should design circuits that exploit resistor matching and should avoid designs that require a specific resistor value.

All diffused resistors are self-isolated by the reverse-biased  $pn$  junctions. A serious drawback for these resistors is the fact that they are accompanied by a substantial parasitic junction capacitance, making them not very useful for high-frequency applications. The reverse-biased  $pn$  junctions also exhibit a JFET effect, leading to a variation in the resistance value as the supply voltage is changed (a large voltage coefficient is undesirable). Since the mobilities of carriers vary with temperature, diffused resistors also exhibit a significant temperature coefficient.

A more useful resistor can be fabricated using the polysilicon layer that is placed on top of the thick field oxide. The thin polysilicon layer provides better surface area matching and hence more accurate resistor ratios. Furthermore, the polyresistor is physically separated from the substrate, resulting in a much lower parasitic capacitance and voltage coefficient.

### A.2.5 Capacitors

Two types of capacitor structure are available in CMOS processes: MOS and interpoly capacitors. The latter are also similar to metal–insulator–metal (MIM) capacitors. The cross sections of these structures are as shown in Fig. A.8. The MOS gate capacitance, depicted by the center structure, is basically the gate-to-source capacitance of a MOSFET. The capacitance value is dependent on the gate area. The oxide thickness is the same as the gate oxide

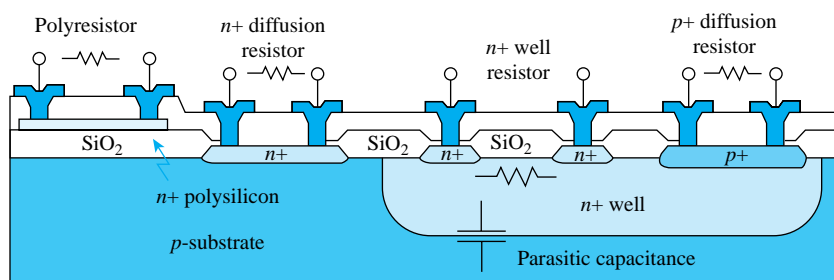


**Figure A.7** Cross sections of various resistor types available from a typical  $n$ -well CMOS process.

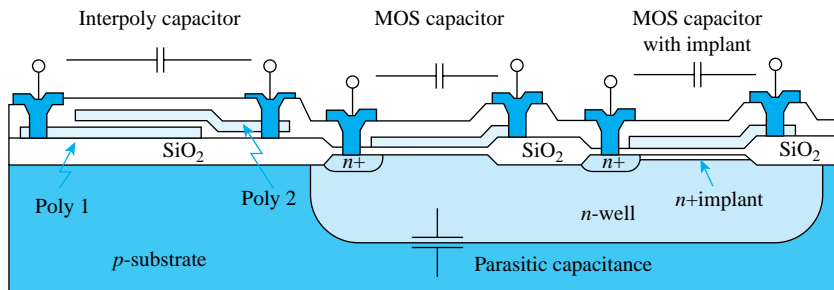


**Figure A.8** Interpoly and MOS capacitors in an *n*-well CMOS process.

thickness in the MOSFETs. This capacitor exhibits a large voltage dependence. To eliminate this problem, an addition *n*<sub>+</sub> implant is required to form the bottom plate of the capacitors, as shown in the structure on the right. Both these MOS capacitors are physically in contact with the substrate, resulting in a large parasitic *pn* junction capacitance at the bottom plate.

The interpoly capacitor exhibits near-ideal characteristics but at the expense of the inclusion of a second polysilicon layer to the CMOS process. Since this capacitor is placed on top of the thick field oxide, parasitic effects are kept to a minimum.

A third and less often used capacitor is the junction capacitor. Any *pn* junction under reversed bias produces a depletion region that acts as a dielectric between the *p* and the *n* regions. The capacitance is determined by geometry and doping levels and has a large voltage coefficient. This type of capacitor is often used as a varactor (variable capacitor) for tuning circuits. However, this capacitor works only with reverse-bias voltages.

For the interpoly and MOS capacitors, the capacitance values can be controlled to within 1%. Practical capacitance values range from 0.5 pF to a few tens of picofarads. The matching between capacitors of similar size can be within 0.1%. This property is extremely useful for designing precision analog CMOS circuits.

## A.2.6 *pn* Junction Diodes

Whenever *n*-type and *p*-type diffusion regions are placed next to each other, a *pn* junction diode results. A useful structure is the *n*-well diode shown in Fig. A.9. The diode fabricated in an *n* well can provide a high breakdown voltage. This diode is essential for the input clamping circuits for protection against electrostatic discharge. The diode is also very useful as an on-chip temperature sensor by monitoring the variation of its forward voltage drop.

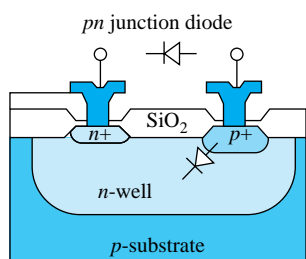


**Figure A.9** A *pn* junction diode in an *n*-well CMOS process.

### A.2.7 BiCMOS Process

An *npn* vertical bipolar transistor can be integrated into the *n*-well CMOS process with the addition of a *p*-base diffusion region (Fig. A.10). The characteristics of this device depend on the base width and the emitter area. The base width is determined by the difference in junction depth between the *n*<sub>+</sub> and the *p*-base diffusions. The emitter area is determined by the junction area of the *n*<sub>+</sub> diffusion at the emitter. The *n*-well serves as the collector for the *npn* transistor. Typically, the *npn* transistor has a  $\beta$  in the range of 50 to 100 and a cutoff frequency of greater than tens of gigahertz.

Normally, an *n*<sub>+</sub> buried layer is used to reduce the series resistance of the collector, since the *n* well has a very high resistivity. However, this would further complicate the process by introducing *p*-type epitaxy and one more masking step. Other variations on the bipolar transistor includes poly-emitter and self-aligned base contact to minimize parasitic effects.

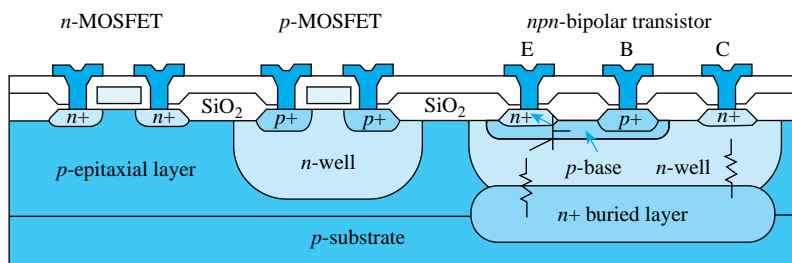


Figure A.10 Cross-sectional diagram of a BiCMOS process.

### A.2.8 Lateral *pnp* Transistor

The fact that most BiCMOS processes do not have optimized *pnp* transistors makes circuit design somewhat difficult. However, in noncritical situations, a parasitic lateral *pnp* transistor can be used (Fig. A.11).

In this case, the *n* well serves as the *n*-base region, with the *p*<sub>+</sub> diffusions as the emitter and the collector. The base width is determined by the separation between the two *p*<sub>+</sub> diffusions. Since the doping profile is not optimized for the base–collector junctions and because the base width is limited by the minimum photolithographic resolution, the performance of this device is not very good: typically,  $\beta$  of around 10, and the cutoff frequency is low.

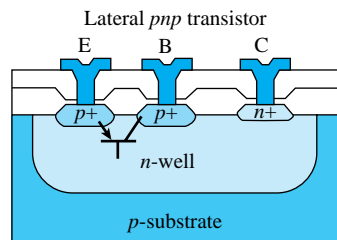
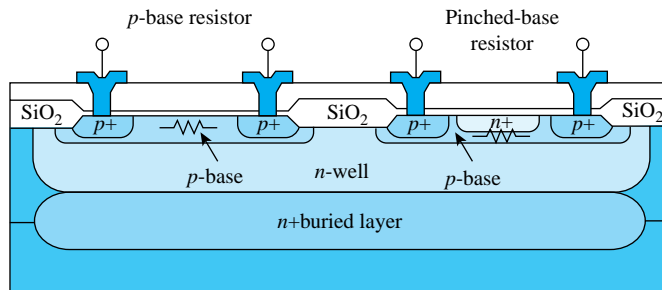


Figure A.11 Lateral *pnp* transistor.

### A.2.9 *p*-Base and Pinched-Base Resistors

With the additional *p*-base diffusion in the BiCMOS process, two additional resistor structures are available. The *p*-base diffusion can be used to form a straightforward *p*-base



**Figure A.12** *p*-base and pinched *p*-base resistors.

resistor as shown in Fig. A.12. Since the base region is usually of a relatively low doping level and has a moderate junction depth, it is suitable for medium-value resistors (a few kilohms). If a large resistor value is required, the pinched-base resistor can be used. In this structure, the *p*-base region is encroached by the *n*<sup>+</sup> diffusion, restricting the conduction path. Resistor values in the range of 10 kΩ to 100 kΩ can be obtained. As with the diffusion resistors discussed earlier, these resistors exhibit poor tolerance and temperature coefficients but relatively good matching.

### A.2.10 SiGe BiCMOS Process

With the burgeoning of wireless applications, the demand for high-performance, high-frequency RF integrated circuits is tremendous. Owing to the fundamental limitations of physical material properties, silicon-based technology was not able to compete with more expensive technologies relying on compounds from groups III through IV, such as GaAs. By incorporating a controlled amount (typically no more than 15–20% mole fraction) of germanium (Ge) into crystal silicon (Si) in the BJT's base region, the energy bandgap can be altered. The specific concentration profile of the Ge can be engineered in such a way that the energy bandgap can be gradually reduced from the pure Si region to a lower value in the SiGe region. This energy bandgap reduction produces a built-in electric field that can assist the movement of carriers, hence resulting in faster operating speed. Therefore, SiGe bipolar transistors can achieve significant higher cutoff frequency (e.g., in the 100–200 GHz range). Another benefit is that the SiGe process is compatible with existing Si-based fabrication technology, ensuring a very favorable cost/performance ratio.

To take advantage of the SiGe material characteristics, the basic bipolar transistor structure must also be modified to further reduce parasitic capacitance (for higher speed) and to improve the injection efficiency (for higher gain). A symmetric bipolar device structure is shown in Fig. A.13. The device made use of trench isolation to reduce the collector sidewall capacitance between the *n*-well/*n*<sup>+</sup> buried layer and the *p* substrate. The emitter size and the *p*<sup>+</sup> base contact size are defined by a self-aligned process to minimize the base–collector junction (Miller) capacitance. This type of device is called a heterojunction bipolar transistor (HBT) since the emitter–base junction is formed from two different types of material, polysilicon emitter and SiGe base. The injection efficiency is significantly better than a homojunction device (as in a conventional BJT). This advantage, coupled with the fact that base width is typically only around 50 nm, makes it easy to achieve current gain of more than 100. In addition, not shown in Fig. A.13, is the possible use of multiple layers of metalization to further reduce the device size and interconnect resistance. All these device features are necessary to complement the high-speed performance of SiGe material.

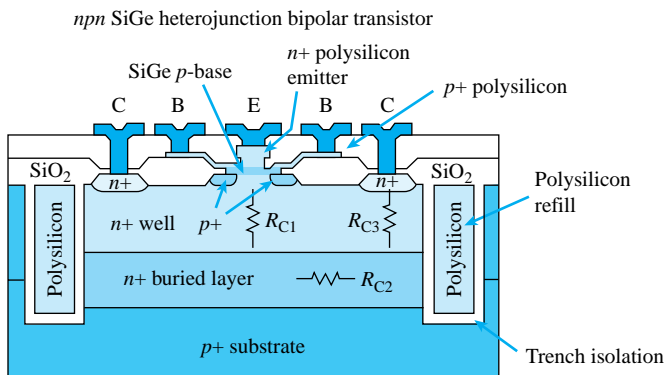


**Figure A.13** Cross-sectional diagram of a symmetric self-aligned SiGe heterojunction bipolar transistor, or HBT.

### A.3 VLSI Layout

The designed circuit schematic must be transformed into a layout that consists of the geometric representation of the circuit components and interconnections. Today, computer-aided design tools allow many of the conversion steps, from schematic to layout, to be carried out semi- or fully automatically. However, any good mixed-signal IC designer must have practiced full custom layout at one point or another. An example of a CMOS inverter can be used to illustrate this procedure (Fig. A.14).

The circuit must first be “flattened” and redrawn to eliminate any interconnection crossovers, similar to the requirement of a printed-circuit-board layout. Each process is made up of a specific set of masking layers. In this case, seven layers are used. Each layer is usually assigned a unique color and fill pattern for ease of identification on a computer screen or on a printed color plot. The layout begins with the placement of the transistors. For illustration purposes, the *p* and *n* MOSFETs are placed in an arrangement similar to that shown in the schematic. In practice, the designer is free to choose the most area-efficient layout. The MOSFETs are defined by the active areas overlapped by the “poly 1” layer. The MOS channel length and width are defined by the width of the “poly 1” strip and that of the active region, respectively. The *p*-MOSFET is enclosed in an *n* well. For more complex circuits, multiple *n* wells can be used for different groups of *p*-MOSFETs. The *n*-MOSFET is enclosed by the *n*+ diffusion mask to form the source and drain, while the *p*-MOSFET is enclosed by the *p*+ diffusion mask. Contact holes are placed in regions where connection to the metal layer is required. Finally, the “metal 1” layer completes the interconnections.

The corresponding cross-sectional diagram of the CMOS inverter along the AA' plane is as shown in Fig. A.15. The poly-Si gates for both transistors are connected to form the input terminal, *X*. The drains of both transistors are tied together via “metal 1” to form the output terminal, *Y*. The sources of the *n*- and *p*-MOSFETs are connected to GND and  $V_{DD}$ , respectively. Note that butting contacts consist of side-by-side *n*+/*p*+ diffusions that are used to tie the body potential of the *n*- and *p*-MOSFETs to the appropriate voltage levels.

When the layout is completed, the circuit must be verified using CAD tools such as the circuit extractor, the design rule checker (DRC), and the circuit simulator. Once these

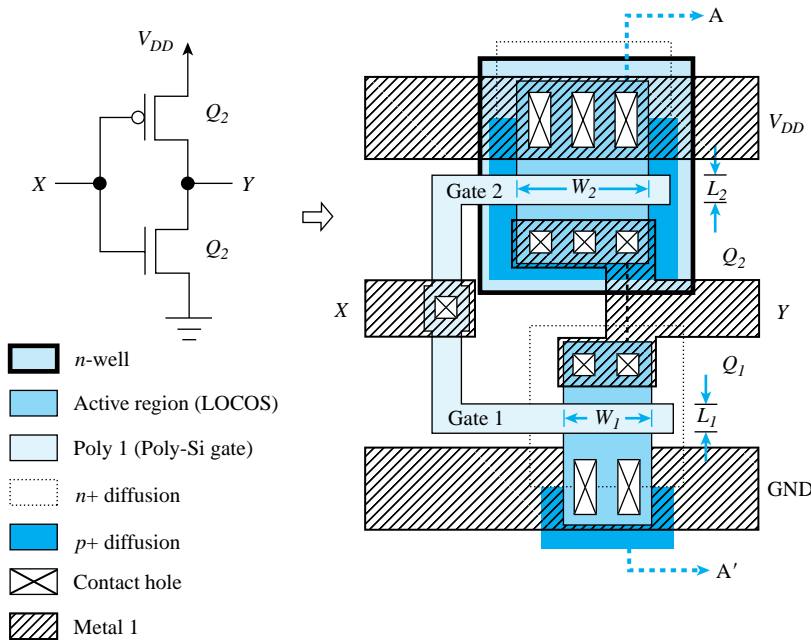


**Figure A.14** A CMOS inverter schematic and its layout.

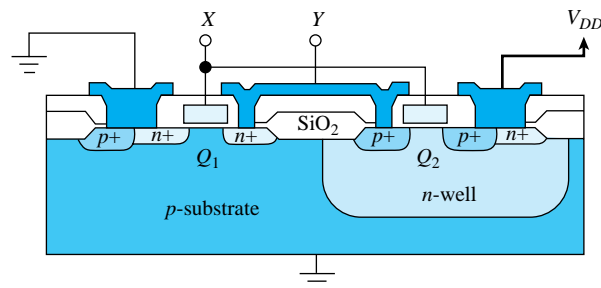


**Figure A.15** Cross section along the plane AA' of a CMOS inverter. Note that this particular layout is good for illustration purposes, but is not necessarily appropriate for latchup prevention.

verifications have been satisfied, the design can be “taped out” to a mask-making facility. A pattern generator (PG) machine can then draw the geometries on a glass or quartz photoplate using electronically driven shutters. Layers are drawn one by one onto different photoplates. After these plates have been developed, clear and dark patterns resembling the geometries on the layout will result. A set of the photoplates for the CMOS inverter example is shown in Fig. A.16. Depending on whether the drawn geometries are meant to be opened as windows or kept as patterns, the plates can be **clear** or **dark field**. Note that each of these layers must be processed in sequence. The layers must be aligned within very fine tolerance to form the transistors and interconnections. Naturally, the greater the number of layers, the more difficult it is to maintain the alignment. This also requires better photolithography

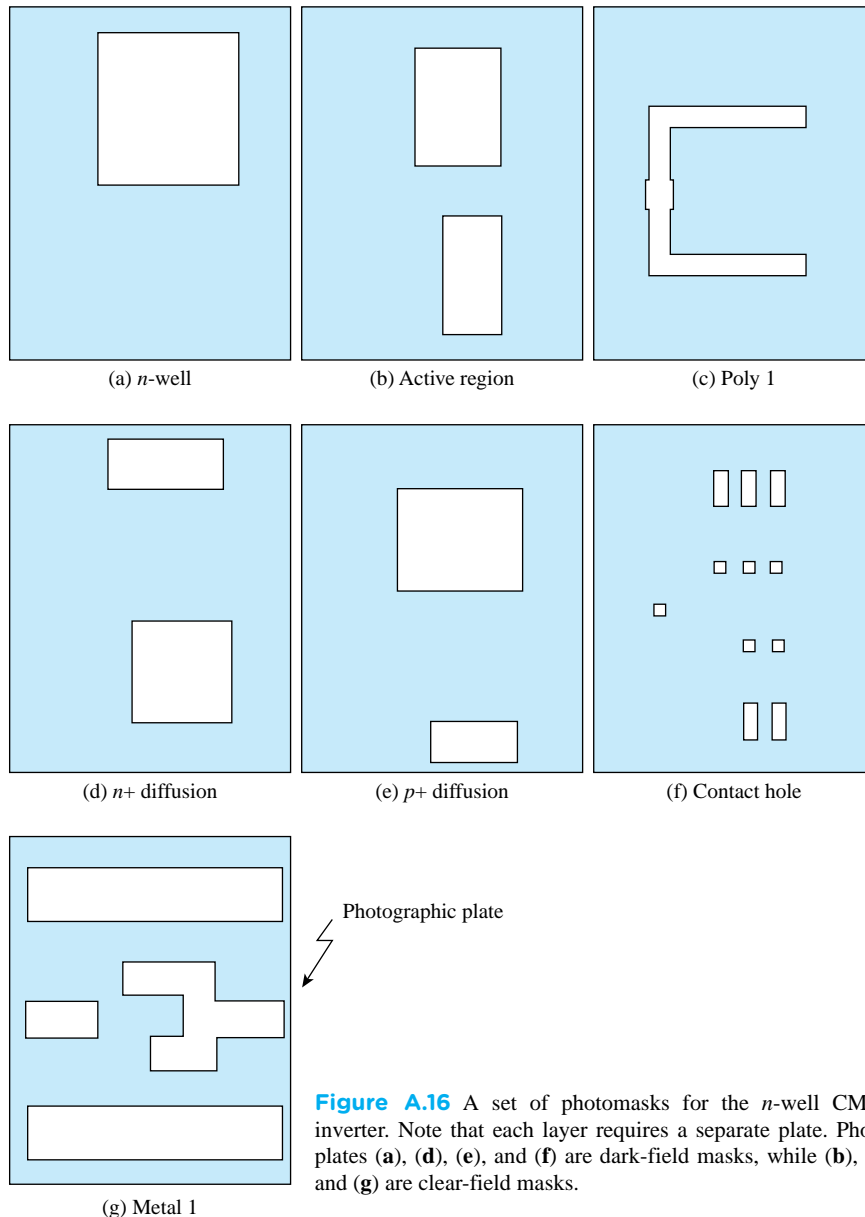


**Figure A.16** A set of photomasks for the  $n$ -well CMOS inverter. Note that each layer requires a separate plate. Photo-plates (a), (d), (e), and (f) are dark-field masks, while (b), (c), and (g) are clear-field masks.

equipment and may result in lower yield. Hence, each additional mask will be reflected in an increase in the final cost of the IC chip.

## Summary

This appendix presents an overview of the various aspects of VLSI fabrication procedures. This includes component characteristics, process flows, and layouts. This is by no means a

complete account of state-of-the-art VLSI technologies. Interested readers should consult other references on this subject for more detailed descriptions.

## Bibliography

J. D. Plummer, M.D. Deal, and P.B. Griffin, *Silicon VLSI Technology*, Upper Saddle River, NJ, Prentice Hall, 2000.

R. S. Muller, T.I. Kamins, and M. Chan, *Device Electronics for Integrated Circuits*, 3rd ed., Hoboken, NJ, John Wiley & Sons, 2003.

S. Wolf, *Microchip Manufacturing*, Lattice Press ([www.latticepress.com](http://www.latticepress.com)), 2004.

## APPENDIX B

# SPICE DEVICE MODELS AND DESIGN SIMULATION EXAMPLES USING PSPICE AND MULTISIM

## Introduction

This appendix is concerned with the very important topic of using PSpice and Multisim to simulate the operation of electronic circuits. The need for and the role of computer simulation in circuit design was described in the preface. The appendix has three sections: Section B.1 presents a brief description of the models that SPICE uses to describe the operation of op amps, diodes, MOSFETs, and BJTs. Section B.2 presents design and simulation examples using PSpice. Finally, design and simulation examples utilizing Multisim are presented in Section B.3.

Besides the descriptions presented in this appendix, the reader will find the complete simulation files for each example on the CD accompanying the book.

## B.1 SPICE Device Models

To the designer, the value of simulation results is a direct function of the quality of the models used for the devices. The more faithfully the model represents the various characteristics of the device, the more accurately the simulation results will describe the operation of an actual fabricated circuit. In other words, to see the effect on circuit performance of various imperfections in device operation, these imperfections must be included in the device model used by the circuit simulator.

### B.1.1 The Op-Amp Model

In simulating circuits that use one or more op amps, it is useful to utilize a **macromodel** to represent each op amp. A macromodel is based on the observed terminal characteristics of the op amp rather than on the modeling of every transistor in the op-amp internal circuit. Macromodels can be developed from data-sheet specifications without knowledge of the details of the internal circuitry of the op amp.

**Linear Macromodel** The schematic capture of a linear macromodel for an internally compensated op amp with finite gain and bandwidth is shown in Fig. B.1. In this equivalent-circuit model, the gain constant  $A_{0d}$  of the voltage-controlled voltage source  $E_d$  corresponds

to the differential gain of the op amps at dc. Resistor  $R_b$  and capacitor  $C_b$  form a single-time-constant (STC) filter with a corner frequency

$$f_b = \frac{1}{2\pi R_b C_b} \quad (\text{B.1})$$

The low-pass response of this filter is used to model the frequency response of the internally compensated op amp. The values of  $R_b$  and  $C_b$  used in the macromodel are chosen such that  $f_b$  corresponds to the 3-dB frequency of the op amp being modeled. This is done by arbitrarily selecting a value for either  $R_b$  or  $C_b$  (the selected value does not need to be a practical one) and then using Eq. (B.1) to compute the other value. In Fig. B.1, the voltage-controlled voltage source  $E_b$  with a gain constant of unity is used as a buffer to isolate the low-pass filter from any load at the op-amp output. Thus any op-amp loading will not affect the frequency response of the filter and hence that of the op amp.

The linear macromodel in Fig. B.1 can be further expanded to account for other op-amp nonidealities. For example, the equivalent-circuit model in Fig. B.2 can be used to model an internally compensated op amp while accounting for the following op-amp nonidealities:

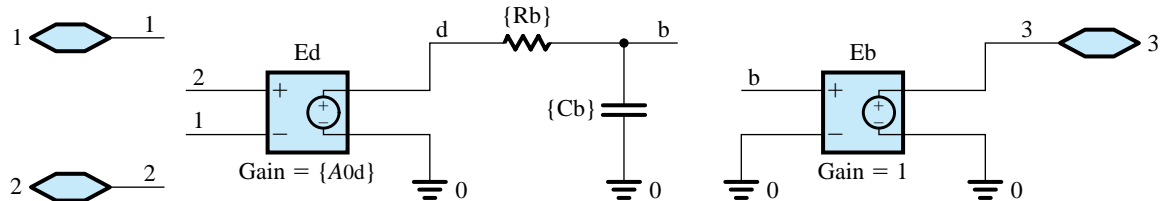


**Figure B.1** A linear macromodel used to model the finite gain and bandwidth of an internally compensated op amp.

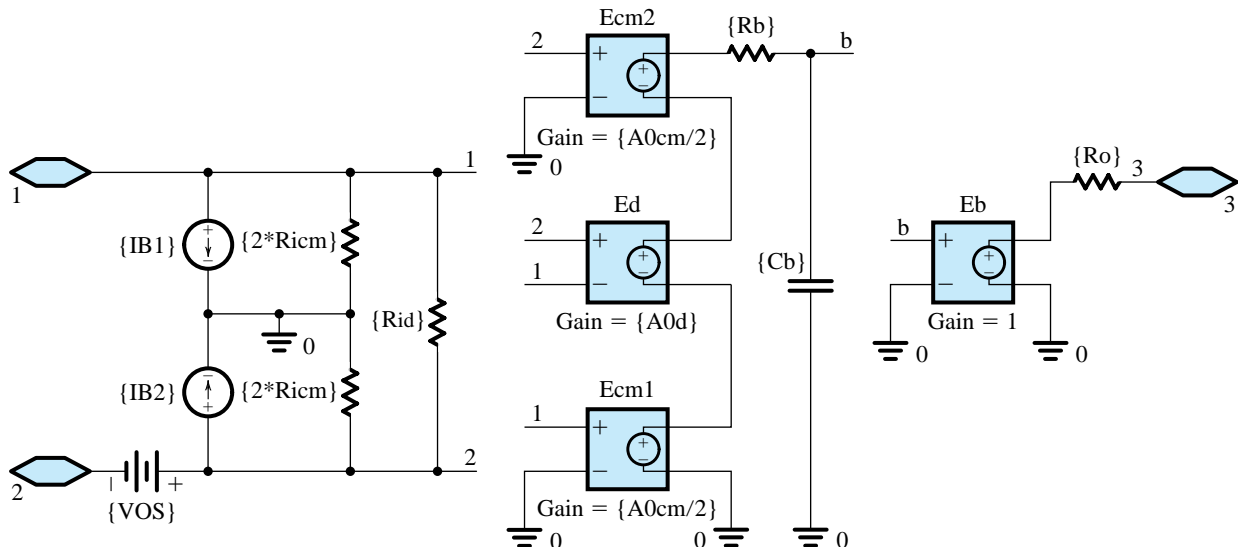


**Figure B.2** A comprehensive linear macromodel of an internally compensated op amp.

- 1. Input Offset Voltage ( $V_{os}$ ).** The dc voltage source  $V_{os}$  models the op-amp input offset voltage.
- 2. Input Bias Current ( $I_B$ ) and Input Offset Current ( $I_{os}$ ).** The dc current sources  $I_{B1}$  and  $I_{B2}$  model the input bias current at each input terminal of the op amp, with

$$I_{B1} = I_B + \frac{I_{os}}{2} \quad \text{and} \quad I_{B2} = I_B - \frac{I_{os}}{2}$$

where  $I_B$  and  $I_{os}$  are, respectively, the input bias current and the input offset current specified by the op-amp manufacturer.

- 3. Common-Mode Input Resistance ( $R_{icm}$ ).** If the two input terminals of an op amp are tied together and the input resistance (to ground) is measured, the result is the common-mode input resistance  $R_{icm}$ . In the macromodel of Fig. B.2, we have split  $R_{icm}$  into two equal parts ( $2R_{icm}$ ), each connected between one of the input terminals and ground.
- 4. Differential-Input Resistance ( $R_{id}$ ).** The resistance seen between the two input terminals of an op amp is the differential input resistance  $R_{id}$ .
- 5. Differential Gain at DC ( $A_{0d}$ ) and Common-Mode Rejection Ratio (CMRR).** The output voltage of an op amp at dc can be expressed as

$$V_3 = A_{0d}(V_2 - V_1) + \frac{A_{0cm}}{2}(V_1 + V_2) \quad (\text{B.2})$$

where  $A_{0d}$  and  $A_{0cm}$  are, respectively, the differential and common-mode gains of the op amp at dc. For an op amp with a finite CMRR,

$$A_{0cm} = A_{0d}/\text{CMRR} \quad (\text{B.3})$$

where CMRR is expressed in V/V (not in dB). In the macromodel of Fig. B.2, the voltage-controlled voltage sources  $E_{cm1}$  and  $E_{cm2}$  with gain constants of  $A_{0cm}/2$  account for the finite CMRR while source  $E_d$  models  $A_{0d}$ .

- 6. Unity-Gain Frequency ( $f_b$ ).** From Eq. (2.46), the 3-dB frequency  $f_b$  and the unity-gain frequency (or gain-bandwidth product)  $f_t$  of an internally compensated op amp with an STC frequency response are related by

$$f_b = \frac{f_t}{A_{0d}} \quad (\text{B.4})$$

As in Fig. B.1, the finite op-amp bandwidth is accounted for in the macromodel of Fig. B.2 by setting the corner frequency of the filter formed by resistor  $R_b$  and capacitor  $C_b$  (Eq. B.1) to equal the 3-dB frequency of the op amp,  $f_b$ .

- 7. Output Resistance ( $R_o$ ).** The resistance seen at the output terminal of an op amp is the output resistance  $R_o$ .

The linear macromodels in Figs. B.1 and B.2 assume that the op-amp circuit is operating in its linear range and do not account for its nonideal performance when large signals are present at the output. Therefore, nonlinear effects, such as output saturation and slew rate, are not modeled.

**Nonlinear Macromodel** The linear macromodel in Fig. B.2 can be expanded to account for the op-amp nonlinear performance. For example, the finite output voltage swing of the op amp can be modeled by placing limits on the output voltage of the voltage-controlled voltage

source  $E_b$ . In PSpice, this can be done using the ETABLE component in the analog-behavioral-modeling (ABM) library and setting the output voltage limits in the lookup table of this component. Further details on how to build nonlinear macromodels for the op amp can be found in the references on SPICE simulation. In general, robust macromodels that account for the nonlinear effects in an IC are provided by the op-amp manufacturers. Most simulators include such macromodels for some of the popular off-the-shelf ICs in their libraries. For example, PSpice and Multisim include models for the  $\mu$ A741, the LF411, and the LM324 op amps.

### B.1.2 The Diode Model

The large-signal SPICE model for the diode is shown in Fig. B.3. The static behavior is modeled by the exponential  $i-v$  relationship. Here, for generality, a constant  $n$  is included in the exponential. It is known as the **emission coefficient**, and its value ranges from 1 to 2. In our study of the diode in Chapter 3, we assumed  $n = 1$ . The dynamic behavior is represented by the nonlinear capacitor  $C_D$ , which is the sum of the diffusion capacitance  $C_d$  and the junction capacitance  $C_j$ . The series resistance  $R_s$  represents the total resistance of the  $p$  and  $n$  regions on both sides of the junction. The value of this parasitic resistance is ideally zero, but it is typically in the range of a few ohms for small-signal diodes. For small-signal analysis, SPICE uses the diode incremental resistance  $r_d$  and the incremental values of  $C_d$  and  $C_j$ .

Table B.1 provides a partial listing of the diode-model parameters used by SPICE, all of which should be familiar to the reader. But having a good device model solves only half of the modeling problem; the other half is to determine appropriate values for the model parameters. This is by no means an easy task. The values of the model parameters are determined using a combination of characterization of the device-fabrication process and specific measurements performed on the actual manufactured devices. Semiconductor manufacturers expend enormous effort and money to extract the values of the model parameters for their devices. For discrete diodes, the values of the SPICE model parameters can be determined from the diode data sheets, supplemented if needed by key measurements. Circuit simulators (such as PSpice) include in their libraries the model parameters of some of the popular off-the-shelf components. For instance, in Example PS4.1, we will use the commercially available D1N418  $pn$ -junction diode whose SPICE model parameters are available in PSpice.

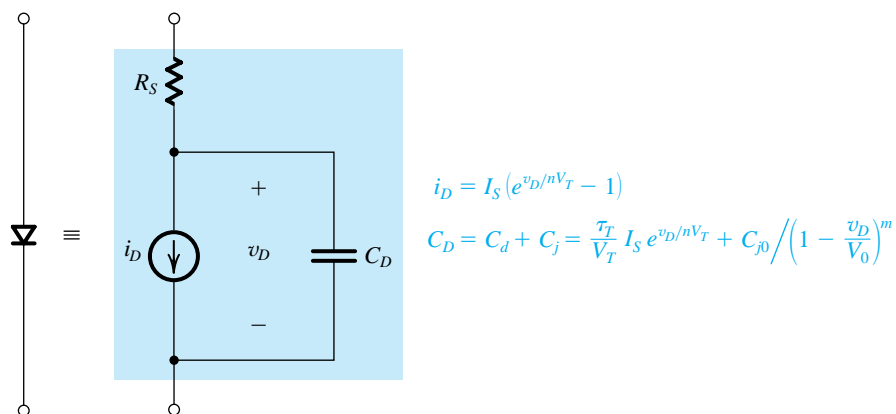


**Figure B.3** The SPICE diode model.

**Table B.1** Parameters of the SPICE Diode Model (Partial Listing)

SPICE Parameter	Book Symbol	Description	Units
IS	$I_s$	Saturation current	A
N	$n$	Emission coefficient	
RS	$R_s$	Ohmic resistance	$\Omega$
VJ	$V_0$	Built-in potential	V
CJO	$C_{j0}$	Zero-bias depletion (junction) capacitance	F
M	$m$	Grading coefficient	
TT	$\tau_T$	Transit time	s
BV	$V_{ZK}$	Breakdown voltage	V
IBV	$I_{ZK}$	Reverse current at $V_{ZK}$	A

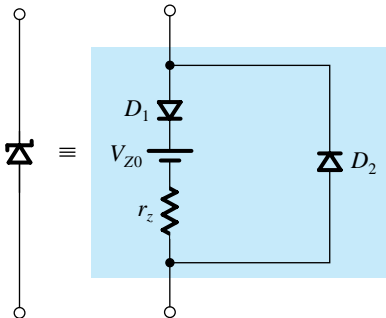


**Figure B.4** Equivalent-circuit model used to simulate the zener diode in SPICE. Diode  $D_1$  is ideal and can be approximated in SPICE by using a very small value for  $n$  (say  $n = 0.01$ ). Diode  $D_2$  is a regular diode that models the forward-bias region of the zener (for most applications, the parameters of  $D_2$  are of little consequence).

### B.1.3 The Zener Diode Model

The diode model in Fig. B.3 does not adequately describe the operation of the diode in the breakdown region. Hence, it does not provide a satisfactory model for zener diodes. However, the equivalent-circuit model shown in Fig. B.4 can be used to simulate a zener diode in SPICE. Here, diode  $D_1$  is an ideal diode that can be approximated in SPICE by using a very small value for  $n$  (say  $n = 0.01$ ). Diode  $D_2$  is a regular diode that models the forward-bias region of the zener (for most applications, the parameters of  $D_2$  are of little consequence).

### B.1.4 MOSFET Models

To simulate the operation of a MOSFET circuit, a simulator requires a mathematical model to represent the characteristics of the MOSFET. The model we derived in Chapter 5 to represent the MOSFET is a simplified or first-order model. This model, called the **square-law model** because of the quadratic  $i-v$  relationship in saturation, works well for transistors with relatively *long* channels. However, for devices with *short* channels, especially deep-submicron transistors, many physical effects that we neglected come into play, with the result that the derived first-order model no longer accurately represents the actual operation of the MOSFET (see Section 14.5).

The simple square-law model is useful for understanding the basic operation of the MOSFET as a circuit element and is indeed used to obtain approximate pencil-and-paper circuit designs. However, more elaborate models, which account for short-channel effects, are required to be able to predict the performance of integrated circuits with a certain degree of precision prior to fabrication. Such models have indeed been developed and continue to

be refined to more accurately represent the higher-order effects in short-channel transistors through a mix of physical relationships and empirical data. Examples include the Berkeley short-channel IGFET model (BSIM) and the EKV model, popular in Europe. Currently, semiconductor manufacturers rely on such sophisticated models to accurately represent the fabrication process. These manufacturers select a MOSFET model and then extract the values for the corresponding model parameters using both their knowledge of the details of the fabrication process and extensive measurements on a variety of fabricated MOSFETs. A great deal of effort is expended on extracting the model parameter values. Such effort pays off in fabricated circuits exhibiting performance very close to that predicted by simulation, thus reducing the need for costly redesign.

Although it is beyond the scope of this book to delve into the subject of MOSFET modeling and short-channel effects, it is important that the reader be aware of the limitations of the square-law model and of the availability of more accurate but, unfortunately, more complex MOSFET models. In fact, the power of computer simulation is more apparent when one has to use these complex device models in the analysis and design of integrated circuits.

SPICE-based simulators, like PSpice and Multisim, provide the user with a choice of MOSFET models. The corresponding SPICE model parameters (whose values are provided by the semiconductor manufacturer) include a parameter called LEVEL, which selects the MOSFET model to be used by the simulator. Although the value of this parameter is not always indicative of the accuracy, nor of the complexity of the corresponding MOSFET model, LEVEL = 1 corresponds to the simplest first-order model (called the Shichman-Hodges model), which is based on the square-law MOSFET equations presented in Chapter 5. For simplicity, we will use this model to illustrate the description of the MOSFET model parameters in SPICE and to simulate the example circuits in PSpice and Multisim. However, the reader is again reminded of the need to use a more sophisticated model than the level-1 model to accurately predict the circuit performance, especially for deep, sub-micron transistors.

**MOSFET Model Parameters** Table B.2 provides a listing of some of the MOSFET model parameters used in the level-1 model of SPICE. The reader should already be familiar with these parameters, except for a few, which are described next.

**MOSFET Diode Parameters** For the two reverse-biased diodes formed between each of the source and drain diffusion regions and the body (see Fig B.4), the saturation-current density is modeled in SPICE by the parameter JS. Furthermore, based on the parameters specified in Table B.2, SPICE will calculate the depletion-layer (junction) capacitances discussed in Section 8.2.1 as

$$C_{db} = \frac{CJ}{\left(1 + \frac{V_{DB}}{PB}\right)^{MJ}} AD + \frac{CJSW}{\left(1 + \frac{V_{DB}}{PB}\right)^{MJSW}} PD \quad (B.5)$$

$$C_{sb} = \frac{CJ}{\left(1 + \frac{V_{SB}}{PB}\right)^{MJ}} AS + \frac{CJSW}{\left(1 + \frac{V_{SB}}{PB}\right)^{MJSW}} PS \quad (B.6)$$

where AD and AS are the areas, while PD and PS are the perimeters of, respectively, the drain and source regions of the MOSFET. The first capacitance term in Eqs. (B.5) and (B.6) represents the depletion-layer (junction) capacitance over the bottom plate of the drain and source regions. The second capacitance term accounts for the depletion-layer capacitance along the sidewall (periphery) of these regions. Both terms are expressed using the formula

**Table B.2** Parameters of the SPICE Level-1 MOSFET Model (Partial Listing)

SPICE Parameter	Book Symbol	Description	Units
<b>Basic Model Parameters</b>			
LEVEL		MOSFET model selector	
TOX	$t_{ox}$	Gate-oxide thickness	m
COX	$C_{ox}$	Gate-oxide capacitance, per unit area	F/m <sup>2</sup>
UO	$\mu$	Carrier mobility	cm <sup>2</sup> /V·s
KP	$k'$	Process transconductance parameter	A/V <sup>2</sup>
LAMBDA	$\lambda$	Channel-length modulation coefficient	V <sup>-1</sup>
<b>Threshold Voltage Parameters</b>			
VTO	$V_{t0}$	Zero-bias threshold voltage	V
GAMMA	$\gamma$	Body-effect parameter	V <sup>1/2</sup>
NSUB	$N_A, N_D$	Substrate doping	cm <sup>-3</sup>
PHI	$2\Phi_f$	Surface inversion potential	V
<b>MOSFET Diode Parameters</b>			
JS		Body-junction saturation-current density	A/m <sup>2</sup>
CJ		Zero-bias body-junction capacitance, per unit area over the drain/source region	F/m <sup>2</sup>
MJ		Grading coefficient, for area component	
CJSW		Zero-bias body-junction capacitance, per unit length along F/m the sidewall (periphery) of the drain/source region	
MJSW		Grading coefficient, for sidewall component	
PB	$V_0$	Body-junction built-in potential	V
<b>MOSFET Dimension Parameters</b>			
LD	$L_{ov}$	Lateral diffusion into the channel from the source/drain diffusion regions	m
WD		Sideways diffusion into the channel from the body along the width	m
<b>MOS Gate-Capacitance Parameters</b>			
CGBO		Gate-body overlap capacitance, per unit channel length	F/m
CGDO	$C_{ov}/W$	Gate-drain overlap capacitance, per unit channel width	F/m
CGSO	$C_{ov}/W$	Gate-source overlap capacitance, per unit channel width	F/m

developed in Section 1.12.1 (Eq. 1.80). The values of AD, AS, PD, and PS must be specified by the user based on the dimensions of the device being used.

**MOSFET Dimension and Gate-Capacitance Parameters** In a fabricated MOSFET, the effective channel length  $L_{eff}$  is shorter than the nominal (or drawn) channel length  $L$  (as specified by the designer) because the source and drain diffusion regions extend slightly under the gate oxide during fabrication. Furthermore, the effective channel width  $W_{eff}$  of the MOSFET is shorter than the nominal or drawn channel width  $W$  because of the sideways diffusion into the channel from the body along the width. Based on the parameters specified in Table B.2,

$$L_{eff} = L - 2LD \quad (B.7)$$

$$W_{eff} = W - 2WD \quad (B.8)$$

In a manner analogous to using  $L_{ov}$  to denote LD, we will use the symbol  $W_{ov}$  to denote WD. Consequently, as indicated in Section 8.2.1, the gate-source capacitance  $C_{gs}$  and the gate-drain capacitance  $C_{gd}$  must be increased by an overlap component of, respectively,

$$C_{gs, ov} = W \text{CGSO} \quad (\text{B.9})$$

and

$$C_{gd, ov} = W \text{CGDO} \quad (\text{B.10})$$

Similarly, the gate-body capacitance  $C_{gb}$  must be increased by an overlap component of

$$C_{gb, ov} = L \text{CGBO} \quad (\text{B.11})$$

The reader may have observed that there is a built-in redundancy in specifying the MOSFET model parameters in SPICE. For example, the user may specify the value of KP for a MOSFET or, alternatively, specify TOX and UO and let SPICE compute KP as UO TOX. Similarly, GAMMA can be directly specified, or the physical parameters that enable SPICE to determine it can be specified (e.g., NSUB). In any case, *the user-specified values will always take precedence over (i.e., override) those values calculated by SPICE*. As another example, note that the user has the option of either directly specifying the overlap capacitances CGBO, CGDO, and CGSO or letting SPICE compute them as CGDO = CGSO = LD COX and CGBO = WD COX.

Table B.3 provides typical values for the level-1 MOSFET model parameters of a modern 0.18-μm CMOS technology and for older 0.5-μm and 5-μm CMOS technologies. The corresponding values for the minimum channel length  $L_{\min}$ , minimum channel width  $W_{\min}$ , and the maximum supply voltage  $(V_{DD} + |V_{SS}|)_{\max}$  are as follows:

Technology	$L_{\min}$	$W_{\min}$	$(V_{DD} +  V_{SS} )_{\max}$
5-μm CMOS	5 μm	12.5 μm	10 V
0.5-μm CMOS	0.5 μm	1.25 μm	3.3 V
0.18-μm CMOS	0.18 μm	0.22 μm	1.8 V

When simulating a MOSFET circuit, the user needs to specify both the values of the model parameters and the dimensions of each MOSFET in the circuit being simulated. At least the channel length  $L$  and width  $W$  must be specified. The areas AD and AS and the perimeters PD and PS need to be specified for SPICE to model the body-junction capacitances (otherwise, zero capacitances would be assumed). The exact values of these geometry parameters depend on the actual layout of the device (Appendix A). However, to estimate these dimensions, we will assume that a metal contact is to be made to each of the source and drain regions of the MOSFET. For this purpose, typically, these diffusion regions must be extended *past* the end of the channel (i.e., in the  $L$ -direction in Fig. 5.1) by at least  $2.75L_{\min}$ . Thus, the minimum area and perimeter of a drain/source diffusion region with a contact are, respectively,

$$\text{AD} = \text{AS} = 2.75L_{\min}W \quad (\text{B.12})$$

**Table B.3** Values of the Level-1 MOSFET Model Parameters for Two CMOS Technologies<sup>1</sup>

	5-μm CMOS Process		0.5-μm CMOS Process		0.18-μm CMOS Process	
	NMOS	PMOS	NMOS	PMOS	NMOS	PMOS
LEVEL	1	1	1	1	1	1
TOX	8.50e-08	8.50e-08	9.50e-09	9.50e-09	4.08e-09	4.08e-09
UO	750	250	460	115	291	102
LAMBDA	0.01	0.03	0.1	0.2	0.08	0.11
GAMMA	1.4	0.65	0.5	0.45	0.3	0.3
VTO	1	-1	0.7	-0.8	0.5	-0.45
PHI	0.7	0.65	0.8	0.75	0.84	0.8
LD	7.00e-07	6.00e-07	8.00e-08	9.00e-08	10e-9	10e-9
JS	1.00e-06	1.00e-06	1.00e-08	5.00e-09	8.38e-6	4.00e-07
CJ	4.00e-04	1.80e-04	5.70e-04	9.30e-04	1.60e-03	1.00e-03
MJ	0.5	0.5	0.5	0.5	0.5	0.45
CJSW	8.00e-10	6.00e-10	1.20e-10	1.70e-10	2.04e-10	2.04e-10
MJSW	0.5	0.5	0.4	0.35	0.2	0.29
PB	0.7	0.7	0.9	0.9	0.9	0.9
CGBO	2.00e-10	2.00e-10	3.80e-10	3.80e-10	3.80e-10	3.50e-10
CGDO	4.00e-10	4.00e-10	4.00e-10	3.50e-10	3.67e-10	3.43e-10
CGSO	4.00e-10	4.00e-10	4.00e-10	3.50e-10	3.67e-10	3.43e-10

<sup>1</sup>In PSpice, we have created MOSFET parts corresponding to the above models. Readers can find these parts in the SEDRA.olb library, which is available on the CD accompanying this book. The NMOS and PMOS parts for the 0.5-μm CMOS technology are labeled NMOSOP5\_BODY and PMOSOP5\_BODY, respectively. The NMOS and PMOS parts for the 5-μm CMOS technology are labelled NMOS5P0\_BODY and PMOS5P0\_BODY, respectively. Furthermore, parts NMOS5P0 and PMOS5P0 are created to correspond to, respectively, part NMOSOP5\_BODY with its body connected to net 0 and part PMOSOP5\_BODY with its body connected to net  $V_{DD}$ .

and

$$PD = PS = 2 \times 2.75L_{\min} + W \quad (B.13)$$

Unless otherwise specified, we will use Eqs. (B.12) and (B.13) to estimate the dimensions of the drain/source regions in our examples.

Finally, we note that SPICE computes *the values for the parameters of the MOSFET small-signal model based on the dc operating point (bias point)*. These are then used by SPICE to perform the small-signal analysis (ac, or hand, analysis).

### B.1.5 The BJT Model

SPICE uses a general form of the BJT model that we discussed in Chapter 4 (Fig. 4.7). Known as the *transport* form of the **Ebers-Moll model**, it is shown in Fig. B.5. Here, the currents of the base-emitter diode ( $D_{BE}$ ) and the base-collector diode ( $D_{BC}$ ) are given, respectively, by

$$i_{BE} = \frac{I_S}{\beta_F} (e^{\frac{v_{BE}}{n_F V_T}} - 1) \quad (B.14)$$

and

$$i_{BC} = \frac{I_S}{\beta_R} (e^{\frac{v_{BC}}{n_R V_T}} - 1) \quad (B.15)$$

where  $n_F$  and  $n_R$  are the emission coefficients of the BEJ and BCJ, respectively. These coefficients are generalizations of the constant  $n$  of the *pn*-junction diode (Fig. B.3). (We have so

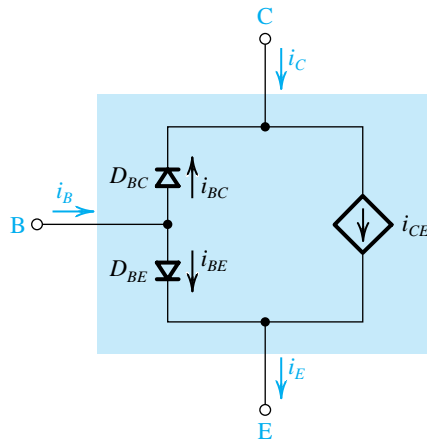


**Figure B.5** The transport form of the Ebers-Moll model for an *npn* BJT.

far assumed  $n_F = n_R = 1$ ). The parameters  $\beta_F$  and  $\beta_R$  are, respectively, the forward and reverse  $\beta$  of the BJT. The reverse  $\beta$  is the current gain obtained when the collector and emitter are interchanged and is much smaller than the forward  $\beta$ . In fact,  $\beta_R \ll 1$ . The controlled current-source  $i_{CE}$  in the transport model is defined as

$$i_{CE} = I_S(e^{v_{BE}/n_F V_T} - e^{v_{BC}/n_R V_T}) \quad (\text{B.16})$$

Observe that  $i_{CE}$  represents the current component of  $i_C$  and  $i_E$  that arises as a result of the minority carrier diffusion across the base, or **carrier transport** across the base (hence the name transport model).

The transport model can account for the Early effect in a forward-biased BJT by including the factor  $(1 - v_{BC}/V_A)$  in the expression for the transport current  $i_{CE}$  as follows:

$$i_{CE} = I_S(e^{v_{BE}/n_F V_T} - e^{v_{BC}/n_R V_T}) \left( 1 - \frac{v_{BC}}{V_A} \right) \quad (\text{B.17})$$

Figure B.6 shows the model used in SPICE. Here, resistors  $r_B$ ,  $r_E$ , and  $r_C$  are added to represent the ohmic resistance of, respectively, the base, emitter, and collector regions. The dynamic operation of the BJT is modeled by two nonlinear capacitors,  $C_{BC}$  and  $C_{BE}$ . Each of these capacitors generally includes a diffusion component (i.e.,  $C_{DC}$  and  $C_{DE}$ ) and a depletion or junction component (i.e.,  $C_{JC}$  and  $C_{JE}$ ) to account for the charge-storage effects within the BJT (as described in Section 8.2.2). Furthermore, the BJT model includes a depletion junction capacitance  $C_{JS}$  to account for the collector-substrate junction in integrated-circuit BJTs, where a reverse-biased *pn*-junction is formed between the collector and the substrate (which is common to all components of the IC).

For small-signal (ac) analysis, the SPICE BJT model is equivalent to the hybrid- $\pi$  model of Fig. 8.8, but augmented with  $r_E$ ,  $r_C$ , and (for IC BJTs)  $C_{JS}$ . Furthermore, the model includes a large resistance  $r_\mu$  between the base and collector (in parallel with  $C_\mu$ ) to account for the dependence of  $i_B$  on  $v_{CB}$ . The resistance  $r_\mu$  is very large, typically greater than  $10\beta r_o$ .

Although Fig. B.5 shows the SPICE model for the *npn* BJT, the corresponding model for the *pnp* BJT can be obtained by reversing the direction of the currents and the polarity of the diodes and terminal voltages.

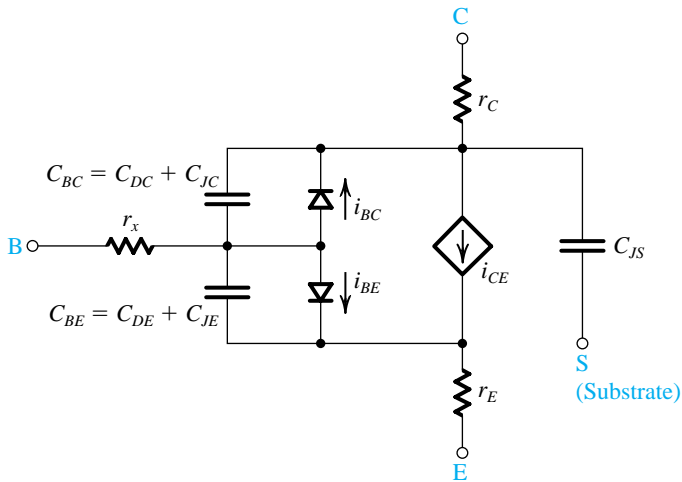


**Figure B.6** The SPICE large-signal model for an *npn* BJT.

**The SPICE Gummel-Poon Model of the BJT** The BJT model described above lacks a representation of some second-order effects present in actual devices. One of the most important such effects is the variation of the current gains,  $\beta_F$  and  $\beta_R$ , with the current  $i_C$ . The Ebers-Moll model assumes  $\beta_F$  and  $\beta_R$  to be constant, thereby neglecting their current dependence (as depicted in Fig. 4.19). To account for this, and other second-order effects, SPICE uses a more accurate, yet more complex, BJT model called the Gummel-Poon model (named after H. K. Gummel and H. C. Poon, two pioneers in this field). This model is based on the relationship between the electrical terminal characteristics of a BJT and its base charge. It is beyond the scope of this book to delve into the model details. However, it is important for the reader to be aware of the existence of such a model.

In SPICE, the Gummel-Poon model automatically simplifies to the Ebers-Moll model when certain model parameters are not specified. Consequently, the BJT model to be used by SPICE need not be explicitly specified by the user (unlike the MOSFET case in which the model is specified by the LEVEL parameter). For discrete BJTs, the values of the SPICE model parameters can be determined from the data specified on the BJT data sheets, supplemented (if needed) by key measurements. For instance, in Example PS5.6.1, we will use the Q2N3904 *npn* BJT (from Fairchild Semiconductor) whose SPICE model is available in PSpice. In fact, the PSpice and Multisim library already includes the SPICE model parameters for many of the commercially available discrete BJTs. For IC BJTs, the values of the SPICE model parameters are determined by the IC manufacturer (using both measurements on the fabricated devices and knowledge of the details of the fabrication process) and are provided to the IC designers.

**The SPICE BJT Model Parameters** Table B.4 provides a listing of some of the BJT model parameters used in SPICE. The reader should be already familiar with these parameters. In the absence of a user-specified value for a particular parameter, SPICE uses a default value that typically results in the corresponding effect being ignored. For example, if no value is specified for the forward Early voltage (VAF), SPICE assumes that VAF =  $\infty$  and does not account for the Early effect. Although ignoring VAF can be a serious issue in some circuits, the same is not true, for example, for the value of the reverse Early voltage (VAR).

**The BJT Model Parameters BF and BR in SPICE** Before leaving the SPICE model, a comment on  $\beta$  is in order. SPICE interprets the user-specified model parameters BF and BR as the *ideal maximum* values of the forward and reverse dc current gains, respectively, versus the operating current. These parameters are not equal to the constant-current-independent parameters  $\beta_F$  ( $\beta_{dc}$ ) and  $\beta_R$  used in the Ebers-Moll model for the forward and reverse dc current gains of the BJT. SPICE uses a current-dependent model for  $\beta_F$  and  $\beta_R$ , and the user can specify other parameters (not shown in Table B.4) for this model. Only when such parameters are not specified, and the Early effect is neglected, will SPICE assume that  $\beta_F$  and  $\beta_R$  are constant and equal to BF and BR, respectively. Furthermore, SPICE computes values for both  $\beta_{dc}$  and  $\beta_{ac}$ , the two parameters that we generally assume to be approximately equal. SPICE then uses  $\beta_{ac}$  to perform small-signal (ac) analysis.

**Table B.4** Parameters of the SPICE BJT Model (Partial Listing)

SPICE Parameter	Book Symbol	Description	Units
IS	$I_s$	Saturation current	A
BF	$\beta_F$	Ideal maximum forward current gain	
BR	$\beta_R$	Ideal maximum reverse current gain	
NF	$n_F$	Forward current emission coefficient	
NR	$n_R$	Reverse current emission coefficient	
VAF	$V_A$	Forward Early voltage	V
VAR		Reverse Early voltage	V
RB	$r_x$	Zero-bias base ohmic resistance	$\Omega$
RC	$r_c$	Collector ohmic resistance	$\Omega$
RE	$r_E$	Emitter ohmic resistance	$\Omega$
TF	$\tau_F$	Ideal forward transit time	s
TR	$\tau_R$	Ideal reverse transit time	s
CJC	$C_{\mu 0}$	Zero-bias base-collector depletion (junction) capacitance	F
MJC	$m_{BCJ}$	Base-collector grading coefficient	
VJC	$V_{0c}$	Base-collector built-in potential	V
CJE	$C_{je0}$	Zero-bias base-emitter depletion (junction) capacitance	F
MJE	$m_{BEJ}$	Base-emitter grading coefficient	
VJE	$V_{0e}$	Base-emitter built-in potential	V
CJS		Zero-bias collector-substrate depletion (junction) capacitance	F
MJS		Collector-substrate grading coefficient	
VJS		Collector-substrate built-in potential	V

## B.2 PSpice Examples

### Example PS.2.1

#### Performance of a Noninverting Amplifier

Consider an op amp with a differential input resistance of  $2 \text{ M}\Omega$ , an input offset voltage of 1 mV, a dc gain of 100 dB, and an output resistance of  $75 \Omega$ . Assume the op amp is internally compensated and has an STC frequency response with a gain-bandwidth product of 1 MHz.

- Create a subcircuit model for this op amp in PSpice.
- Using this subcircuit, simulate the closed-loop noninverting amplifier in Fig. 2.12 with resistors  $R_1 = 1 \text{ k}\Omega$  and  $R_2 = 100 \text{ k}\Omega$  to find:
  - Its 3-dB bandwidth  $f_{3\text{dB}}$ .
  - Its output offset voltage  $V_{OSout}$ .
  - Its input resistance  $R_{in}$ .
  - Its output resistance  $R_{out}$ .
- Simulate the step response of the closed-loop amplifier, and measure its rise time  $t_r$ . Verify that this time agrees with the 3-dB frequency measured above.

#### Solution

To model the op amp in PSpice, we use the equivalent circuit in Fig. B.2, but with  $R_{id} = 2 \text{ M}\Omega$ ,  $R_{icm} = \infty$  (open circuit),  $I_{B1} = I_{B2} = 0$  (open circuit),  $V_{OS} = 1 \text{ mV}$ ,  $A_{0d} = 10^5 \text{ V/V}$ ,  $A_{0cm} = 0$  (short circuit), and  $R_o = 75 \Omega$ . Furthermore, we set  $C_b = 1 \mu\text{F}$  and  $R_b = 15.915 \text{ k}\Omega$  to achieve an  $f_t = 1 \text{ MHz}$ .

To measure the 3-dB frequency of the closed-loop amplifier, we apply a 1-V ac voltage at its input, perform an ac-analysis simulation in PSpice, and plot its output versus frequency. The output voltage, plotted in Fig. B.7, corresponds to the gain of the amplifier because we chose an input voltage of 1 V.

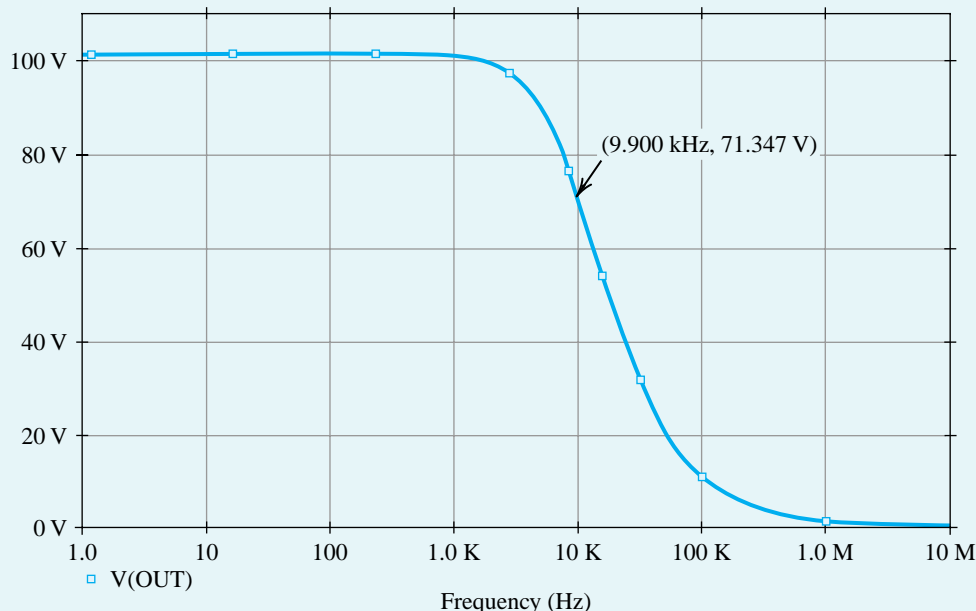


**Figure B.7** Frequency response of the closed-loop amplifier in Example PS.2.1.

**Example PS.2.1** *continued*

Thus, from Fig. B.7, the closed-loop amplifier has a dc gain of  $G_0 = 100.9 \text{ V/V}$ , and the frequency at which its gain drops to  $G_0/\sqrt{2} = 71.35 \text{ V/V}$  is  $f_{3\text{dB}} = 9.9 \text{ kHz}$ , which agrees with Eq. (B.7).

The input resistance  $R_{\text{in}}$  corresponds to the reciprocal of the current drawn out of the 1-V ac voltage source used in the above ac-analysis simulation at 0.1 Hz. (Theoretically,  $R_{\text{in}}$  is the small-signal input resistance at dc. However, ac-analysis simulations must start at frequencies greater than zero, so we use 0.1 Hz to approximate the dc point.) Accordingly,  $R_{\text{in}}$  is found to be  $2 \text{ G}\Omega$ .

To measure  $R_{\text{out}}$ , we short-circuit the amplifier input to ground, inject a 1-A ac current at its output, and perform an ac-analysis simulation.  $R_{\text{out}}$  corresponds to the amplifier output voltage at 0.1 Hz and is found to be  $76 \text{ m}\Omega$ . Although an ac test voltage source could equally well have been used to measure the output resistance in this case, it is a good practice to attach a current source rather than a voltage source between the output and ground. This is because an ac current source appears as an open circuit when the simulator computes the dc bias point of the circuit while an ac voltage source appears as a short circuit, which can erroneously force the dc output voltage to zero. For similar reasons, an ac test voltage source should be attached in series with the biasing dc voltage source for measuring the input resistance of a voltage amplifier.

A careful look at  $R_{\text{in}}$  and  $R_{\text{out}}$  of the closed-loop amplifier reveals that their values have, respectively, increased and decreased by a factor of about 1000, relative to the corresponding resistances of the op amp. Such a large input resistance and small output resistance are indeed desirable characteristics for a voltage amplifier. This improvement in the small-signal resistances of the closed-loop amplifier is a direct consequence of applying negative feedback (through resistors  $R_1$  and  $R_2$ ) around the open-loop op amp. We will study negative feedback in Chapter 9, where we will also learn how the improvement factor (1000 in this case) corresponds to the ratio of the open-loop op-amp gain ( $10^5$ ) to the closed-loop amplifier gain (100).

From Eqs. (2.55) and (2.53), the closed-loop amplifier has an STC low-pass response given by

$$\frac{V_o(s)}{V_i(s)} = \frac{G_0}{1 + \frac{s}{2\pi f_{3\text{dB}}}}$$

As described in Appendix E, the response of such an amplifier to an input step of height  $V_{\text{step}}$  is given by

$$v_o(t) = V_{\text{final}}(1 - e^{-t/\tau}) \quad (\text{B.18})$$

where  $V_{\text{final}} = G_0 V_{\text{step}}$  is the final output-voltage value (i.e., the voltage value toward which the output is heading) and  $\tau = 1/(2\pi f_{3\text{dB}})$  is the time constant of the amplifier. If we define  $t_{10\%}$  and  $t_{90\%}$  to be the time it takes for the output waveform to rise to, respectively, 10% and 90% of  $V_{\text{final}}$ , then from Eq. (B.18),  $t_{10\%} \approx 0.1\tau$  and  $t_{90\%} \approx 2.3\tau$ . Therefore, the rise time  $t_r$  of the amplifier can be expressed as

$$t_r = t_{90\%} - t_{10\%} = 2.2\tau = \frac{2.2}{2\pi f_{3\text{dB}}}$$

Therefore, if  $f_{3\text{dB}} = 9.9 \text{ kHz}$ , then  $t_r = 35.4 \mu\text{s}$ . To simulate the step response of the closed-loop amplifier, we apply a step voltage at its input, using a piecewise-linear (PWL) source (with a very short rise time); then perform a transient-analysis simulation, and measure the voltage at the output versus time. In our simulation, we applied a 1-V step input, plotted the output waveform in Fig. B.8, and measured  $t_r$  to be  $35.3 \mu\text{s}$ .

The linear macromodels in Figs. B.1 and B.2 assume that the op-amp circuit is operating in its linear range; they do not account for its nonideal performance when large signals are present at the output. Therefore, nonlinear effects, such as output saturation and slew rate, are not modeled. This is why, in the step response of Fig. B.8, we could see an output voltage of 100 V when we applied a 1-V step input. However, IC op amps are not capable of producing such large output voltages. Hence, a designer must be very careful when using these models.

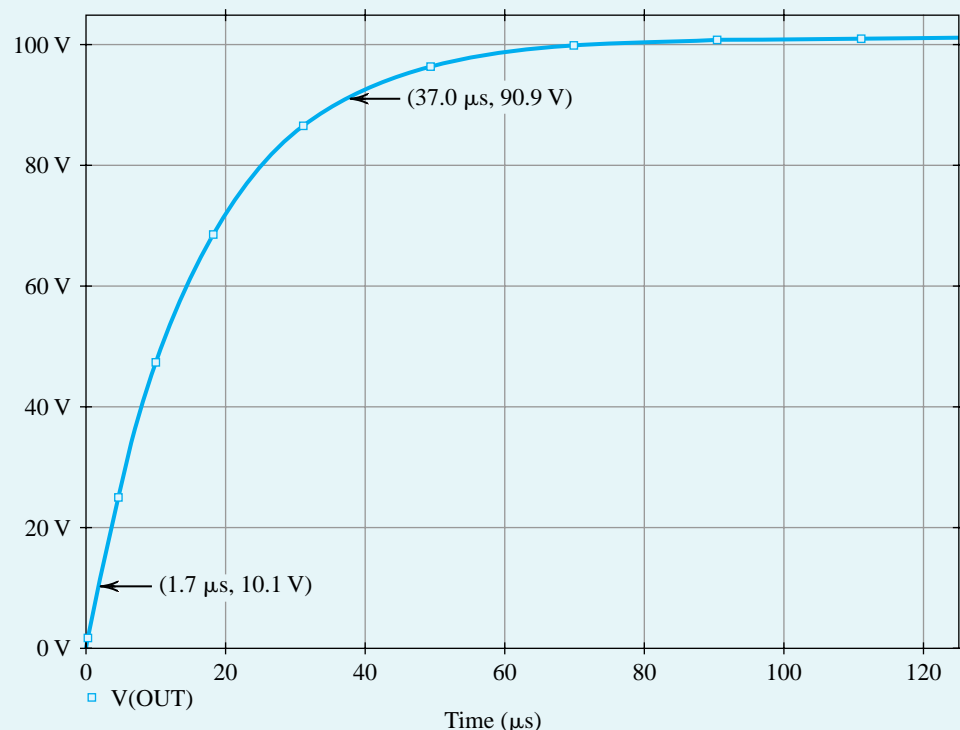


**Figure B.8** Step response of the closed-loop amplifier in Example PS.2.1.

It is important to point out that we also saw output voltages of 100 V or so in the ac analysis of Fig. B.7, where for convenience we applied a 1-V ac input to measure the gain of the closed-loop amplifier. So, would we see such large output voltages if the op-amp macromodel accounted for nonlinear effects (particularly output saturation)? The answer is yes, because in an ac analysis PSpice uses a linear model for nonlinear devices with the linear-model parameters evaluated at a bias point. Thus, we must keep in mind that the voltage magnitudes encountered in an ac analysis may not be realistic. In this case, the voltage and current ratios (e.g., the output-to-input voltage ratio as a measure of voltage gain) are of importance to the designer.

## Example PS.2.2

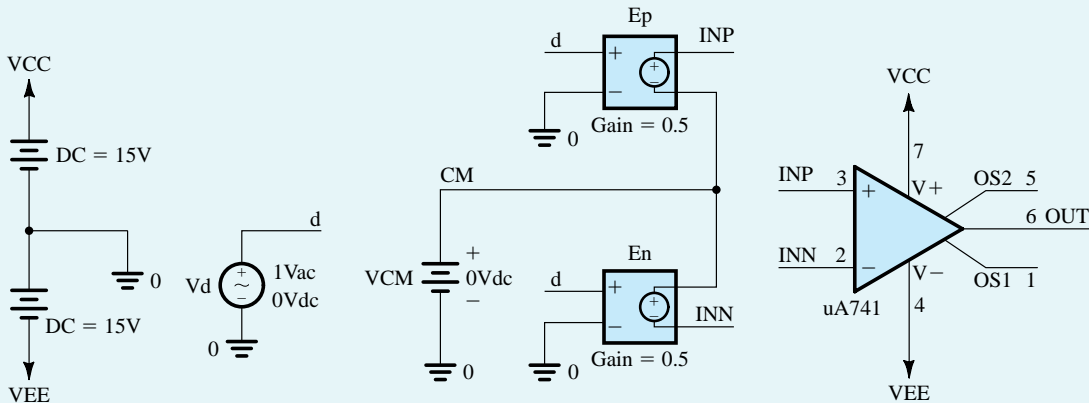
### Characteristics of the 741 OP Amp

Consider the  $\mu$ A741 op amp whose macromodel is available in PSpice. Use PSpice to plot the open-loop gain and hence determine  $f_r$ . Also, investigate the SR limitation and the output saturation of this op amp.

### Solution

Figure B.9 shows the schematic capture used to simulate the frequency response of the  $\mu$ A741 op amp.<sup>1</sup> The  $\mu$ A741 part has seven terminals. Terminals 7 and 4 are, respectively, the positive and negative dc power-supply

<sup>1</sup>The reader is reminded that the schematic capture diagram and the corresponding PSpice simulation files of all SPICE examples in this book can be found on the text's CD.

**Example PS.2.2** *continued*


**Figure B.9** Simulating the frequency response of the  $\mu$ A741 op-amp in Example PS.2.2.

terminals of the op amp. The 741-type op amps are typically operated from  $\pm 15$ -V power supplies; therefore we connected the dc voltage sources  $V_{CC} = +15$  V and  $V_{EE} = -15$  V to terminals 7 and 4, respectively. Terminals 3 and 2 of the  $\mu$ A741 part correspond to the positive and negative input terminals, respectively, of the op amp. In general, as outlined in Section 2.1.3, the op-amp input signals are expressed as

$$v_{INP} = V_{CM} + \frac{V_d}{2}$$

$$v_{INN} = V_{CM} - \frac{V_d}{2}$$

where  $v_{INP}$  and  $v_{INN}$  are the signals at, respectively, the positive- and negative-input terminals of the op amp with  $V_{CM}$  being the common-mode input signal (which sets the dc bias voltage at the op-amp input terminals) and  $V_d$  being the differential input signal to be amplified. The dc voltage source  $V_{CM}$  in Fig. B.9 is used to set the common-mode input voltage. Typically,  $V_{CM}$  is set to the average of the dc power-supply voltages  $V_{CC}$  and  $V_{EE}$  to maximize the available input signal swing. Hence, we set  $V_{CM} = 0$ . The voltage source  $V_d$  in Fig. B.9 is used to generate the differential input signal  $V_d$ . This signal is applied differentially to the op-amp input terminals using the voltage-controlled voltage sources  $E_p$  and  $E_n$ , whose gain constants are set to 0.5.

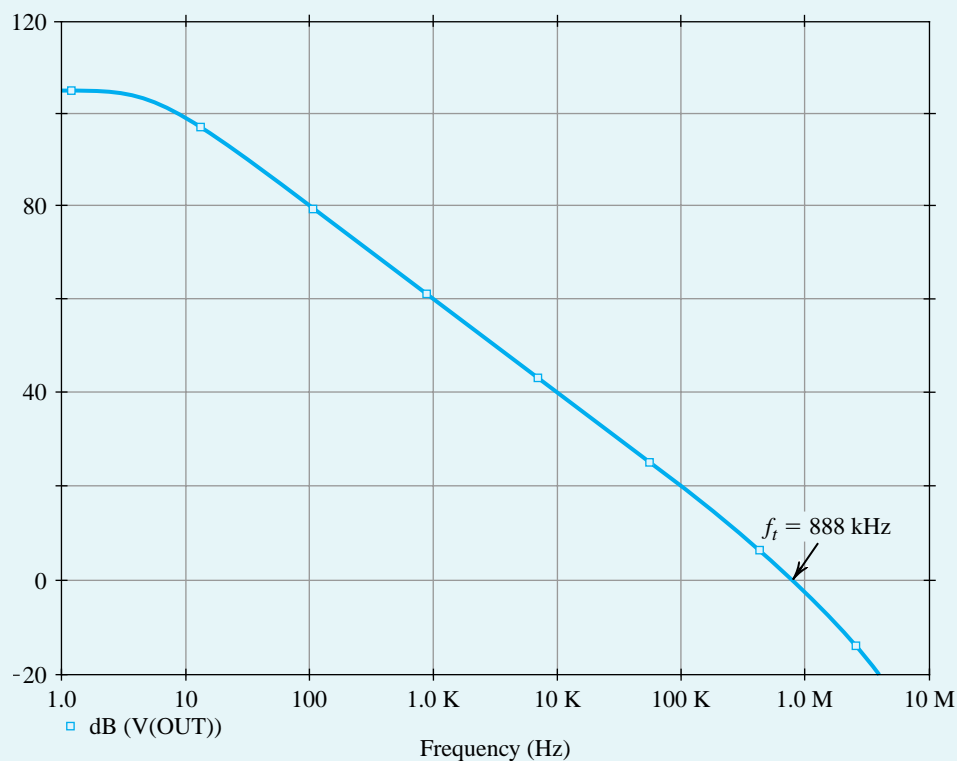
Terminals 1 and 5 of part  $\mu$ A741 are the offset-nulling terminals of the op amp (as depicted in Fig. 2.36). However, a check of the PSpice netlist of this part (by selecting Edit  $\rightarrow$  PSpice Model, in the Capture menus), reveals that these terminals are floating; therefore the offset-nulling characteristic of the op amp is not incorporated in this macromodel.

To measure  $f_t$  of the op amp, we set the voltage of source  $V_d$  to be 1-V ac, perform an ac-analysis simulation in PSpice, and plot the output voltage versus frequency as shown in Fig. B.10. Accordingly, the frequency at which the op-amp voltage gain drops to 0 dB is  $f_t = 0.9$  MHz (which is close to the 1-MHz value reported in the data sheets for 741-type op amps).

To determine the slew rate of the  $\mu$ A741 op amp, we connect the op amp in a unity-gain configuration, as shown in Fig. B.11, apply a large pulse signal at the input with very short rise and fall times to

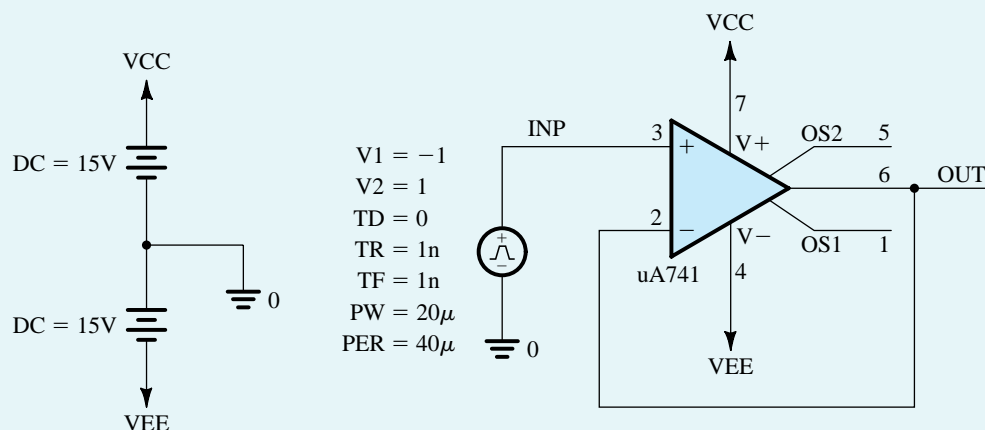
---

In these schematics (as shown in Fig. B.13), we use variable parameters to enter the values of the various circuit components. This allows one to investigate the effect of changing component values by simply changing the corresponding parameter values.

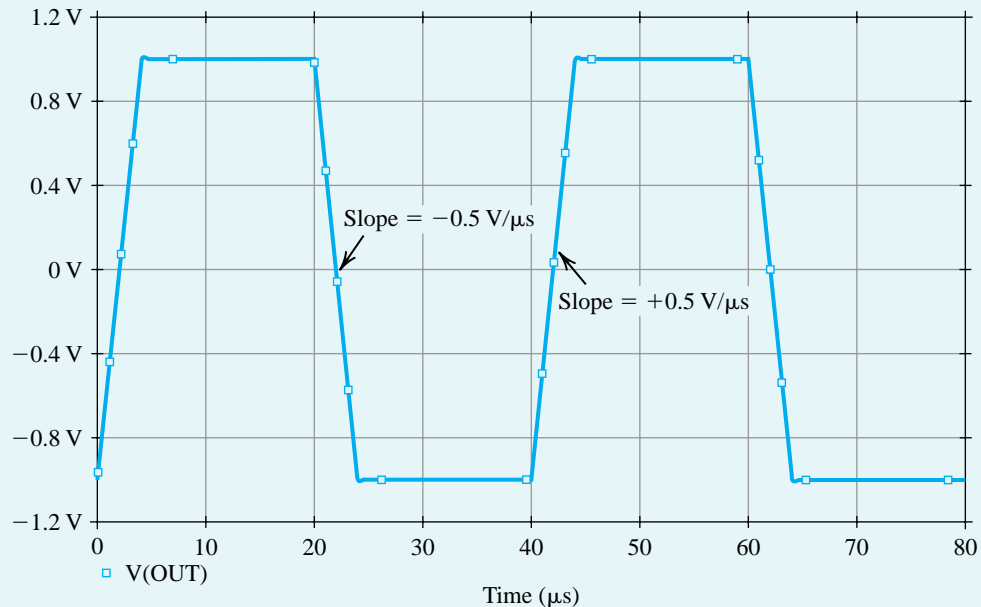


**Figure B.10** Frequency response of the  $\mu$ A741 op amp in Example PS.2.2.

cause slew-rate limiting at the output, perform a transient-analysis simulation in PSpice, and plot the output voltage as shown in Fig. B.12. The slope of the slew-rate limited output waveform corresponds to the slew-rate of the op amp and is found to be  $SR = 0.5 \text{ V}/\mu\text{s}$  (which agrees with the value specified in the data sheets for 741-type op amps).



**Figure B.11** Circuit for determining the slew rate of the  $\mu$ A741 op amp in Example PS.5.2.2.

**Example PS.2.2** *continued*

**Figure B.12** Square-wave response of the  $\mu$ A741 op amp connected in the unity-gain configuration shown in Fig. B.11.

To determine the maximum output voltage of the  $\mu$ A741 op amp, we set the dc voltage of the differential voltage source  $V_d$  in Fig. B.9 to a large value, say +1 V, and perform a bias-point simulation in PSpice. The corresponding dc output voltage is the positive-output saturation voltage of the op amp. We repeat the simulation with the dc differential input voltage set to -1 V to find the negative-output saturation voltage. Accordingly, we find that the  $\mu$ A741 op amp has a maximum output voltage  $V_{omax} = 14.8$  V.

**Example PS.4.1****Design of a DC Power Supply**

In this example, we will design a dc power supply using the rectifier circuit whose capture schematic is shown in Fig. B.13. This circuit consists of a full-wave diode rectifier, a filter capacitor, and a zener voltage regulator. The only perhaps puzzling component is the  $R_{isolation}$ , the 100-M $\Omega$  resistor between the secondary winding of the transformer and ground. This resistor is included to provide dc continuity and thus “keep SPICE happy”; it has little effect on circuit operation.

Let it be required that the power supply (in Fig. B.13) provide a nominal dc voltage of 5 V and be able to supply a load current  $I_{load}$  as large as 25 mA; that is,  $R_{load}$  can be as low as 200  $\Omega$ . The power supply is fed from a 120-V (rms) 60-Hz ac line. Note that in the PSpice schematic (Fig. B.13), we use a sinusoidal voltage source with a 169-V peak amplitude to represent the 120-V rms supply (as 120-V rms = 169-V peak). Assume the availability of a 5.1-V zener diode having  $r_z = 10 \Omega$  at  $I_z = 20$  mA (and thus  $V_{z0} = 4.9$  V), and that the required minimum current through the zener diode is  $I_{zmin} = 5$  mA.

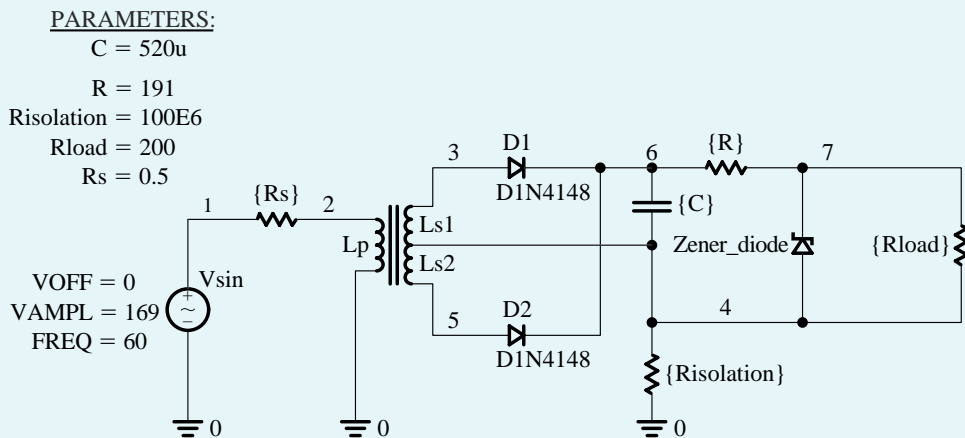


**Figure B.13** Schematic capture of the 5-V dc power supply in Example PS.4.1.

An approximate first-cut design can be obtained as follows: The 120-V (rms) supply is stepped down to provide 12-V (peak) sinusoids across each of the secondary windings using a 14:1 turns ratio for the center-tapped transformer. The choice of 12 V is a reasonable compromise between the need to allow for sufficient voltage (above the 5-V output) to operate the rectifier and the regulator, while keeping the PIV ratings of the diodes reasonably low. To determine a value for  $R$ , we can use the following expression:

$$R = \frac{V_{C_{\min}} - V_{Z_0} - r_z I_{Z_{\min}}}{I_{Z_{\min}} + I_{L_{\max}}}$$

where an estimate for  $V_{C_{\min}}$ , the minimum voltage across the capacitor, can be obtained by subtracting a diode drop (say, 0.8 V) from 12 V and allowing for a ripple voltage across the capacitor of, say,  $V_r = 0.5$  V. Thus,  $V_{S_{\min}} = 10.7$  V. Furthermore, we note that  $I_{L_{\max}} = 25$  mA and  $I_{Z_{\min}} = 5$  mA, and that  $V_{Z_0} = 4.9$  V and  $r_z = 10 \Omega$ . The result is that  $R = 191 \Omega$ .

Next, we determine  $C$  using a restatement of Eq. (3.33) with  $V_p/R$  replaced by the current through the  $191\Omega$  resistor. This current can be estimated by noting that the voltage across  $C$  varies from 10.7 V to 11.2 V, and thus has an average value of 10.95 V. Furthermore, the desired voltage across the zener is 5 V. The result is  $C = 520 \mu F$ .

Now, with an approximate design in hand, we can proceed with the SPICE simulation. For the zener diode, we use the model of Fig. B.4, and assume (arbitrarily) that  $D_1$  has  $I_s = 100$  pA and  $n = 0.01$  while  $D_2$  has  $I_s = 100$  pA and  $n = 1.7$ . For the rectifier diodes, we use the commercially available 1N4148 type<sup>2</sup> (with  $I_s = 2.682$  nA,  $n = 1.836$ ,  $R_s = 0.5664 \Omega$ ,  $V_0 = 0.5$  V,  $C_{j0} = 4$  pF,  $m = 0.333$ ,  $\tau_T = 11.54$  ns,  $V_{ZK} = 100$  V,  $I_{ZK} = 100$   $\mu A$ ).

In PSpice, we perform a transient analysis and plot the waveforms of both the voltage  $v_C$  across the smoothing capacitor  $C$  and the voltage  $v_o$  across the load resistor  $R_{load}$ . The simulation results for  $R_{load} = 200 \Omega$  ( $I_{load} = 25$  mA) are presented in Fig. B.14. Observe that  $v_C$  has an average of 10.85 V and a ripple of  $\pm 0.21$  V. Thus,  $V_r = 0.42$  V, which is close to the 0.5-V value that we would expect from the chosen value of  $C$ . The output voltage  $v_o$  is very close to the required 5 V, with  $v_o$  varying between 4.957 V and 4.977 V for a ripple of only 20 mV. The variations of  $v_o$  with  $R_{load}$  are illustrated in Fig. B.15 for  $R_{load}$  as 500  $\Omega$ , 250  $\Omega$ , 200  $\Omega$ , and 150  $\Omega$ . Accordingly,  $v_o$  remains close to the nominal value of 5 V for  $R_{load}$  as

<sup>2</sup>The 1N4148 model is included in the evaluation (EVAL) library of PSpice, which is available on the CD accompanying this book.

**Example PS.4.1 continued**

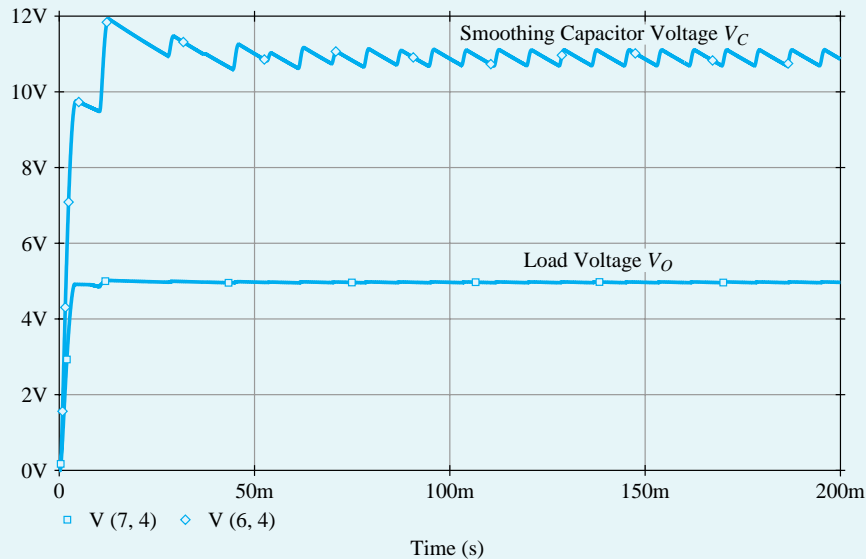


**Figure B.14** The voltage  $v_C$  across the smoothing capacitor  $C$  and the voltage  $v_O$  across the load resistor  $R_{\text{load}} = 200 \Omega$  in the 5-V power supply of Example PS.4.1.

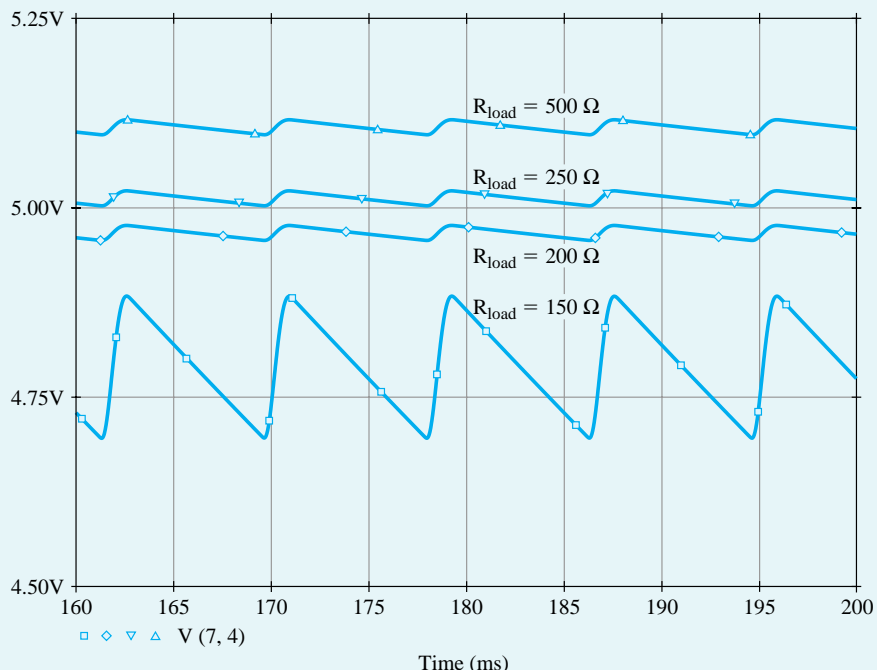


**Figure B.15** The output-voltage waveform from the 5-V power supply (in Example PS.4.1) for various load resistances:  $R_{\text{load}} = 500 \Omega$ ,  $250 \Omega$ ,  $200 \Omega$ , and  $150 \Omega$ . The voltage regulation is lost at a load resistance of  $150 \Omega$ .

low as  $200\ \Omega$  ( $I_{\text{load}} \approx 25\ \text{mA}$ ). For  $R_{\text{load}} = 150\ \Omega$  (which implies  $I_{\text{load}} \approx 33.3\ \text{mA}$ , greater than the maximum designed value), we see a significant drop in  $v_o$  (to about 4.8 V), as well as a large increase in the ripple voltage at the output (to about 190 mV). This is because the zener regulator is no longer operational; the zener has in fact cut off.

We conclude that the design meets the specifications, and we can stop here. Alternatively, we may consider using further runs of PSpice to help with the task of fine-tuning the design. For instance, we could consider what happens if we use a lower value of  $C$ , and so on. We can also investigate other properties of the present design (e.g., the maximum current through each diode) and ascertain whether this maximum is within the rating specified for the diode.

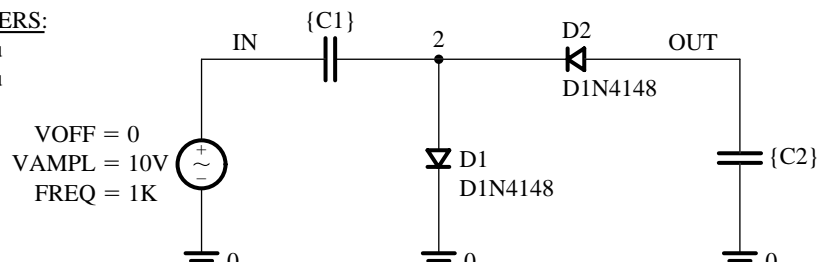
### EXERCISE

- B.1** Use PSpice to investigate the operation of the voltage doubler whose schematic capture is shown in Fig. B.16(a). Specifically, plot the transient behavior of the voltages  $v_2$  and  $v_{\text{out}}$  when the input is a sinusoid of 10-V peak and 1-kHz frequency. Assume that the diodes are of the 1N4148 type (with  $I_s = 2.682\ \text{nA}$ ,  $n = 1.836$ ,  $R_s = 0.5664\ \Omega$ ,  $V_0 = 0.5\ \text{V}$ ,  $C_{j0} = 4\ \text{pF}$ ,  $m = 0.333$ ,  $\tau_T = 11.54\ \text{ns}$ ,  $V_{ZK} = 100\ \text{V}$ ,  $I_{ZK} = 100\ \mu\text{A}$ ).

**Ans.** The voltage waveforms are shown in Fig. B.16(b).

PARAMETERS:

$$\begin{aligned} C1 &= 1\text{u} \\ C2 &= 1\text{u} \end{aligned}$$



(a)

**Figure B.16** (a) Schematic capture of the voltage-doubler circuit in Exercise B.1. (b) Various voltage waveforms in the voltage-doubler circuit. The top graph displays the input sine-wave voltage signal, the middle graph displays the voltage across diode  $D_1$ , and the bottom graph displays the voltage that appears at the output.

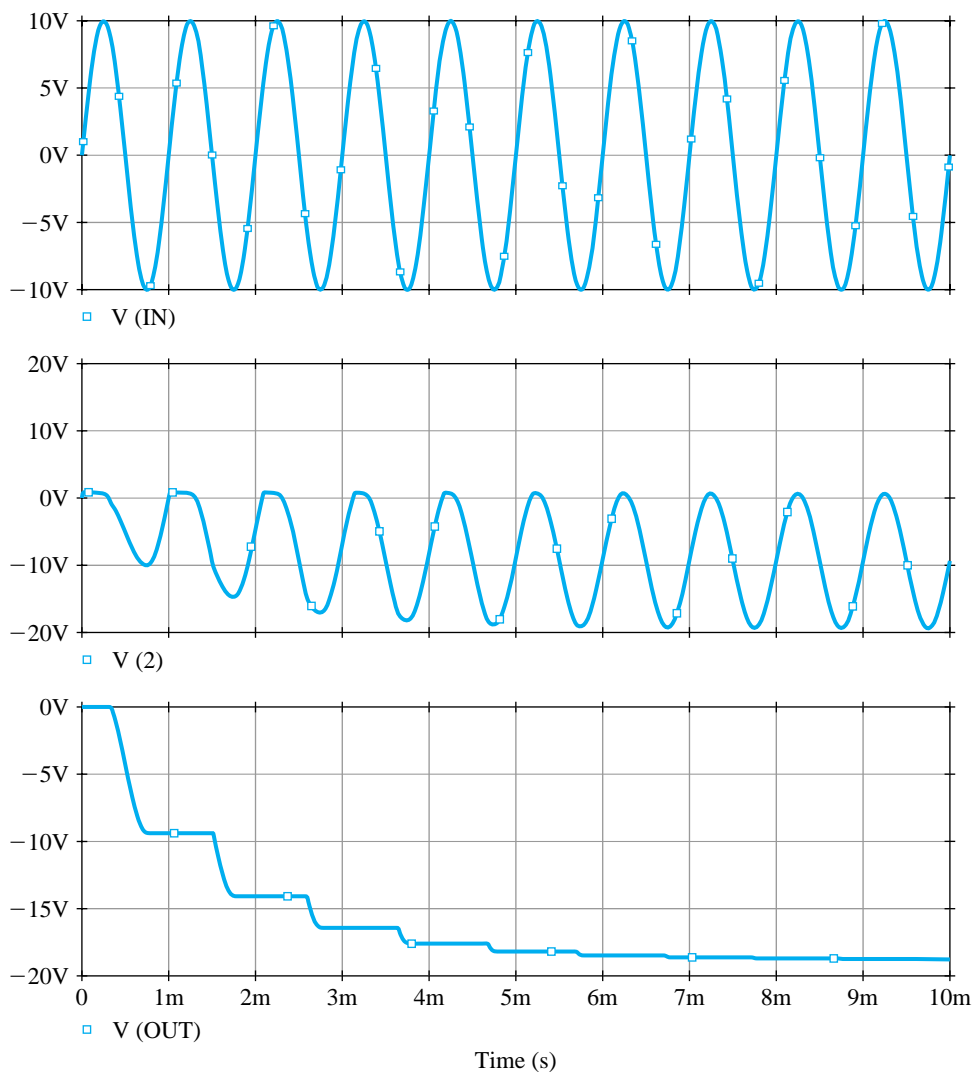


**Figure B.16** continued

## Example PS.5.1

### The CS Amplifier

In this example, we will use PSpice to analyze and verify the design of the CS amplifier whose capture schematic is shown in Fig. B.17.<sup>3</sup> Observe that the MOSFET has its source and body connected in order to cancel the body effect. We will assume a 0.5- $\mu\text{m}$  CMOS technology for the MOSFET and use the SPICE level-1 model parameters listed in Table B.3. We will also assume a signal-source resistance  $R_{\text{sig}} = 10 \text{ k}\Omega$ , a load resistance  $R_L = 50 \text{ k}\Omega$ , and bypass and coupling capacitors of  $10 \mu\text{F}$ . The targeted specifications for this CS amplifier are a midband gain  $A_M = 10 \text{ V/V}$  and a maximum power consumption  $P = 1.5 \text{ mW}$ . As should always be the case with computer simulation, we will begin with an approximate pencil-and-paper design. We will then use PSpice to fine-tune our design and to investigate the performance of the final design. In this way, maximum advantage and insight can be obtained from simulation.

With a 3.3-V power supply, the drain current of the MOSFET must be limited to  $I_D = P/V_{DD} = 1.5 \text{ mW}/3.3 \text{ V} = 0.45 \text{ mA}$  to meet the power consumption specification. Choosing  $V_{OV} = 0.3 \text{ V}$  (a typical value in low-voltage designs) and  $V_{DS} = V_{DD}/3$  (to achieve a large signal swing at the output), the MOSFET can now be sized as

$$\frac{W}{L_{\text{eff}}} = \frac{I_D}{\frac{1}{2}k'_nV_{OV}^2(1 + \lambda V_{DS})} = \frac{0.45 \times 10^{-3}}{\frac{1}{2}(170.1 \times 10^{-6})(0.3)^2[1 + 0.1(1.1)]} \approx 53 \quad (\text{B.19})$$

where  $k'_n = \mu_n C_{ox} = 170.1 \mu\text{A/V}^2$  (from Table B.3). Here,  $L_{\text{eff}}$  rather than  $L$  is used to more accurately compute  $I_D$ . The effect of using  $W_{\text{eff}}$  rather than  $W$  is much less important because typically  $W \gg W_{ov}$ . Thus, choosing  $L = 0.6 \mu\text{m}$  results in  $L_{\text{eff}} = L - 2L_{ov} = 0.44 \mu\text{m}$  and  $W = 23.3 \mu\text{m}$ . Note that we chose  $L$

#### PARAMETERS:

CCI = 10u  
 CCO = 10u  
 CS = 10u  
 RD = 4.2K  
 RG1 = 2E6  
 RG2 = 1.3E6  
 RL = 50K  
 RS = 630  
 Rsig = 10K  
 W = 22u  
 L = 0.6u  
 VDD = 3.3

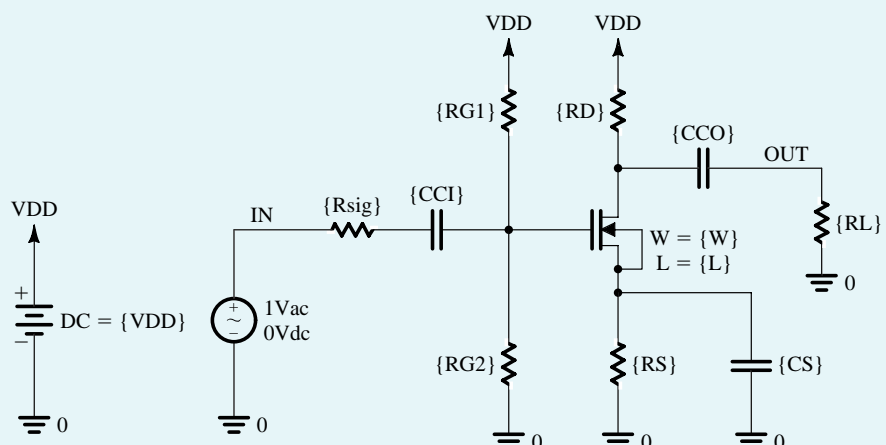


**Figure B.17** Schematic capture of the CS amplifier in Example PS.5.1.

<sup>3</sup>The reader is reminded that the schematic capture diagrams and the corresponding PSpice simulation files of all SPICE examples in this book can be found on the text's CD. In these schematics (as shown in Fig. B.17), we used variable parameters to enter the values of the various circuit components, including the dimensions of the MOSFET. This will allow the reader to investigate the effect of changing component values by simply changing the corresponding parameter values.

**Example PS.5.1** continued

slightly larger than  $L_{\min}$ . This is a common practice in the design of analog ICs to minimize the effects of fabrication nonidealities on the actual value of  $L$ . As shown in the text, this is particularly important when the circuit performance depends on the matching between the dimensions of two or more MOSFETs (e.g., in the current-mirror circuits studied in Chapter 6).

Next,  $R_D$  is calculated based on the desired voltage gain:

$$|A_v| = g_m(R_D \parallel R_L \parallel r_o) = 10 \text{ V/V} \Rightarrow R_D \approx 4.2 \text{ k}\Omega \quad (\text{B.20})$$

where  $g_m = 3.0 \text{ mA/V}$  and  $r_o = 22.2 \text{ k}\Omega$ . Hence, the output bias voltage is  $V_O = V_{DD} - I_D R_D = 1.39 \text{ V}$ . An  $R_S = (V_O - V_{DD}/3)/I_D = 630 \Omega$  is needed to bias the MOSFET at a  $V_{DS} = V_{DD}/3$ . Finally, resistors  $R_{G1} = 2 \text{ M}\Omega$  and  $R_{G2} = 1.3 \text{ M}\Omega$  are chosen to set the gate bias voltage at  $V_G = I_D R_S + V_{OV} + V_m \approx 1.29 \text{ V}$ . Using large values for these gate resistors ensures that both their power consumption and the loading effect on the input signal source are negligible. Note that we neglected the body effect in the expression for  $V_G$  to simplify our hand calculations.

We will now use PSpice to verify our design and investigate the performance of the CS amplifier. We begin by performing a bias-point simulation to verify that the MOSFET is properly biased in the saturation region and that the dc voltages and currents are within the desired specifications. Based on this simulation, we have decreased the value of  $W$  to 22  $\mu\text{m}$  to limit  $I_D$  to about 0.45 mA. Next, to measure the midband gain  $A_M$  and the 3-dB frequencies<sup>4</sup>  $f_L$  and  $f_H$ , we apply a 1-V ac voltage at the input, perform an ac-analysis simulation, and plot the output-voltage magnitude (in dB) versus frequency as shown in Fig. B.18. This corresponds to the magnitude response of the CS amplifier because we chose a 1-V input signal.<sup>5</sup> Accordingly, the midband gain is  $A_M = 9.55 \text{ V/V}$  and the 3-dB bandwidth is  $BW = f_H - f_L \approx 122.1 \text{ MHz}$ . Figure B.18 further shows that the gain begins to fall off at about 300 Hz but flattens out again at about 10 Hz. This flattening in the gain at low frequencies is due to a real transmission zero<sup>6</sup> introduced in the transfer function of the amplifier by  $R_S$  together with  $C_s$ . This zero occurs at a frequency  $f_Z = 1/(2\pi R_S C_s) = 25.3 \text{ Hz}$ , which is typically between the break frequencies  $f_{P2}$  and  $f_{P3}$  derived in Section 8.1.1. So, let us now verify this phenomenon by resimulating the CS amplifier with a  $C_s = 0$  (i.e., removing  $C_s$ ) in order to move  $f_Z$  to infinity and remove its effect. The corresponding frequency response is plotted also in Fig. B.18. As expected, with  $C_s = 0$ , we do not observe any flattening in the low-frequency response of the amplifier. However, because the CS amplifier now includes a source resistor  $R_S$ ,  $A_M$  has dropped by a factor of 2.6. This factor is approximately equal to  $(1 + g_m R_S)$ , as expected from our study of the CS amplifier with a source-degeneration resistance in Section 5.6.4. Note that the bandwidth  $BW$  has increased by approximately the same factor as the drop in gain  $A_M$ . As we will learn in Chapter 9 when we study negative feedback, the source-degeneration resistor  $R_S$  provides negative feedback, which allows us to trade off gain for wider bandwidth.

To conclude this example, we will demonstrate the improved bias stability achieved when a source resistor  $R_S$  is used (see the discussion in Section 5.7.2). Specifically, we will change (in the MOSFET level-1 model for part NMOSOP5) the value of the zero-bias threshold voltage parameter  $VT0$  by  $\pm 15\%$  and perform a bias-point simulation in PSpice. Table B.5 shows the corresponding variations in  $I_D$  and  $V_O$  for the case in which  $R_S = 630 \Omega$ . For the case without source degeneration, we use an  $R_S = 0$  in the

<sup>4</sup>No detailed knowledge of frequency-response calculations is required for this example; all that is needed is Section 5.8.6. Nevertheless, after the study of the frequency response of the CS amplifier in Sections 8.1 through 8.3, the reader will benefit by returning to this example and using PSpice to experiment further with the circuit.

<sup>5</sup>The reader should not be alarmed about the use of such a large signal amplitude. Recall that in a small-signal (ac) simulation, SPICE first finds the small-signal equivalent circuit at the bias point and then analyzes this linear circuit. Such ac analysis can, of course, be done with any ac signal amplitude. However, a 1-V ac input is convenient to use because the resulting ac output corresponds to the voltage gain of the circuit.

<sup>6</sup>Readers who have not yet studied poles and zeros can skip these few sentences.

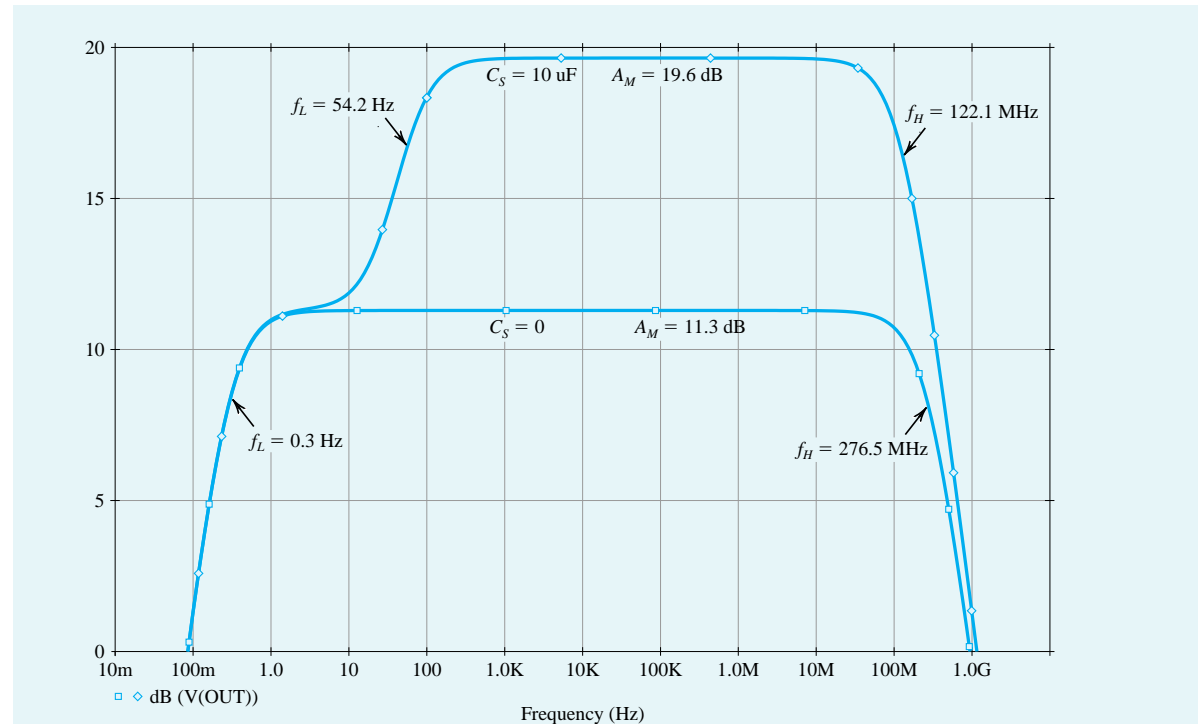


**Figure B.18** Frequency response of the CS amplifier in Example PS.5.1 with  $C_s = 10 \mu\text{F}$  and  $C_s = 0$  (i.e.,  $C_s$  removed).

schematic of Fig. B.17. Furthermore, to obtain the same  $I_D$  and  $V_o$  in both cases (for the nominal threshold voltage  $V_{tn0} = 0.7 \text{ V}$ ), we use an  $R_{G2} = 0.88 \text{ M}\Omega$  to reduce  $V_G$  to around  $V_{OV} + V_{tn} = 1 \text{ V}$ . The corresponding variations in the bias point are shown in Table B.5. Accordingly, we see that the source-degeneration resistor makes the bias point of the CS amplifier less sensitive to changes in the threshold voltage. In fact, the reader can show for the values displayed in Table B.5 that the variation in bias current ( $\Delta I/I$ ) is reduced by approximately the same factor,  $(1 + g_m R_S)$ . However, unless a large bypass capacitor  $C_s$  is used, this reduced sensitivity comes at the expense of a reduction in the midband gain (as we observed in this example when we simulated the frequency response of the CS amplifier with a  $C_s = 0$ ).

**Table B.5** Variations in the Bias Point with the MOSFET Threshold Voltage

$V_{tn0}$	$R_s = 630 \Omega$		$R_s = 0$	
	$I_D$ (mA)	$V_o$ (V)	$I_D$ (mA)	$V_o$ (V)
0.60	0.56	0.962	0.71	0.33
0.7	0.46	1.39	0.45	1.40
0.81	0.36	1.81	0.21	2.40

### Example PS.6.1

#### Dependence of the BJT $\beta$ on the Bias Current

In this example, we use PSpice to simulate the dependence of  $\beta_{dc}$  on the collector bias current for the Q2N3904 discrete BJT (from Fairchild Semiconductor) whose model parameters are listed in Table B.6 and are available in PSpice.<sup>7</sup> As shown in the schematic capture<sup>8</sup> of Fig. B.19, the  $V_{CE}$  of the BJT is fixed using a constant voltage source (in this example,  $V_{CE} = 2$  V) and a dc current source  $I_B$  is applied at the base. To illustrate the dependence of  $\beta_{dc}$  on the collector current  $I_C$ , we perform a dc-analysis simulation in which the sweep variable is the current source  $I_B$ . The  $\beta_{dc}$  of the BJT, which corresponds to the ratio of the collector current  $I_C$  to the base current  $I_B$ , can then be plotted versus  $I_C$  using Probe (the graphical interface of PSpice), as shown in Fig. B.20. We see that to operate at the maximum value of  $\beta_{dc}$  (i.e.,  $\beta_{dc} = 163$ ), at  $V_{CE} = 2$  V, the BJT must be biased at an  $I_C = 10$  mA. Since increasing the bias current of a transistor increases the power dissipation, it is clear from Fig. B.20 that the choice of current  $I_C$  is a trade-off between the current gain  $\beta_{dc}$  and the power dissipation. Generally speaking, the optimum  $I_C$  depends on the application and technology in hand. For example, for the Q2N3904 BJT operating at  $V_{CE} = 2$  V, decreasing  $I_C$  by a factor of 20 (from 10 mA to 0.5 mA) results in a drop in  $\beta_{dc}$  of about 25% (from 163 to 123).

PARAMETERS:

$IB = 10\text{u}$   
 $VCE = 2\text{V}$

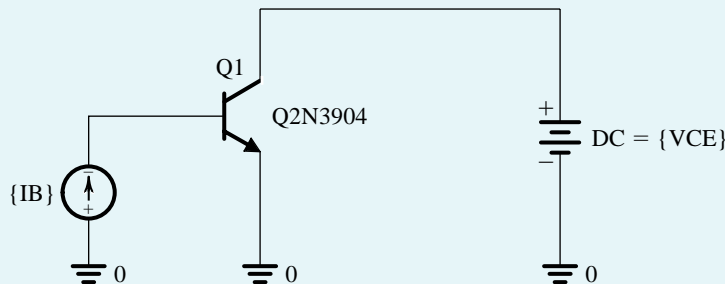


**Figure B.19** The PSpice test bench used to demonstrate the dependence of  $\beta_{dc}$  on the collector bias current  $I_C$  for the Q2N3904 discrete BJT (Example PS.6.1).

**Table B.6** Spice Model Parameters of the Q2N3904 Discrete BJT

IS=6.734F	XTI=3	EG=1.11	VAF=74.03	BF=416.4	NE=1.259	ISE=6.734F
IKF=66.78M	XTB=1.5	BR=.7371	NC=2	ISC=0	IKR=0	RC=1
CJC=3.638P	MJC=.3085	VJC=.75	FC=.5	CJE=4.493P	MJE=.2593	VJE=.75
TR=239.5N	TF=301.2P	ITF=.4	VTF=4	XTF=2	RB=10	

<sup>7</sup>The Q2N3904 model is included in the evaluation (EVAL) library of PSpice which is available on the CD accompanying this book.

<sup>8</sup>The reader is reminded that the schematics diagrams and the corresponding PSpice simulation files of all SPICE examples in this book can be found on the text's CD. In these schematics (as shown in Fig. B.19), we use variable parameters to enter the values of the various circuit components. This allows one to investigate the effect of changing component values by simply changing the corresponding parameter values.

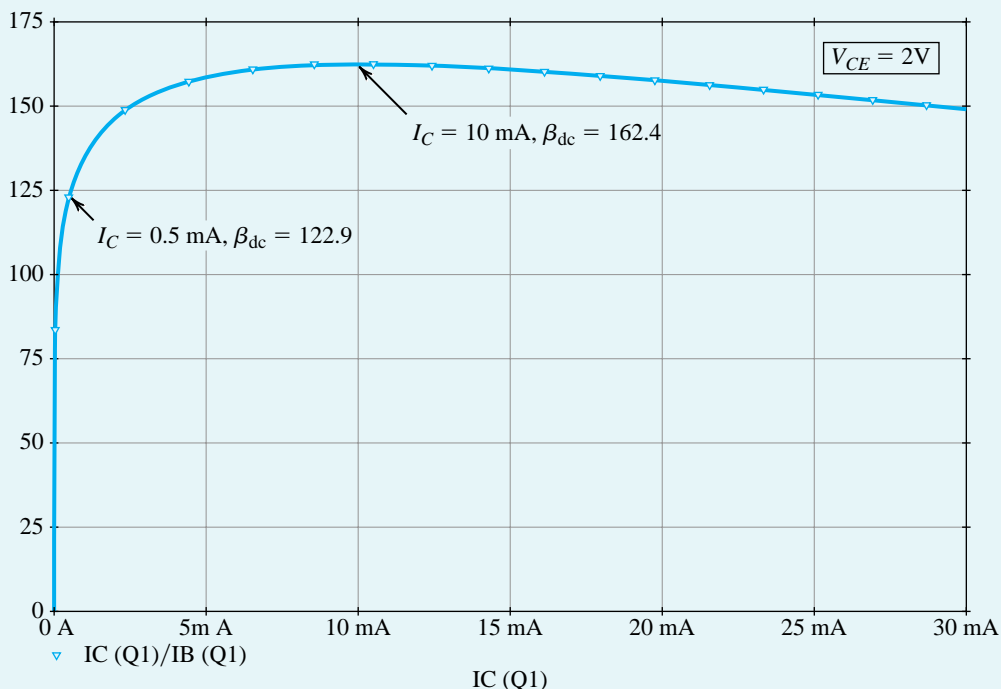


**Figure B.20** Dependence of  $\beta_{dc}$  on  $I_C$  (at  $V_{CE} = 2$  V) in the Q2N3904 discrete BJT (Example PS.6.1).

## Example PS.6.2

### The CE Amplifier with Emitter Resistance

In this example, we use PSpice to analyze and verify the design of the CE amplifier. A schematic capture of the CE amplifier is shown in Fig. B.21. We will use part Q2N3904 for the BJT and a  $\pm 5$ -V power supply. We will also assume a signal source resistor  $R_{sig} = 10 \text{ k}\Omega$ , a load resistor  $R_L = 10 \text{ k}\Omega$ , and bypass and coupling capacitors of  $10 \mu\text{F}$ . To enable us to investigate the effect of including a resistance in the signal path of the emitter, a resistor  $R_{ce}$  is connected in series with the emitter bypass capacitor  $C_E$ . Note that the roles of  $R_E$  and  $R_{ce}$  are different. Resistor  $R_E$  is the **dc emitter-degeneration resistor** because it appears in the dc path between the emitter and ground. It is therefore used to help stabilize the bias point for the amplifier. The equivalent resistance  $R_e = R_E \parallel R_{ce}$  is the **small-signal emitter-degeneration resistance** because it appears in the ac (small-signal) path between the emitter and ground and helps stabilize the gain of the amplifier. In this example, we will investigate the effects of both  $R_E$  and  $R_e$  on the performance of the CE amplifier. However, as should always be the case with computer simulation, we will begin with an approximate pencil-and-paper design. In this way, maximum advantage and insight can be obtained from simulation.

Based on the plot of  $\beta_{dc}$  versus  $I_C$  in Fig. B.20, a collector bias current  $I_C$  of  $0.5$  mA is selected for the BJT, resulting in  $\beta_{dc} = 123$ . This choice of  $I_C$  is a reasonable compromise between power dissipation and current gain. Furthermore, a collector bias voltage  $V_C$  of  $0$  V (i.e., at the mid-supply rail) is selected to

**Example PS.6.2** *continued*

**PARAMETERS:**

$CE = 10\text{u}$   
 $CCI = 10\text{u}$   
 $CCO = 10\text{u}$   
 $RC = 10\text{K}$   
 $RB = 340\text{K}$   
 $RE = 6\text{K}$   
 $Rce = 130$   
 $RL = 10\text{K}$   
 $Rsig = 10\text{K}$   
 $VCC = 5$   
 $VEE = -5$

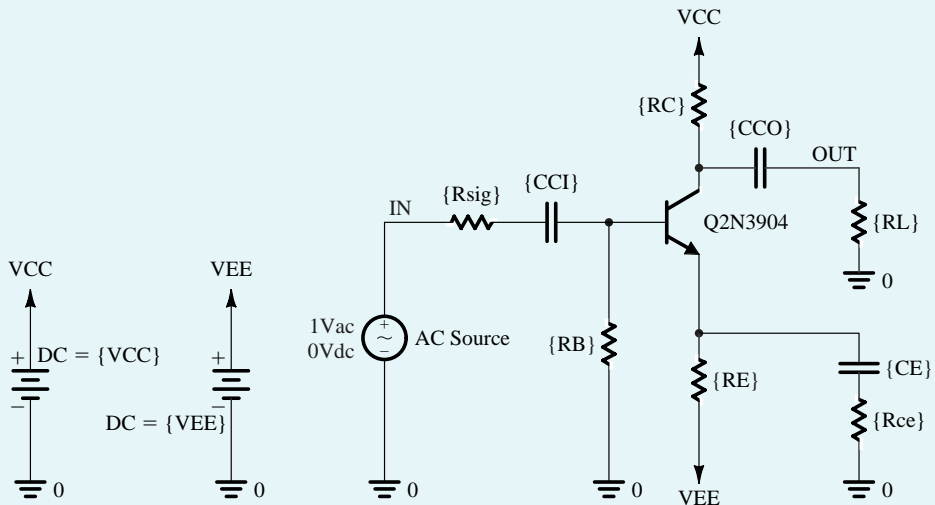


**Figure B.21** Schematic capture of the CE amplifier in Example PS.6.2.

achieve a high signal swing at the amplifier output. For  $V_{CE} = 2$  V, the result is that  $V_E = -2$  V requires bias resistors with values

$$R_C = \frac{V_{CC} - V_C}{I_C} = 10 \text{ k}\Omega$$

and

$$R_E = \frac{V_E - V_{EE}}{I_C} = 6 \text{ k}\Omega$$

Assuming  $V_{BE} = 0.7$  V and using  $\beta_{dc} = 123$ , we can determine

$$R_B = -\frac{V_B}{I_B} = -\frac{0 - (V_{BE} + V_E)}{I_C/\beta_{dc}} = 320 \text{ k}\Omega$$

Next, the formulas of Section 4.8.3 can be used to determine the input resistance  $R_{in}$  and the midband voltage gain  $|A_M|$  of the CE amplifier:

$$R_{in} = R_B \parallel (\beta_{ac} + 1)(r_e + R_e) \quad (\text{B.21})$$

$$|A_M| = \left| -\frac{R_{in}}{R_{sig} + R_{in}} \times \frac{R_C \parallel R_L}{r_e + R_e} \right| \quad (\text{B.22})$$

For simplicity, we will assume  $\beta_{ac} \approx \beta_{dc} = 123$ , resulting in

$$r_e = \left( \frac{\beta_{ac}}{\beta_{ac} + 1} \right) \left( \frac{V_T}{I_C} \right) = 49.6 \text{ }\Omega$$

Thus, with no small-signal emitter degeneration (i.e.,  $R_{ce} = 0$ ),  $R_{in} = 6.1 \text{ k}\Omega$  and  $|A_M| = 38.2 \text{ V/V}$ . Using Eq. (B.22) and assuming  $R_B$  is large enough to have a negligible effect on  $R_{in}$ , it can be shown that

the emitter-degeneration resistor  $R_e$  decreases the voltage gain  $|A_M|$  by a factor of

$$\frac{1 + \frac{R_e}{r_e} + \frac{R_{\text{sig}}}{r_\pi}}{1 + \frac{R_{\text{sig}}}{r_\pi}}$$

Therefore, to limit the reduction in voltage gain to a factor of 2, we will select

$$R_e = r_e + \frac{R_{\text{sig}}}{\beta_{\text{ac}} + 1} \quad (\text{B.23})$$

Thus,  $R_{ce} \approx R_e = 130 \Omega$ . Substituting this value in Eqs. (B.21) and (B.22) shows that  $R_{\text{in}}$  increases from  $6.1 \text{ k}\Omega$  to  $20.9 \text{ k}\Omega$  while  $|A_M|$  drops from  $38.2 \text{ V/V}$  to  $18.8 \text{ V/V}$ .

We will now use PSpice to verify our design and investigate the performance of the CE amplifier. We begin by performing a bias-point simulation to verify that the BJT is properly biased in the active region and that the dc voltages and currents are within the desired specifications. Based on this simulation, we have increased the value of  $R_B$  to  $340 \text{ k}\Omega$  in order to limit  $I_C$  to about  $0.5 \text{ mA}$  while using a standard 1% resistor value (Appendix H). Next, to measure the midband gain  $A_M$  and the 3-dB frequencies<sup>9</sup>  $f_L$  and  $f_H$ , we apply a 1-V ac voltage at the input, perform an ac-analysis simulation, and plot the output-voltage magnitude (in dB) versus frequency as shown in Fig. B.22. This corresponds to the magnitude response of the CE amplifier because we chose a 1-V input signal.<sup>10</sup> Accordingly, with no emitter degeneration, the midband gain is  $|A_M| = 38.5 \text{ V/V} = 31.7 \text{ dB}$  and the 3-dB bandwidth is  $BW = f_H - f_L = 145.7 \text{ kHz}$ . Using an  $R_{ce}$  of  $130 \Omega$  results in a drop in the midband gain  $|A_M|$  by a factor of 2 (i.e., 6 dB). Interestingly, however,  $BW$  has now increased by approximately the same factor as the drop in  $|A_M|$ . As we learned in Chapter 9 in our study of negative feedback, the emitter-degeneration resistor  $R_e$  provides negative feedback, which allows us to trade off gain for other desirable properties, such as a larger input resistance and a wider bandwidth.

To conclude this example, we will demonstrate the improved bias-point (or dc operating-point) stability achieved when an emitter resistor  $R_E$  is used (see the discussion in Section 4.7.1). Specifically, we will increase/decrease the value of the parameter BF (i.e., the ideal maximum forward current gain) in the SPICE model for part Q2N3904 by a factor of 2 and perform a bias-point simulation. The corresponding change in BJT parameters ( $\beta_{\text{dc}}$  and  $\beta_{\text{ac}}$ ) and bias-point (including  $I_C$  and  $CE$ ) are presented in Table B.7 for the case of  $R_E = 6 \text{ k}\Omega$ . Note that  $\beta_{\text{ac}}$  is not equal to  $\beta_{\text{dc}}$  as we assumed, but is slightly larger. For the case without emitter degeneration, we will use  $R_E = 0$  in the schematic of Fig. B.21. Furthermore, to maintain the same  $I_C$  and  $V_C$  in both cases at the values obtained for nominal BF, we use  $R_B = 1.12 \text{ M}\Omega$  to limit  $I_C$  to approximately  $0.5 \text{ mA}$ . The corresponding variations in the BJT bias point are also shown in Table B.7. Accordingly, we see that emitter degeneration makes the bias point of the CE amplifier much less sensitive to changes in  $\beta$ . However, unless a large bypass capacitor  $C_E$  is used, this reduced bias sensitivity comes at the expense of a reduction in the midband gain (as we observed in this example when we simulated the frequency response of the CE amplifier with an  $R_e = 130 \Omega$ ).

<sup>9</sup>No detailed knowledge of frequency-response calculations is required for this example; all that is needed is Section 4.8.6. Nevertheless, after the study of the frequency of the CE amplifier in Sections 8.1 through 8.3, the reader will benefit by returning to this example to experiment further with the circuit using PSpice.

<sup>10</sup>The reader should not be alarmed about the use of such a large signal amplitude. Recall that in a small-signal (ac) simulation, SPICE first finds the small-signal equivalent circuit at the dc bias point and then analyzes this linear circuit. Such ac analysis can, of course, be done with any ac signal amplitude. However, an I–V ac input is convenient to use because the resulting ac output corresponds to the voltage gain of the circuit.

**Example PS.6.2 continued**

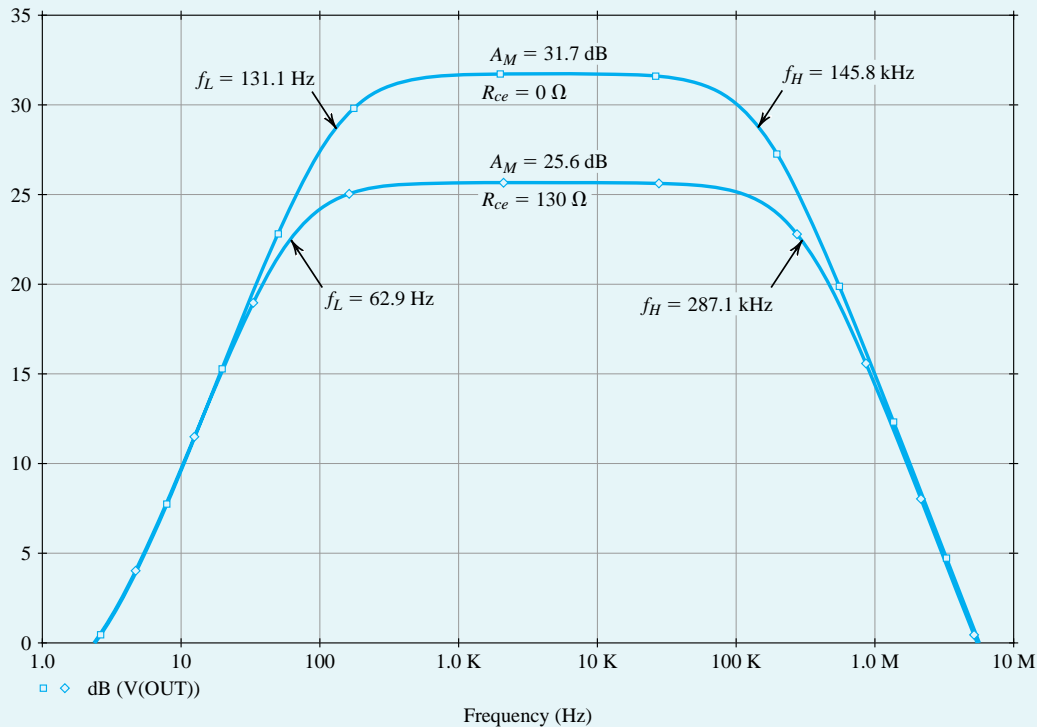


**Figure B.22** Frequency response of the CE amplifier in Example PS.6.2 with  $R_{ce} = 0$  and  $R_{ce} = 130 \Omega$ .

**Table B.7** Variations in the Bias Point of the CE Amplifier with the SPICE Model-Parameter BF of BJT

BF (in SPICE)	$R_E = 6 \text{ k}$				$R_E = 0$			
	$\beta_{ac}$	$\beta_{dc}$	$I_c$ (mA)	$V_c$ (V)	$\beta_{ac}$	$\beta_{dc}$	$I_c$ (mA)	$V_c$ (V)
208	106	94.9	0.452	0.484	109	96.9	0.377	1.227
416.4 (nominal value)	143	123	0.494	0.062	148	127	0.494	0.060
832	173	144	0.518	-0.183	181	151	0.588	-0.878

**Example PS.7.1**

**The CMOS CS Amplifier**

In this example, we will use PSpice to compute the dc transfer characteristic of the CS amplifier whose capture schematic is shown in Fig. B.23. We will assume a 5-μm CMOS technology for the MOSFETs and use parts NMOS5P0 and PMOS5P0 whose SPICE level-1 parameters are listed in Table B.3. To specify the dimensions of the MOSFETs in PSpice, we will use the multiplicative factor  $m$  together with the channel length  $L$  and the channel width  $W$ . The MOSFET parameter  $m$ , whose default value is 1, is used in SPICE to specify the number of MOSFETs connected in parallel. As depicted in Fig. B.24, a wide transistor with channel length  $L$  and channel width  $m \times W$  can be implemented using  $m$  narrower transistors in parallel, each having a channel length  $L$  and a channel width  $W$ . Thus, neglecting the channel-length modulation effect, the drain current of a MOSFET operating in the saturation region can be expressed as

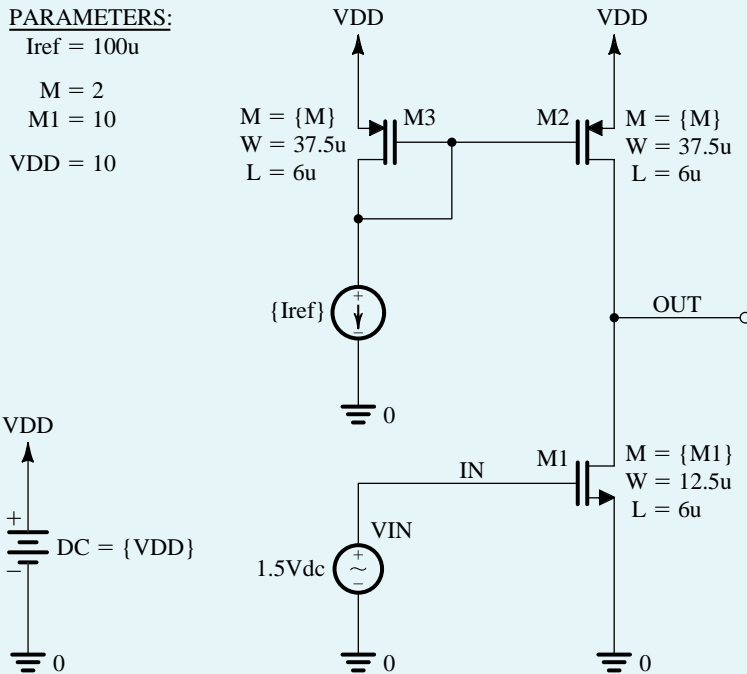
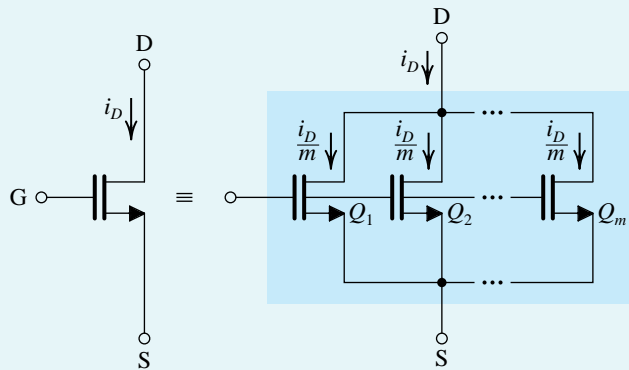


**Figure B.23** Schematic capture of the CS amplifier in Example PS.7.1.



$$\text{Aspect ratio} = \frac{mW}{L} \quad \text{Aspect ratio of each MOSFET} = \frac{W}{L}$$

**Figure B.24** Transistor equivalency.

$$I_D = \frac{1}{2} \mu C_{ox} m \frac{W}{L_{\text{eff}}} V_{ov}^2 \quad (\text{B.24})$$

where  $L_{\text{eff}}$  rather than  $L$  is used to more accurately estimate the drain current.

The CS amplifier in Fig. B.23 is designed for a bias current of 100  $\mu\text{A}$  assuming a reference current  $I_{\text{ref}} = 100 \mu\text{A}$  and  $V_{DD} = 10 \text{ V}$ . The current mirror transistors  $M_2$  and  $M_3$  are sized for  $V_{ov2} = V_{ov3} = 1 \text{ V}$ ,

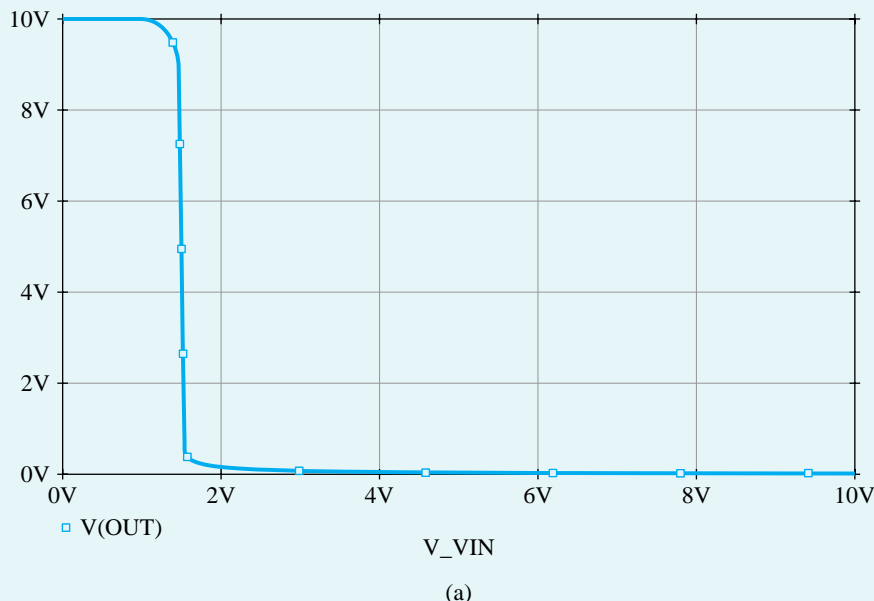
**Example PS.7.1** continued

while the input transistor  $M_1$  is sized for  $V_{OV1} = 0.5$  V. Note that a smaller overdrive voltage is selected for  $M_1$  to achieve a larger voltage gain  $G_v$  for the CS amplifier, since

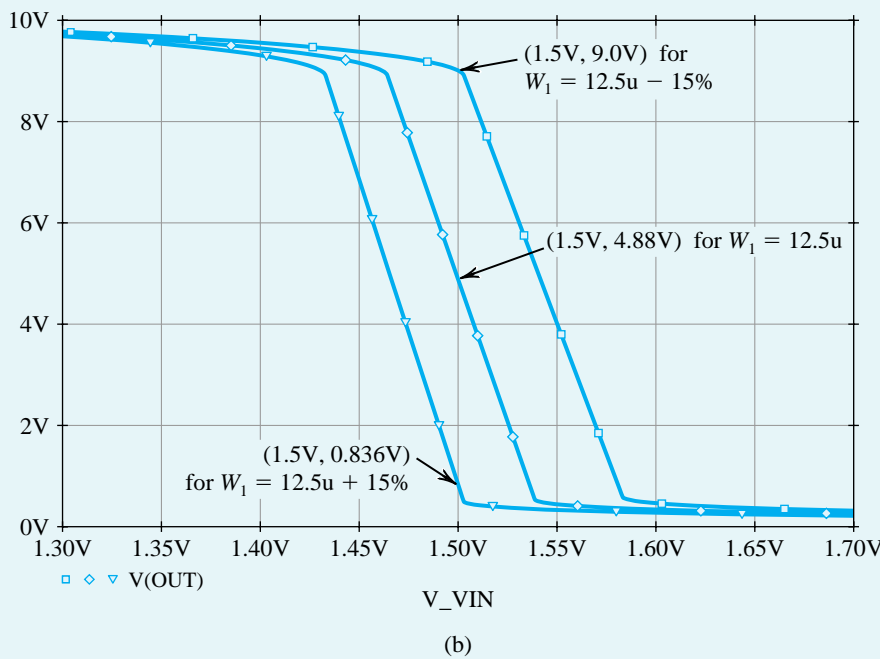
$$G_v = -g_m R'_L = -g_m (r_{o1} \parallel r_{o2}) = -\frac{2}{V_{OV1}} \left( \frac{V_{An} V_{Ap}}{V_{An} + V_{Ap}} \right) \quad (\text{B.25})$$

where  $V_{An}$  and  $V_{Ap}$  are the magnitudes of the Early voltages of, respectively, the NMOS and PMOS transistors. Unit-size transistors are used with  $W/L = 12.5 \mu\text{m}/6 \mu\text{m}$  for the NMOS devices and  $W/L = 37.5 \mu\text{m}/6 \mu\text{m}$  for the PMOS devices. Thus, using Eq. (B.24) together with the 5- $\mu\text{m}$  CMOS process parameters in Table B.4, we find  $m_1 = 10$  and  $m_2 = m_3 = 2$  (rounded to the nearest integer). Furthermore, Eq. (B.25) gives  $G_v = -100 \text{ V/V}$ .

To compute the dc transfer characteristic of the CS amplifier, we perform a dc analysis in PSpice with  $V_{IN}$  swept over the range 0 to  $V_{DD}$  and plot the corresponding output voltage  $V_{OUT}$ . Figure B.25 (a) shows the resulting transfer characteristic. The slope of this characteristic (i.e.,  $dV_{OUT}/dV_{IN}$ ) corresponds to the gain of the amplifier. The high-gain segment is clearly visible for  $V_{IN}$  around 1.5 V. This corresponds to an overdrive voltage for  $M_1$  of  $V_{OV1} = V_{IN} - V_{tn} = 0.5$  V, as desired. To examine the high-gain region more closely, we repeat the dc sweep for  $V_{IN}$  between 1.3 V and 1.7 V. The resulting transfer characteristic is plotted in Fig. B.25 (b, middle curve). Using the Probe graphical interface of PSpice, we find that the linear region of this dc transfer characteristic is bounded approximately by  $V_{IN} = 1.465$  V and  $V_{IN} = 1.539$  V. The corresponding values of  $V_{OUT}$  are 8.838 V and 0.573 V. These results are close to the expected values. Specifically, transistors  $M_1$  and  $M_2$  will remain in the saturation region and, hence, the amplifier will operate in its linear region if  $V_{OV1} \leq V_{OUT} \leq V_{DD} - V_{ov2}$  or  $0.5 \text{ V} \leq V_{OUT} \leq 9 \text{ V}$ . From the results above, the voltage gain  $G_v$  (i.e., the slope of the linear segment of the dc transfer characteristic) is approximately  $-112 \text{ V/V}$ , which is reasonably close to the value obtained by hand ianalysis.



**Figure B.25** (a) Voltage transfer characteristic of the CS amplifier in Example PS.7.1. (b) Expanded view of the transfer characteristic in the high-gain region. Also shown are the transfer characteristics where process variations cause the width of transistor  $M_1$  to change by +15% and -15% from its nominal value of  $W_1 = 12.5 \mu\text{m}$ .

**Figure 8.25** continued

Note from the dc transfer characteristic in Fig. B.25(b) that for an input dc bias of  $V_{IN} = 1.5$  V, the output dc bias is  $V_{OUT} = 4.88$  V. This choice of  $V_{IN}$  maximizes the available signal swing at the output by setting  $V_{OUT}$  at the middle of the linear segment of the dc transfer characteristic. However, because of the high resistance at the output node (or, equivalently, because of the high voltage gain), this value of  $V_{OUT}$  is highly sensitive to the effect of process and temperature variations on the characteristics of the transistors. To illustrate this point, consider what happens when the width of  $M_1$  (i.e.,  $W_1$ , which is normally 12.5  $\mu\text{m}$ ) changes by  $\pm 15\%$ . The corresponding dc transfer characteristics are shown in Fig. B.25(b). Accordingly, when  $V_{IN} = 1.5$  V,  $V_{OUT}$  will drop to 0.84 V if  $W_1$  increases by 15% and will rise to 9.0 V if  $W_1$  decreases by 15%. In practical circuit implementations, this problem is circumvented by using negative feedback to accurately set the dc bias voltage at the output of the amplifier and, hence, to reduce the sensitivity of the circuit to process variations. We studied negative feedback in Chapter 9.

### Example PS.8.1

#### A Multistage Differential BJT Amplifier

The schematic capture of the multistage op-amp circuit analyzed in Examples 7.1 and 7.7 is shown in Fig. B.26.<sup>11</sup> Observe the manner in which the differential signal input  $V_d$  and the common-mode input voltage  $V_{CM}$  are applied. Such an input bias configuration for an op-amp circuit was presented and used in Example PS.2.2. In the following simulations, we will use parts Q2N3904 and Q2N3906 (from Fairchild

<sup>11</sup>This circuit cannot be simulated using the student evaluation version of PSpice. This is because, in this free version of PSpice, circuit simulation is restricted to circuits with no more than 10 transistors.

**Example PS.8.1** *continued*

Semiconductor) for the *npn* and *pnp* BJTs, respectively. The model parameters of these discrete BJTs are listed in Table B.8 and are available in PSpice.

**Table B.8** Spice Model Parameters of the Q2N3904 and Q2N3906 Discrete BJTs

Q2N3904 Discrete BJT						
IS = 6.734f	XTI = 3	EG = 1.11	VAF = 74.03	BF = 416.4	NE = 1.259	ISE = 6.734f
IKF = 66.78m	XTB = 1.5	BR = .7371	NC = 2	ISC = 0	IKR = 0	RC = 1
CJC = 3.638p	MJC = .3085	VJC = .75	FC = .5	CJE = 4.493p	MJE = .2593	VJE = .75
TR = 239.5n	TF = 301.2p	ITF = .4	VTF = 4	XTF = 2	RB = 10	
Q2N3906 Discrete BJT						
IS = 1.41f	XTI = 3	EG = 1.11	VAF = 18.7	BF = 180.7	NE = 1.5	ISE = 0
IKF = 80m	XTB = 1.5	BR = 4.977	NC = 2	ISC = 0	IKR = 0	RC = 2.5
CJC = 9.728p	MJC = .5776	VJC = .75	FC = .5	CJE = 8.063p	MJE = .3677	VJE = .75
TR = 33.42n	TF = 179.3p	ITF = .4	VTF = 4	XTF = 6	RB = 10	

**Table B.9** DC Collector Currents of the Op-Amp Circuit in Fig. B.26 as Computed by Hand Analysis (Example 8.6) and by PSpice

Transistor	Collector Currents (mA)		
	Hand Analysis (Example 8.6)	PSpice	Error (%)
$Q_1$	0.25	0.281	-11.0
$Q_2$	0.25	0.281	-11.0
$Q_3$	0.5	0.567	-11.8
$Q_4$	1.0	1.27	-21.3
$Q_5$	1.0	1.21	-17.4
$Q_6$	2.0	2.50	-20.0
$Q_7$	1.0	1.27	-21.3
$Q_8$	5.0	6.17	-18.9
$Q_9$	0.5	0.48	+4.2

In PSpice, the common-mode input voltage  $V_{CM}$  of the op-amp circuit is set to 0 V (i.e., to the average of the dc power-supply voltages  $V_{CC}$  and  $V_{EE}$ ) to maximize the available input signal swing. A bias-point simulation is performed to determine the dc operating point. Table B.9 summarizes the value of the dc collector currents as computed by PSpice and as calculated by the hand analysis in Example 7.6. Recall that our hand analysis assumed both  $\beta$  and the Early voltage  $V_A$  of the BJTs to be infinite. However, our SPICE simulations in Example PS.6.1 (where we investigated the dependence of  $\beta$  on the collector current  $I_C$ ) indicate that the Q2N3904 has  $\beta \approx 125$  at  $I_C = 0.25$  mA. Furthermore, its forward Early voltage (SPICE parameter VAF) is 74 V, as given in Table B.8. Nevertheless, we observe from Table B.9 that the largest error in the calculation of the dc bias currents is on the order of 20%. Accordingly, we can conclude that a quick hand analysis using gross approximations can still yield reasonable results for a preliminary estimate and, of course, hand analysis yields much insight into the circuit operation. In addition to the dc bias currents listed in Table B.9, the bias-point simulation in PSpice shows that the output dc offset (i.e.,  $V_{OUT}$  when  $V_d = 0$ ) is 3.62 V and that the input bias current  $I_{B1}$  is 2.88  $\mu$ A.

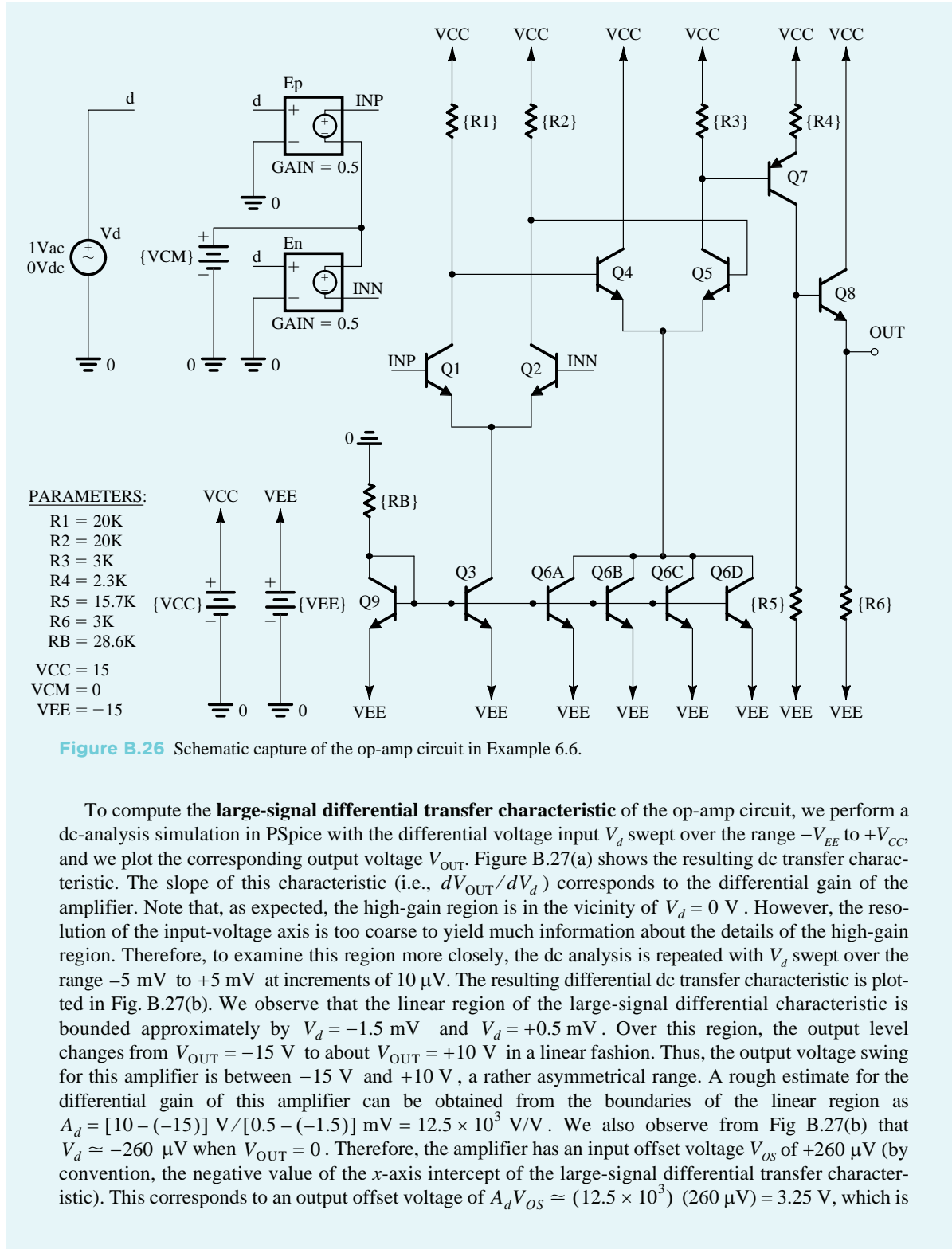
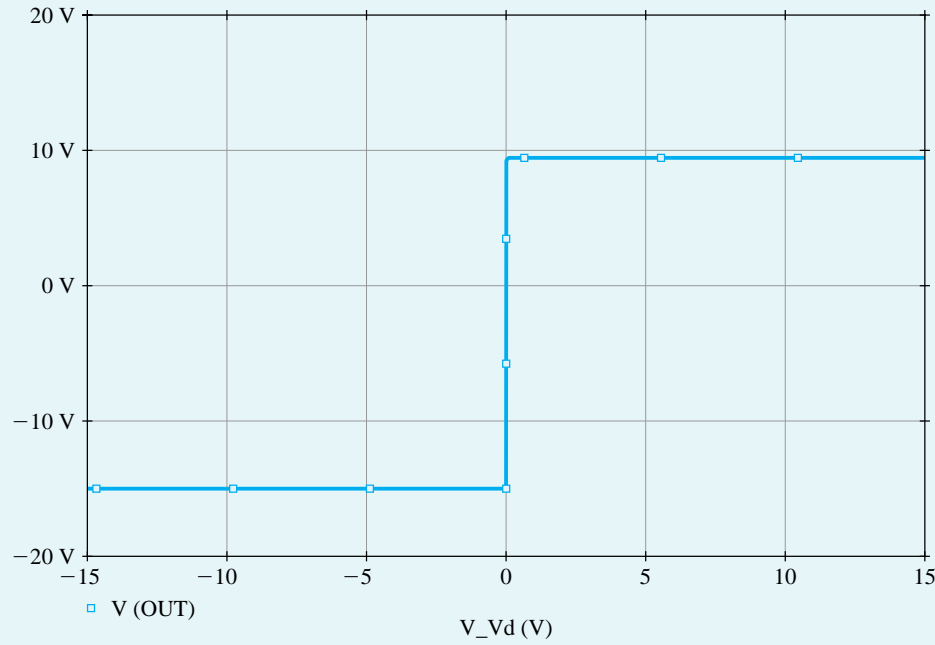


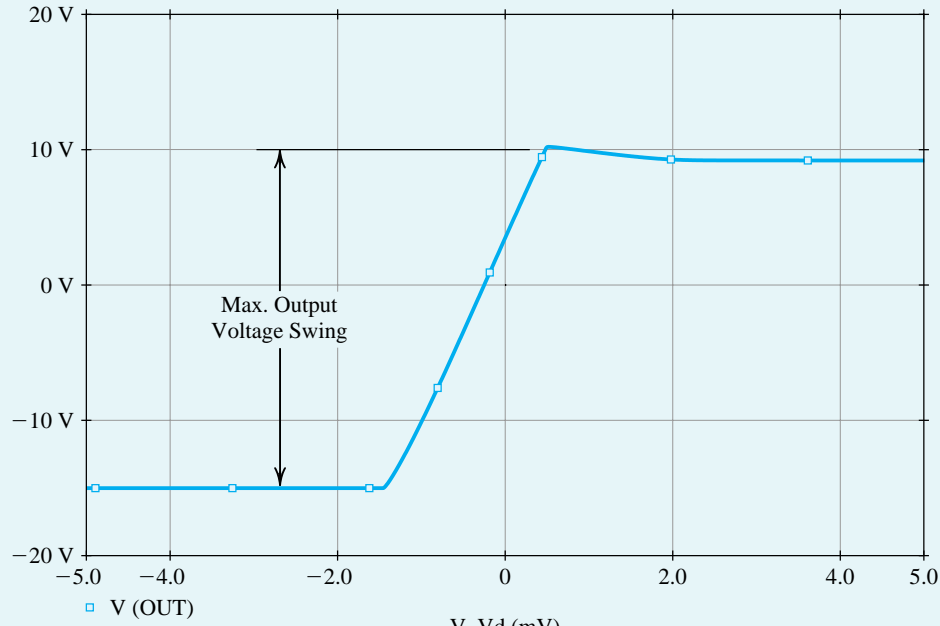
**Figure B.26** Schematic capture of the op-amp circuit in Example 6.6.

To compute the **large-signal differential transfer characteristic** of the op-amp circuit, we perform a dc-analysis simulation in PSpice with the differential voltage input  $V_d$  swept over the range  $-V_{EE}$  to  $+V_{CC}$ , and we plot the corresponding output voltage  $V_{OUT}$ . Figure B.27(a) shows the resulting dc transfer characteristic. The slope of this characteristic (i.e.,  $dV_{OUT}/dV_d$ ) corresponds to the differential gain of the amplifier. Note that, as expected, the high-gain region is in the vicinity of  $V_d = 0$  V. However, the resolution of the input-voltage axis is too coarse to yield much information about the details of the high-gain region. Therefore, to examine this region more closely, the dc analysis is repeated with  $V_d$  swept over the range  $-5$  mV to  $+5$  mV at increments of  $10$   $\mu$ V. The resulting differential dc transfer characteristic is plotted in Fig. B.27(b). We observe that the linear region of the large-signal differential characteristic is bounded approximately by  $V_d = -1.5$  mV and  $V_d = +0.5$  mV. Over this region, the output level changes from  $V_{OUT} = -15$  V to about  $V_{OUT} = +10$  V in a linear fashion. Thus, the output voltage swing for this amplifier is between  $-15$  V and  $+10$  V, a rather asymmetrical range. A rough estimate for the differential gain of this amplifier can be obtained from the boundaries of the linear region as  $A_d = [10 - (-15)] \text{ V} / [0.5 - (-1.5)] \text{ mV} = 12.5 \times 10^3 \text{ V/V}$ . We also observe from Fig. B.27(b) that  $V_d \approx -260$   $\mu$ V when  $V_{OUT} = 0$ . Therefore, the amplifier has an input offset voltage  $V_{os}$  of  $+260$   $\mu$ V (by convention, the negative value of the  $x$ -axis intercept of the large-signal differential transfer characteristic). This corresponds to an output offset voltage of  $A_d V_{os} \approx (12.5 \times 10^3) (260 \mu\text{V}) = 3.25$  V, which is

**Example PS.8.1** *continued*



(a)



(b)

**Figure B.27** (a) The large-signal differential transfer characteristic of the op-amp circuit in Fig. B.26. The common-mode input voltage  $V_{CM}$  is set to 0 V. (b) An expanded view of the transfer characteristic in the high-gain region.

close to the value found through the bias-point simulation. It should be emphasized that this offset voltage is inherent in the design and is not the result of component or device mismatches. Thus, it is usually referred to as a **systematic offset**.

Next, to compute the frequency response of the op-amp circuit<sup>12</sup> and to measure its differential gain  $A_d$  and its 3-dB frequency  $f_H$  in PSpice, we set the differential input voltage  $V_d$  to be a 1-V ac signal (with 0-V dc level), perform an ac-analysis simulation, and plot the output voltage magnitude  $|V_{\text{OUT}}|$  versus frequency. Figure B.28(a) shows the resulting frequency response. Accordingly,  $A_d = 13.96 \times 10^3$  V/V or 82.8 dB, and  $f_H = 256.9$  kHz. Thus, this value of  $A_d$  is close to the value estimated using the large-signal differential transfer characteristic.

An approximate value of  $f_H$  can also be obtained using the expressions derived in Section 8.8. Specifically,

$$f_H \approx \frac{1}{2\pi R_{\text{eq}} C_{\text{eq}}} \quad (\text{B.26})$$

where

$$C_{\text{eq}} = C_{\mu 2} + C_{\pi 5} + C_{\mu 5}[1 + g_{m5}(R_3 \parallel r_{o5} \parallel (r_{\pi 7} + (\beta + 1)R_4))] \quad (\text{B.27})$$

and

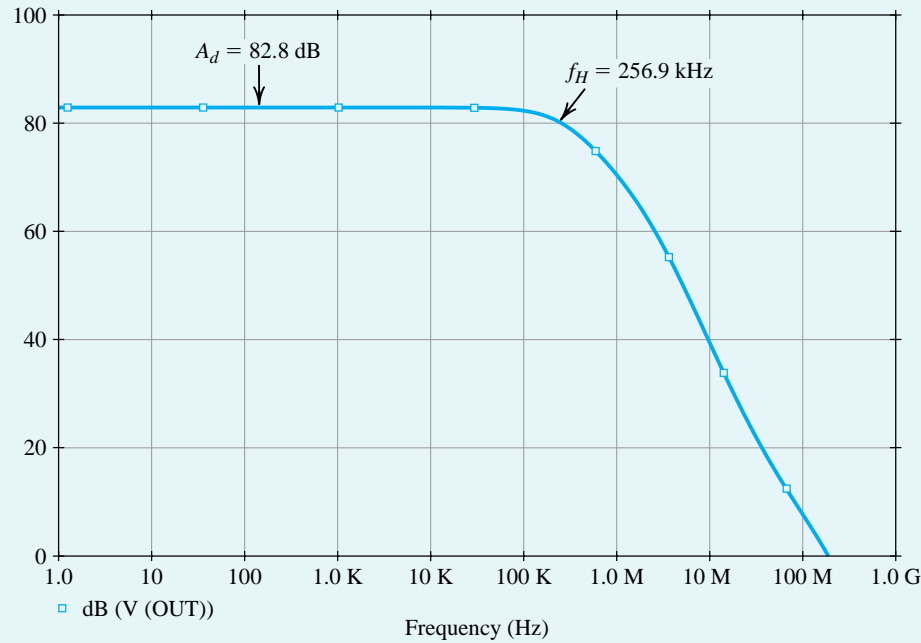
$$R_{\text{eq}} = R_2 \parallel r_{o2} \parallel r_{\pi 5}$$

The values of the small-signal parameters as computed by PSpice can be found in the output file of a bias-point (or an ac-analysis) simulation. Using these values results in  $C_{\text{eq}} = 338$  pF,  $R_{\text{eq}} = 2.91$  kΩ, and  $f_H = 161.7$  kHz. However, this approximate value of  $f_H$  is much smaller than the value computed by PSpice. The reason for this disagreement is that the foregoing expression for  $f_H$  was derived (in Section 8.8) using the equivalent differential half-circuit concept. However, the concept is accurate only when it is applied to a symmetrical circuit. The op-amp circuit in Fig. B.26 is not symmetrical because the second gain stage formed by the differential pair  $Q_4-Q_5$  has a load resistor  $R_3$  in the collector of  $Q_5$  only. To verify that the expression for  $f_H$  in Eq. (B.26) gives a close approximation for  $f_H$  in the case of a symmetric circuit, we insert a resistor  $R'_3$  (whose size is equal to  $R_3$ ) in the collector of  $Q_4$ . Note that this will have only a minor effect on the dc operating point. The op-amp circuit with  $Q_4$  having a collector resistor  $R'_3$  is then simulated in PSpice. Figure B.28(b) shows the resulting frequency response of this symmetric op amp, where  $f_H = 155.7$  kHz. Accordingly, in the case of a perfectly symmetric op-amp circuit, the value of  $f_H$  in Eq. (B.26) closely approximates the value computed by PSpice. Comparing the frequency responses of the nonsymmetric (Fig. B.28a) and the symmetric (Fig. B.28b) op-amp circuits, we note that the 3-dB frequency of the op amp drops from 256.9 kHz to 155.7 kHz when resistor  $R'_3$  is inserted in the collector of  $Q_4$  to make the op-amp circuit symmetrical. This is because, with a resistor  $R'_3$ , the collector of  $Q_4$  is no longer at signal ground and, hence,  $C_{\mu 4}$  experiences the Miller effect. Consequently, the high-frequency response of the op-amp circuit is degraded.

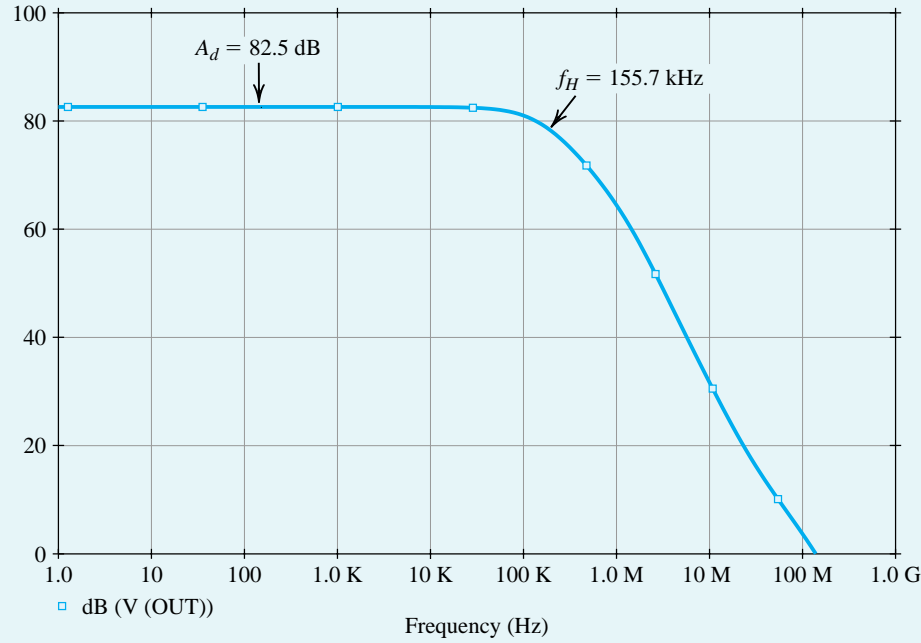
Observe that in the preceding ac-analysis simulation, owing to the systematic offset inherent in the design, the op-amp circuit is operating at an output dc voltage of 3.62 V. However, in an actual circuit implementation (with  $V_{CM} = 0$ ), negative feedback is employed (see Chapters 2 and 9) and the output dc voltage is stabilized at zero. Thus, the small-signal performance of the op-amp circuit can be more accurately simulated by biasing the circuit so as to force operation at this level of output voltage. This can be easily done by applying a differential dc input of  $-V_{os}$ . Superimposed on this dc

<sup>12</sup>This part of the example requires study of Sections 8.8 and 8.10.2.

**Example PS.8.1** continued



(a)

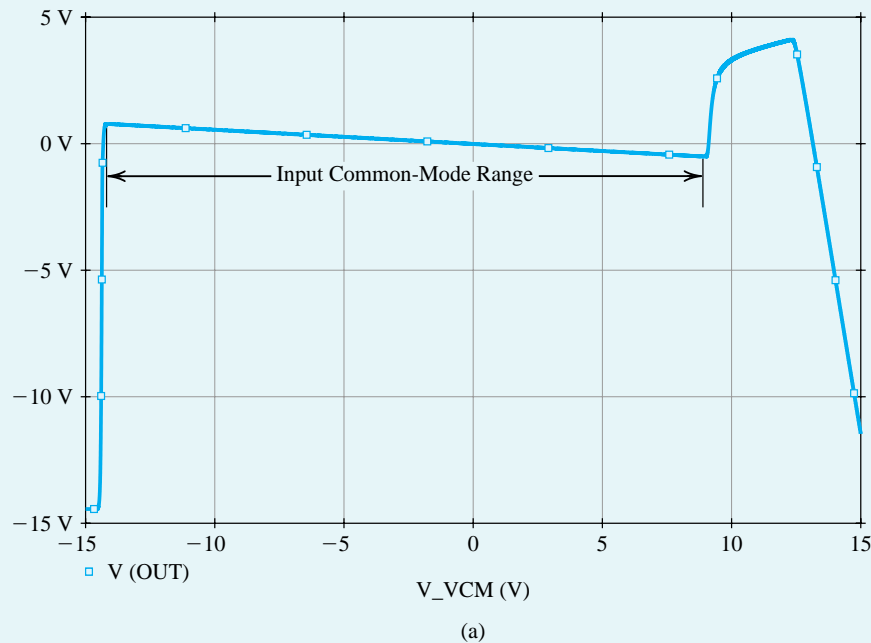


(b)

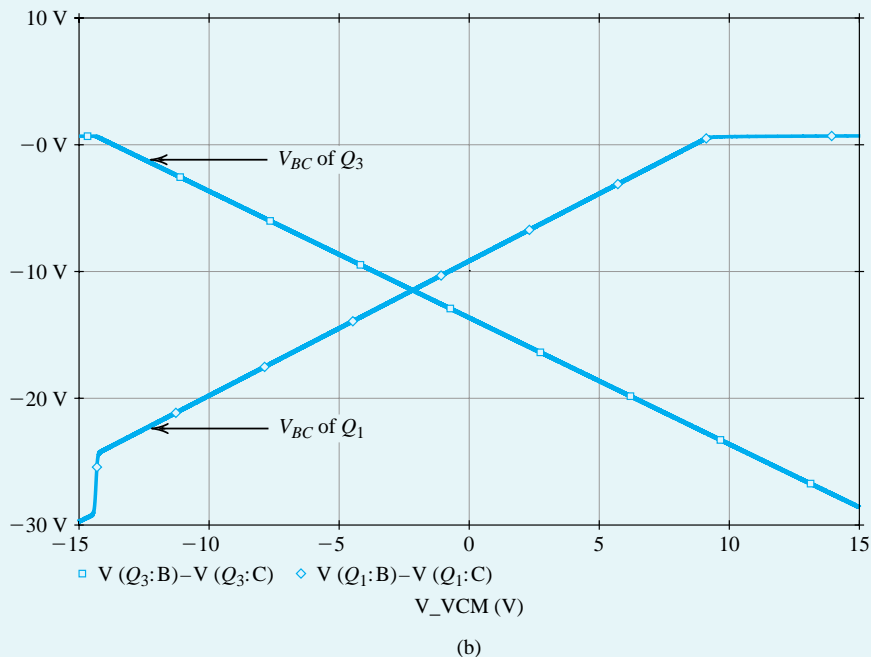
**Figure B.28** Frequency response of (a) the op-amp circuit in Fig. B.26 and (b) the op-amp circuit in Fig. B.26 but with a resistor  $R'_3 = R_3$  inserted in the collector of  $Q_4$  to make the op-amp circuit symmetrical.

input, we can apply an ac signal to perform an ac-analysis simulation for the purpose of, for example, computing the differential gain and the 3-dB frequency.

Finally, to compute the input common-mode range of the op-amp circuit in Fig. B.26, we perform a dc-analysis simulation in PSpice with the input common-mode voltage swept over the range  $-V_{EE}$  to  $V_{CC}$ , while maintaining  $V_d$  constant at  $-V_{os}$  in order to cancel the output offset voltage (as discussed earlier) and, thus, prevent premature saturation of the BJTs. The corresponding output voltage  $V_{OUT}$  is plotted in Fig. B.29(a). From this common-mode dc transfer characteristic we find that the amplifier behaves linearly over the  $V_{CM}$  range  $-14.1$  V to  $+8.9$  V, which is therefore the **input common-mode range**. In Example 7.6, we noted that the upper limit of this range is determined by  $Q_1$  and  $Q_2$  saturating, whereas the lower limit is determined by  $Q_3$  saturating. To verify this assertion, we requested PSpice to plot the values of the collector-base voltages of these BJTs versus the input common-mode voltage  $V_{CM}$ . The results are shown in Fig. B.29(b), from which we note that our assertion is indeed correct (recall that an *n*p*n* BJT enters its saturation region when its base-collector junction becomes forward biased, i.e.,  $V_{BC} \geq 0$  ).



**Figure B.29** (a) The large-signal common-mode transfer characteristic of the op-amp circuit in Fig. B.26. The differential input voltage  $V_d$  is set to  $-V_{os} = -260 \mu\text{V}$  to prevent premature saturation. (b) The effect of the common-mode input voltage  $V_{CM}$  on the linearity of the input stage of the op-amp circuit in Fig. B.26. The base–collector voltage of  $Q_1$  and  $Q_3$  is shown as a function of  $V_{CM}$ . The input stage of the op-amp circuit leaves the active region when the base–collector junction of either  $Q_1$  or  $Q_3$  becomes forward biased (i.e., when  $V_{BC} \geq 0$  ).

**Example PS.8.1** *continued*

**Figure B.29** (Contd.).

**Example PS.9.1**
**Frequency Response of the CMOS CS and the Folded-Cascode Amplifiers**

In this example, we will use PSpice to compute the frequency response of both the CS and the folded-cascode amplifiers whose schematic capture diagrams are shown shortly in Figs. B.30 and B.32, respectively. We will assume that the dc bias levels at the output of the amplifiers are stabilized using negative feedback. However, before performing a small-signal analysis (an ac-analysis simulation) in SPICE to measure the frequency response, we will perform a dc analysis (a bias-point simulation) to verify that all MOSFETs are operating in the saturation region and, hence, ensure that the amplifier is operating in its linear region.

In the following, we will assume a  $0.5\text{-}\mu\text{m}$  CMOS technology for the MOSFETs and use parts NMOSOP5 and PMOSOP5 whose SPICE level-1 model parameters are listed in Table B.3. To specify the dimensions of the MOSFETs in PSpice, we will use the multiplicative factor  $m$ , together with the channel length  $L$  and channel width  $W$  (as we did in Example PS.7.1).

**The CMOS CS Amplifier**

The CS amplifier circuit in Fig. B.30 is identical to the one shown in Fig. 6.4, except that a current source is connected to the source of the input transistor  $M_1$  to set its drain current  $I_{D1}$  independently of its drain voltage  $V_{D1}$ . Furthermore, in our PSpice simulations, we used an impractically large bypass capacitor  $C_s$  of 1 F. This sets the source of  $M_1$  at approximately signal ground during the ac-analysis simulation. Accordingly, the CS amplifier circuits in Figs. 6.4 and B.30 are equivalent for the purpose of frequency-response

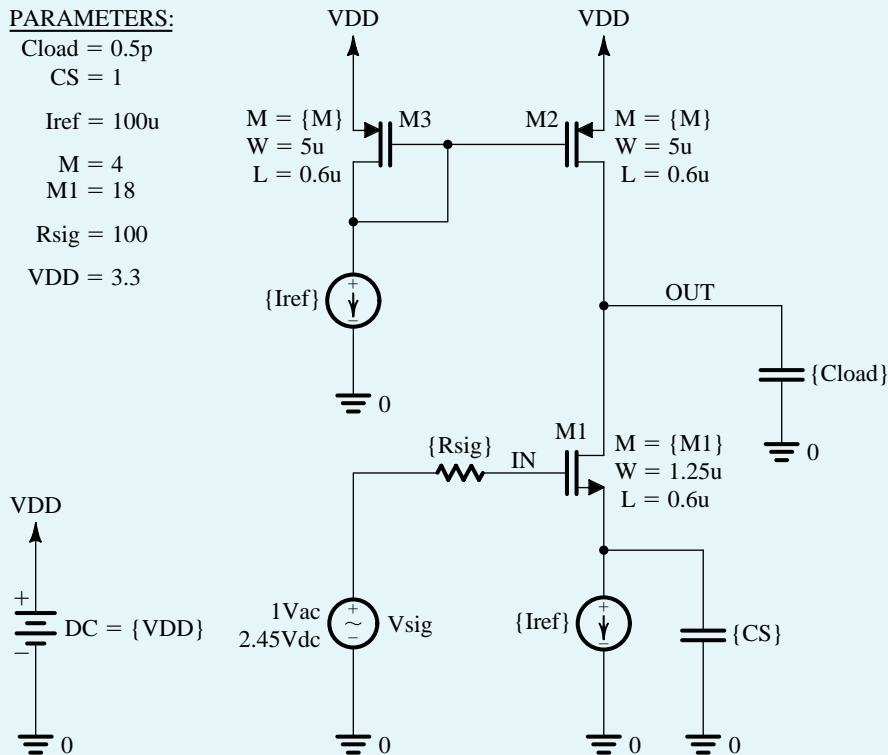


**Figure B.30** Schematic capture of the CS amplifier in Example PS.9.1

analysis. In Chapter 7, we found out, in the context of studying the differential pair, how the goals of this biasing approach for the CS amplifier are realized in practical IC implementations.

The CS amplifier in Fig. B.30 is designed assuming a reference current  $I_{\text{ref}} = 100 \mu\text{A}$  and  $V_{DD} = 3.3 \text{ V}$ . The current-mirror transistors,  $M_2$  and  $M_3$ , are sized for  $V_{OV2} = V_{OV3} = 0.3 \text{ V}$ , while the input transistor  $M_1$  is sized for  $V_{OV1} = 0.15 \text{ V}$ . Unit-size transistors are used with  $W/L = 1.25 \mu\text{m}/0.6 \mu\text{m}$  for the NMOS devices and  $W/L = 5 \mu\text{m}/0.6 \mu\text{m}$  for the PMOS devices. Thus, using the square law  $I_D - V_{OV}$  of the MOSFET together with the 0.5- $\mu\text{m}$  CMOS process parameters in Table B.4, we find  $m_1 = 18$  and  $m_2 = m_3 = 4$ . Furthermore, Eq. (B.25) gives  $G_v = -44.4 \text{ V/V}$  for the CS amplifier.

In the PSpice simulations of the CS amplifier in Fig. B.30, the dc bias voltage of the signal source is set such that the voltage at the source terminal of  $M_1$  is  $V_{SI} = 1.3 \text{ V}$ . This requires the dc level of  $V_{\text{sig}}$  to be  $V_{OV1} + V_{m1} + V_{SI} = 2.45 \text{ V}$  because  $V_{m1} \approx 1 \text{ V}$  as a result of the body effect on  $M_1$ . The reasoning behind this choice of  $V_{SI}$  is that, in a practical circuit implementation, the current source that feeds the source of  $M_1$  is realized using a cascode current mirror such as the one in Fig. 6.32. In this case, the minimum voltage required across the current source (i.e., the minimum  $V_{SI}$ ) is  $V_t + 2V_{OV} = 1.3 \text{ V}$ , assuming  $V_{OV} = 0.3 \text{ V}$  for the current-mirror transistors.

A bias-point simulation is performed in PSpice to verify that all MOSFETs are biased in the saturation region. Next, to compute the frequency response of the amplifier, we set the ac voltage of the signal source to 1 V, perform an ac-analysis simulation, and plot the output voltage magnitude versus frequency. Figure B.31(a) shows the resulting frequency response for  $R_{\text{sig}} = 100 \Omega$  and  $R_{\text{out}} = 1 \text{ M}\Omega$ . In both cases, a load capacitance of  $C_{\text{load}} = 0.5 \text{ pF}$  is used. The corresponding values of the 3-dB frequency  $f_H$  of the amplifier are given in Table B.10.

## Example PS.9.1 continued

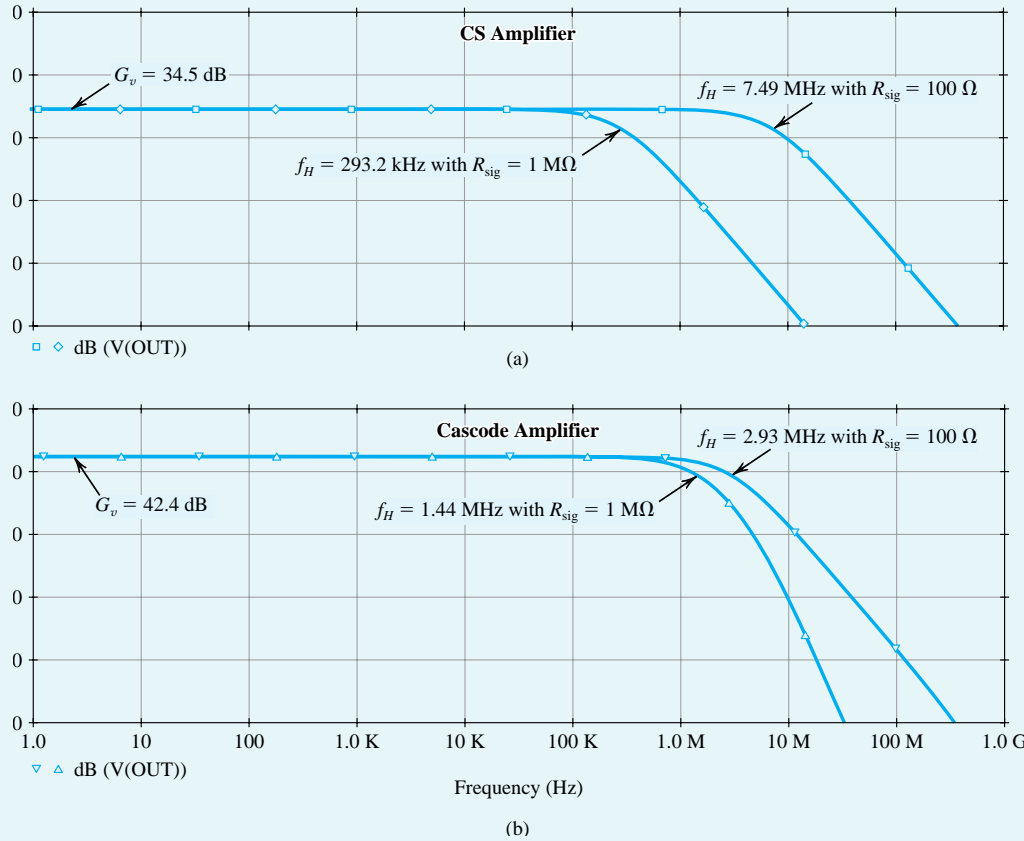


**Figure B.31** Frequency response of (a) the CS amplifier and (b) the folded-cascode amplifier in Example PS.9.1, with  $R_{\text{sig}} = 100 \Omega$  and  $R_{\text{sig}} = 1 \text{ M}\Omega$ .

Observe that  $f_H$  drops when  $R_{\text{sig}}$  is increased. This is anticipated from our study of the high-frequency response of the CS amplifier in Section 8.3. Specifically, as  $R_{\text{sig}}$  increases, the pole

$$f_{p,\text{in}} = \frac{1}{2\pi R_{\text{sig}} C_{\text{in}}} \quad (\text{B.27})$$

formed at the amplifier input will have an increasingly significant effect on the overall frequency response of the amplifier. As a result, the effective time constant  $\tau_H$  in Eq. (8.85) increases and  $f_H$  decreases. When  $R_{\text{sig}}$  becomes very large, as it is when  $R_{\text{sig}} = 1 \text{ M}\Omega$ , a dominant pole is formed by  $R_{\text{sig}}$  and  $C_{\text{in}}$ . This results in

$$f_H \approx f_{p,\text{in}} \quad (\text{B.28})$$

To estimate  $f_{p,\text{in}}$ , we need to calculate the input capacitance  $C_{\text{in}}$  of the amplifier. Using Miller's theorem, we have

$$\begin{aligned} C_{\text{in}} &= C_{gs1} + C_{gd1}(1 + g_{m1}R'_L) \\ &= \left(\frac{2}{3}m_1W_1L_1C_{ox} + C_{gs,ov1}\right) + C_{gd,ov1}(1 + g_{m1}R'_L) \end{aligned} \quad (\text{B.29})$$

**Table B.10** Dependence of the 3-dB Bandwidth  $f_H$  on  $R_{sig}$  for the CS and the Folded-Cascode Amplifiers in Example PS.9.1

$R_{sig}$	$f_H$	
	CS Amplifier	Folded-Cascode Amplifier
100 $\Omega$	7.49 MHz	2.93 MHz
1 M $\Omega$	293.2 kHz	1.44 MHz

where

$$R'_L = r_{o1} \parallel r_{o2} \quad (\text{B.30})$$

Thus,  $C_{in}$  can be calculated using the values of  $C_{gs1}$  and  $C_{gd1}$ , which are computed by PSpice and can be found in the output file of the bias-point simulation. Alternatively,  $C_{in}$  can be found using Eq. (B.29) with the values of the overlap capacitances  $C_{gs, ov1}$  and  $C_{gd, ov1}$  calculated using the process parameters in Table B.4 (as described in Eqs. B.9 and B.10); that is:

$$C_{gs, ov1} = m_1 W_1 C_{GSO} \quad (\text{B.31})$$

$$C_{gd, ov1} = m_1 W_1 C_{GDO} \quad (\text{B.32})$$

This results in  $C_{in} = 0.53$  pF when  $|G_v| = g_{m1} R'_L = 53.2$  V/V. Accordingly, using Eqs. (B.27) and (B.28),  $f_H = 300.3$  kHz when  $R_{sig} = 1$  M $\Omega$ , which is close to the value computed by PSpice.

### The Folded-Cascode Amplifier

The folded-cascode amplifier circuit in Fig. B.32 is equivalent to the one in Fig. 6.16, except that a current source is placed in the source of the input transistor  $M_1$  (for the same dc-biasing purpose as in the case of the CS amplifier). Note that, in Fig. B.32, the PMOS current mirror  $M_3-M_4$  and the NMOS current mirror  $M_5-M_6$  are used to realize, respectively, current sources  $I_1$  and  $I_2$  in the circuit of Fig. 6.16. Furthermore, the current transfer ratio of mirror  $M_3-M_4$  is set to 2 (i.e.,  $m_3/m_4 = 2$ ). This results in  $I_{D3} \simeq 2I_{ref}$ . Hence, transistor  $M_2$  is biased at  $I_{D2} = I_{D3} - I_{D1} = I_{ref}$ . The gate bias voltage of transistor  $M_2$  is generated using the diode-connected transistors  $M_7$  and  $M_8$ . The size and drain current of these transistors are set equal to those of transistor  $M_2$ . Therefore, ignoring the body effect,

$$V_{G2} = V_{DD} - V_{SG7} - V_{SG8} \simeq V_{DD} - 2(|V_{tp}| + |V_{OVP}|)$$

where  $V_{OVP}$  is the overdrive voltage of the PMOS transistors in the amplifier circuit. These transistors have the same overdrive voltage because their  $I_D/m$  is the same. Thus, such a biasing configuration results in  $V_{SG2} = |V_{tp}| + |V_{OVP}|$  as desired, while setting  $V_{SD3} = |V_{tp}| + |V_{OVP}|$  to improve the bias matching between  $M_3$  and  $M_4$ .

The folded-cascode amplifier in Fig. B.32 is designed assuming a reference current  $I_{ref} = 100$   $\mu$ A and  $V_{DD} = 3.3$  V (similar to the case of the CS amplifier). All transistors are sized for an overdrive voltage of 0.3 V, except for the input transistor  $M_1$ , which is sized for  $V_{OVI} = 0.15$  V. Thus, since  $I_D = \frac{1}{2} u C_{ox} m (W/L_{eff}) V_{OV}^2$ , all the MOSFETs in the amplifier circuit are designed using  $m = 4$ , except for  $m_1 = 18$ .

The midband voltage gain of the folded-cascode amplifier in Fig. B.32 can be expressed as

$$G_v = -g_{m1} R_{out} \quad (\text{B.33})$$

where

$$R_{out} = R_{out2} \parallel R_{out5} \quad (\text{B.34})$$

**Example PS.9.1** continued

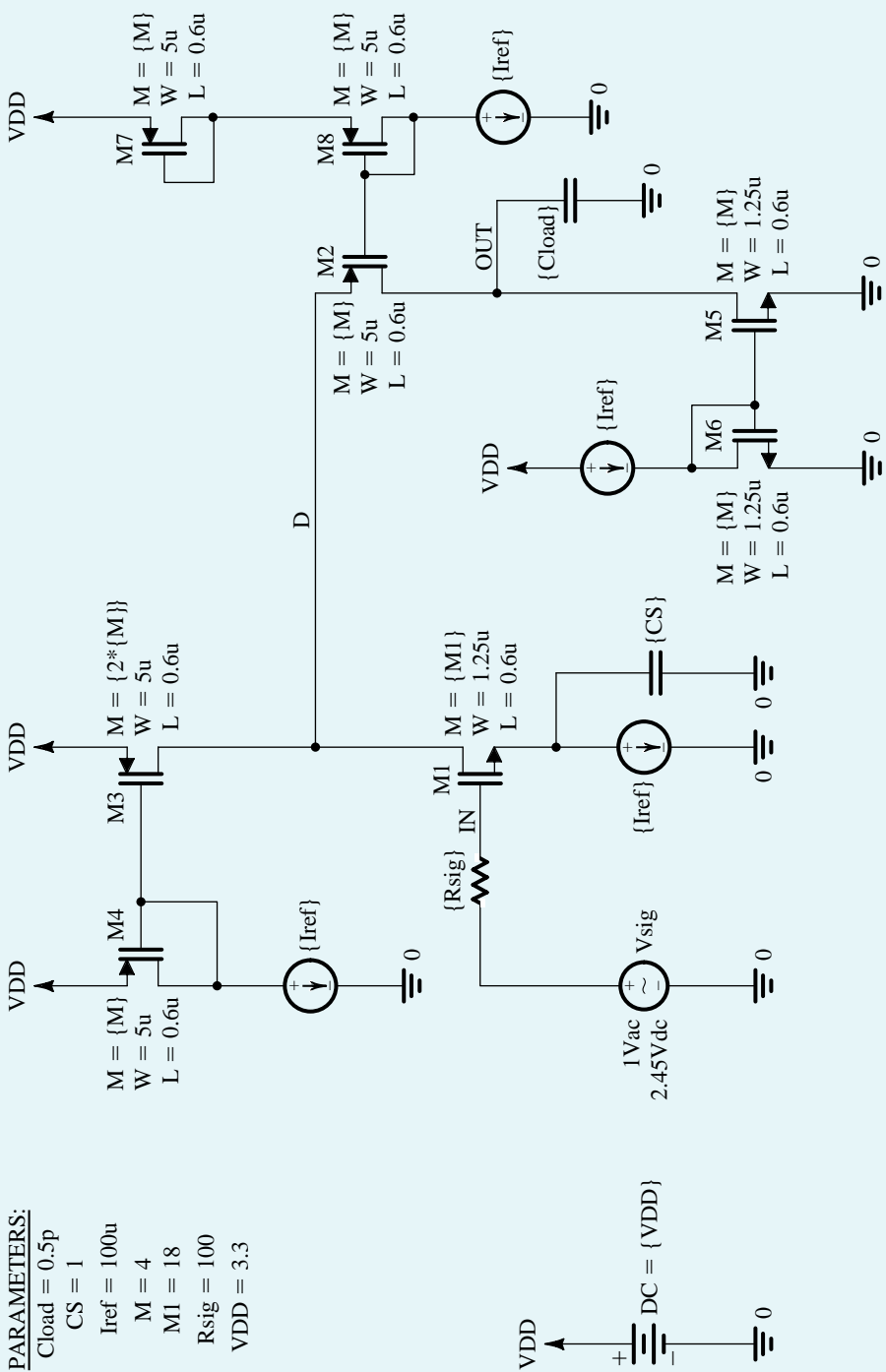


**Figure B.32** Schematic capture of the folded cascode amplifier in Example PS.9.1.

is the output resistance of the amplifier. Here,  $R_{\text{out}2}$  is the resistance seen looking into the drain of the cascode transistor  $M_2$ , while  $R_{\text{out}5}$  is the resistance seen looking into the drain of the current-mirror transistor  $M_5$ . Using Eq. (6.25), we have

$$R_{\text{out}2} \simeq (g_{m2}r_{o2})R_{s2} \quad (\text{B.35})$$

where

$$R_{s2} = r_{o1} \parallel r_{o3} \quad (\text{B.36})$$

is the effective resistance at the source of  $M_2$ . Furthermore,

$$R_{\text{out}5} = r_{o5} \quad (\text{B.37})$$

Thus, for the folded-cascoded amplifier in Fig. B.32,

$$R_{\text{out}} \simeq r_{o5} \quad (\text{B.38})$$

and

$$G_v \simeq -g_{m1}r_{o5} = -2 \frac{V_{An}}{V_{OVI}} \quad (\text{B.39})$$

Using the 0.5-μm CMOS parameters, this gives  $R_{\text{out}} = 100 \text{ k}\Omega$  and  $G_v = -133 \text{ V/V}$ . Therefore,  $R_{\text{out}}$  and hence  $|G_v|$  of the folded-cascode amplifier in Fig. B.32 are larger than those of the CS amplifier in Fig. B.30 by a factor of 3.

Figure B.31(b) shows the frequency response of the folded-cascode amplifier as computed by PSpice for the cases of  $R_{\text{sig}} = 100 \Omega$  and  $R_{\text{sig}} = 1 \text{ M}\Omega$ . The corresponding values of the 3-dB frequency  $f_H$  of the amplifier are given in Table B.10. Observe that when  $R_{\text{sig}}$  is small,  $f_H$  of the folded-cascode amplifier is lower than that of the CS amplifier by a factor of approximately 2.6, approximately equal to the factor by which the gain is increased. This is because when  $R_{\text{sig}}$  is small, the frequency response of both amplifiers is dominated by the pole formed at the output node, that is,

$$f_H \simeq f_{p,\text{out}} = \frac{1}{2\pi R_{\text{out}} C_{\text{out}}} \quad (\text{B.40})$$

Since the output resistance of the folded-cascode amplifier is larger than that of the CS amplifier (by a factor of approximately 3, as found through the hand analysis above) while their output capacitances are approximately equal, the folded-cascode amplifier has a lower  $f_H$  in this case.

On the other hand, when  $R_{\text{sig}}$  is large,  $f_H$  of the folded-cascode amplifier is much higher than that of the CS amplifier. This is because, in this case, the effect of the pole at  $f_{p,\text{in}}$  on the overall frequency response of the amplifier becomes significant. Since, due to the Miller effect,  $C_{\text{in}}$  of the CS amplifier is much larger than that of the folded-cascode amplifier, its  $f_H$  is much lower in this case. To confirm this point, observe that  $C_{\text{in}}$  of the folded-cascode amplifier can be estimated by replacing  $R'_L$  in Eq. (B.29) with the total resistance  $R_{d1}$  between the drain of  $M_1$  and ground. Here,

$$R_{d1} = r_{o1} \parallel r_{o3} \parallel R_{\text{in}2} \quad (\text{B.41})$$

where  $R_{\text{in}2}$  is the input resistance of the common-gate transistor  $M_2$  and can be obtained using an approximation of the relationship in Eq. (6.34) as

$$R_{\text{in}2} \simeq \frac{r_{o2} + r_{o5}}{g_{m2}r_{o2}} \quad (\text{B.42})$$

Thus,

$$R_{d1} \simeq r_{o1} \parallel r_{o3} \parallel \left( \frac{r_{o2} + r_{o5}}{g_{m2}r_{o2}} \simeq \frac{2}{g_{m2}} \right) \quad (\text{B.43})$$

**Example PS.9.1** continued

Therefore,  $R_{d1}$  is much smaller than  $R'_L$  in Eq. (B.30). Hence,  $C_{in}$  of the folded-cascode amplifier in Fig. B.32 is indeed much smaller than that of the CS amplifier in Fig. B.30. This confirms that the folded-cascode amplifier is much less impacted by the Miller effect and, therefore, can achieve a much higher  $f_H$  when  $R_{sig}$  is large.

The midband gain of the folded-cascode amplifier can be significantly increased by replacing the current mirror  $M_5-M_6$  with a current mirror having a larger output resistance, such as the cascode current mirror in Fig. 6.32 whose output resistance is approximately  $g_m r_o^2$ . In this case, however,  $R_{in2}$  and hence  $R_{d1}$  increase, causing an increased Miller effect and a corresponding reduction in  $f_H$ .

Finally, it is interesting to observe that the frequency response of the folded-cascode amplifier, shown in Fig. B.31(b), drops beyond  $f_H$  at approximately -20 dB/decade when  $R_{sig} = 100 \Omega$  and at approximately -40 dB/decade when  $R_{sig} = 1 \text{ M}\Omega$ . This is because when  $R_{sig}$  is small, the frequency response is dominated by the pole at  $f_{p,out}$ . However, when  $R_{sig}$  is increased,  $f_{p,in}$  is moved closer to  $f_{p,out}$  and both poles contribute to the gain falloff.

**Example PS.10.1**

**Determining the Loop Gain of a Feedback Amplifier**

This example illustrates the use of SPICE to compute the loop gain  $A\beta$ . For this purpose, we shall use the shunt-series feedback amplifier shown in Fig. B.33 (see also Problem 9.101).

To compute the loop gain, we set the input signal  $V_s$  to zero, and we choose to break the feedback loop between the collector of  $Q_1$  and the base of  $Q_2$ . However, in breaking the feedback loop, we must ensure that the following two conditions that existed prior to breaking the feedback loop do not change: (1) the dc bias situation and (2) the ac signal termination.

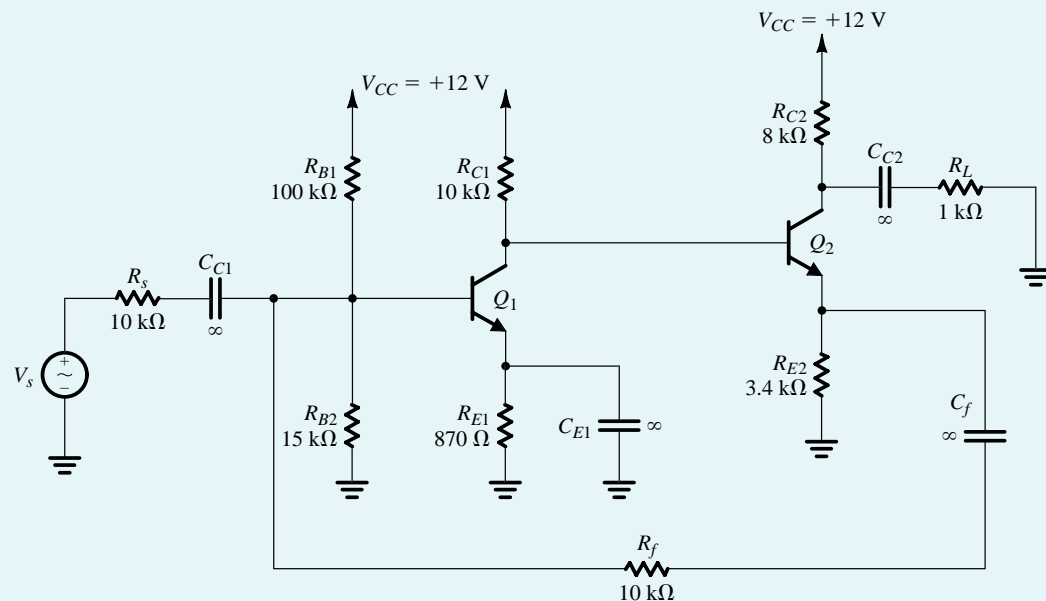


**Figure B.33** Circuit of the shunt-series feedback amplifier in Example PS.10.1.

To break the feedback loop without disturbing the dc bias conditions of the circuit, we insert a large inductor  $L_{\text{break}}$ , as shown in Fig. B.34(a). Using a value of, say,  $L_{\text{break}} = 1 \text{ GH}$  will ensure that the loop is opened for ac signals while keeping dc bias conditions unchanged.

To break the feedback loop without disturbing the signal termination conditions, we must load the loop output at the collector of  $Q_1$  with a termination impedance  $Z_t$  whose value is equal to the impedance seen looking into the loop input at the base of  $Q_2$ . Furthermore, to avoid disturbing the dc bias conditions,  $Z_t$  must be connected to the collector of  $Q_1$  via a large coupling capacitor. However, it is not always easy to determine the value of the termination impedance  $Z_t$ . So, we will describe two simulation methods to compute the loop gain without explicitly determining  $Z_t$ .

### Method 1 Using the open-circuit and short-circuit transfer functions

As described in Section 9.9, the loop gain can be expressed as

$$A\beta = -1 / \left( \frac{1}{T_{oc}} + \frac{1}{T_{sc}} \right)$$

where  $T_{oc}$  is the open-circuit voltage transfer function and  $T_{sc}$  is the short-circuit voltage transfer function.

The circuit for determining  $T_{oc}$  is shown in Fig. B.34(b). Here, an ac test signal voltage  $V_t$  is applied to the loop input at the base of  $Q_2$  via a large coupling capacitor (having a value of, say,  $1 \text{ kF}$ ) to avoid disturbing the dc bias conditions. Then,

$$T_{oc} = \frac{V_{oc}}{V_t}$$

where  $V_{oc}$  is the ac open-circuit output voltage at the collector of  $Q_1$ .

In the circuit for determining  $T_{sc}$  (Fig. B.34), an ac test signal current  $I_t$  is applied to the loop input at the base of  $Q_2$ . Note that a coupling capacitor is not needed in this case because the ac current source appears as an open circuit at dc, and, hence, does not disturb the dc bias conditions.

The loop output at the collector of  $Q_1$  is ac short-circuited to ground via a large capacitor  $C_{to}$ . Then,

$$T_{sc} = \frac{I_{sc}}{I_t}$$

where  $I_{sc}$  is the ac short-circuit output current at the collector of  $Q_1$ .

### Method 2 Using a replica circuit

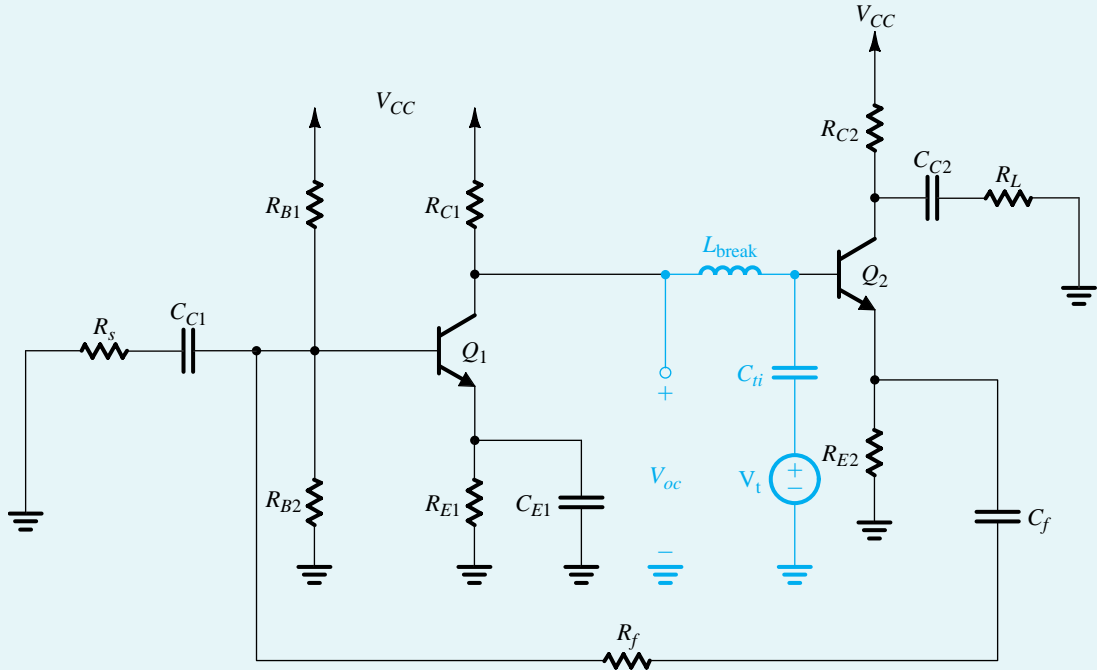
As shown in Fig. B.35, a replica of the feedback amplifier circuit can be simply used as a termination impedance. Here, the feedback loops of both the amplifier circuit and the replica circuit are broken using a large inductor  $L_{\text{break}}$  to avoid disturbing the dc bias conditions. The loop output at the collector of  $Q_1$  in the amplifier circuit is then connected to the loop input at the base of  $Q_2$  in the replica circuit via a large coupling capacitor  $C_{ti}$  (again, to avoid disturbing the dc bias conditions). Thus, for ac signals, the loop output at the collector of  $Q_1$  in the amplifier circuit sees an impedance equal to that seen before the feedback loop is broken. Accordingly, we have ensured that the conditions that existed in the amplifier circuit prior to breaking the loop have not changed.

Next, to determine the loop gain  $A\beta$ , we apply an ac test signal voltage  $V_t$  via a large coupling capacitor  $C_{ti}$  to the loop input at the base of  $Q_2$  in the amplifier circuit. Then, as described in Section 9.9,

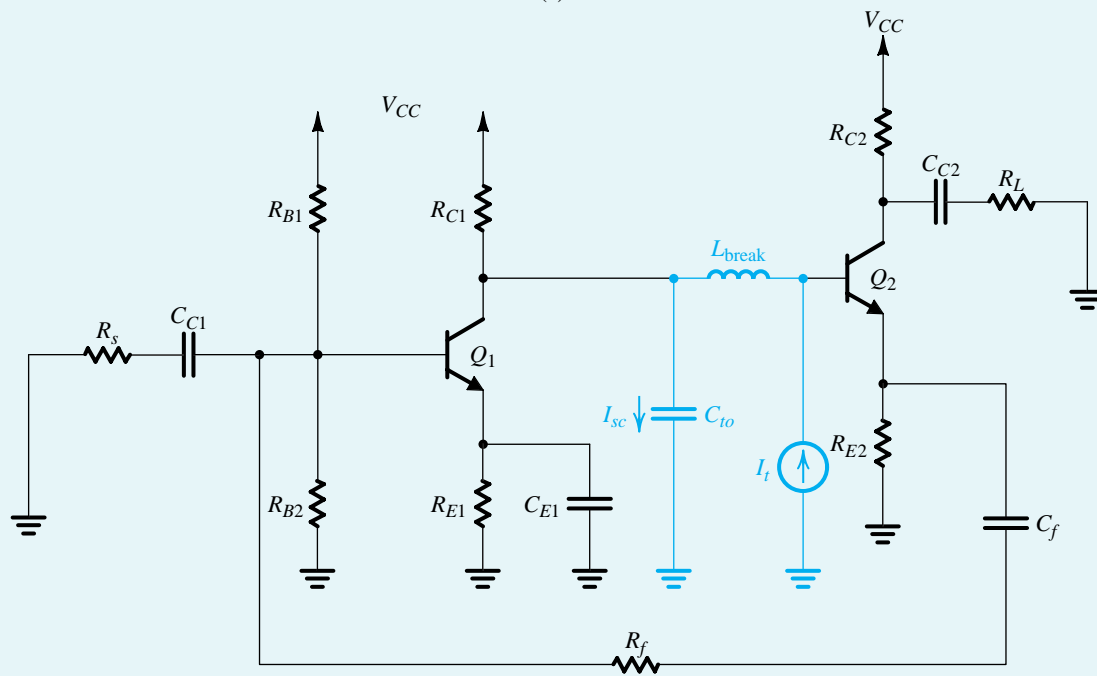
$$A\beta = -\frac{V_r}{V_t}$$

where  $V_r$  is the ac returned signal at the loop output at the collector of  $Q_1$  in the amplifier circuit.

### Example PS.10.1 *continued*

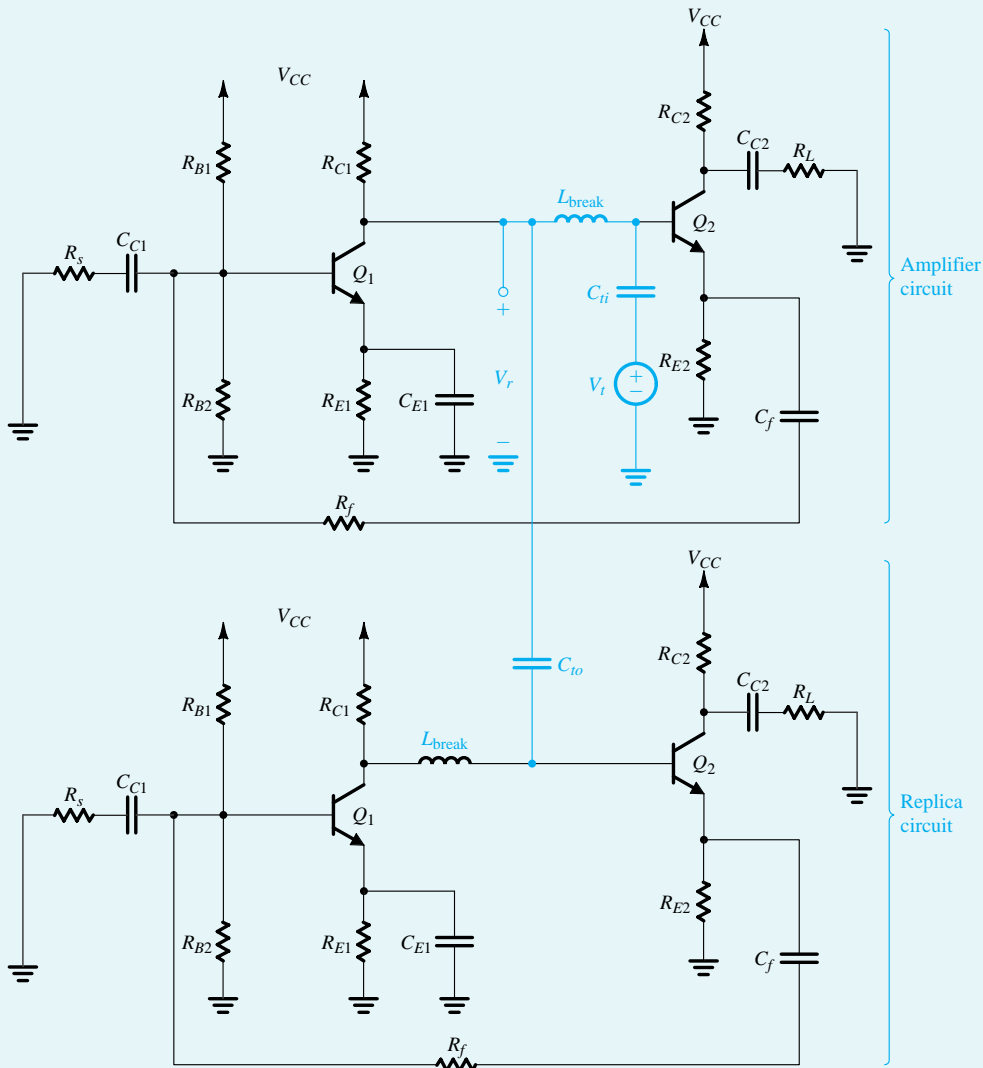


(a)



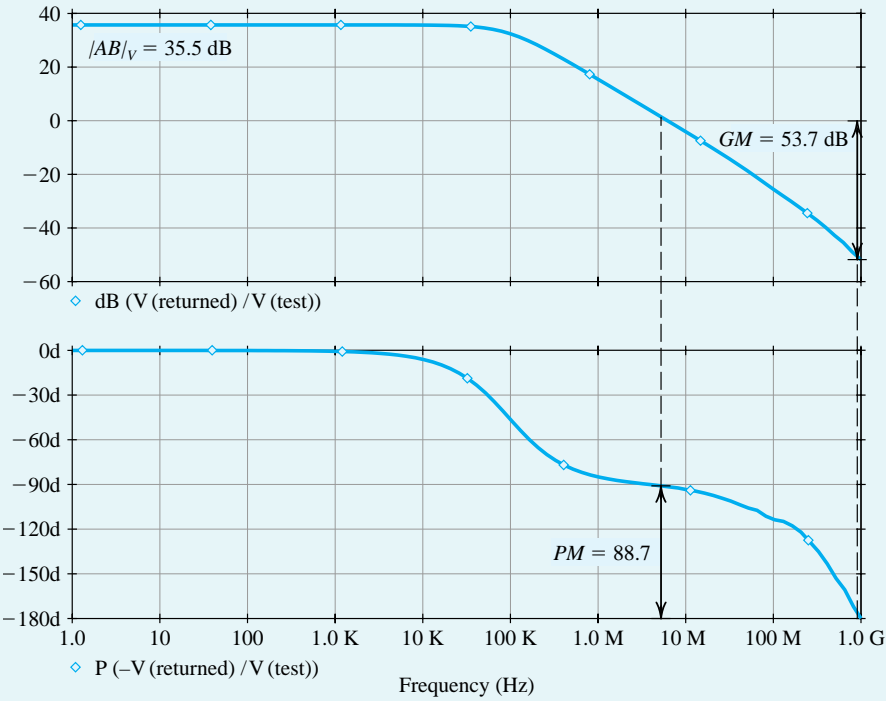
(b)

**Figure B.34** Circuits for simulating (a) the open-circuit voltage transfer function  $T_{oc}$  and (b) the short-circuit current transfer function  $T_{sc}$  of the feedback amplifier in Fig. B.33 for the purpose of computing its loop gain.



**Figure B.35** Circuit for simulating the loop gain of the feedback amplifier circuit in Fig. B.33 using the replica-circuit method.

To compute the loop gain  $A\beta$  of the feedback amplifier circuit in Fig. B.33 using PSpice, we choose to simulate the circuit in Fig. B.35. In the PSpice simulations, we used part Q2N3904 (whose SPICE model is given in Table B.6) for the BJTs, and we set  $L_{\text{break}}$  to be 1 GH and the coupling and bypass capacitors to be 1 kF. The magnitude and phase of  $A\beta$  are plotted in Fig. B.36, from which we see that the feedback amplifier has a gain margin of 53.7 dB and a phase margin of 88.7°.

**Example PS.10.1 continued**


**Figure B.36** (a) Magnitude and (b) phase of the loop gain  $A\beta$  of the feedback amplifier circuit in Fig. B.33.

**Example PS.11.1**
**Class B BJT Output Stage**

We investigate the operation of the class B output stage whose schematic capture is shown in Fig. B.37. For the power transistors, we use the discrete BJTs MJE243 and MJE253 (from ON Semiconductor),<sup>13</sup> which are rated for a maximum continuous collector current  $I_{C\max} = 4 \text{ A}$  and a maximum collector-emitter voltage of  $V_{CE\max} = 100 \text{ V}$ . To permit comparison with the hand analysis performed in Example 13.1, in the simulation, we use component and voltage values identical (or close) to those of the circuit designed in Example 13.1. Specifically, we use a load resistance of  $8 \Omega$ , an input sine-wave signal of 17.9-V peak and 1-kHz frequency, and 23-V power supplies. In PSpice, a transient-analysis simulation is performed over the interval 0 ms to 3 ms, and the waveforms of various node voltages and branch currents are plotted. In this example, Probe (the graphical interface of PSpice) is utilized to compute various power-dissipation values. Some of the resulting waveforms are displayed in Fig. B.38. The upper and middle graphs show the load voltage and current, respectively. The peak voltage amplitude is 16.9 V, and the peak current amplitude is 2.1 A. If one looks carefully, one can observe that both exhibit crossover distortion. The bottom

<sup>13</sup>In PSpice, we have created BJT parts for these power transistors based on the values of the SPICE model parameters available on the data sheets available from ON Semiconductor. Readers can find these parts (labeled QMJE243 and QMJE253) in the SEDRA.olb library, which is available on the CD accompanying this book.

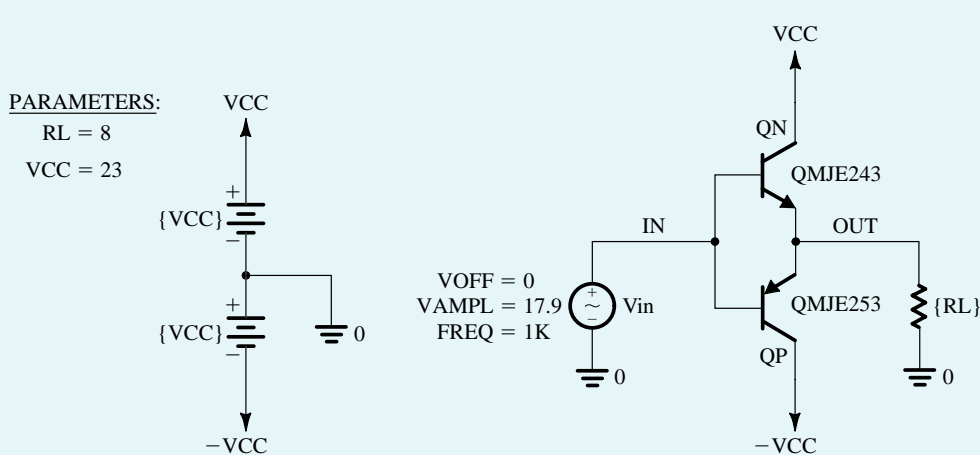


**Figure B.37** Capture schematic of the class B output stage in Example PS.11.1.

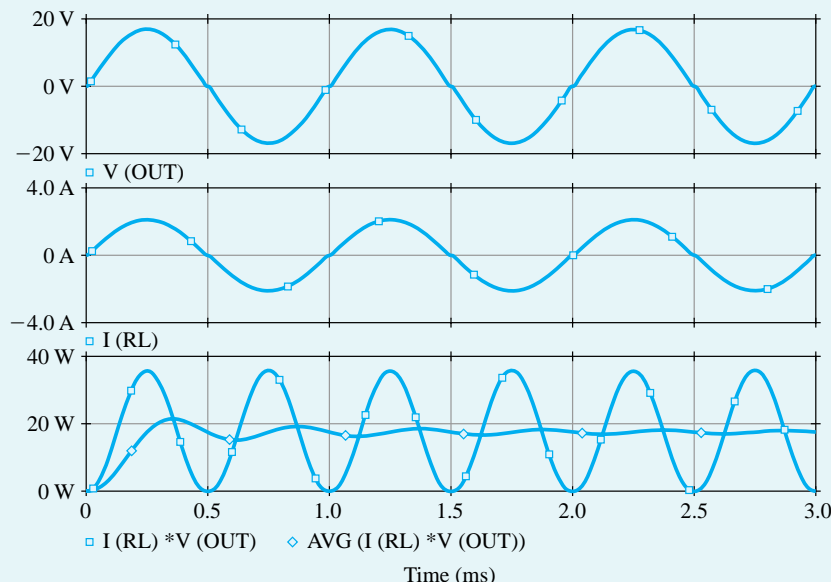


**Figure B.38** Several waveforms associated with the class B output stage (shown in Fig. B.37) when excited by a 17.9-V, 1-kHz sinusoidal signal. The upper graph displays the voltage across the load resistance, the middle graph displays the load current, and the lower graph displays the instantaneous and average power dissipated by the load.

graph displays the instantaneous and the average power dissipated in the load resistance as computed using Probe by multiplying the voltage and current values to obtain the instantaneous power, and taking a running average for the average load power  $P_L$ . The transient behavior of the average load power, which eventually settles into a quasiconstant steady state of about 17.6 W, is an artifact of the PSpice algorithm used to compute the running average of a waveform.

The upper two graphs of Fig. B.39 show the voltage and current waveforms, respectively, of the positive supply,  $+V_{CC}$ . The bottom graph shows the instantaneous and average power supplied by  $+V_{CC}$ .

**Example PS.11.1** *continued*

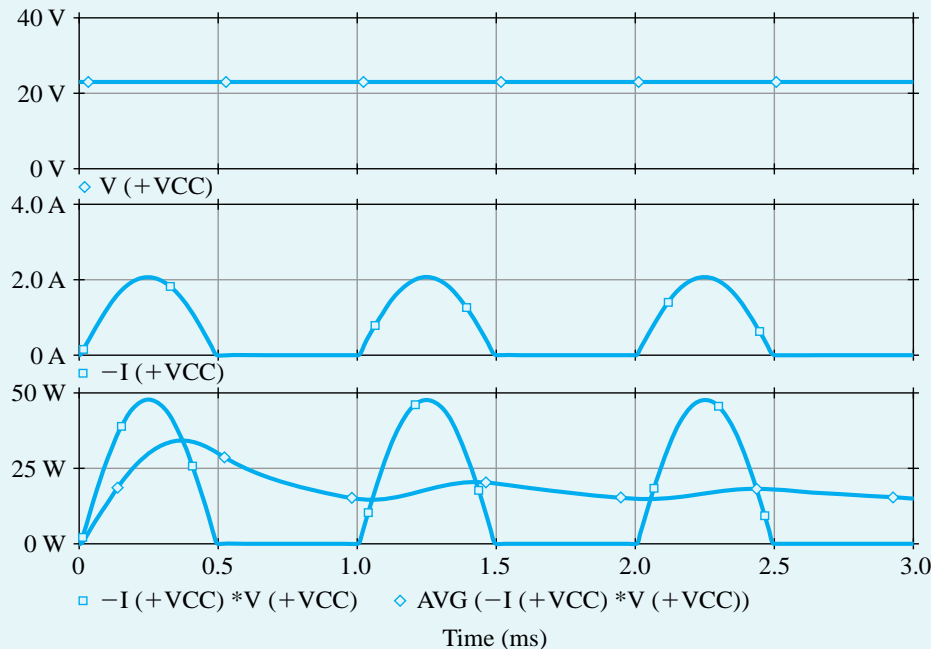


**Figure B.39** The voltage (upper graph), current (middle graph), and instantaneous and average power (bottom graph) supplied by the positive voltage supply ( $+V_{CC}$ ) in the circuit of Fig. B.37.

Similar waveforms can be plotted for the negative supply,  $-V_{CC}$ . The average power provided by each supply is found to be about 15 W, for a total supply power  $P_s$  of 30 W. Thus, the power-conversion efficiency can be computed to be

$$\eta = P_L/P_S = \frac{17.6}{30} \times 100\% = 58.6\%$$

Figure B.40 shows plots of the voltage, current, and power waveforms associated with transistor  $Q_P$ . Similar waveforms can be obtained for  $Q_N$ . As expected, the voltage waveform is a sinusoid, and the current waveform consists of half-sinusoids. The waveform of the instantaneous power, however, is rather unusual. It indicates the presence of some distortion as a result of driving the transistors rather hard. This can be verified by reducing the amplitude of the input signal. Specifically, when the amplitude is reduced to about 17 V, the “dip” in the power waveform vanishes. The average power dissipated in each of  $Q_N$  and  $Q_P$  can be computed by Probe and are found to be approximately 6 W.

Table B.11 provides a comparison of the results found from the PSpice simulation and the corresponding values obtained using hand analysis in Example 13.1. Observe that the two sets of results are quite close.

To investigate the crossover distortion further, we present in Fig. B.41 a plot of the voltage transfer characteristic (VTC) of the class B output stage. This plot is obtained through a dc-analysis simulation with  $v_{IN}$  swept over the range  $-10$  V to  $+10$  V in 1.0-mV increments. Using Probe, we determine that the slope of the VTC is nearly unity and that the dead band extends from  $-0.60$  V to  $+0.58$  V. The effect of the crossover distortion can be quantified by performing a Fourier analysis on the output voltage waveform in PSpice. This analysis decomposes the waveform generated through a transient analysis into its

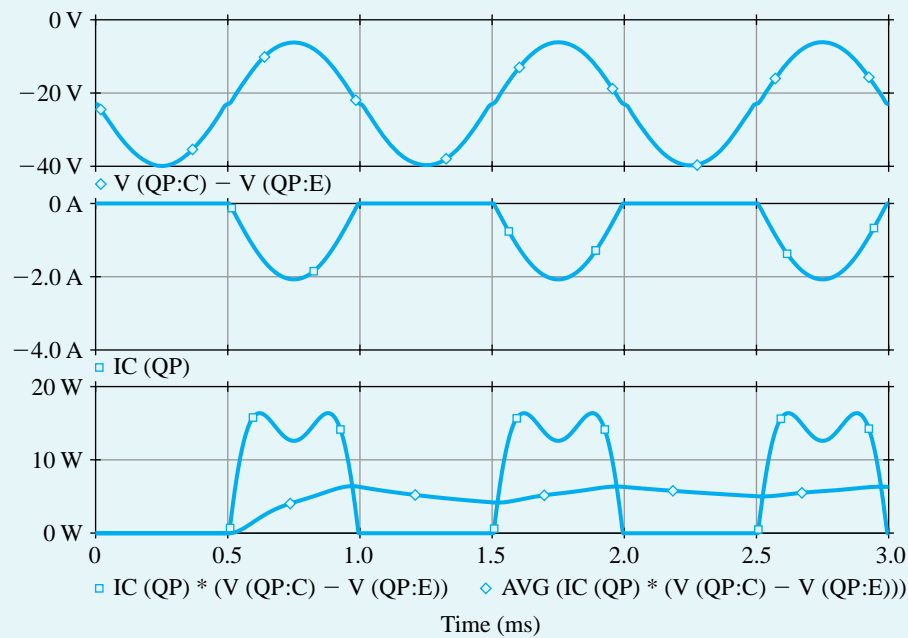


**Figure B.40** Waveforms of the voltage across, the current through, and the power dissipated in the *pnp* transistor  $Q_p$  of the output stage shown in Fig. B.37.

**Table B.11** Various Power Terms Associated with the Class B Output Stage Shown in Fig. B.37 as Computed by Hand and by PSpice Analysis

Power/Efficiency	Equation	Hand Analysis (Example PS.11.1)	PSpice	Error % <sup>1</sup>
$P_S$	$\frac{2\hat{V}_o}{\pi R_L} V_{CC}$	31.2 W	30.0 W	4
$P_D$	$\frac{2\hat{V}_o}{\pi R_L} V_{CC} - \frac{1}{2} \frac{\hat{V}_o^2}{R_L}$	13.0 W	12.4 W	4.6
$P_L$	$\frac{1}{2} \frac{\hat{V}_o^2}{R_L}$	18.2 W	17.6 W	3.3
$\eta$	$\frac{P_L}{P_S} \times 100\%$	58.3%	58.6%	-0.5

<sup>1</sup>Relative percentage error between the values predicted by hand and by PSpice.

Fourier-series components. Further, PSpice computes the total harmonic distortion (THD) of the output waveform. The results obtained from the simulation output file are shown on the next page.

These Fourier components are used to plot the line spectrum shown in Fig. B.42. We note that the output waveform is rather rich in odd harmonics and that the resulting THD is rather high (2.14%).

**Example PS.11.1 continued**

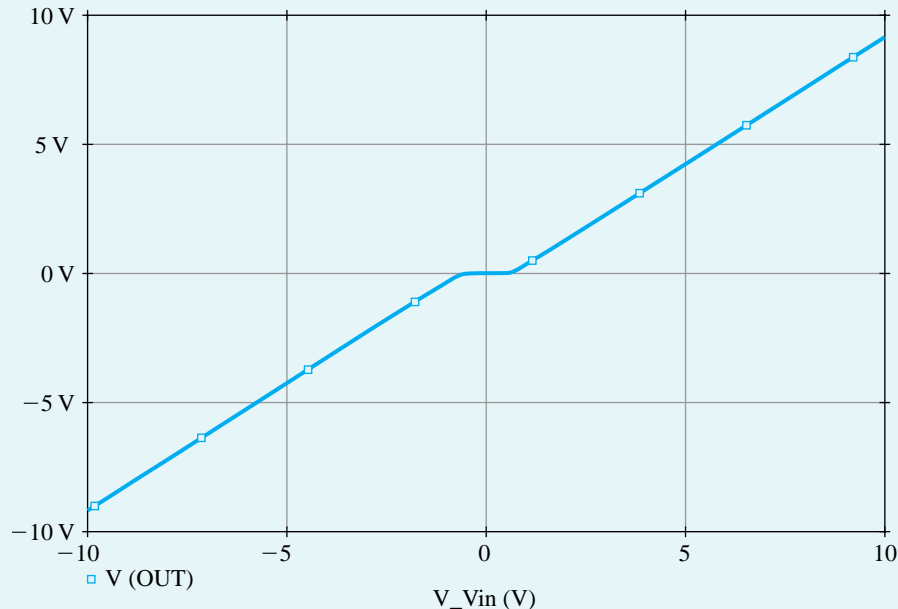


**Figure B.41** Transfer characteristic of the class B output stage of Fig. B.37.

FOURIER COMPONENTS OF TRANSIENT RESPONSE V(OUT)

DC COMPONENT = -1.525229E-02

HARMONIC NO	FREQUENCY (HZ)	FOURIER COMPONENT	NORMALIZED COMPONENT	PHASE (DEG)	NORMALIZED PHASE (DEG)
1	1.000E+03	1.674E+01	1.000E+00	-2.292E-03	0.000E+00
2	2.000E+03	9.088E-03	5.428E-04	9.044E+01	9.044E+01
3	3.000E+03	2.747E-01	1.641E-02	-1.799E+02	-1.799E+02
4	4.000E+03	4.074E-03	2.433E-04	9.035E+01	9.036E+01
5	5.000E+03	1.739E-01	1.039E-02	-1.799E+02	-1.799E+02
6	6.000E+03	5.833E-04	3.484E-05	9.159E+01	9.161E+01
7	7.000E+03	1.195E-01	7.140E-03	-1.800E+02	-1.799E+02
8	8.000E+03	5.750E-04	3.435E-05	9.128E+01	9.129E+01
9	9.000E+03	9.090E-02	5.429E-03	-1.800E+02	-1.799E+02
10	1.000E+04	3.243E-04	1.937E-05	9.120E+01	9.122E+01

TOTAL HARMONIC DISTORTION = 2.140017E+00 PERCENT

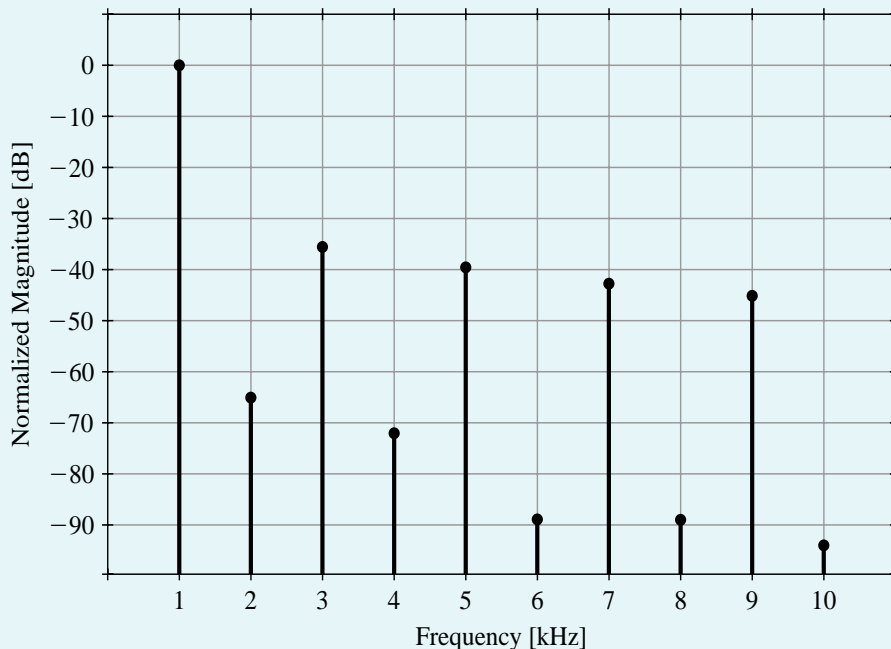


**Figure B.42** Fourier-series components of the output waveform of the class B output stage in Fig. B.37.

## Example PS.12.1

### Frequency Compensation of the Two-Stage CMOS Op Amp

In this example, we will use PSpice to aid in designing the frequency compensation of the two-stage CMOS circuit whose capture schematic is shown in Fig. B.43. PSpice will then be employed to determine the frequency response and the slew rate of the op amp. We will assume a  $0.5\text{-}\mu\text{m}$   $n$ -well CMOS technology for the MOSFETs and will use the SPICE level-1 model parameters listed in Table B.4. Observe that to eliminate the body effect and improve the matching between  $M_1$  and  $M_2$ , the source terminals of the input PMOS transistors  $M_1$  and  $M_2$  are connected to their  $n$  well.

The op-amp circuit in Fig. B.43 is designed using a reference current  $I_{\text{REF}} = 90 \mu\text{A}$ , a supply voltage  $V_{DD} = 3.3 \text{ V}$ , and a load capacitor  $C_L = 1 \text{ pF}$ . Unit-size transistors with  $W/L = 1.25 \mu\text{m}/0.6 \mu\text{m}$  are used for both the NMOS and PMOS devices. The transistors are sized for an overdrive voltage  $V_{OV} = 0.3 \text{ V}$ . The corresponding multiplicative factors are given in Fig. B.43.

In PSpice, the common-mode input voltage  $V_{CM}$  of the op-amp circuit is set to  $V_{DD}/2 = 1.65 \text{ V}$ . A bias-point simulation is performed to determine the dc operating point. Using the values found in the simulation output file for the small-signal parameters of the MOSFETs, we obtain<sup>14</sup>

<sup>14</sup>Recall that  $G_{m1}$  and  $G_{m2}$  are the transconductances of, respectively, the first and second stages of the op amp. Capacitors  $C_1$  and  $C_2$  represent the total capacitance to ground at the output nodes of, respectively, the first and second stages of the op amp.

**Example PS.12.1 continued**

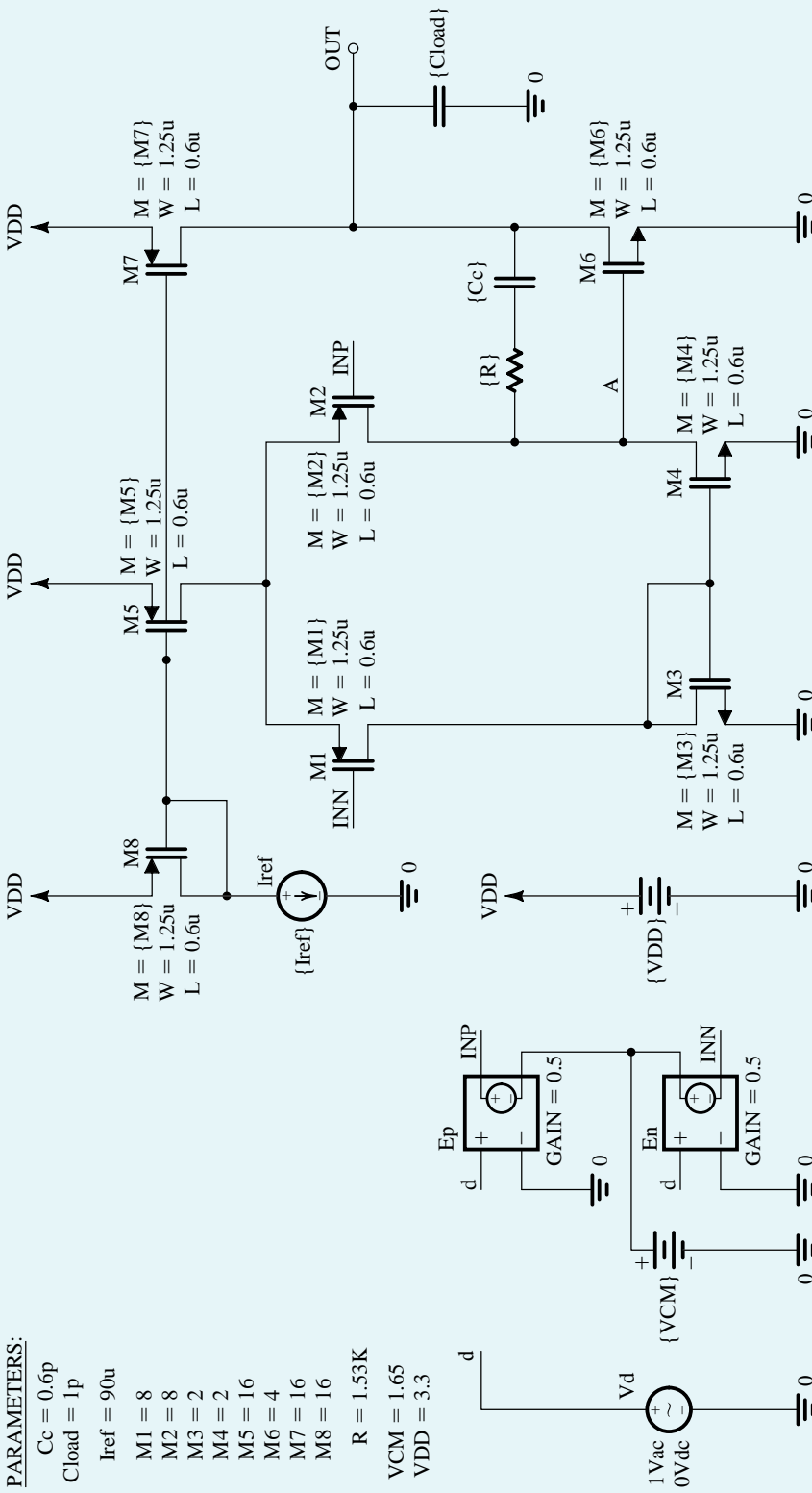


**Figure B.43** Schematic capture of the two-stage CMOS op amp in Example PS.12.1

$$\begin{aligned}G_{m1} &= 0.333 \text{ mA/V} \\G_{m2} &= 0.650 \text{ mA/V} \\C_1 &= 26.5 \text{ fF} \\C_2 &= 1.04 \text{ pF}\end{aligned}$$

using Eqs. (10.7), (10.14), (10.25), and (10.26), respectively. Then, using Eq. (10.28), the frequency of the second, nondominant, pole can be found as

$$f_{P2} \approx \frac{G_{m2}}{2\pi C_2} = 97.2 \text{ MHz}$$

In order to place the transmission zero, given by Eq. (10.38), at infinite frequency, we select

$$R = \frac{1}{G_{m2}} = 1.53 \text{ k}\Omega$$

Now, using Eq. (10.38), the phase margin of the op amp can be expressed as

$$\text{PM} = 90^\circ - \tan^{-1}\left(\frac{f_t}{f_{P2}}\right) \quad (\text{B.44})$$

where  $f_t$  is the unity-gain frequency, given in Eq. (10.31),

$$f_t = \frac{G_{m1}}{2\pi C_C} \quad (\text{B.45})$$

Using Eqs. (B.44) and (B.45), we determine that compensation capacitors of  $C_c = 0.78 \text{ pF}$  and  $C_c = 2 \text{ pF}$  are required to achieve phase margins of  $\text{PM} = 55^\circ$  and  $\text{PM} = 75^\circ$ , respectively.

Next, an ac-analysis simulation is performed in PSpice to compute the frequency response of the op amp and to verify the foregoing design values. It was found that with  $R = 1.53 \text{ k}\Omega$ , we needed  $C_c = 0.6 \text{ pF}$  and  $C_c = 1.8 \text{ pF}$  to set  $\text{PM} = 55^\circ$  and  $\text{PM} = 75^\circ$ , respectively. We note that these values are reasonably close to those predicted by hand analysis. The corresponding frequency responses for the compensated op amp are plotted in Figs. B.44 and B.45. For comparison, we also show the frequency response of the uncompensated op amp ( $C_c = 0$ ). Observe that the unity gain frequency  $f_t$  drops from 70.2 MHz to 26.4 MHz as  $C_c$  is increased to improve PM (as anticipated from Eq. B.45).

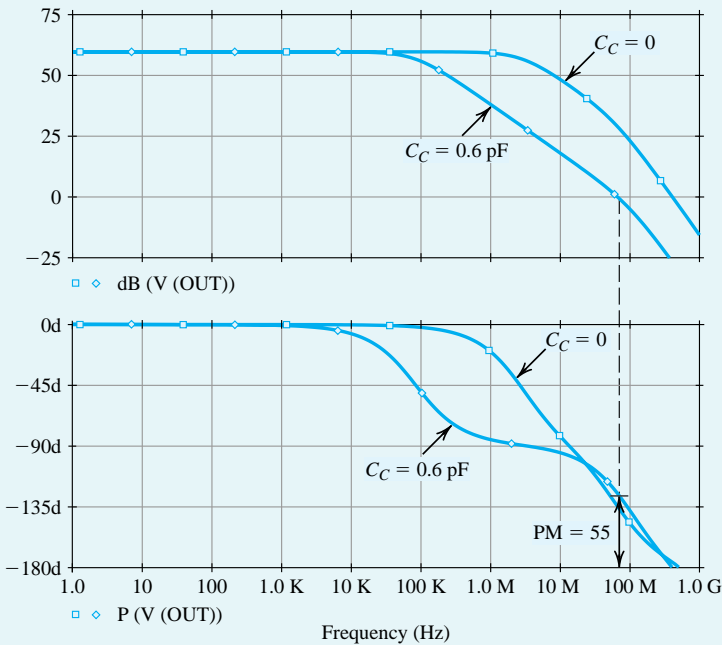
Rather than increasing the compensation capacitor  $C_c$ , the value of the series resistor  $R$  can be increased to improve the phase margin PM: For a given  $C_c$ , increasing  $R$  above  $1/G_{m2}$  places the transmission zero at a negative real-axis location (Eq. 10.38), where the phase it introduces adds to the phase margin. Thus, PM can be improved without affecting  $f_t$ . To verify this point, we set  $C_c$  to 0.6 pF and simulate the op-amp circuit in PSpice for the cases of  $R = 1.53 \text{ k}\Omega$  and  $R = 3.2 \text{ k}\Omega$ . The corresponding frequency response is plotted in Fig. B.46. Observe how  $f_t$  is approximately independent of  $R$ . However, by increasing  $R$ , PM is improved from  $55^\circ$  to  $75^\circ$ .

Increasing the PM is desirable because it reduces the overshoot in the step response of the op amp. To verify this point, we simulate in PSpice the step response of the op amp for  $\text{PM} = 55^\circ$  and  $\text{PM} = 75^\circ$ . To do that, we connect the op amp in a unity-gain configuration, apply a small (10-mV) pulse signal at the input with very short (1-ps) rise and fall times to emulate a step input, perform a transient-analysis simulation, and plot the output voltage as shown in Fig. B.47. Observe that the overshoot in the step response drops from 15% to 1.4% when the phase margin is increased from  $55^\circ$  to  $75^\circ$ .

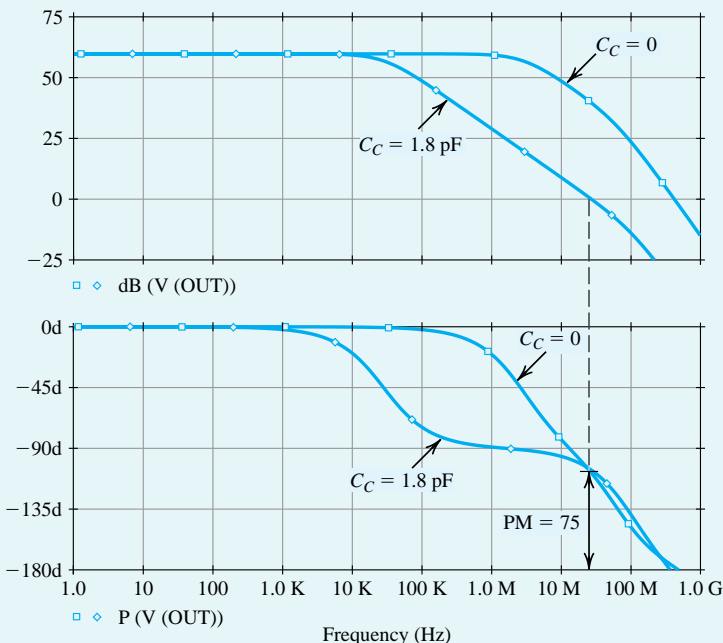
We conclude this example by computing  $SR$ , the slew rate of the op amp. From Eq. (10.40),

$$SR = 2\pi f_t V_{OV} = \frac{G_{m1}}{C_c} V_{OV} = 166.5 \text{ V}/\mu\text{s}$$

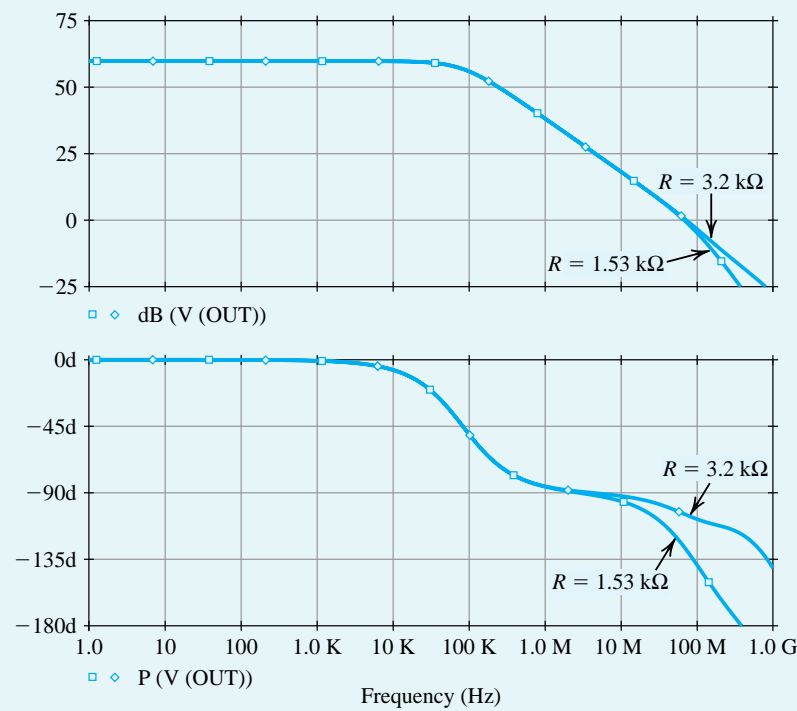
**Example PS.12.1** *continued*



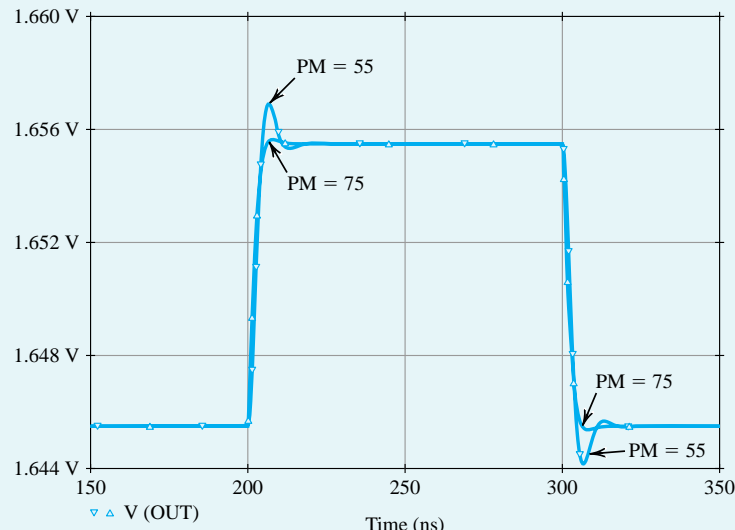
**Figure B.44** Magnitude and phase response of the op-amp circuit in Fig. B.43:  $R = 1.53 \text{ k}\Omega$ ,  $C_c = 0$  (no frequency compensation), and  $C_c = 0.6 \text{ pF}$  ( $\text{PM} = 55^\circ$ ).



**Figure B.45** Magnitude and phase response of the op-amp circuit in Fig. B.43:  $R = 1.53 \text{ k}\Omega$ ,  $C_c = 0$  (no frequency compensation), and  $C_c = 1.8 \text{ pF}$  ( $\text{PM} = 75^\circ$ ).

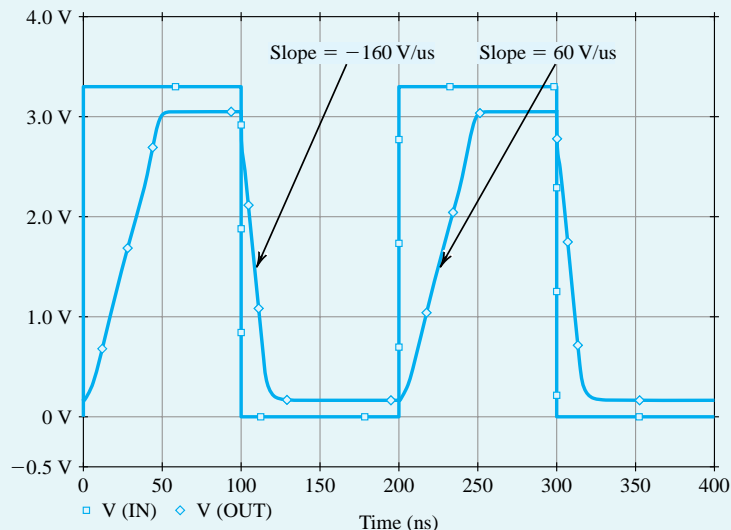


**Figure B.46** Magnitude and phase response of the op-amp circuit in Fig. B.43:  $C_c = 0.6 \text{ pF}$ ,  $R = 1.53 \text{ k}\Omega$  (PM = 55°), and  $R = 3.2 \text{ k}\Omega$  (PM = 75°).



**Figure B.47** Small-signal step response (for a 10-mV step input) of the op-amp circuit in Fig. B.43 connected in a unity-gain configuration: PM = 55° ( $C_c = 0.6 \text{ pF}$ ,  $R = 1.53 \text{ k}\Omega$ ) and PM = 75° ( $C_c = 0.6 \text{ pF}$ ,  $R = 3.2 \text{ k}\Omega$ ).

when  $C_c = 0.6 \text{ pF}$ . Next, to determine SR using PSpice (see Example PS.2.2), we again connect the op amp in a unity-gain configuration and perform a transient-analysis simulation. However, we now apply

**Example PS.12.1** *continued*

**Figure B.48** Large-signal step response (for a 3.3-V step-input) of the op-amp circuit in Fig. B.43 connected in a unity-gain configuration. The slope of the rising and falling edges of the output waveform correspond to the slew rate of the op amp.

a large pulse signal (3.3 V) at the input to cause slew-rate limiting at the output. The corresponding output-voltage waveform is plotted in Fig. B.48. The slope of the slew-rate-limited output waveform corresponds to the slew rate of the op amp and is found to be  $SR = 160 \text{ V}/\mu\text{s}$  and  $60 \text{ V}/\mu\text{s}$  for the negative- and positive-going output, respectively. These results, with the unequal values of  $SR$  in the two directions, differ from those predicted by the simple model for the slew-rate limiting of the two-stage op-amp circuit (Section 10.1.6). The difference can perhaps be said to be a result of transistor  $M_4$  entering the triode region and its output current (which is sourced through  $C_C$ ) being correspondingly reduced. Of course, the availability of PSpice should enable the reader to explore this point further.

**Example PS.13.1****Operation of the CMOS Inverter**

In this example, we will use PSpice to simulate the CMOS inverter whose schematic capture is shown in Fig. B.49. We will assume a  $0.5\text{-}\mu\text{m}$  CMOS technology for the MOSFETs and use parts NMOS0P5 and PMOS0P5 whose level-1 model parameters are listed in Table B.4. In addition to the channel length  $L$  and the channel width  $W$ , we have used the multiplicative factor  $m$  to specify the dimensions of the MOSFETs. The MOSFET parameter  $m$ , whose default value is 1, is used in SPICE to specify the number of unit-size MOSFETs connected in parallel (see Fig. B.24). In our simulations, we will use unit-size transistors with  $L = 0.5 \mu\text{m}$  and  $W = 1.25 \mu\text{m}$ . We will simulate the inverter for two cases: (a) setting  $m_p/m_n = 1$  so that the NMOS and PMOS transistors have equal widths, and (b) setting  $m_p/m_n = \mu_n/\mu_p = 4$  so that the PMOS transistor is four times wider than the NMOS transistor (to compensate for the lower mobility in  $p$ -channel devices as compared with  $n$ -channel ones). Here,  $m_n$  and  $m_p$  are the multiplicative factors of, respectively, the NMOS and PMOS transistors of the inverter.

**PARAMETERS:**

$$CL = 0.5p$$

$$MN = 1$$

$$MP = 1$$

$$VDD = 3.3$$

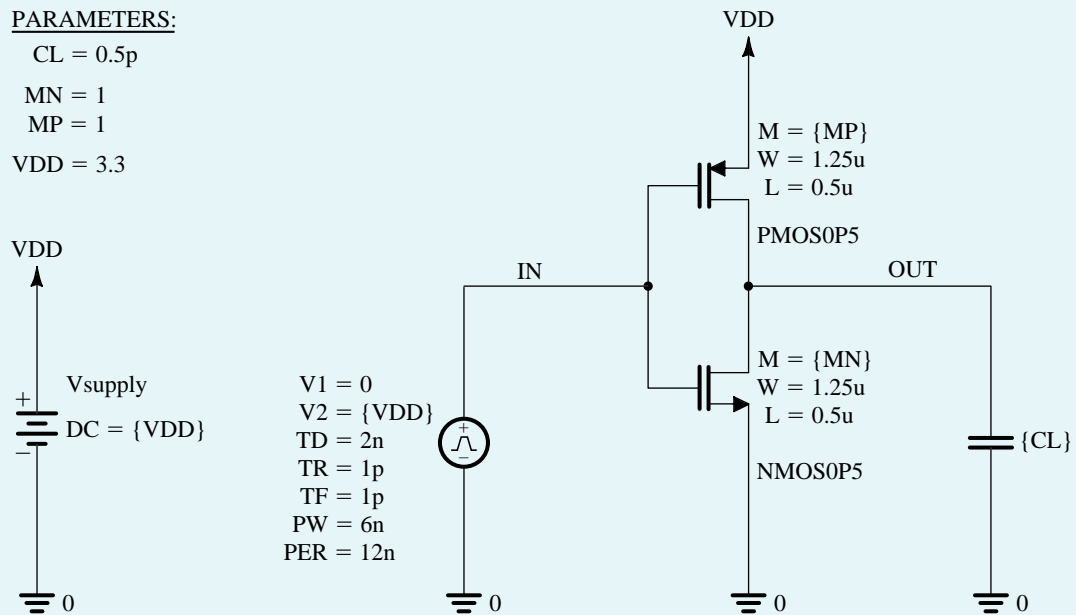


**Figure B.49** Schematic capture of the CMOS inverter in Example PS.13.1.

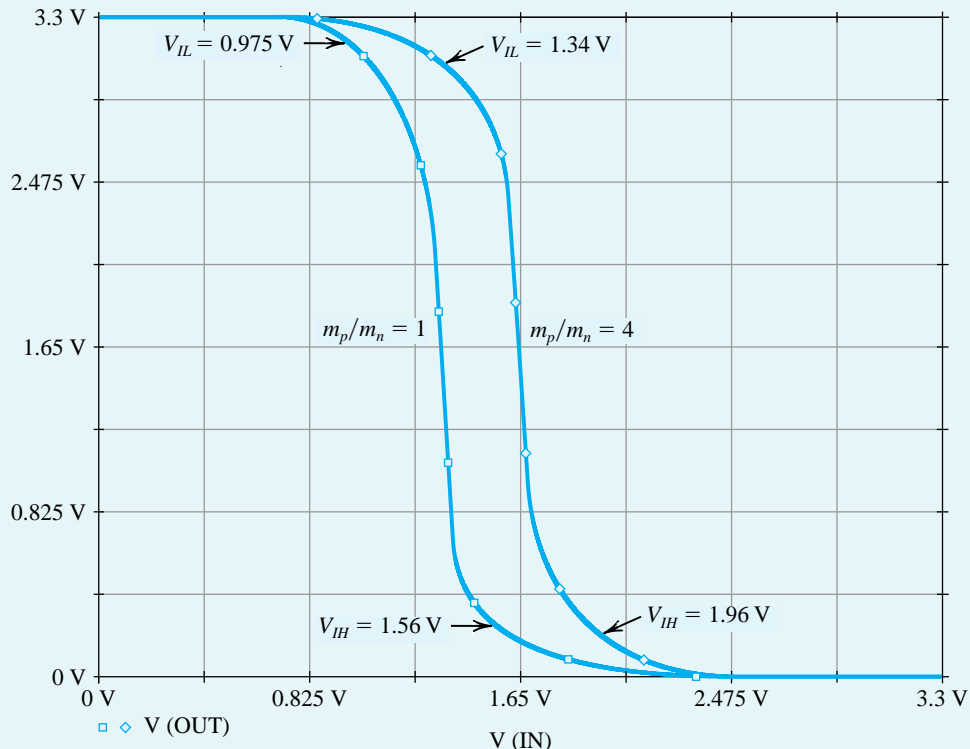
To compute both the voltage transfer characteristic (VTC) of the inverter and its supply current at various values of the input voltage  $V_{in}$ , we apply a dc voltage source at the input and perform a dc analysis with  $V_{in}$  swept over the range of 0 to  $V_{DD}$ . The resulting VTC is plotted in Fig. B.50. Note that the slope of the VTC in the switching region (where both the NMOS and PMOS devices are in saturation) is not infinite as predicted from the simple theory presented in Chapter 14 (Section 14.2, Fig. 14.20). Rather, the nonzero value of  $\lambda$  causes the inverter gain to be finite. Using the derivative feature of Probe, we can find the two points on the VTC at which the inverter gain is unity (i.e., the VTC slope is  $-1 \text{ V/V}$ ) and, hence, determine  $V_{LH}$  and  $V_{IH}$ . Using the results given in Fig. B.50, the corresponding noise margins are  $NM_L = NM_H = 1.34 \text{ V}$  for the inverter with  $m_p/m_n = 4$ , while  $NM_L = 0.975 \text{ V}$  and  $NM_H = 1.74 \text{ V}$  for the inverter with  $m_p/m_n = 1$ . Observe that these results correlate reasonably well with the values obtained using the approximate formula in Eq. (14.58). Furthermore, note that with  $m_p/m_n = \mu_n/\mu_p = 4$ , the NMOS and PMOS devices are closely matched and, hence, the two noise margins are equal.

The threshold voltage  $V_M$  of the CMOS inverter is defined as the input voltage  $v_{IN}$  that results in an identical output voltage  $v_{OUT}$ , that is,

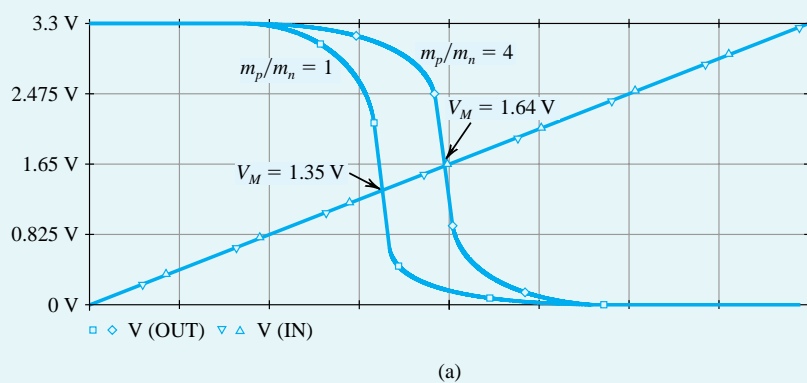
$$V_M = v_{IN} \Big|_{v_{OUT} = v_{IN}} \quad (\text{B.46})$$

Thus, as shown in Fig. B.51,  $V_M$  is the intersection of the VTC, with the straight line corresponding to  $v_{OUT} = v_{IN}$  (this line can be simply generated in Probe by plotting  $v_{IN}$  versus  $v_{OUT}$ , as shown in Fig. B.51). Note that  $V_M \approx (V_{DD}/2)$  for the inverter with  $m_p/m_n = 4$ . Furthermore, decreasing  $m_p/m_n$  decreases  $V_M$ . Figure B.51 also shows the inverter supply current versus  $v_{IN}$ . Observe that the location of the supply-current peak shifts with the threshold voltage.

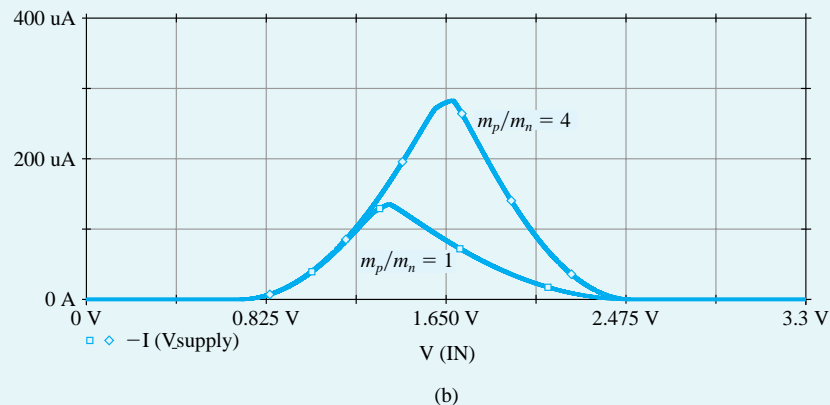
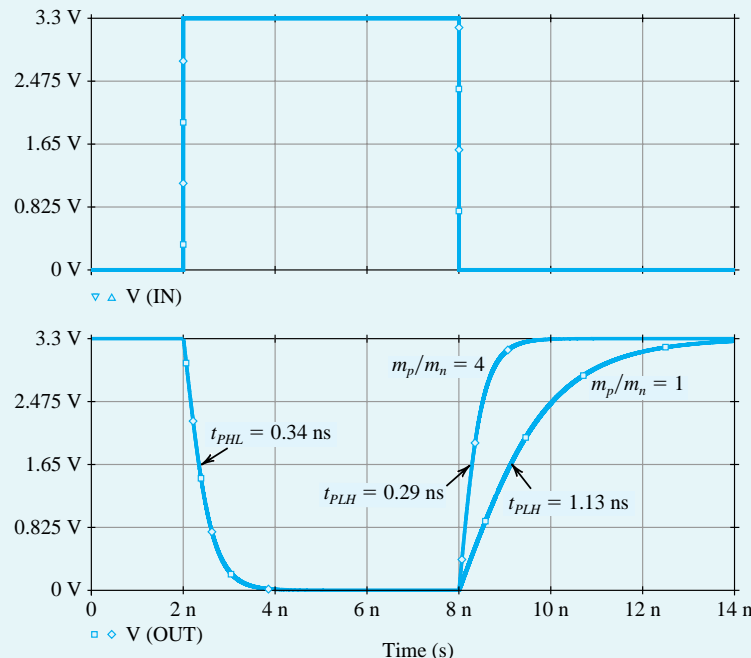
**Example PS.13.1 continued**



**Figure B.50** Input–output voltage transfer characteristic (VTC) of the CMOS inverter in Example PS.13.1 with  $m_p/m_n = 1$  and  $m_p/m_n = 4$ .



**Figure B.51 (a)** Output voltage and (b) supply current versus input voltage for the CMOS inverter in Example PS.13.1 with  $m_p/m_n = 1$  and  $m_p/m_n = 4$ .

**Figure B.51** (Contd.)**Figure B.52** Transient response of the CMOS inverter in Example PS.13.1 with  $m_p/m_n = 1$  and  $m_p/m_n = 4$ .

To investigate the dynamic operation of the inverter with PSpice, we apply a pulse signal at the input (Fig. B.49), perform a transient analysis, and plot the input and output waveforms as shown in Fig. B.52. The rise and fall times of the pulse source are chosen to be very short. Note that increasing  $m_p/m_n$  from 1 to 4 decreases  $t_{PLH}$  (from 1.13 ns to 0.29 ns) because of the increased current available to charge  $C_L$ , with only a minor increase in  $t_{PHL}$  (from 0.33 ns to 0.34 ns). The two propagation delays,  $t_{PLH}$  and  $t_{PHL}$ , are not exactly equal when  $m_p/m_n = 4$ , because the NMOS and PMOS transistors are still not perfectly matched (e.g.,  $V_{tn} \neq |V_{tp}|$ ).

### Example PS.14.1

#### Static and Dynamic Operation of an ECL Gate

In this example, we use PSpice to investigate the static and dynamic operation of the ECL gate (studied in Section 15.4) whose schematic capture is shown in Fig. B.53.

Having no access to the actual values for the SPICE model parameters of the BJTs utilized in commercially available ECL, we have selected parameter values representative of the technology utilized that, from our experience, would lead to reasonable agreement between simulation results and the measured

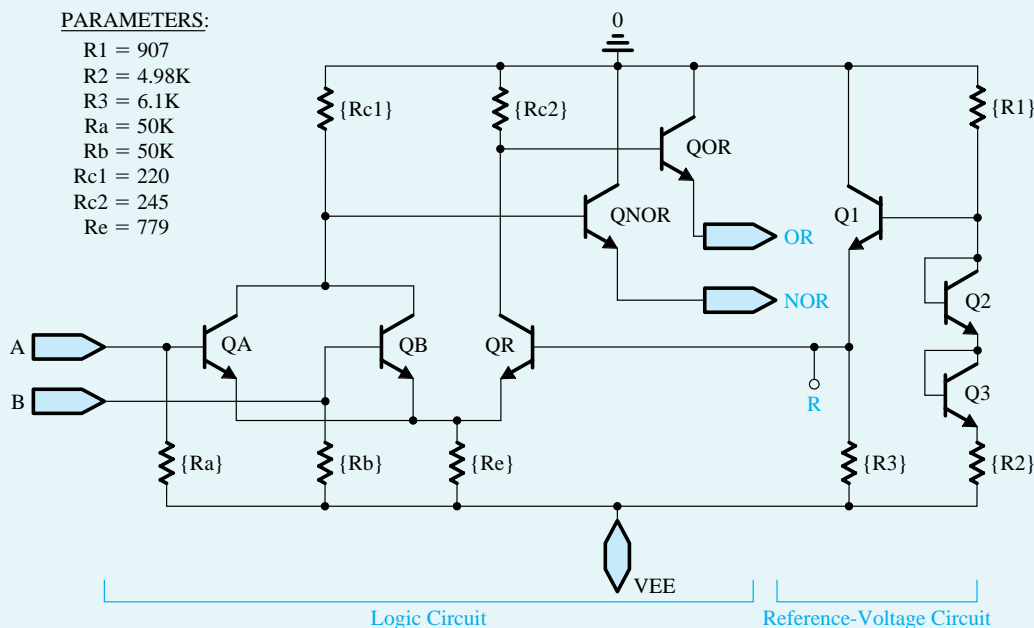


Figure B.53 Schematic capture of the two-input ECL gate for Example PS.14.1

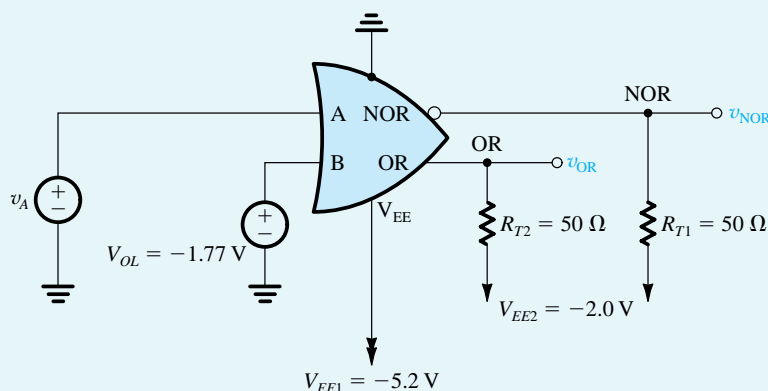


Figure B.54 Circuit arrangement for computing the voltage transfer characteristics of the ECL gate in Fig. B.53.

performance data supplied by the manufacturer. It should be noted that this problem would not be encountered by an IC designer using SPICE as an aid; presumably, the designer would have full access to the proprietary process parameters and the corresponding device model parameters. In any case, for the simulations we conducted, we have utilized the following BJT model parameter values<sup>15</sup>:  $I_s = 0.26 \text{ fA}$ ,  $\beta_F = 100$ ;  $\beta_R = 1$ ,  $\tau_F = 0.1 \text{ ns}$ ,  $C_{je} = 1 \text{ pF}$ ,  $C_{jc} = C_\mu = 1.5 \text{ pF}$ , and  $|V_A| = 100 \text{ V}$ .

We use the circuit arrangement of Fig. B.54 to compute the voltage transfer characteristics of the ECL gate, that is,  $v_{OR}$  and  $v_{NOR}$  versus  $v_A$ , where  $v_A$  is the input voltage at terminal A. For this investigation, the other input is deactivated by applying a voltage  $v_B = V_{OL} = -1.77 \text{ V}$ . In PSpice, we perform a dc-analysis simulation with  $v_A$  swept over the range  $-2 \text{ V}$  to  $0 \text{ V}$  in  $10\text{-mV}$  increments and plot  $v_{OR}$  and  $v_{NOR}$  versus  $v_A$ . The simulation results are shown in Fig. B.55. We immediately recognize the VTCs as those we have seen and (partially) verified by manual analysis in Section 15.4. The two transfer curves are symmetrical about an input voltage of  $-1.32 \text{ V}$ . PSpice also determined that the voltage  $V_R$  at the base of the reference transistor  $Q_R$  has exactly this value ( $-1.32 \text{ V}$ ), which is also identical to the value we determined by hand analysis of the reference-voltage circuit.

Utilizing Probe (the graphical interface of PSpice), one can determine the values of the important parameters of the VTC, as follows:

OR output:  $V_{OL} = -1.77 \text{ V}$ ,  $V_{OH} = -0.88 \text{ V}$ ,  $V_{IL} = -1.41 \text{ V}$ , and  $V_{IH} = -1.22 \text{ V}$ ; thus,  
 $NM_H = 0.34 \text{ V}$  and  $NM_L = 0.36 \text{ V}$

NOR output:  $V_{OL} = -1.78 \text{ V}$ ,  $V_{OH} = -0.88 \text{ V}$ ,  $V_{IL} = -1.41 \text{ V}$ , and  $V_{IH} = -1.22 \text{ V}$ ; thus,  
 $NM_H = 0.34 \text{ V}$  and  $NM_L = 0.37 \text{ V}$

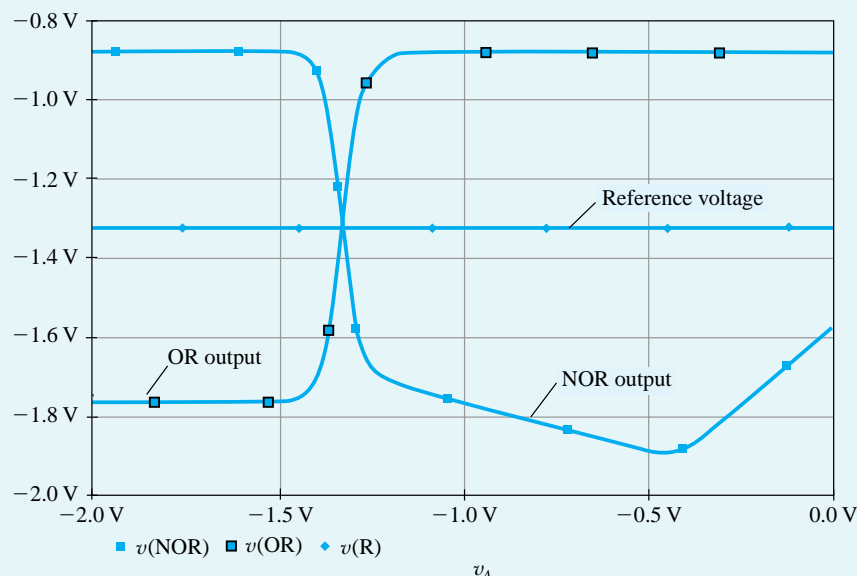


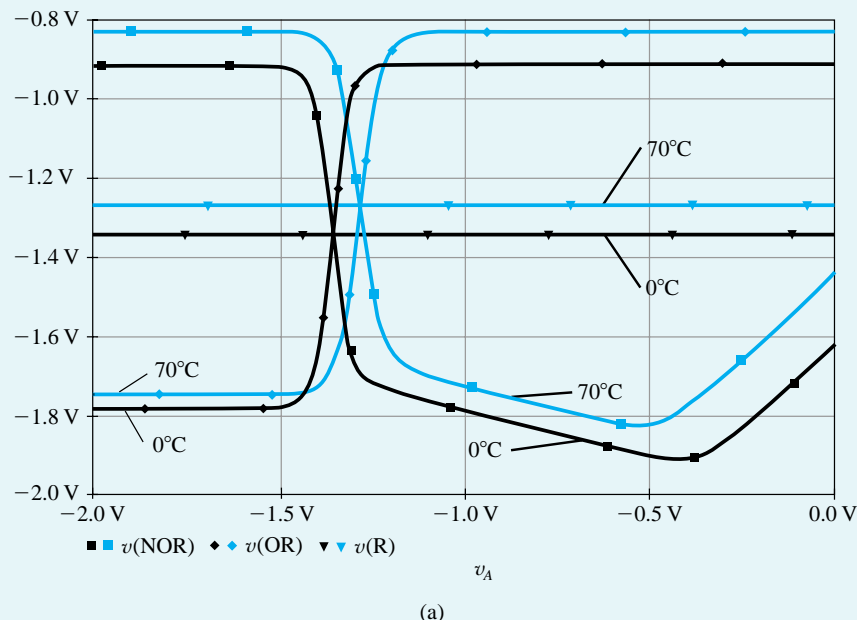
**Figure B.55** Voltage transfer characteristics of the OR and NOR outputs (see Fig. B.54) for the ECL gate shown in Fig. B.53. Also indicated is the reference voltage,  $V_R = -1.32 \text{ V}$ .

<sup>15</sup>In PSpice, we have created a part called QECL based on these BJT model parameter values. Readers can find this part in the SEDRA.olb library, which is available on the CD accompanying this book.

**Example PS.14.1** *continued*

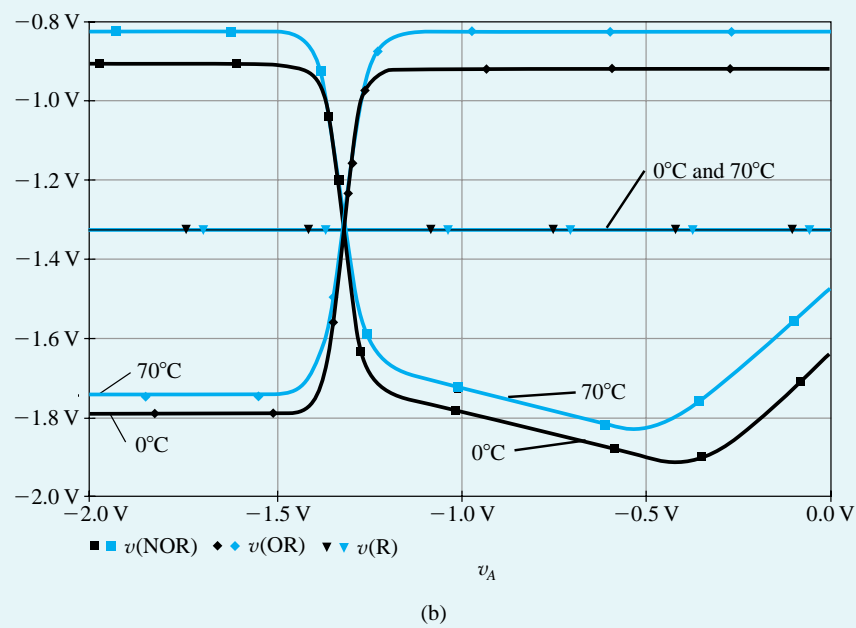
These values are remarkably close to those found by pencil-and-paper analysis in Section 15.4.

We next use PSpice to investigate the temperature dependence of the transfer characteristics. The reader will recall that in Section 15.4, we discussed this point at some length and carried out a hand analysis in Example 15.7. Here, we use PSpice to find the voltage transfer characteristics at two temperatures, 0°C and 70°C (the VTCs shown in Fig. B.55 were computed at 27°C) for two different cases: the first case with  $V_R$  generated as in Fig. B.53, and the second with the reference-voltage circuit eliminated and a constant, temperature-independent reference voltage of -1.32 V applied to the base of  $Q_R$ . The simulation results are displayed in Fig. B.56. Figure B.56(a) shows plots of the transfer characteristics for the case in which the reference circuit is utilized, and Fig. B.56(b) shows plots for the case in which a constant reference voltage is employed. Figure B.56(a) indicates that as the temperature is varied and  $V_R$  changes, the values of  $V_{OH}$  and  $V_{OL}$  also change but remain centered on  $V_R$ . In other words, the low and high noise margins remain nearly equal. As mentioned in Section 15.4 and demonstrated in the analysis of Example 15.4, this is the basic idea behind making  $V_R$  temperature dependent. When  $V_R$  is not temperature dependent, the symmetry of  $V_{OL}$  and  $V_{OH}$  around  $V_R$  is no longer maintained, as demonstrated in Fig. B.56(b). Finally, we show some of the values obtained in Table B.12. Observe that for the temperature-compensated case, the average value of  $V_{OL}$  and  $V_{OH}$  remains very close to  $V_R$ . The reader is encouraged to compare these results to those obtained in Example 15.4.



(a)

**Figure B.56** Comparing the voltage transfer characteristics of the OR and NOR outputs (see Fig. B.54) of the ECL gate shown in Fig. B.53, with the reference voltage  $V_R$  generated using: (a) the temperature-compensated bias network of Fig. B.53; (b) a temperature-independent voltage source.

**Figure B.56 (Contd.).****Table B.12** PSpice-Computed Parameter Values of the ECL Gate, With and Without Temperature Compensation, at Two Different Temperatures

Temperature	Parameter	Temperature-Compensated		Not Temperature-Compensated	
		OR	NOR	OR	NOR
0°C	$V_{OL}$	-1.779 V	-1.799 V	-1.786 V	-1.799 V
	$V_{OH}$	-0.9142 V	-0.9092 V	-0.9142 V	-0.9092 V
	$V_{avg} = \frac{V_{OL} + V_{OH}}{2}$	-1.3466 V	-1.3541 V	-1.3501 V	-1.3541 V
	$V_R$	-1.345 V	-1.345 V	-1.32 V	-1.32 V
	$ V_{avg} - V_R $	1.6 mV	9.1 mV	30.1 mV	34.1 mV
70°C	$V_{OL}$	-1.742 V	-1.759 V	-1.729 V	-1.759 V
	$V_{OH}$	-0.8338 V	-0.8285 V	-0.8338 V	-0.8285 V
	$V_{avg} = \frac{V_{OL} + V_{OH}}{2}$	-1.288 V	-1.294 V	-1.2814 V	-1.294 V
	$V_R$	-1.271 V	-1.271 V	-1.32 V	-1.32 V
	$ V_{avg} - V_R $	17 mV	23 mV	38 mV	26.2 mV

The dynamic operation of the ECL gate is investigated using the arrangement of Fig. B.57. Here, two gates are connected by a 1.5-m coaxial cable having a characteristic impedance ( $Z_0$ ) of  $50\ \Omega$ . The manufacturer specifies that signals propagate along this cable (when it is *properly terminated*) at about half the speed of light, or  $15\ \text{cm/ns}$ . Thus we would expect the 1.5-m cable we are using to introduce a delay  $t_d$  of  $10\ \text{ns}$ . Observe that in this circuit (Fig. B.57), resistor  $R_{T1}$  provides the proper cable termination. The cable is

**Example PS.14.1** *continued*

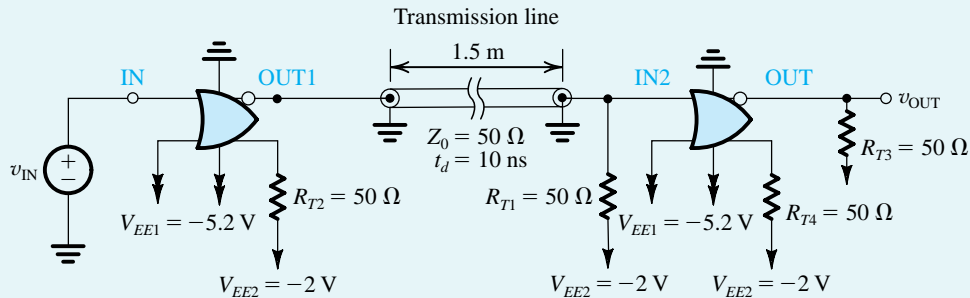


**Figure B.57** Circuit arrangement for investigating the dynamic operation of ECL. Two ECL gates (Fig. B.53) are connected in cascade via a 1.5-m coaxial cable which has a characteristic impedance  $Z_0 = 50 \Omega$  and a propagation delay  $t_d = 10 \text{ ns}$ . Resistor  $R_{T1}$  ( $50 \Omega$ ) provides proper termination for the coaxial cable.

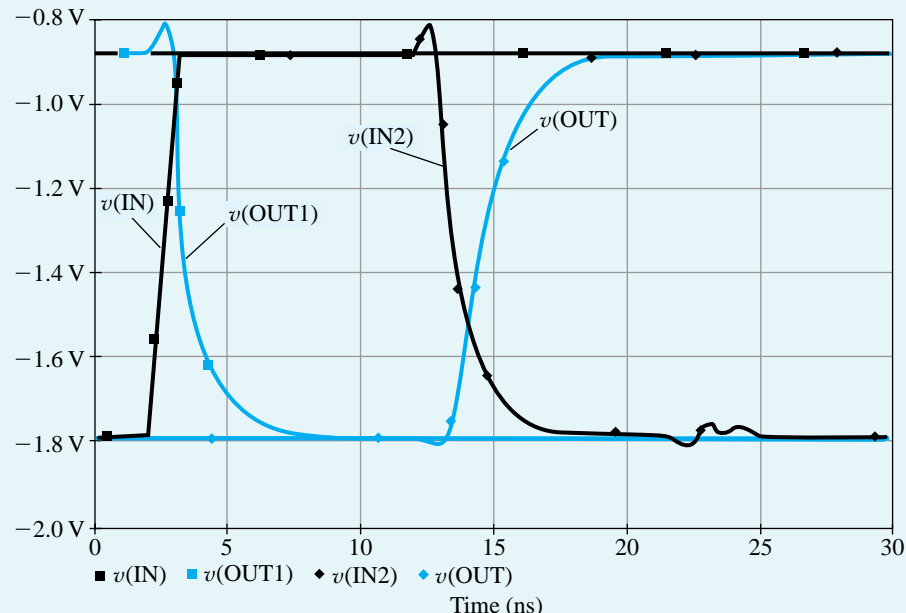


**Figure B.58** Transient response of a cascade of two ECL gates interconnected by a 1.5-m coaxial cable having a characteristic impedance of  $50 \Omega$  and a delay of  $10 \text{ ns}$  (see Fig. B.57).

assumed to be lossless and is modeled in PSpice using the *transmission line* element (the T part in the Analog library) with  $Z_0 = 50 \Omega$  and  $t_d = 10 \text{ ns}$ . A voltage step, rising from  $-1.77 \text{ V}$  to  $-0.884 \text{ V}$  in  $1 \text{ ns}$ , is applied to the input of the first gate, and a transient analysis over a  $30\text{-ns}$  interval is requested. Figure B.58 shows plots of the waveforms of the input, the voltage at the output of the first gate, the voltage at the input of the second gate, and the output. Observe that despite the very high edge speeds involved, the waveforms are reasonably clean and free of excessive ringing and reflections. This is particularly remarkable because the signal is being transported over a relatively long distance. A detailed examination of the waveforms reveals that the delay along the cable is indeed  $10 \text{ ns}$ , and the delay of the second gate is about  $1.06 \text{ ns}$ .

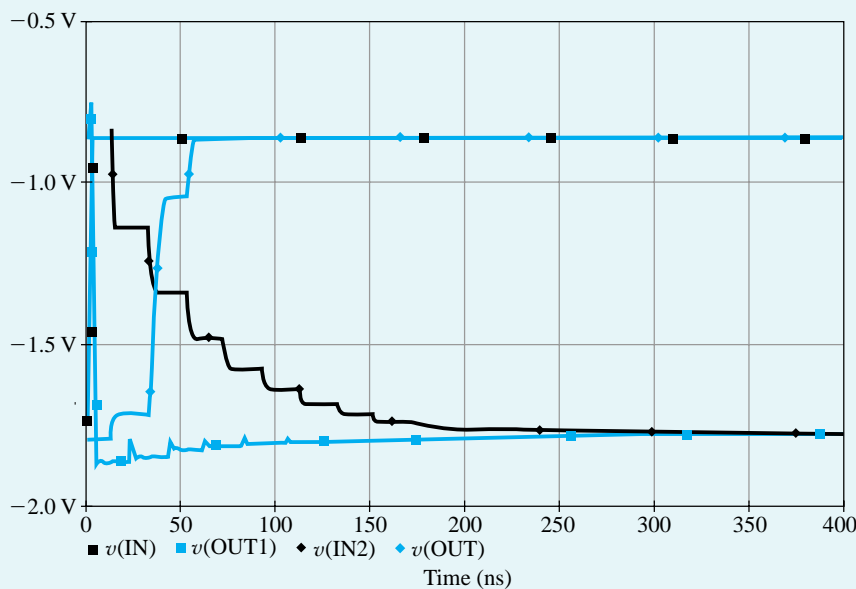


**Figure B.59** Transient response of a cascade of two ECL gates interconnected by a 1.5-m cable having a characteristic impedance of  $300\ \Omega$ . The termination resistance  $R_{Tl}$  (see Fig. B.57) was kept unchanged at  $50\ \Omega$ . Note the change in time scale of the plot.

Finally, to verify the need for properly terminating the transmission line, the dynamic analysis is repeated, this time with the  $50\ \Omega$  coaxial cable replaced with a  $300\ \Omega$  twisted-pair cable while keeping the termination resistance unchanged. The results are the slow rising and falling and long-delayed waveforms shown in Fig. B.59. (Note the change of plotting scale.)

## Example PS.16.1

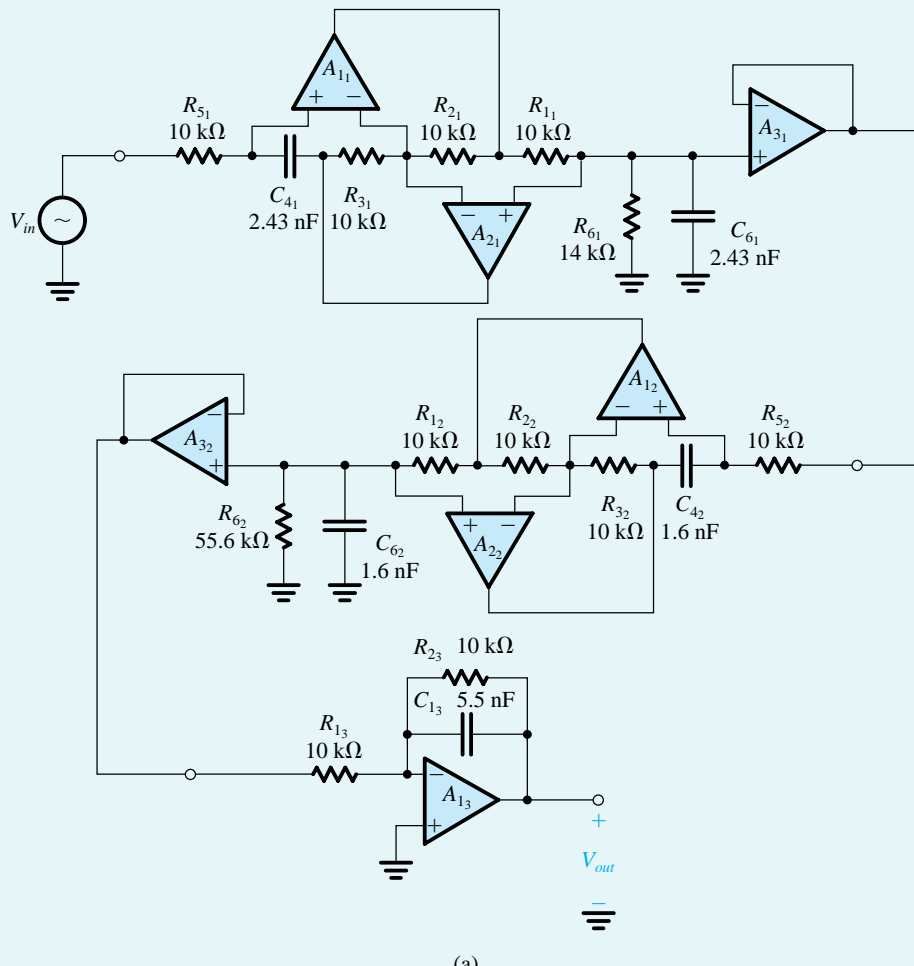
### Verification of the Design of a Fifth-Order Chebyshev Filter

In this example we show how SPICE can be utilized to verify the design of a fifth-order Chebyshev filter. Specifically, we simulate the operation of the circuit whose component values were obtained in Exercise 11.20. The complete circuit is shown in Fig. B.60(a). It consists of a cascade of two second-order simulated-LCR resonators using the Antoniou circuit and a first-order op amp–RC circuit. Using PSpice, we would like to compare the magnitude of the filter response with that computed directly from its transfer function. Here, we note that PSpice can also be used to perform the latter task by using the Laplace transfer-function block in the analog-behavioral-modeling (ABM) library.

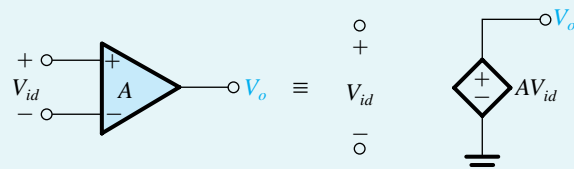
Since the purpose of the simulation is simply to verify the design, we assume ideal components. For the op amps, we utilize a near-ideal model, namely, a voltage-controlled voltage source (VCVS) with a gain of  $10^6\ \text{V/V}$ , as shown in Fig. B.60(b).<sup>16</sup>

<sup>16</sup>SPICE models for the op amp are described in Section B.1.1

**Example PS.16.1** *continued*



(a)



(b)

**Figure B.60** Circuits for Example PS.16.1 (a) Fifth-order Chebyshev filter circuit implemented as a cascade of two second-order simulated LCR resonator circuits and a single first-order op amp-RC circuit. (b) VCVS representation of an ideal op amp with gain  $A$ .

In SPICE, we apply a 1-V ac signal at the filter input, perform an ac-analysis simulation over the range 1 Hz to 20 kHz, and plot the output voltage magnitude versus frequency, as shown in Fig. B.61.

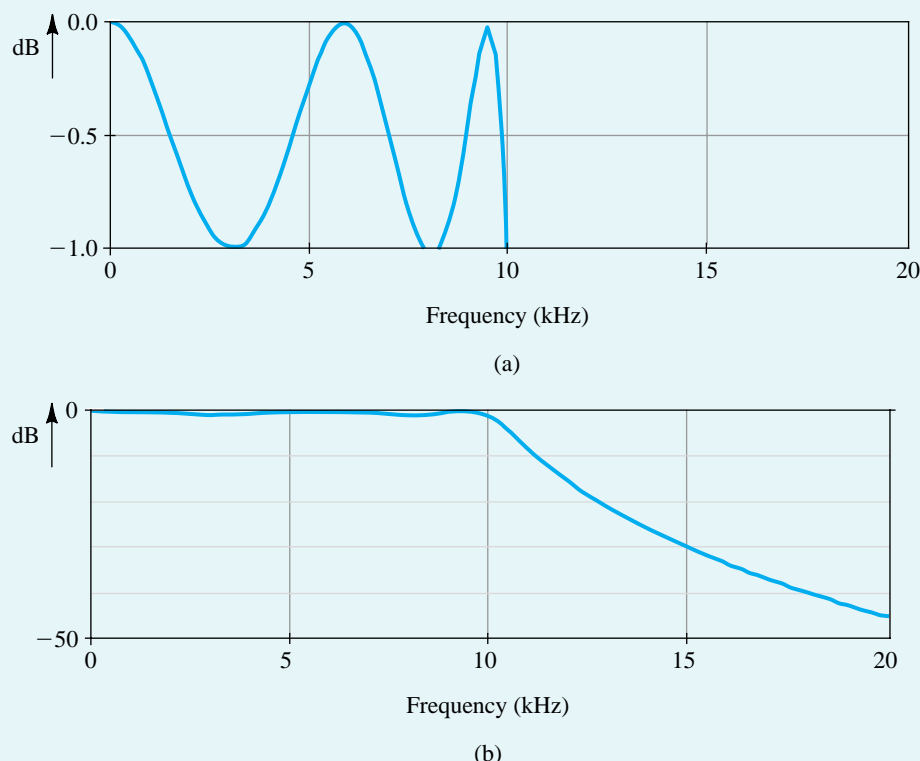


**Figure B.61** Magnitude response of the fifth-order lowpass filter circuit shown in Fig. B.60: (a) an expanded view of the passband region; (b) a view of both the passband and stopband regions.

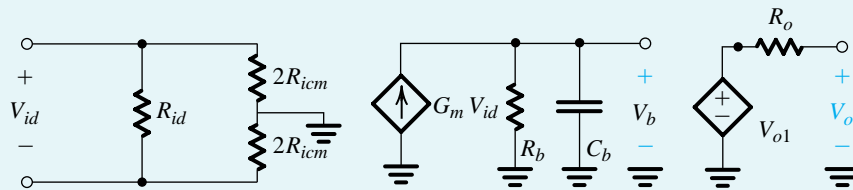
Both an expanded view of the passband and a view of the entire magnitude response are shown. These results are almost identical to those computed directly from the ideal transfer function, thereby verifying the correctness of the design.

### Example PS.16.2

#### Effect of Finite Op-Amp Bandwidth on the Operation of the Two-Integrator-Loop Filter

In this example, we investigate the effect of the finite bandwidth of practical op amps on the response of a two-integrator-loop bandpass filter utilizing the Tow-Thomas biquad circuit of Fig. 11.25(b). The circuit is designed to provide a bandpass response with  $f_0 = 10$  kHz,  $Q = 20$ , and a unity center-frequency gain. The op amps are assumed to be of the 741 type. Specifically, we model the terminal behavior of the op amp with the single-time-constant linear network shown in Fig. B.62. Since the analysis performed here is a small-signal (ac) analysis that ignores nonlinearities, no nonlinearities are included in this op-amp

**Example PS.16.2** continued



$$A_0 = G_m R_1 \quad \omega_b = 1/R_b C_b$$

**Figure B.62** One-pole equivalent-circuit macromodel of an op amp operated within its linear region.

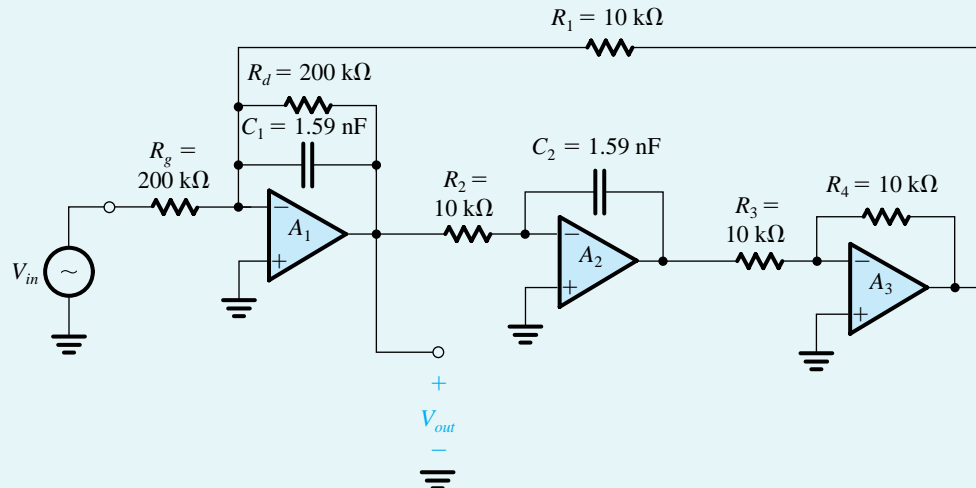


**Figure B.63** Circuit for Example PS.16.2 Second-order bandpass filter implemented with a Tow-Thomas biquad circuit having  $f_0 = 10$  kHz,  $Q = 20$ , and unity center-frequency gain.

macromodel. (If the effects of op-amp nonlinearities are to be investigated, a transient analysis should be performed.) The following values are used for the parameters of the op-amp macromodel in Fig. B.62:

$$\begin{aligned} R_{id} &= 2 \text{ M}\Omega & R_{icm} &= 500 \text{ M}\Omega & R_o &= 75 \Omega \\ G_m &= 0.19 \text{ mA/V} & R_b &= 1.323 \times 10^9 \Omega & C_b &= 30 \text{ pF} \end{aligned}$$

These values result in the specified input and output resistances of the 741-type op amp. Further, they provide a dc gain  $A_0 = 2.52 \times 10^5$  V/V and a 3-dB frequency  $f_b$  of 4 Hz, again equal to the values specified for the 741. Note that the selection of the individual values of  $G_m$ ,  $R_b$ , and  $C_b$  is immaterial as long as  $G_m R_b = A_0$  and  $C_b R_b = 1/2 \pi f_b$ .

The Tow-Thomas circuit simulated is shown in Fig. B.63. The circuit is simulated in PSpice for two cases: (1) assuming 741-type op amps and using the linear macromodel in Fig. B.62; and (2) assuming ideal op amps with dc gain of  $A_0 = 10^6$  V/V and using the near-ideal model in Fig. B.60. In both cases,

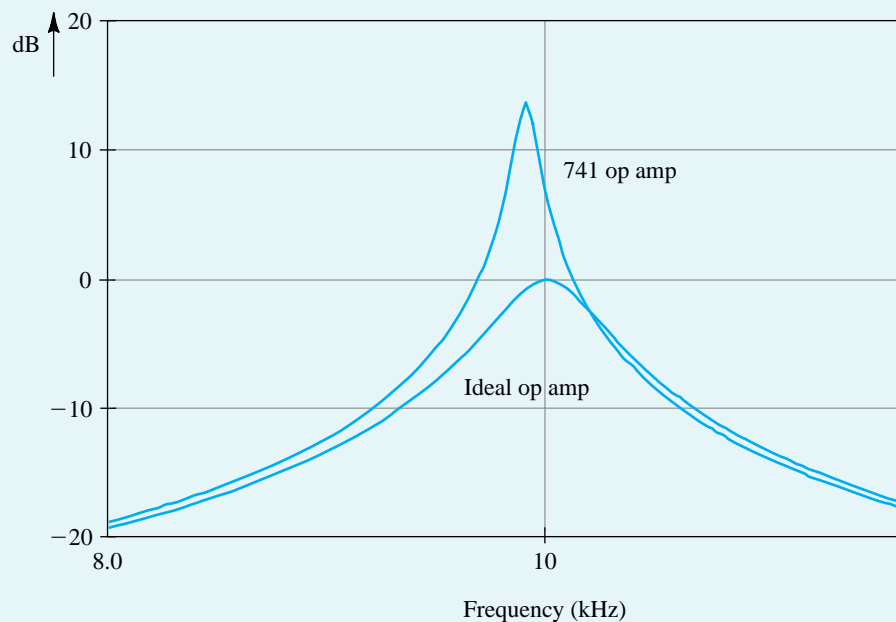


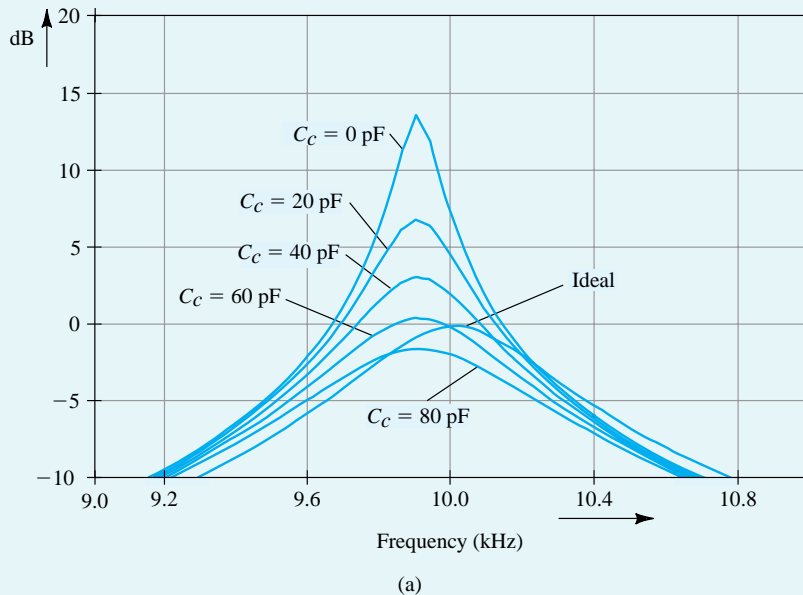
**Figure B.64** Comparing the magnitude response of the Tow-Thomas biquad circuit (shown in Fig. B.63) constructed with 741-type op amps, with the ideal magnitude response. These results illustrate the effect of the finite dc gain and bandwidth of the 741 op amp on the frequency response of the Tow-Thomas biquad circuit.

we apply a 1-V ac signal at the filter input, perform an ac-analysis simulation over the range 8 kHz to 12 kHz, and plot the output-voltage magnitude versus frequency.

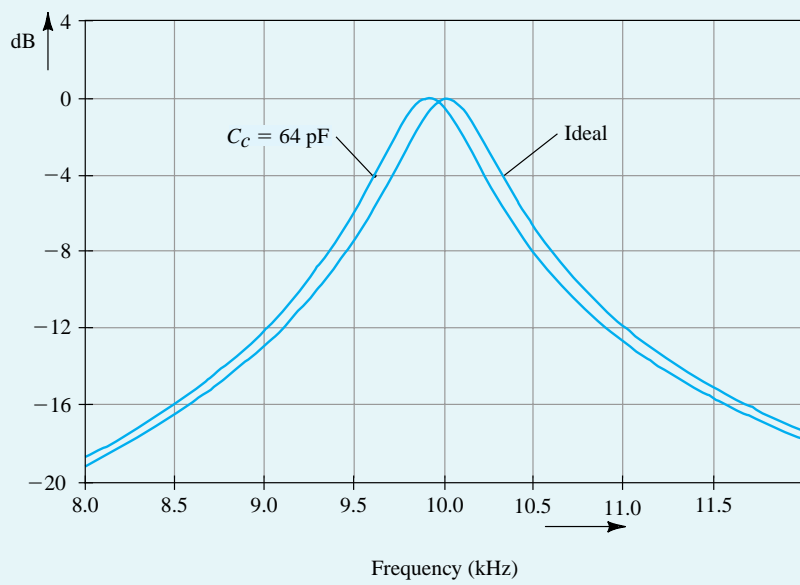
The simulation results are shown in Fig. B.64, from which we observe the significant deviation between the response of the filter using the 741 op amp and that using the near-ideal op-amp model. Specifically, the response with practical op amps shows a deviation in the center frequency of about -100 Hz, and a reduction in the 3-dB bandwidth from 500 Hz to about 110 Hz. Thus, in effect, the filter  $Q$  factor has increased from the ideal value of 20 to about 90. This phenomenon, known as *Q-enhancement*, is predictable from an analysis of the two-integrator-loop biquad with the finite op-amp bandwidth taken into account [see Sedra and Brackett (1978)]. Such an analysis shows that *Q*-enhancement occurs as a result of the excess phase lag introduced by the finite op-amp bandwidth. The theory also shows that the *Q*-enhancement effect can be compensated for by introducing phase lead around the feedback loop. This can be accomplished by connecting a small capacitor,  $C_c$ , across resistor  $R_2$ . To investigate the potential of such a compensation technique, we repeat the PSpice simulation with various capacitance values. The results are displayed in Fig. B.65(a). We observe that as the compensation capacitance is increased from 0 pF, both the filter  $Q$  and the resonance peak of the filter response move closer to the desired values. It is evident, however, that a compensation capacitance of 80 pF causes the response to deviate further from the ideal. Thus, optimum compensation is obtained with a capacitance value between 60 pF and 80 pF. Further experimentation using PSpice enabled us to determine that such an optimum is obtained with a compensation capacitance of 64 pF. The corresponding response is shown, together with the ideal response, in Fig. B.65(b). We note that although the filter  $Q$  has been restored to its ideal value, there remains a deviation in the center frequency. We shall not pursue this matter any

**Example PS.16.2** *continued*

further here; our objective is not to present a detailed study of the design of two-integrator-loop biquads; rather, it is to illustrate the application of SPICE in investigating the nonideal performance of active-filter circuits, generally.



(a)



(b)

**Figure B.65** (a) Magnitude response of the Tow-Thomas biquad circuit with different values of compensation capacitance. For comparison, the ideal response is also shown. (b) Comparing the magnitude response of the Tow-Thomas biquad circuit using a 64-pF compensation capacitor and the ideal response.

**Example PS.17.1****Wien-Bridge Oscillator**

For our first example on oscillators, we shall simulate the operation of the Wien-bridge oscillator whose schematic capture is shown in Fig. B.66. The component values are selected to yield oscillations at 1 kHz. We would like to investigate the operation of the circuit for different settings of  $R_{1a}$  and  $R_{1b}$ , with  $R_{1a} + R_{1b} = 50 \text{ k}\Omega$ . Since oscillation just starts when  $(R_2 + R_{1b})/R_{1a} = 2$  (see Exercise 12.4), that is, when  $R_{1a} = 20 \text{ k}\Omega$  and  $R_{1b} = 30 \text{ k}\Omega$ , we consider three possible settings: (a)  $R_{1a} = 15 \text{ k}\Omega$ ,  $R_{1b} = 35 \text{ k}\Omega$ ; (b)  $R_{1a} = 18 \text{ k}\Omega$ ,  $R_{1b} = 32 \text{ k}\Omega$ ; and (c)  $R_{1a} = 25 \text{ k}\Omega$ ,  $R_{1b} = 25 \text{ k}\Omega$ . These settings correspond to loop gains of 1.33, 1.1, and 0.8, respectively.

In PSpice, a 741-type op amp and 1N4148-type diodes are used to simulate the circuit in Fig. 12.42.<sup>17</sup> A transient-analysis simulation is performed with the capacitor voltages initially set to zero. This demonstrates that the op-amp offset voltage is sufficient to cause the oscillations to start without the need for special start-up circuitry. Figure B.67 shows the simulation results. The graph in Fig. B.67(a) shows the

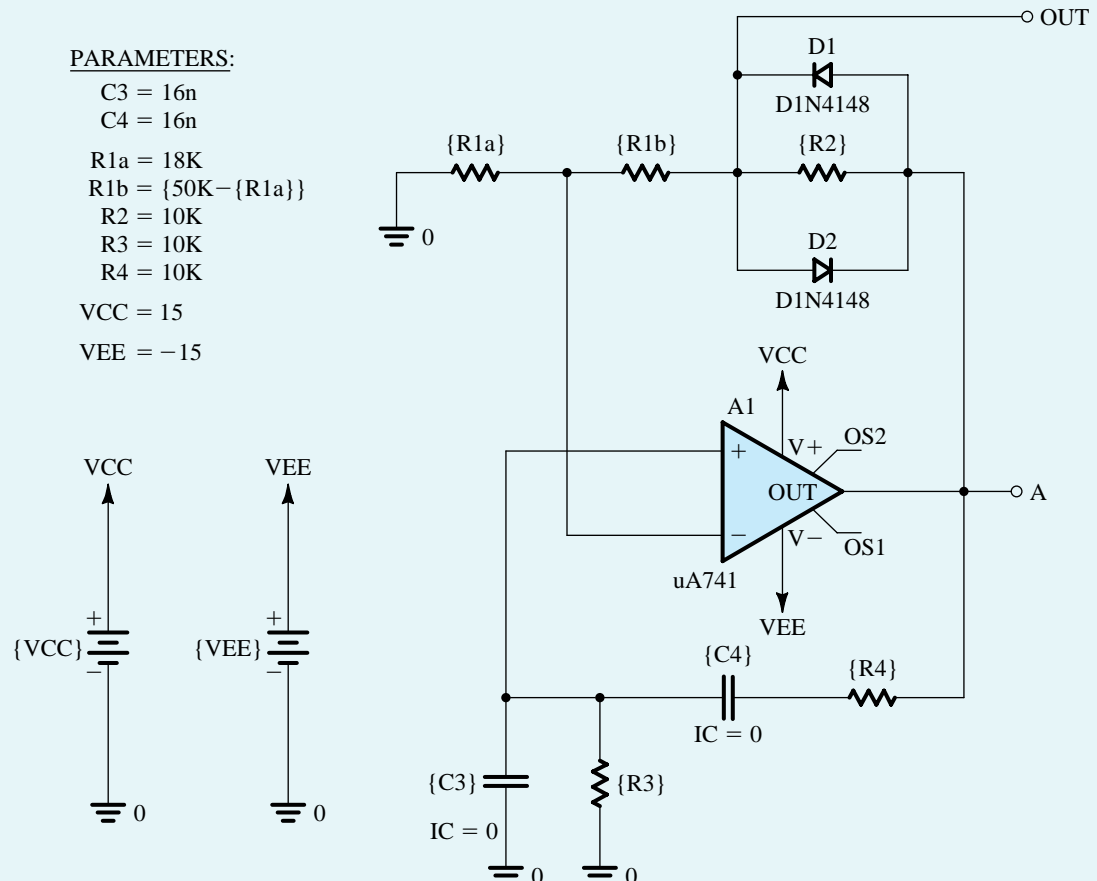
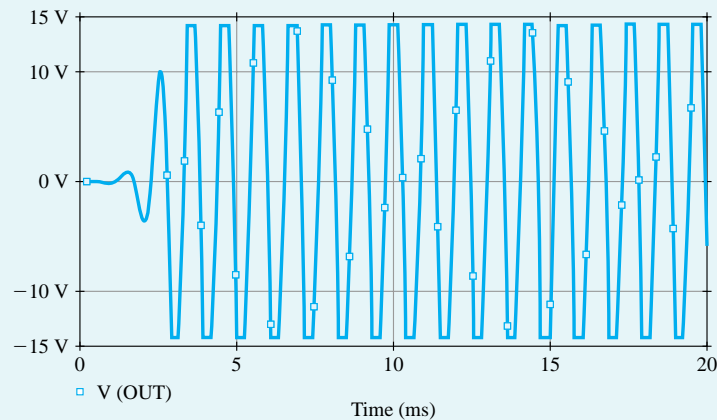


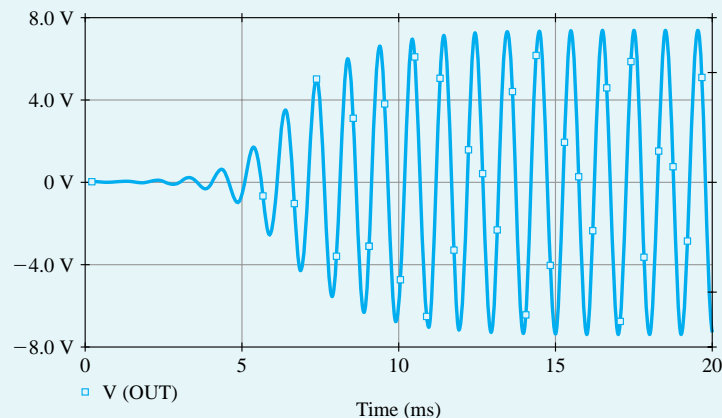
**Figure B.66** Example PS.17.1: Schematic capture of a Wien-bridge oscillator.

<sup>17</sup>The SPICE models for the 741 op amp and the 1N4148 diode are available in PSpice. The 741 op amp was characterized in Example PS.2.2. The 1N4148 diode was used in Example PS.4.1.

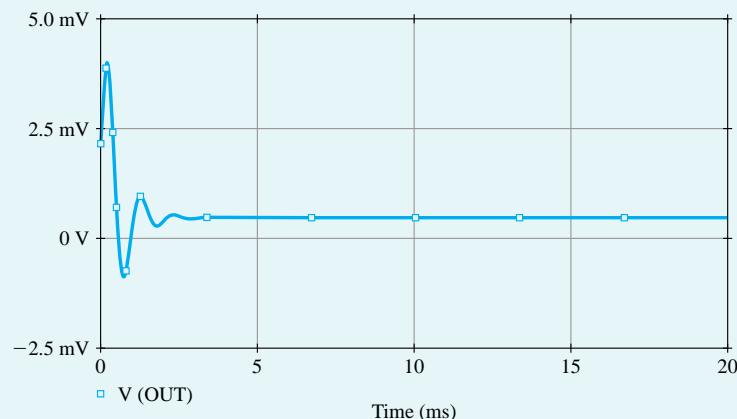
**Example PS.17.1** *continued*



(a)  $R_{1a} = 15 \text{ k}\Omega$ , Loop Gain = 1.33



(b)  $R_{1a} = 18 \text{ k}\Omega$ , Loop Gain = 1.1



(c)  $R_{1a} = 25 \text{ k}\Omega$ , Loop Gain = 0.8

**Figure B.67** Start-up transient behavior of the Wien-bridge oscillator shown in Fig. B.66 for various values of loop gain.

output waveform obtained for a loop gain of  $1.33 \text{ V/V}$ . Observe that although the oscillations grow and stabilize rapidly, the distortion is considerable. The output obtained for a loop gain of 1.1, shown in Fig. B.67(b), is much less distorted. However, as expected, as the loop gain is reduced toward unity, it takes longer for the oscillations to build up and for the amplitude to stabilize. For this case, the frequency is 986.6 Hz, which is reasonably close to the design value of 1 kHz, and the amplitude is 7.37 V. Finally, for a loop gain of 0.8, the output shown in Fig. B.67(c) confirms our expectation that sustained oscillations cannot be obtained when the loop gain is less than unity.

PSpice can be used to investigate the spectral purity of the output sine wave. This is achieved using the Fourier analysis facility. It is found that in the steady state, the output for the case of a loop gain of 1.1 has a THD figure of 1.88%. When the oscillator output is taken at the op-amp output (voltage  $v_A$ ), a THD of 2.57% is obtained, which, as expected, is higher than that for the voltage  $v_{\text{OUT}}$ , but not by very much. The output terminal of the op amp is of course a much more convenient place to take the output.

## Example PS.17.2

### Active-Filter-Tuned Oscillator

In this example, we use PSpice to verify our contention that a superior op amp–oscillator can be realized using the active-filter-tuned circuit of Fig. 12.11. We also investigate the effect of changing the value of the filter  $Q$  factor on the spectral purity of the output sine wave.

Consider the circuit whose schematic capture is shown in Fig. B.68. For this circuit, the center frequency is 1 kHz, and the filter  $Q$  is 5 when  $R_1 = 50 \text{ k}\Omega$  and 20 when  $R_1 = 200 \text{ k}\Omega$ . As in the case of the Wien-bridge circuit in Example PS.17.1, 741-type op amps and 1N4148-type diodes are utilized. In PSpice, a transient-analysis simulation is performed with the capacitor voltages initially set to zero. To be able to compute the Fourier components of the output, the analysis interval chosen must be long enough to allow the oscillator to reach a steady state. The time to reach a steady state is in turn determined by the value of the filter  $Q$ ; the higher the  $Q$ , the longer it takes the output to settle. For  $Q = 5$ , it was determined, through a combination of approximate calculations and experimentation using PSpice, that 50 ms is a reasonable estimate for the analysis interval. For plotting purposes, we use 200 points per period of oscillation.

The results of the transient analysis are plotted in Fig. B.69. The upper graph shows the sinusoidal waveform at the output of op amp  $A_1$  (voltage  $v_1$ ). The lower graph shows the waveform across the diode limiter (voltage  $v_2$ ). The frequency of oscillation is found to be very close to the design value of 1 kHz. The amplitude of the sine wave is determined using Probe (the graphical interface of PSpice) to be 1.15 V (or 2.3 V p-p). Note that this is lower than the 3.6 V estimated in Exercise 12.7. The latter value, however, was based on an estimate of 0.7-V drop across each conducting diode in the limiter. The lower waveform in Fig. B.69 indicates that the diode drop is closer to 0.5 V for a 1 V peak-to-peak amplitude of the pseudo-square wave. We should therefore expect the peak-to-peak amplitude of the output sinusoid to be lower than 3.6 V by the same factor, and indeed it is approximately the case.

In PSpice, the Fourier analysis of the output sine wave indicates that THD = 1.61%. Repeating the simulation with  $Q$  increased to 20 (by increasing  $R_1$  to 200 k $\Omega$ ), we find that the value of THD is reduced to 1.01%. Thus, our expectations that the value of the filter  $Q$  can be used as an effective means for controlling the THD of the output waveform are confirmed.

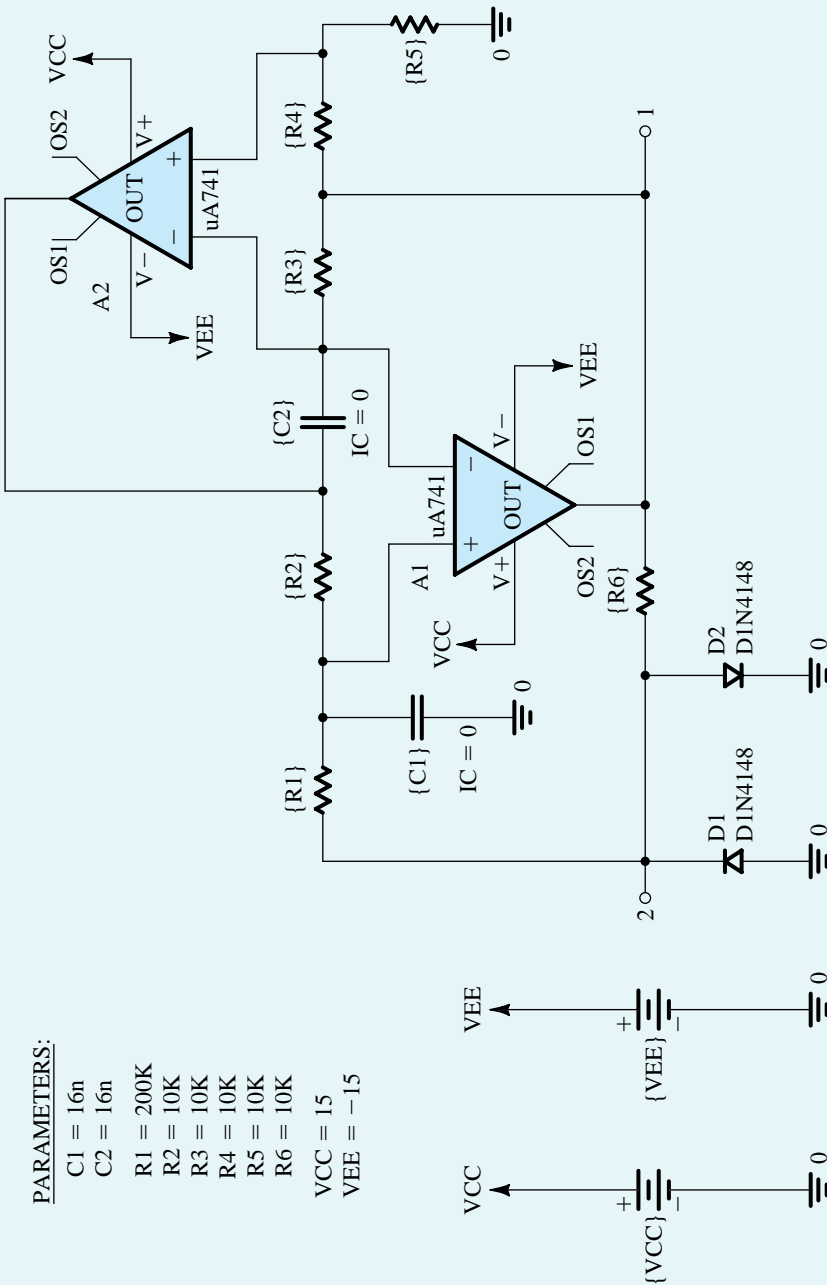


**Figure B.68** Example PS.17.2: Schematic capture of an active-filter-tuned oscillator for which the  $Q$  of the filter is adjustable by changing  $R_1$ .

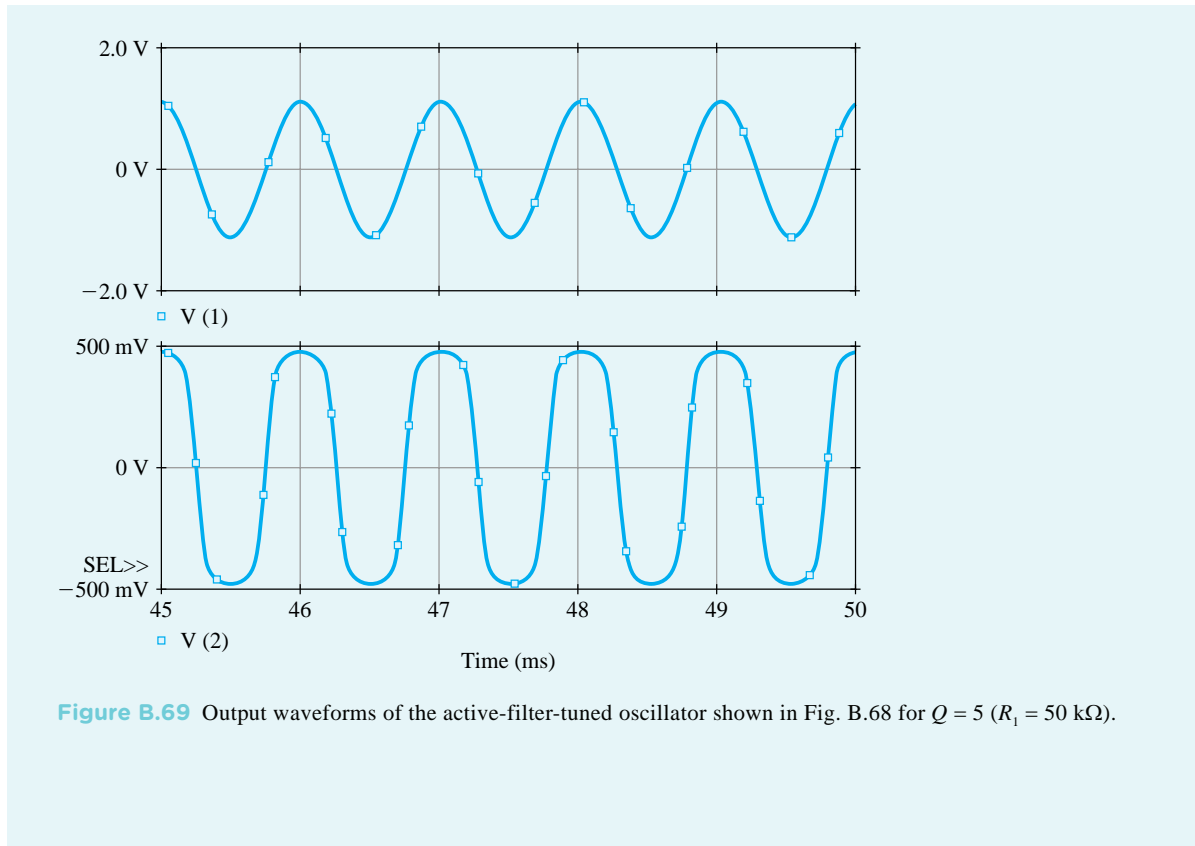


**Figure B.69** Output waveforms of the active-filter-tuned oscillator shown in Fig. B.68 for  $Q = 5$  ( $R_1 = 50 \text{ k}\Omega$ ).

## B.3 Multisim Examples

### Example MS.5.1

#### The CS Amplifier

In this example, we will use Multisim to characterize a CS amplifier whose schematic capture is shown in Fig. B.70. We will assume a 0.18- $\mu\text{m}$  CMOS technology for the MOSFET and use typical SPICE level-1 model parameters for this technology, as provided in Table B.4. We will also assume a signal-source resistance  $R_{\text{sig}} = 10 \text{ k}\Omega$ , a load resistance  $R_L = 50 \text{ k}\Omega$ , and bypass and coupling capacitors of  $10 \mu\text{F}$ . The targeted specifications for this CS amplifier are a voltage gain  $|A_v| = 10 \text{ V/V}$  and a maximum power consumption  $P = 0.45 \text{ mW}$ . As should always be the case with computer simulation, we will begin with an approximate hand-analysis design. We will then use Multisim to fine-tune our design and to investigate the performance of the final design.

The amplifier specifications are summarized in Table B.13.

#### Hand Design

With a 1.8-V power supply, the drain current of the MOSFET must be limited to  $I_D = P/V_{DD} = 0.45 \text{ mW}/1.8 \text{ V} = 0.25 \text{ mA}$  to meet the power consumption specification. Choosing  $V_{OV} = 0.15 \text{ V}$  and  $V_{DS} = V_{DD}/3 = 0.6 \text{ V}$  (to achieve a large signal swing at the output), the MOSFET can now be sized as

## Example MS.5.1 continued

DEVICE PARAMETERS	
NAME	Q1:NMOS
W	15.48u
L	0.2u
KP	291u
LD	0.01u
VID	0.45
LAMBDA	0.08
GAMMA	0.3

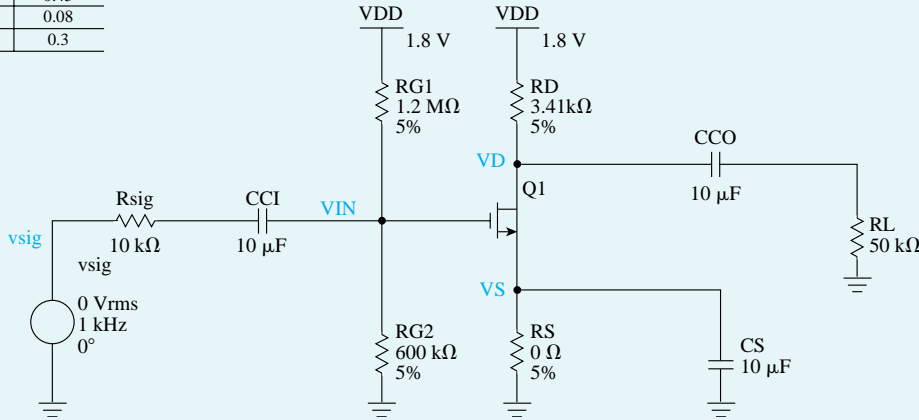


Figure B.70 Capture schematic of the CS amplifier.

Table B.13 CS Amplifier Specifications

Parameters	Value
Power	0.45 mW
$R_{\text{sig}}$	10 kΩ
$R_L$	50 kΩ
$ A_v $	10 V/V
$V_{DD}$	1.8 V

$$\frac{W}{L_{\text{eff}}} = \frac{I_D}{\frac{1}{2}k'_n V_{OV}^2 (1 + \lambda V_{DS})} = \frac{250 \times 10^{-6}}{\frac{1}{2} \times 246.2 \times 10^{-2} \times 0.15^6 \times (1 + 0.08 \times 0.6)} \approx 86$$

where  $k'_n = \mu_n C_{ox} = 246.2 \mu\text{A}/\text{V}^2$ . Here,  $L_{\text{eff}}$  rather than  $L$  is used to more accurately compute  $I_D$ .

The effect of using  $W_{\text{eff}}$  instead of  $W$  is much less important, because typically  $W \gg W_{ov}$ . Thus, choosing  $L = 0.200 \mu\text{m}$  results in  $L_{\text{eff}} = L - 2L_{ov} = 0.180 \mu\text{m}$ , and  $W = 86 \times L_{\text{eff}} = 15.48 \mu\text{m}$ .

Note that we chose  $L$  slightly larger than  $L_{\text{min}}$ . This is a common practice in the design of analog ICs to minimize the effects of fabrication nonidealities on the actual value of  $L$ . As we have seen, this is particularly important when the circuit performance depends on the matching between the dimensions of two or more MOSFETs (e.g., in the current-mirror circuits studied in Chapter 6).

Next,  $R_D$  is calculated based on the desired voltage gain:

$$|A_v| = g_m (R_D || R_L || r_o) = 10 \text{V/V} \Rightarrow R_D \approx 3.41 \text{k}\Omega$$

where

$$g_m = \frac{2I_D}{V_{OV}} = \frac{2 \times 0.25 \times 10^{-3}}{0.15} = 3.33 \text{ mA/V}$$

and

$$r_o = \frac{V_A}{I_D} = \frac{12.5}{0.25 \times 10^{-3}} = 50 \text{ k}\Omega$$

Hence, the dc bias voltage is  $V_D = V_{DD} - I_D R_D = 0.9457 \text{ V}$ .

To stabilize the bias point of the CS amplifier, we include a resistor in the source lead. In other words, to bias the MOSFET at  $V_{DS} = V_{DD}/3$ , we need an

$$R_s = \frac{V_S}{I_D} = \frac{(V_D - V_{DD}/3)}{I_D} = \frac{0.3475}{0.25 \times 10^{-3}} = 1.39 \text{ k}\Omega$$

However, as a result of including such a resistor, the gain drops by a factor of  $(1 + g_m R_s)$ . Therefore, we include a capacitor,  $C_s$ , to eliminate the effect of  $R_s$  on ac operation of the amplifier and gain.

Finally, choosing the current in the biasing branch to be 1  $\mu\text{A}$  gives  $R_{G1} + R_{G2} = V_{DD}/1\mu\text{A} = 1.8 \Omega$ . Also, we know that

$$V_{GS} = V_{OV} + V_t = 0.15 + 0.45 = 0.6 \text{ V} \Rightarrow V_G = V_S + 0.6 = 0.3475 + 0.6 = 0.9475 \text{ V}$$

Hence,

$$\frac{R_{G2}}{R_{G1} + R_{G2}} = \frac{V_G}{V_{DD}} = \frac{0.9475}{1.8} \Rightarrow R_{G1} = 0.8525 \text{ M}\Omega, R_{G2} = 0.9475 \text{ M}\Omega$$

Using large values for these gate resistors ensures that both their power consumption and the loading effect on the input signal source are negligible.

## Simulation

**Amplifier Biasing** We will now use Multisim to verify our design and investigate the performance of the CS amplifier. We begin by performing a bias-point simulation to verify that the MOSFET is properly biased in the saturation region and that the dc voltages and currents match the expected values (refer to this example's simulation file: Ch5\_CS\_Amplifier\_Ex\_DC.ms10). The results are shown in Fig. B.71.

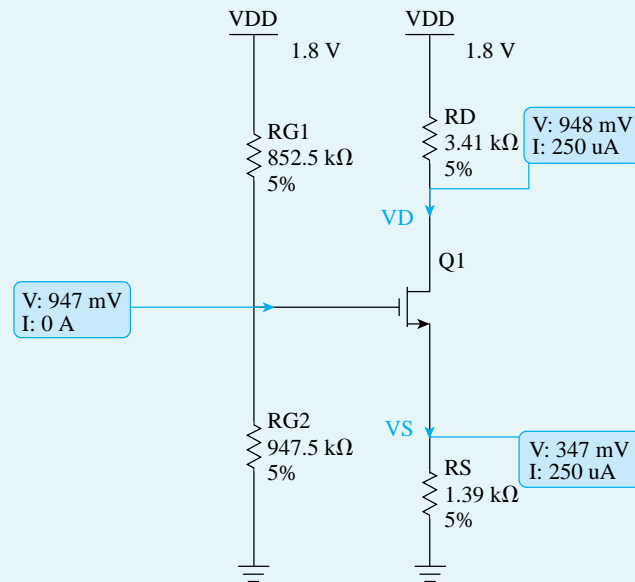


**Figure B.71** DC bias-point analysis of the CS amplifier.

**Example MS.5.1** *continued*

**Amplifier Gain** We can also verify if our design provides the desired gain. This can be done by performing transient response analysis, as set up in Ch5\_CS\_Amplifier\_Ex\_gain.ms10. As can be seen from Fig. B.72,  $|G_v| \approx |A_v| \approx 11 \text{ V/V}$ . Note the values of overall voltage gain  $G_v$  and  $A_v$  are close since  $R_m = (R_{G1}/R_{G2}) \gg R_{\text{sig}}$ . In the case where the capacitor  $C_s$  is not included ( $C_s = 0$ ), the gain drops by a factor of 5.63 (approximately equal to  $1 + g_m R_s$ ) to 1.95. This is as expected from our study of the CS amplifier with a source-degeneration resistance.

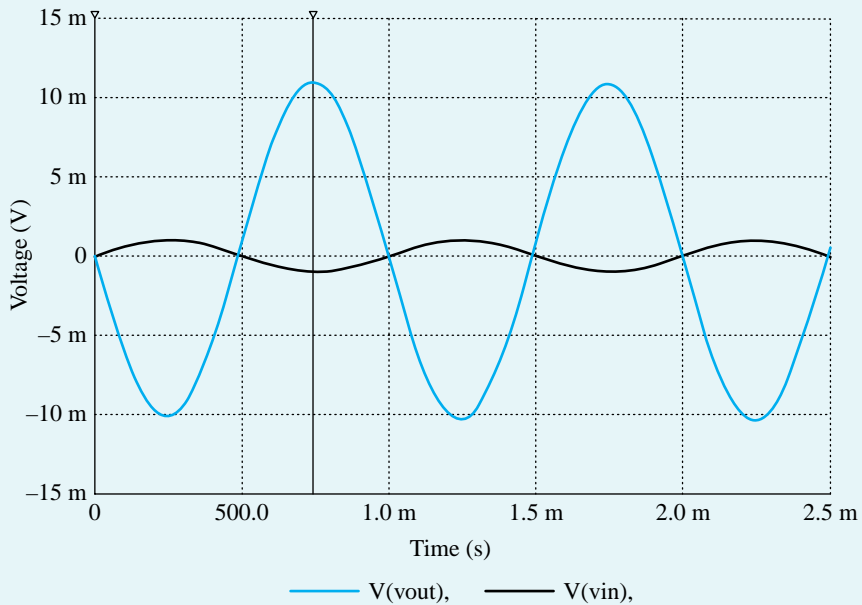


**Figure B.72**  $A_v$  and  $G_v$  of the CS amplifier: transient analysis.

**Investigating Amplifier Bias Stability** We can also demonstrate the improved bias stability achieved when a source resistor  $R_s$  is used. Specifically, we change (in the MOSFET level-1 model) the value of the zero-bias threshold voltage parameter  $VT0$  by  $\pm 0.1 \text{ V}$  and perform bias-point simulation in Multisim. Table B.14 shows the corresponding variations in  $I_D$  and  $V_D$  for the case in which  $R_s = 1.39 \text{ k}\Omega$ . For the case without source degeneration, we use an  $R_s = 0$  in the given schematic. Furthermore, to obtain the same  $I_D$  and  $V_D$  in both cases (for the nominal threshold voltage  $V_{t0} = 0.45 \text{ V}$ ), we use  $R_{G1} = 1.2 \text{ M}\Omega$  and  $R_{G2} = 0.6 \text{ M}\Omega$ .

**Table B.14** Variations in  $VT0$

With $R_s = 1.39 \text{ k}\Omega$				
$VT0$ (V)	$I_D$ ( $\mu\text{A}$ )	$I_D$ % Change	$V_D$ (V)	$V_D$ % Change
0.45	250	0	0.948	0
0.35	309	23.60%	0.748	-21.10%
0.55	192	-37.86%	1.14	20.25%

Without $R_s$				
0.45	255.96	0	0.9292	0
0.35	492	96.80%	0.122	-87.13%
0.55	30.1	-90.26%	1.7	127.27%

Also, Table B.15 shows the worst case deviation of  $I_D$  and  $V_D$  values, when imposing 5% tolerance on the resistors that determine the gate voltage.

**Table B.15** Variations Due to Resistor Tolerances

With $R_s = 1.39 \text{ k}\Omega$ s						
	$R_{G1}$ (MΩ)	$R_{G2}$ (MΩ)	$I_D$ (μA)	$I_D$ % Change	$V_D$ (V)	$V_D$ % Change
Nominal	0.8525	0.9475	250	0	947.67	0
$I_D$ low $V_D$ high	0.895	0.9	223.86	-10.44%	1.037	9.39%
$I_D$ high $V_D$ low	0.81	0.995	276.1	10.46%	0.858	-9.41%
Without $R_s$						
	$R_{G1}$ (MΩ)	$R_{G2}$ (MΩ)	$I_D$ (μA)	$I_D$ % Change	$V_D$ (V)	$V_D$ % Change
Nominal	1.2	0.6	255.96	0	0.9292	0
$I_D$ low $V_D$ high	1.26	0.57	143.28	-44.02%	1.311	41.44%
$I_D$ high $V_D$ low	1.14	0.63	398.62	55.74%	0.447	-52.47%

Accordingly, we see that the source-degeneration resistor makes the bias point of the CS amplifier less sensitive to changes in the threshold voltage and the values of gate resistors. However, unless a large bypass capacitor  $C_s$  is used, this reduced sensitivity comes at the expense of a reduction in gain.

**Largest Allowable Input Signal Swing** Next, we wish to analyze this amplifier circuit to determine the largest allowable  $v_{\text{sig}}$  for which the transistor remains in saturation:

$$v_{DS} \geq v_{GS} - v_t$$

By enforcing this condition, with equality, at the point  $v_{GS}$  is maximum and  $v_{DS}$  is correspondingly minimum, we write:

$$\begin{aligned} v_{DS,\min} &\geq v_{GS,\max} - v_{t0} \\ v_{DS} - |G_v|v_{\text{sig}} &= V_{GS} + v_{\text{sig}} - v_{t0} \\ v_{\text{sig}} &= \frac{V_{DS} - V_{GS} + V_{t0}}{(1 + |G_v|)} = \frac{0.9475 - 0.6 + 0.45}{11} = 72.5 \text{ mV} \end{aligned}$$

This can be verified from Ch5\_CS\_Amplifier\_Ex\_swing.ms10 simulation setup. If we increase the source signal's amplitude beyond approximately 73 mV, we can observe the distortion in the output signal, indicating that the MOSFET has entered the triode region.

**Amplifier Linearity** Finally, we can investigate the linearity of the designed amplifier. To do so, we use the setup in Ch5\_CS\_Amplifier\_Ex\_linearity.ms10. In this case, we use a triangular waveform and increase the amplitude of the signal until the output waveform begins to show nonlinear distortion (i.e., the rising and falling edges are no longer straight lines). Based on hand analysis, linearity holds as long as  $v_{in} \ll 2V_{ov}$ . According to the simulation results, linearity holds until  $v_{in}$  reaches the value of approximately 30 mV, which is one-tenth of the value of  $2V_{ov}$ .

### Example MS.6.1

#### Dependence of $\beta$ on the Bias Current

In this example, we use Multisim to investigate the dependence of  $\beta_{dc}$  on the collector bias current of the Q2N3904 discrete BJT (from Fairchild Semiconductor) whose model parameters are listed in Table B.16 and are available in Multisim. As shown in the schematic capture of Fig. B.73, the  $V_{CE}$  of the BJT is fixed using a constant voltage source (in this example,  $V_{CE} = 2$  V) and a dc current source  $I_B$  is applied at the base. To obtain the dependence of  $\beta_{dc}$  on the collector current  $I_C$ , we perform a dc-analysis simulation in which the sweep variable is the current source  $I_B$ . The  $\beta_{dc}$  of the BJT, which corresponds to the ratio of the collector current  $I_C$  to the base current  $I_B$ , can then be plotted versus  $I_C$  (by exporting the data to a graphing software), as shown in Fig. B.74. We see that to operate at the maximum value of  $\beta_{dc}$  (i.e.,  $\beta_{dc} = 163$ ), at  $V_{CE} = 2$  V, the BJT must be biased at an  $I_C = 10$  mA. Since increasing the bias current of a transistor increases the power dissipation, it is clear from Fig. B.74 that the choice of current  $I_C$  is a trade-off between the current gain  $\beta_{dc}$  and the power dissipation. Generally speaking, the optimum  $I_C$  depends on the application and technology in hand. For example, for the Q2N3904 BJT operating at  $V_{CE} = 2$  V, decreasing  $I_C$  by a factor of 20 (from 10 mA to 0.5 mA) results in a drop in  $\beta_{dc}$  of about 25% (from 163 to 123).

**Table B.16** SPICE Model Parameters of the Q2N3904 Discrete BJT

$I_s = 6.734f$	$B_f = 416.4$	$X_{tb} = 1.5$	$I_{kr} = 0$	$V_{jc} = .75$	$V_{je} = .75$	$V_{tf} = 4$
$X_{ti} = 3$	$N_e = 1.259$	$B_r = .7371$	$R_c = 1$	$F_c = .5$	$T_r = 239.5n$	$X_{tf} = 2$
$E_g = 1.11$	$I_{se} = 6.734f$	$N_c = 2$	$C_{jc} = 3.638p$	$C_{je} = 4.493p$	$T_f = 301.2p$	$R_b = 10$
$V_{af} = 74.03$	$I_{kf} = 66.78m$	$I_{sc} = 0$	$M_{jc} = .3085$	$M_{je} = .2593$	$I_{tf} = .4$	

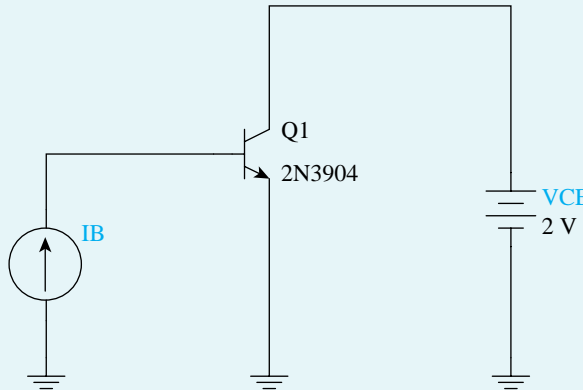


**Figure B.73** The test bench used to investigate the dependence of  $\beta_{dc}$  on the bias current for the Q2N3904 discrete BJT.

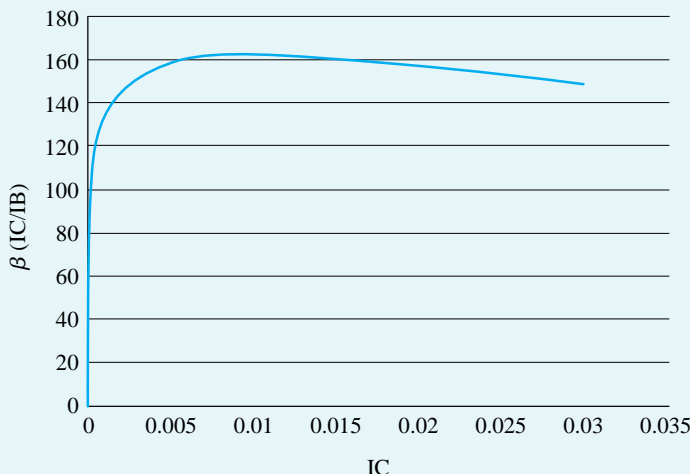


**Figure B.74** Dependence of  $\beta_{dc}$  on  $I_c$  (at  $V_{CE} = 2$  V) in the Q2N3904 discrete BJT.

## Example MS.6.2

### The CE Amplifier with Emitter Resistance

In this example, we use Multisim to compute the voltage gain and frequency response of the CE amplifier and investigate its bias-point stability. A schematic capture of the CE amplifier is shown in Fig. B.75. We will use part Q2N3904 for the BJT and a  $\pm 5$ -V power supply. We will assume a signal-source resistor  $R_{sig} = 10\text{ k}\Omega$ , a load resistor  $R_L = 10\text{ k}\Omega$ , and bypass and coupling capacitors of  $10\text{ }\mu\text{F}$ . To enable us to investigate the effect of including a resistance in the signal path of the emitter, a resistor  $R_{ce}$  is connected in series with the emitter bypass capacitor  $C_E$ . Note that the roles of  $R_E$  and  $R_{ce}$  are different. Resistor  $R_E$  is the dc emitter-degeneration resistor because it appears in the dc path between the emitter and ground. It is therefore used to help stabilize the bias point for the amplifier. The equivalent resistance  $R_e = R_E \parallel R_{ce}$  is the small-signal emitter-degeneration resistance because it appears in the ac (small-signal) path between the emitter and ground and helps stabilize the gain of the amplifier. In this example, we will investigate the effects of both  $R_E$  and  $R_e$  on the performance of the CE amplifier. However, as should always be the case with computer simulation, we will begin with an approximate hand analysis. In this way, maximum advantage and insight can be obtained from simulation.

Based on the plot of  $\beta_{dc}$  versus  $I_B$  in Fig. B.74, a collector bias current  $I_C$  (i.e.,  $\beta_{dc}I_B$ ) of  $0.5\text{ mA}$  is selected for the BJT, resulting in  $\beta_{dc} = 123$ . This choice of  $I_C$  is a reasonable compromise between power dissipation and current gain. Furthermore, a collector bias voltage  $V_C$  of  $0\text{ V}$  (i.e., at the mid-supply rail) is selected to achieve a high signal swing at the amplifier output. For  $V_{CE} = 2\text{ V}$ , the result is that  $V_E = -2\text{ V}$ , requiring bias resistors with values

$$R_C = \frac{V_{CC} - V_C}{I_C} = 10\text{ k}\Omega$$

$$R_E = \frac{V_E - V_{EE}}{I_C} = 320\text{ k}\Omega$$

Assuming  $V_{BE} = 0.7\text{ V}$  and  $\beta_{dc} = 123$ , we can determine

$$R_B = -\frac{V_B}{I_B} = -\frac{V_{BE} + V_E}{I_C/\beta_{dc}} = 320\text{ k}\Omega$$

**Example MS.6.2** *continued*

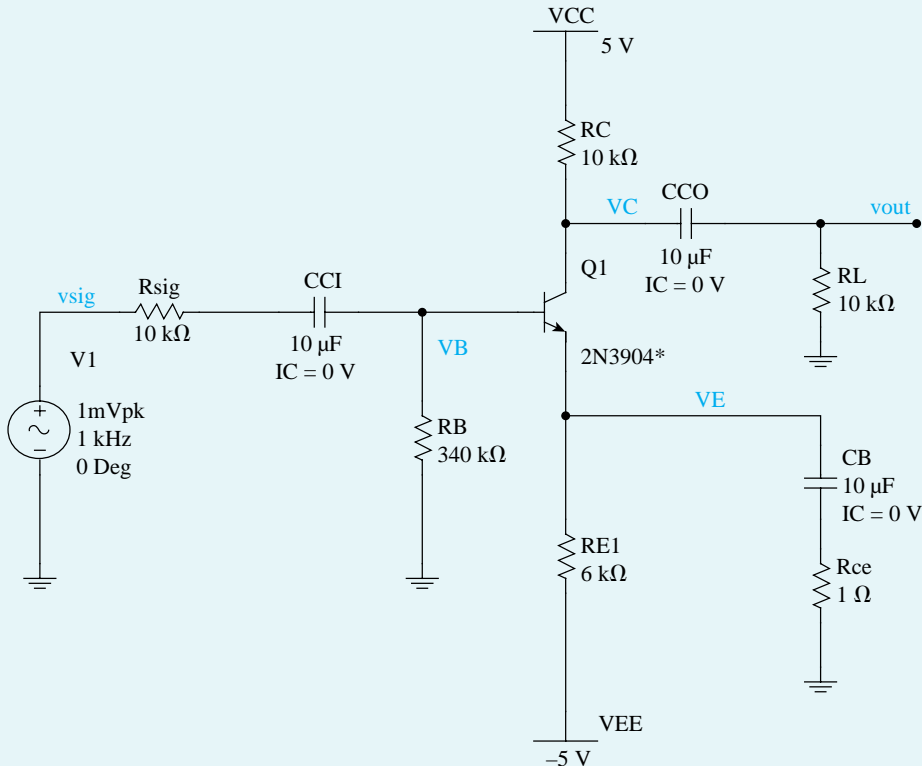


**Figure B.75** Schematic capture of the CE amplifier.

Next, the input resistance  $R_{in}$  and the voltage gain  $|A_v|$  of the CE amplifier:

$$R_{in} = R_B(\beta_{ac} + 1)(r_e + R_e)$$

$$|A_v| = \left| -\frac{R_{in}}{R_{sig} + R_{in}} \times \frac{R_C || R_L}{r_e + R_e} \right|$$

For simplicity, we will assume  $\beta_{ac} \approx \beta_{dc} = 123$ , resulting in

$$r_e = \left( \frac{\beta_{ac}}{\beta_{ac} + 1} \right) \left( \frac{V_T}{I_c} \right) = 49.6\Omega$$

Thus, with no small-signal emitter degeneration (i.e.,  $R_{ce} = 0$ ),  $R_{in} = 6.1\text{ k}\Omega$  and  $|A_v| = 38.2\text{ V/V}$ . Using the equation found for  $|A_v|$  and assuming that  $R_B$  is large enough to have a negligible effect on  $R_{in}$ , it can be shown that the emitter-degeneration resistance  $R_e$  decreases the voltage gain  $|A_v|$  by a factor of

$$\frac{1 + \frac{R_e}{r_e} + \frac{R_{sig}}{r_\pi}}{1 + \frac{R_{sig}}{r_\pi}}$$

Therefore, to limit the reduction in voltage gain to a factor of 2, we will select

$$R_e = r_e + \frac{R_{sig}}{\beta_{ac} + 1}$$

Thus,  $R_{ce} \approx R_e = 130\Omega$ . Substituting this value in the equations found for  $|A_v|$  and  $R_{in}$  shows that  $R_{in}$  increases from  $6.1\text{ k}\Omega$  to  $20.9\text{ k}\Omega$  while  $|A_v|$  drops from  $38.2\text{ V/V}$  to  $18.8\text{ V/V}$ .

We will now use Multisim to verify our design and investigate the performance of the CE amplifier. We begin by performing a bias-point simulation to verify that the BJT is properly biased in the active region and that the dc voltages and currents meet the desired specifications. Based on this simulation forward, we have increased the value of  $R_B$  to  $340\text{ k}\Omega$  in order to limit  $I_C$  to about  $0.5\text{ mA}$  while using a standard 1% resistor value. Next, to measure the gain  $A_v$ , we conduct a transient response analysis, as set up in Ch6\_CE\_Amplifier\_Ex.ms10. Accordingly, with no emitter degeneration, the gain is  $|A_v| = 38.5\text{ V/V}$ . Using  $R_{ce} = 130\Omega$  results in a drop in the gain by a factor of 2 (as can be seen from Fig. B.76).

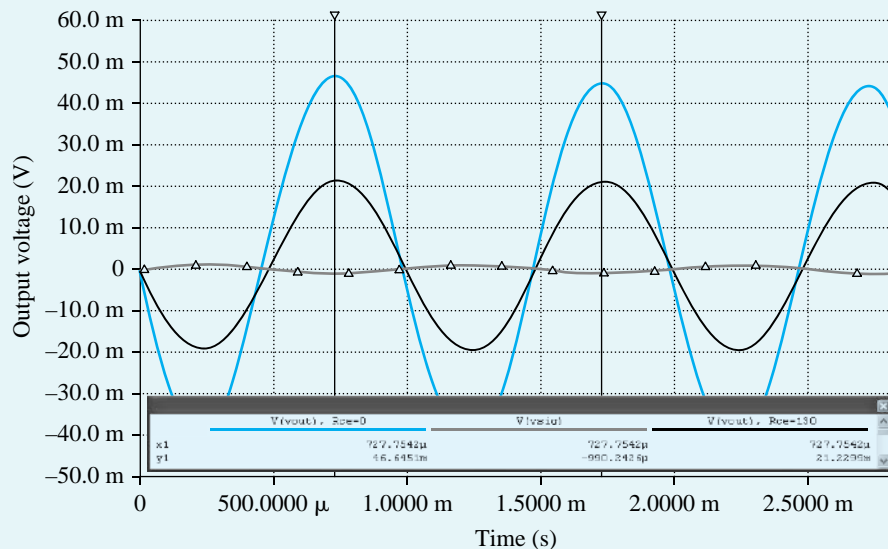


**Figure B.76** Transient analysis of the CE amplifier with  $R_{ce} = 0$  and  $R_{ce} = 130\Omega$ .

Thus far in this example, we have assumed that the voltage gain of the BJT amplifier is constant and independent of the frequency of the input signal. However, as mentioned in Section 4.8.6, this is not true, since it implies that the amplifier has infinite bandwidth. To illustrate the finite bandwidth, we compute the frequency response of the amplifier. The plot of the output-voltage magnitude (in dB) versus frequency is shown in Fig. B.77. With no emitter degeneration, the midband gain is  $|A_M| = 38.5\text{ V/V} = 31.7\text{ dB}$  and the 3-dB bandwidth is  $BW = f_H - f_L = 145.7\text{ kHz}$ . Using an  $R_{ce}$  of  $130\Omega$  results in a drop in the midband gain  $|A_M|$  by a factor of 2 (consistent with what we observed previously in our transient analysis). Interestingly, however,  $BW$  has now increased by approximately the same factor as the drop in  $|A_M|$ . As we learned in Chapter 9, the emitter-degeneration resistor  $R_{ce}$  provides negative feedback, which allows us to trade off gain for other desirable properties such as a larger input resistance and a wider bandwidth.

To conclude this example, we will demonstrate the improved bias-point (or dc operating point) stability achieved when an emitter resistor  $R_E$  is used. Specifically, we will increase/decrease the value of the parameter  $BF$  (i.e., the ideal maximum forward current gain) in the SPICE model for part Q2N3904 by a factor of 2 and read the bias-point probes. The corresponding change in BJT parameter ( $\beta_{dc}$ ) and bias-point ( $I_C$  and  $V_{CE}$ ) are presented in Table B.17 for the case of  $R_E = 6\text{ k}\Omega$ .

**Example MS.6.2** *continued*

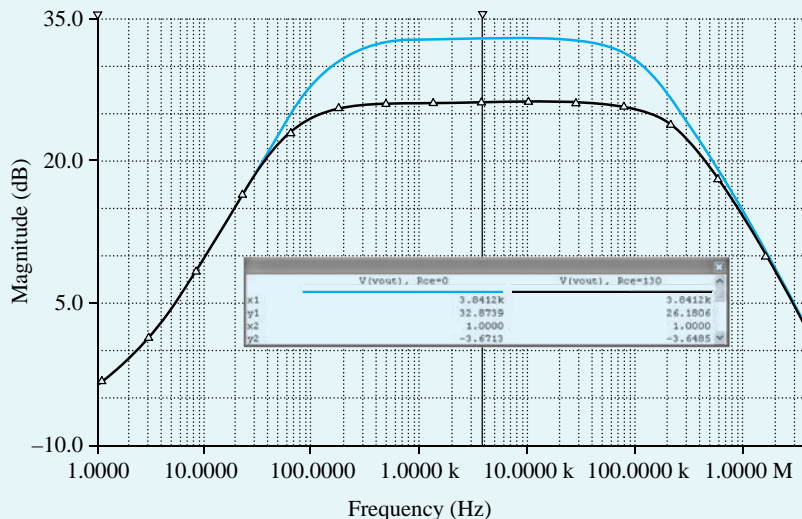


**Figure B.77** Frequency response of the CE amplifier with  $R_{ce} = 0$  and  $R_{ce} = 130\Omega$ .

**Table B.17** Variations in the Bias Point of the CE Amplifier with the SPICE Model Parameter  $BF$  of BJT

$BF$ (in SPICE)	$R_e = 6\text{ k}\Omega$			$R_e = 0$		
	$\beta_{dc}$	$I_c$ (mA)	$V_c$ (V)	$\beta_{dc}$	$I_c$ (mA)	$V_c$ (V)
208	94.9	0.452	0.484	96.9	0.377	1.227
416.4 (nominal value)	123	0.494	0.062	127	0.494	0.060
832	144	0.518	-0.183	151	0.588	-0.878

For the case without emitter degeneration, we will use  $R_e = 0$  in the schematic of Fig. B.75. Furthermore, to maintain the same  $I_c$  and  $V_c$  in both cases at the values obtained for nominal  $BF$ , we use  $R_b = 1.12\text{ M}\Omega$  to limit  $I_c$  to approximately 0.5 mA. The corresponding variations in the BJT bias point are also shown in Table B.17. Accordingly, we see that emitter degeneration makes the bias point of the CE amplifier much less sensitive to changes in  $\beta$ . However, unless a large bypass capacitor  $C_E$  is used, this reduced bias sensitivity comes at the expense of a reduction in gain (as we observed in this example when we simulated the transient response of the CE amplifier with an  $R_{ce} = 130\Omega$ ).

**Example MS.7.1**

**The CMOS CS Amplifier**

In this example, we will use Multisim to characterize the CMOS CS amplifier whose schematic capture is shown in Fig. B.78. We will assume a 0.18- $\mu\text{m}$  CMOS technology for the MOSFET and use typical SPICE level-1 model parameters for this technology as given in Table B.4. We will begin with an approximate hand-analysis design. We will then use Multisim to investigate the performance of the final design. The targeted specifications for this CMOS CS amplifier are a voltage gain  $|G_v| = 50 \text{ V/V}$  and a bias current  $I_D$  of 100  $\mu\text{A}$ .

The amplifier specifications are summarized in Table B.18.

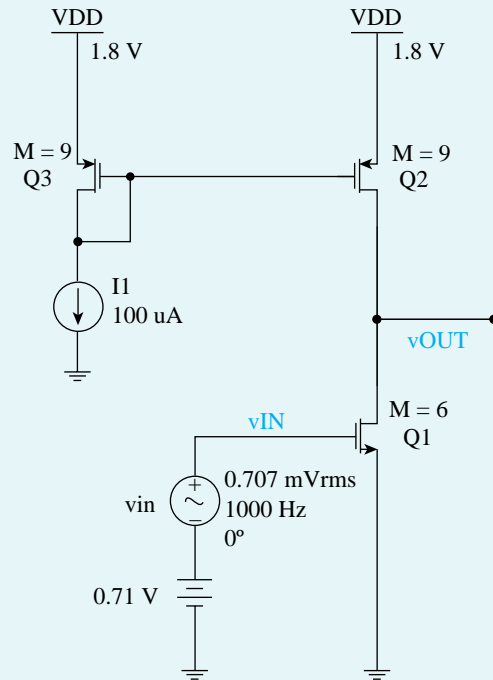
**Table B.18 CMOS CS Amplifier Specifications**

Specification	Value
$I_D$	100 $\mu\text{A}$
$ G_v $	50 $\text{V/V}$
$V_{DD}$	1.8 V

NMOS	
$V_{tn}$	0.5 V
$ V_{An} $	12.5 V
$k_n'$	246.2 $\mu\text{A}/\text{V}^2$
$I$	0.1 mA
$L$	0.2 $\mu\text{m}$
$W$	0.523 $\mu\text{m}$

PMOS	
$V_{tp}$	-0.5 V
$ V_{Ap} $	9 V
$k_p'$	-86.1 $\mu\text{A}/\text{V}^2$
$I$	0.1 mA
$L$	0.2 $\mu\text{m}$
$W$	0.46 $\mu\text{m}$



**Figure B.78** Schematic capture of the CMOS CS amplifier.

### Hand Design

For the design of this amplifier we choose  $L = 0.20 \mu\text{m}$ , so that similar to Example MS.5.1, we have  $L_{\text{eff}} = 0.18 \mu\text{m}$ . For this channel length, and in 0.18- $\mu\text{m}$  CMOS technology, the magnitudes of the Early voltages of the NMOS and PMOS transistors are  $V_{An} = 12.5 \text{ V}$  and  $|V_{Ap}| = 9 \text{ V}$ , respectively. Therefore, the value of  $V_{OVI}$  can now be calculated as follows:

$$G_v = -g_m R'_L = -g_m (r_{o1} \| r_{o2}) = -\frac{2}{V_{OVI}} \left( \frac{|V_{An}| |V_{Ap}|}{V_{An} |V_{Ap}|} \right)$$

$$V_{OVI} = -\frac{2}{G_v} \left( \frac{|V_{An}| |V_{Ap}|}{V_{An} |V_{Ap}|} \right) = -\frac{2}{(-50)} \left( \frac{12.5 \times 9}{12.5 + 9} \right) \simeq 0.21 \text{ V}$$

MOSFET 1 can now be sized (by ignoring the channel-length modulation) as

$$\frac{W_1}{L_{\text{eff}}} = \frac{I_D}{\frac{1}{2} k_n' V_{OVI}^2} = \frac{100 \times 10^{-6}}{\frac{1}{2} \times 246.2 \times 10^{-6} \times 0.21^2} \simeq 18.42$$

**Example MS.7.1 continued**

where, as mentioned,  $L_{\text{eff}} = 0.180 \mu\text{m}$ , and similar to Example MS.5.1,  $k_n' = 246.2 \mu\text{A/V}^2$ . This yields  $W_1 = 18.42 L_{\text{eff}} = 3.32 \mu\text{m}$ . To specify the dimensions of the MOSFETs in Multisim, we will use the multiplicative factor  $m$ ; its default value is 1, and it is used in SPICE to specify the number of MOSFETs connected in parallel. As depicted in Fig. B.79, a transistor with channel length  $L$  and channel width  $m \times W$  can be implemented using  $m$  narrower transistors in parallel, each having a channel length  $L$  and a channel width  $W$ . In this example, a unit-size NMOS transistor is used with  $W_1/L_1 = 0.52 \mu\text{m}/0.2 \mu\text{m}$ . Thus, we find  $m_1 = 3.32/0.52 \approx 6$ .

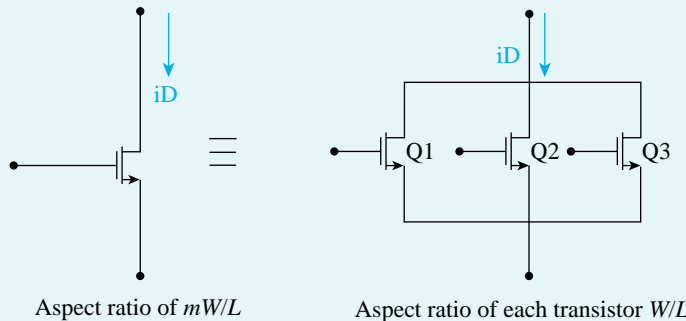


**Figure B.79** Transistor equivalency.

Furthermore, MOSFETs 2 and 3 must be sized to have reasonably small  $V_{ov}$  for the bias current  $I_D$  of 100  $\mu\text{A}$ . This allows large signal-swing at the output of the amplifier. Similar to our previous approach, by choosing  $|V_{ov2}| = 0.3 \text{ V}$ , and noting  $|D_{DS,2}| \approx (V_{DD}/2) = 0.9 \text{ V}$  (mid-rail voltage):

$$\frac{W_2}{L_{\text{eff}}} = \frac{I_D}{\frac{1}{2}|k_p'|V_{ov2}^2(1 + |\lambda_2||V_{DS,2}|)} = \frac{100 \times 10^{-6}}{\frac{1}{2} \times 86.1 \times 10^{-6} \times 0.3^2 \times (1 + 0.11 \times 0.9)} \approx 23.5$$

where  $L_{\text{eff}} = 0.18 \mu\text{m}$  and  $|k_p'| = 86.1 \mu\text{A/V}^2$ . This yields  $W_2 = 23.5 \times L_{\text{eff}} = 4.23 \mu\text{m}$ . In this example, unit-size PMOS transistors are used with  $W_2/L_2 = W_3/L_3 = 0.46 \mu\text{m}/0.2 \mu\text{m}$ . Thus, we find  $m_2 = m_3 = 4.23/0.46 \approx 9$ .

## Simulation

**Amplifier Biasing** Now our design can be verified using the simulation tool. The schematic is in Ch7\_CMOS\_CS\_Amplifier\_Ex\_VTC.ms10. Based on the simulation results,  $|G_v| = 54 \text{ V/V}$  and  $I_D = 101 \mu\text{A}$ . Therefore, the simulation results confirm that the designed CMOS CS amplifier meets the specifications.

**DC Voltage Transfer Characteristic** To compute the dc transfer characteristic of the CS amplifier, we perform a dc analysis in Multisim with  $V_{\text{IN}}$  swept over the range 0 to  $V_{DD}$  and plot the corresponding output voltage  $V_{\text{OUT}}$ .

Figure B.80(a) shows the resulting transfer characteristic. The slope of the VTC curve at  $V_{GS1} = 0.71 \text{ V}$  corresponds to the desired gain of the amplifier. To examine the high-gain region more closely, we repeat the dc sweep for  $V_{\text{IN}}$  between 0.6 V and 0.8 V. The resulting transfer characteristic is plotted in Fig. B.80b (middle curve). Using the cursor of the Grapher in Multisim, we find that the linear region of this dc transfer characteristic is bounded approximately by  $V_{\text{IN}} = 0.698 \text{ V}$  and  $V_{\text{IN}} = 0.721 \text{ V}$ . The corresponding values of  $V_{\text{OUT}}$  are 1.513 V and 0.237 V. These results are close to the expected values. Specifically, transistors  $Q_1$

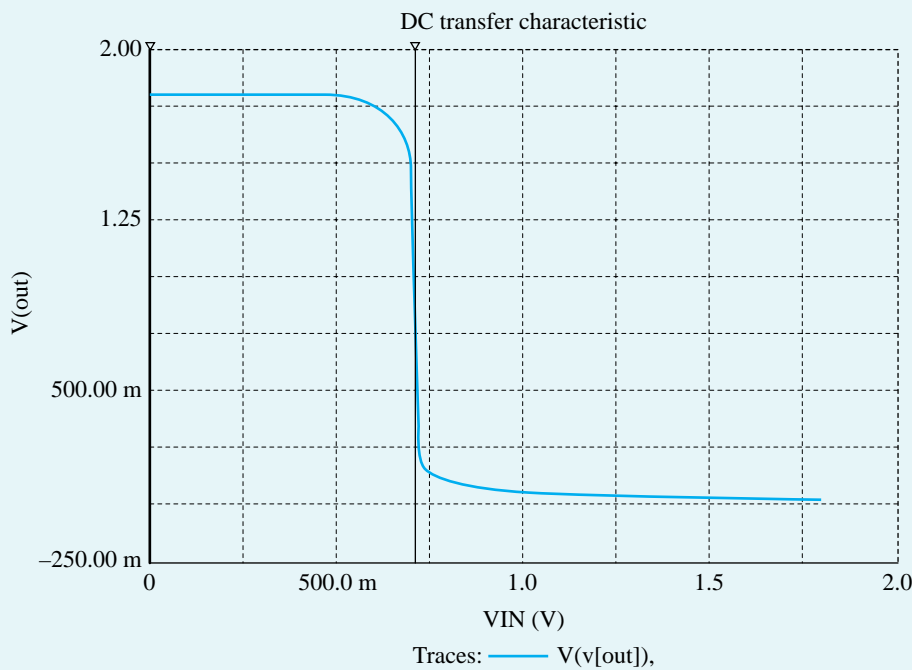


**Figure B.80 (a)** Voltage transfer characteristic of the CMOS CS amplifier.

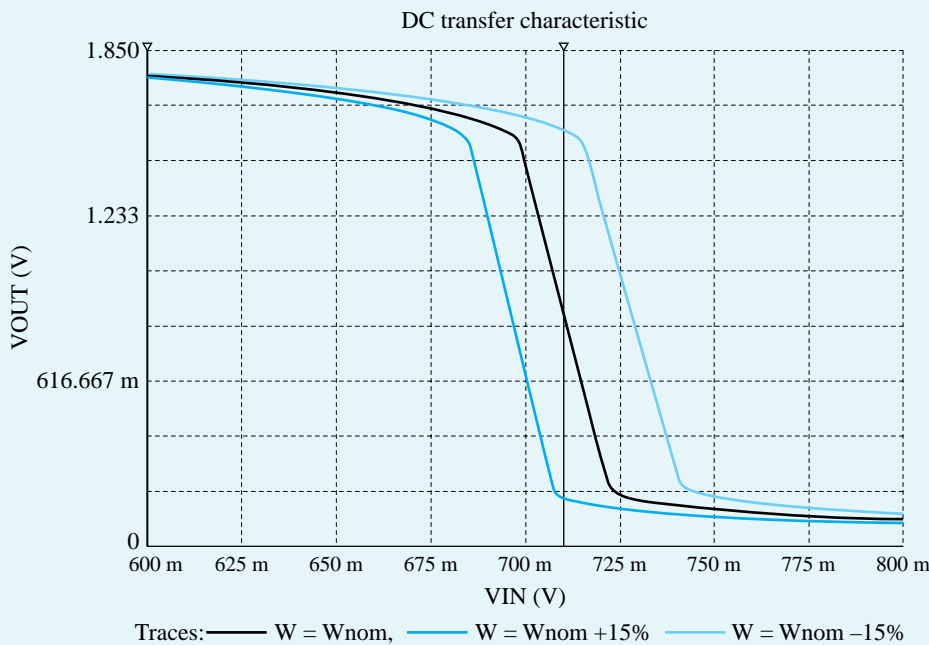


**Figure B.80 (b)** Expanded view of the transfer characteristics in the high-gain region for  $W = W_{\text{nominal}} \pm 15\%$ .

**Example MS.7.1 continued**

and  $Q_2$  will remain in the saturation region and, hence, the amplifier will operate in its linear region if  $V_{OV1} \leq V_{OUT} \leq V_{DD} - |V_{OV2}|$  or  $0.21V \leq V_{OUT} \leq 1.5 V$ . From the results above, the voltage gain  $G_v$  (i.e., the slope of the linear segment of the dc transfer characteristic) is approximately  $-54 V/V$ , which exceeds but is reasonably close to the targeted gain.

Note, from the dc transfer characteristic in Fig. 80(b), that for an input dc bias of  $V_{IN} = 0.710 V$ , the output dc bias is  $V_{OUT} = 0.871 V$ . This choice of  $V_{IN}$  maximizes the available signal swing at the output by setting  $V_{OUT}$  at approximately the middle of the linear segment of the dc transfer characteristic.

**Using Transient Analysis to Verify  $G_v$**  This can be done by conducting transient response analysis, as set up in Ch7\_CMOS\_CS\_Amplifier\_Ex\_gain.ms10. As can be seen from Fig. B.81,  $|G_v| \approx |A_v| \approx 54 V/V$ .

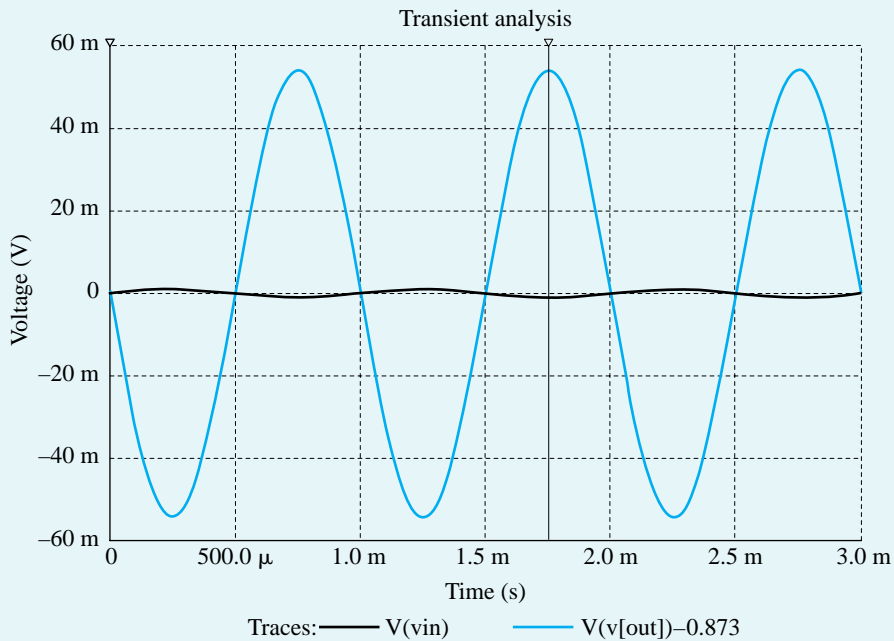


**Figure B.81**  $G_v$  of the CMOS CS amplifier (transient analysis).

**Sensitivity to Process Variations** Because of the high resistance at the output node (or, equivalently, because of the high voltage gain), the value of  $V_{OUT}$  is highly sensitive to the effect of process and temperature variations on the characteristics of the transistors. To illustrate this point, consider what happens when the width of  $Q_1$  (i.e.,  $W_1$ ) changes by  $\pm 15\%$ . The corresponding dc transfer characteristics are shown in Fig. B.80(b). Accordingly, when  $V_{IN} = 0.71 V$ ,  $V_{OUT}$  will drop to  $0.180 V$  if  $W_1$  increases by  $15\%$ , and will rise to  $1.556 V$  if  $W_1$  decreases by  $15\%$ . In practical circuit implementations, this problem is alleviated by using negative feedback to accurately set the dc bias voltage at the output of the amplifier and, hence, to reduce the sensitivity of the circuit to process variations. We studied the topic of negative feedback in Chapter 9.

## Example MS.7.2

# The Folded-Cascode Amplifier

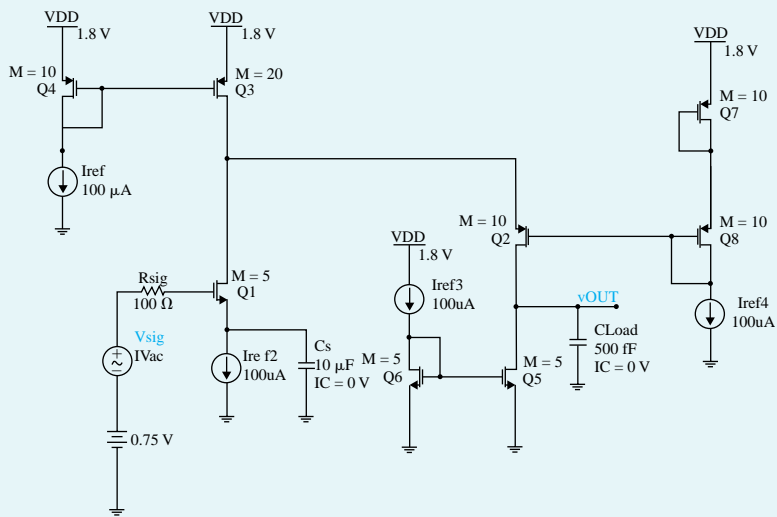
In this example, we will use Multisim to design the folded-cascode amplifier whose schematic capture is shown in Fig. B.82. We will assume a  $0.18\text{-}\mu\text{m}$  CMOS technology for the MOSFET and use typical SPICE level-1 model parameters for this technology, excluding the intrinsic capacitance values. We will begin with an approximate hand-analysis design. We will then use Multisim to verify that the designed circuit meets the specifications. The targeted specifications for this folded-cascode amplifier are a dc gain  $|G_v| = 100 \text{ V/V}$  and a bias current  $I_D$  of  $100 \mu\text{A}$ . Note that while this design does not provide a very high gain, its bandwidth is large (see Chapter 8).

The amplifier specifications are summarized in Table B.19.

NMOS	
V <sub>tn</sub>	0.5 V
V <sub>An</sub>	12.5 V
k <sup>n</sup>	246.2 uA/V <sup>2</sup>
IREF	0.1 mA
L	0.2 um
W	0.48 um

PMOS	
V <sub>tp</sub>	-0.5 V
V <sub>Ap</sub>	9V
k <sup>p</sup>	-86.1 $\mu$ A/V <sup>2</sup>
IREF	0.1 mA
L	0.2 um
W	0.64 um



**Figure B.82** Schematic capture of the folded-cascode amplifier.

**Table B.19** Folded-Cascode Amplifier Specifications

Parameters	Value
$I_D$	100 $\mu\text{A}$
$ G_v $	100 V/V
$V_{DD}$	1.8 V

## Hand Design

For the design of this amplifier we choose  $L = 200 \mu\text{m}$ , so we have  $L_{\text{eff}} = 180 \mu\text{m}$ . For this channel length, and in  $0.18\text{-}\mu\text{m}$  CMOS technology, the magnitudes of the Early voltages of the NMOS and PMOS transistors are  $V_{A_n} = 12.5 \text{ V}$  and  $|V_{A_p}| = 9 \text{ V}$ , respectively.

The folded-cascode amplifier in Fig. B.82 is equivalent to the one in Fig. 6.16, except that a current source is placed in the source of the input transistor  $Q_1$  (for the same dc-biasing purpose as in the case of the CS amplifier). Note that in Fig. B.82, the PMOS current mirror  $Q_3-Q_4$  and the NMOS current mirror  $Q_5-Q_6$  are used to realize, respectively, current sources  $I_1$  and  $I_2$  in the circuit of Fig. 6.16. Furthermore, the current transfer ratio of mirror  $Q_3-Q_4$  is set to 2 (i.e.,  $m_3/m_4 = 2$ ). This results in  $I_{D3} \approx 2I_{\text{ref}}$ . Hence, transistor  $Q_2$  is biased at  $I_{D2} - I_{D3} - I_{D1} = I_{\text{ref}}$ .

**Example MS.7.2** *continued*

The overall dc voltage gain of the folded-cascode amplifier under design can be expressed by using Eq. (6.22) as

$$G_v = -g_{m1}R_{\text{out}}$$

where

$$R_{\text{out}} = R_{\text{out}2} \parallel R_{\text{out}5}$$

is the output resistance of the amplifier. Here,  $R_{\text{out}2}$  is the resistance seen looking into the drain of the cascode transistor  $Q_2$ , while  $R_{\text{out}5}$  is the resistance seen looking into the drain of the current mirror transistor  $Q_5$ . Using Eq. (6.25), we have

$$R_{\text{out}2} \approx (g_{m2}r_{o2})R_{S2}$$

where

$$R_{S2} = (r_{o1} \parallel r_{o3})$$

is the effective resistance at the source of  $Q_2$ . Furthermore,

$$R_{\text{out}5} = r_{o5}$$

Thus, for the folded-cascode amplifier in Fig. B.82,

$$R_{\text{out}} \approx r_{o5}$$

and

$$G_v = -g_{m1}r_{o5} = -2 \frac{V_{A_n}}{V_{OV1}}$$

Therefore, based on the given information, the value of  $V_{OV1}$  can be determined:

$$V_{ov1} = 2 \frac{V_{A_n}}{|G_v|} = 2 \frac{12.5}{100} = 0.25\text{V}$$

The gate bias voltage of transistor  $Q_2$  is generated using the diode-connected transistors  $Q_7$  and  $Q_8$ . The size and drain currents of these transistors are set equal to those of transistor  $Q_2$ . Therefore, ignoring the body effect,

$$V_{G,2} = V_{DD} - V_{SG,7} - V_{SG,8} = V_{DD} - 2(|V_{tp}| + |V_{OV,P}|)$$

where  $V_{OV,P}$  is the overdrive voltage of the PMOS transistors in the amplifier circuit. Thus, such a biasing configuration results in  $V_{SG,2} = |V_{tp}| + |V_{OV,P}| = 0.5 + 0.25 = 0.75\text{V}$  as desired, while setting  $V_{SD,3} = |V_{tp}| + |V_{OV,P}| = 0.75\text{V}$  to improve the bias matching between  $Q_3$  and  $Q_4$ . For this example, all transistors are sized for an overdrive voltage of 0.25 V. Also, to simplify the design procedure, we ignore the channel-length modulation effect. As a result, using unit-size NMOS transistors with  $W_n/L_n = 0.48 \mu\text{m}/0.2 \mu\text{m}$ , and unit-size PMOS transistors with  $W_p/L_p = 0.64 \mu\text{m}/0.2 \mu\text{m}$ , the corresponding multiplicative factor  $m$  for each transistor can be calculated by rounding to the nearest integer the value of  $m$ :

$$m = \frac{I_D}{\frac{1}{2}k' \left( \frac{W}{L_{\text{eff}}} \right) V_{ov}^2}$$

Table B.20 summarizes the relevant design information and the calculated  $m$  values for each transistor.

**Table B.20** Transistor Sizes

Transistor	$I_D$ ( $\mu\text{A}$ )	$V_{ov}$ (V)	$W$ ( $\mu\text{m}$ )	$L_{eff}$ ( $\mu\text{m}$ )	$K$ ( $\mu\text{A}/\text{V}^2$ )	$m$
1	100	0.25	0.48	0.18	246.2	5
2	100	0.25	0.64	0.18	86.1	10
3	200	0.25	0.64	0.18	86.1	20
4	100	0.25	0.64	0.18	86.1	10
5	100	0.25	0.48	0.18	246.2	5
6	100	0.25	0.48	0.18	246.2	5
7	100	0.25	0.64	0.18	86.1	10
8	100	0.25	0.64	0.18	86.1	10

### Simulation

**Verifying  $G_v$**  Now our design can be verified by reading probes or conducting transient response analysis, as set up in Ch7\_Folded\_Cascode\_Ex.ms10. Based on the simulation results,  $|G_v| = 102 \text{ V/V}$  (Fig B.83) and  $I_{D1} = I_{D2} = 100 \mu\text{A}$ . Therefore, the simulation results confirm that the designed folded-cascode amplifier meets the specifications.

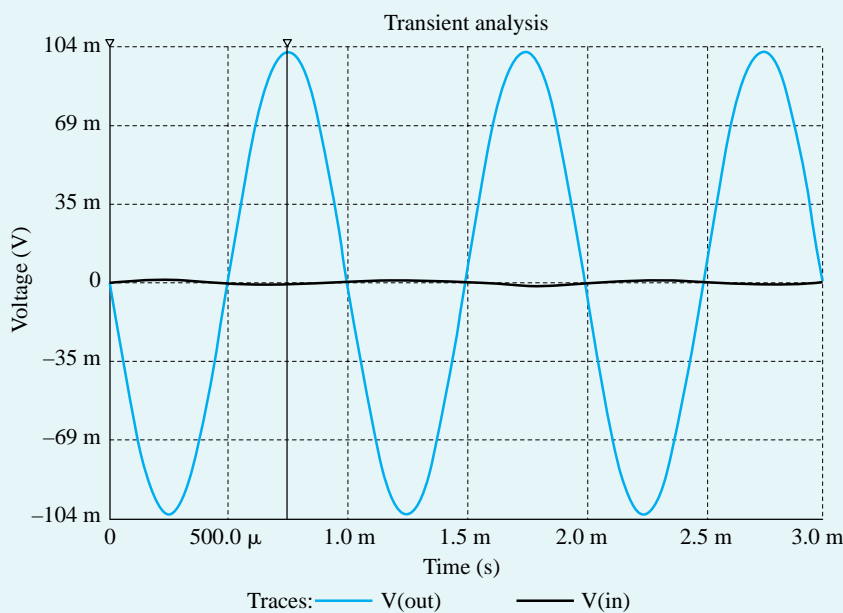


**Figure B.83**  $G_v$  of the folded-cascode amplifier (transient analysis).

**Sensitivity to Channel Length Modulation** In the hand design of this example, the channel-length modulation effect was ignored (except for the role of  $r_{o5}$  in determining the gain). However, the simulation took the finite  $r_o$  of each transistor into account. Furthermore, one can investigate the effect of changes in the Early voltages by modifying the value of lambda for each transistor in the design.

### Example MS.8.1

#### The Two-Stage CMOS Op Amp

In this example, we will design the two-stage CMOS op amp whose schematic capture is shown in Fig. B.84. Once designed, the circuit's characteristics, such as the input common-mode range, the common-mode rejection ratio, the output-voltage range, and the input offset voltage will be evaluated.

The first stage is differential pair  $Q_1-Q_2$  (which is actively loaded with the current mirror formed by  $Q_3$  and  $Q_4$ ), with bias current supplied by the current mirror formed by  $Q_8$ , and  $Q_5$ , which utilizes the reference bias current  $I_{\text{REF}}$ . The second stage consists of  $Q_6$ , which is a common-source amplifier actively loaded with the current source transistor  $Q_7$ .

For the design of this CMOS op amp, we will assume a 0.18- $\mu\text{m}$  CMOS technology for the MOSFETs and use typical SPICE level-1 model parameters for this technology, excluding the intrinsic capacitance values. We will begin with an approximate hand-analysis design. We will then use Multisim to verify that the implemented circuit meets the specifications. The targeted specifications for this op amp are a dc open-loop voltage gain  $|A_v| = 2500 \text{ V/V}$ , with each of transistors  $Q_1$ ,  $Q_2$ ,  $Q_3$ , and  $Q_4$  conducting a drain current of 100  $\mu\text{A}$ .

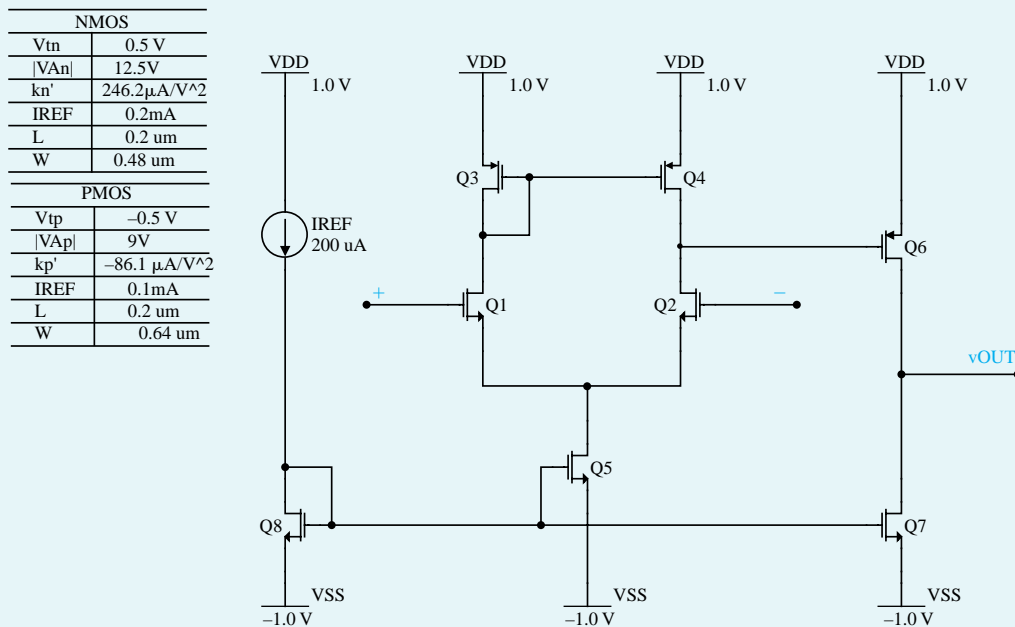


**Figure B.84** Schematic capture of the two-stage CMOS op amp.

To achieve the targeted specifications, a biasing current  $I_{\text{REF}} = 200 \mu\text{A}$  is used, and the transistors  $Q_5$ ,  $Q_6$ ,  $Q_7$ , and  $Q_8$  will be sized so that they conduct the drain current of 200  $\mu\text{A}$ . Also, the open-loop voltage gain for this design is the product of the voltage gains of the two stages. Accordingly, each stage is designed to contribute a voltage gain of -50 V/V, so as to achieve the specified open-loop voltage gain.

The amplifier specifications are summarized in Table B.21.

**Table B.21** Two-Stage CMOS Op-Amp Specifications

Parameter	Value
$I_{(Q1, Q2, Q3, \text{ and } Q4)}$	100 $\mu\text{A}$
$I_{(Q5, Q6, Q7, \text{ and } Q8)}$	200 $\mu\text{A}$
$ A_1 $	50 V/V
$ A_2 $	50 V/V
$V_{DD}$	1 V
$V_{SS}$	-1 V

**Hand Design** For the design of this amplifier we choose  $L = 0.200 \mu\text{m}$ , so we have  $L_{\text{eff}} = 0.180 \mu\text{m}$ . For this channel length, and in 0.18- $\mu\text{m}$  CMOS technology, the magnitudes of the Early voltages of the NMOS and PMOS transistors are  $V_{An} = 12.5 \text{ V}$  and  $|V_{Ap}| = 9 \text{ V}$ .

The two-stage CMOS op amp in Fig. B.84 is equivalent to the one in Fig. 7.41, except that the first stage is an NMOS differential amplifier and the second stage is a PMOS common source. Note that the differential voltage gain of the first stage can be expressed using Eq. (7.176) as:

$$A_1 = -g_{m1}(r_{o2} \parallel r_{o4})$$

Hence,

$$A_1 = -\frac{2}{V_{OV1}} \left( \frac{V_{An}|V_{Ap}|}{V_{An} + |V_{Ap}|} \right)$$

resulting in

$$V_{OV1} = -\frac{2}{A_1} \left( \frac{V_{An}|V_{Ap}|}{V_{An} + |V_{Ap}|} \right) = -\frac{2}{(-50)} \left( \frac{12.5 \times 9}{12.5 + 9} \right) \simeq 0.21 \text{ V}$$

Also, the voltage gain of the second stage is provided by Eq. (7.177) as

$$A_2 = -g_{m6}(r_{o6} \parallel r_{o7})$$

Therefore,

$$A_2 = -\frac{2}{V_{OV6}} \left( \frac{V_{An}|V_{Ap}|}{V_{An} + |V_{Ap}|} \right)$$

resulting in

$$V_{OV6} = -\frac{2}{A_2} \left( \frac{V_{An}|V_{Ap}|}{V_{An} + |V_{Ap}|} \right) = -\frac{2}{(-50)} \left( \frac{12.5 \times 9}{12.5 + 9} \right) \simeq 0.21 \text{ V}$$

For this example, all transistors are sized for an overdrive voltage of 0.21 V. Furthermore, to simplify the design procedure, we ignore the channel-length modulation effect. As a result, using unit-size NMOS transistors with  $W_n/L_n = 0.64 \mu\text{m}/0.2 \mu\text{m}$ , and unit-size PMOS transistors with  $W_n/L_n = 0.48 \mu\text{m}/0.2 \mu\text{m}$ , the corresponding multiplicative factor  $m$  for each transistor can be calculated by rounding to the nearest integer value which is calculated as  $m$ :

$$m = \frac{I_D}{\frac{1}{2} k' \left( \frac{W}{L_{\text{eff}}} \right) V_{OV}^2}$$

Table B.22 summarizes the relevant information and the calculated  $m$  values for each transistor.

**Example MS.8.1** *continued*

**Table B.22** Transistor Sizes

Transistor	$I_D$ ( $\mu\text{A}$ )	$V_{ov}$ (V)	$W$ ( $\mu\text{m}$ )	$L_{eff}$ ( $\mu\text{m}$ )	$k'$ ( $\mu\text{A}/\text{V}^2$ )	$m$
1	100	0.21	0.48	0.18	246.2	7
2	100	0.21	0.48	0.18	246.2	7
3	100	0.21	0.64	0.18	86.1	15
4	100	0.21	0.64	0.18	86.1	15
5	200	0.21	0.48	0.18	246.2	14
6	200	0.21	0.64	0.18	86.1	30
7	200	0.21	0.48	0.18	246.2	14
8	200	0.21	0.48	0.18	246.2	14

### Simulation

**Verifying  $A_v$ .** Now our design can be verified by reading probes, as set up in Ch8\_Two\_Stage\_Op\_Amp\_Ex.ms10. Based on the simulation results we read  $|A_1| = 57 \text{ V/V}$ ,  $|A_2| = 58.6 \text{ V/V}$ ,  $|A_v| = 3340 \text{ V/V}$ ,  $I_{(Q1, Q2, Q3, \text{ and } Q4)} = 97 \mu\text{A}$ ,  $I_{Q5} = 194 \mu\text{A}$ ,  $I_{(Q6, Q7)} = 202 \mu\text{A}$ , and  $I_{Q8} = 200 \mu\text{A}$ . These values are somewhat different from the targeted specifications. The deviations can be attributed to the fact that we rounded the values of  $m$  to the nearest integer and ignored the effect of channel-length modulation, that is, the term  $(1 + \lambda V_{DS})$ , when calculating the multiplicative factor. To get closer to our targeted specifications, we may use the obtained  $V_{DS}$  values for each transistor, from the original design, to estimate new multiplicative factor values by taking the term  $(1 + \lambda V_{DS})$  into account. Table B.23 shows the revised multiplicative factor values.

**Table B.23** Revised Transistor Multiplicative Factors

Transistor	$m$
1	6
2	6
3	14
4	14
5	13
6	26
7	13
8	13

The revised design is evaluated by reading probes, as set up in Ch8\_Two\_Stage\_Op\_Amp\_revised\_Ex.ms10. The simulation results show  $|A_1| = 54 \text{ V/V}$ ,  $|A_2| = 58.2 \text{ V/V}$ ,  $|A_v| = 3145 \text{ V/V}$ ,  $I_{(Q1, Q2, Q3, \text{ and } Q4)} = 103 \mu\text{A}$ ,  $I_{Q5} = 206 \mu\text{A}$ ,  $I_{(Q6, Q7)} = 205 \mu\text{A}$ , and  $I_{Q8} = 200 \mu\text{A}$ , from which we see that the voltage gains are closer to the targeted specifications.

One should note that the discrepancies between the hand-design and simulation results in this simulation example are more apparent because errors in each stage add up.

Next, we will explore some important characteristics of the designed two-stage CMOS op amp.

**Input Common-Mode Range** The upper limit of the input common-mode range is the value of input voltage at which  $Q_1$  and  $Q_2$  leave the saturation region. This occurs when the input voltage exceeds

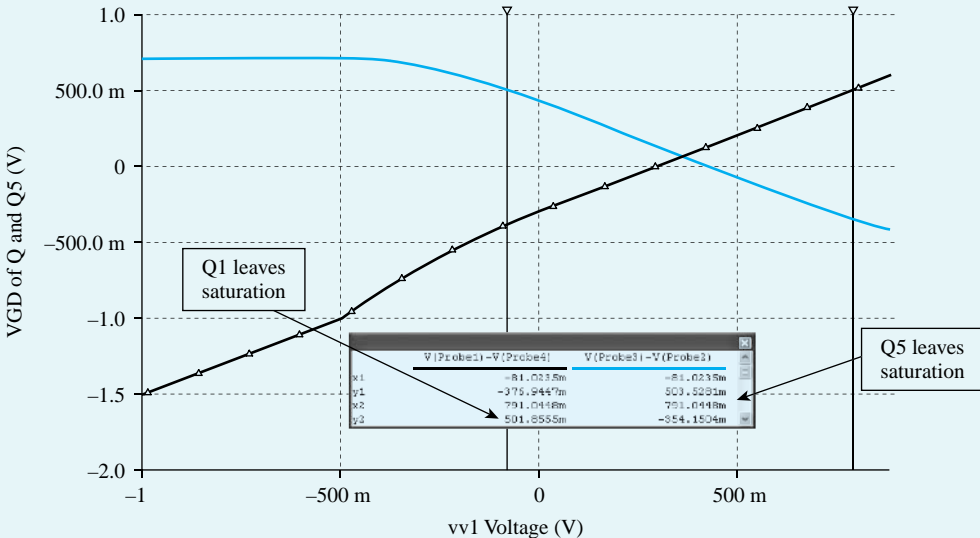


**Figure B.85** Input common-mode range of the two-stage CMOS op amp.

the drain voltage of  $Q_1$  by  $V_m = 0.5$  V. Since the drain of  $Q_1$  is at  $1 - (0.21 + 0.5) = 0.29$  V, then the upper limit of the input common-mode range is  $v_{ICM\max} = 0.29 + 0.5 = 0.79$  V.

The lower limit of the input common-mode range is the value of input voltage at which  $Q_5$  leaves the saturation region. Since for  $Q_5$  to operate in saturation the voltage across it (i.e.,  $V_{DSS}$ ) should at least be equal to the overdrive voltage at which it is operating (i.e., 0.21 V), the highest voltage permitted at the drain of  $Q_5$  should be -0.79 V. It follows that the lowest value of  $v_{ICM}$  should be  $v_{ICM\min} = -0.08$  V.

To verify the results using the simulation tool, we swept the input common-mode voltage  $v_{ICM}$  from -1 V to 1 V and plotted the resulting  $v_{GD}$  of  $Q_1$  and  $Q_5$  (as set up in Ch8\_Two\_Stage\_Op\_Amp\_Ex\_CM\_Range.ms10). As can be seen from Fig. B.85, both transistors  $Q_1$  and  $Q_5$  stay in saturation for the input common-mode range of  $-0.08 \leq v_{ICM} \leq 0.79$  V, as indicated by cursors.

**Common-Mode Rejection Ratio (CMRR) of the First Stage** The value of the CMRR of the first stage (the active-loaded MOS differential amplifier) is determined from Eq. B.147. Note that the value of  $R_{SS}$  in the provided equation corresponds to the output resistance of  $Q_5$  (i.e.,  $r_{o5}$ ). Thus,

$$\text{CMRR} = \frac{|A_1|}{|A_{cm}|} = \frac{50}{1/2g_{m3}r_{o5}} = 100g_{m3}r_{o5} = 100 \frac{2 \times 100 \times 10^{-6}}{0.21} \frac{12.5}{200 \times 10^{-6}} = 5952.4 = 75.5 \text{ dB}$$

Using the simulation tool, the value of CMRR is calculated by dividing the previously obtained  $A_1$  value (54 V/V) by the common-mode gain of the first stage as measured in Ch8\_Two\_Stage\_Op\_Amp\_Ex\_CMRR.ms10. This yields

$$\text{CMRR} = \frac{|A_1|}{|A_{cm}|} = \frac{54}{78 \times 10^{-3}} = 6923 = 76.8 \text{ dB}$$

**Output Voltage Range** The lowest allowable output voltage is the value at which  $Q_7$  leaves the saturation region, which is  $-V_{SS} + V_{OV7} = -1 + 0.21 = 0.79$  V. The highest allowable output voltage is the value at which  $Q_6$  leaves saturation, which is  $V_{DD} - |V_{OV6}| = 1 - 0.21 = 0.79$  V. Thus, the output-voltage range is -0.79 V to 0.79 V.

As set up in Ch8\_Two\_Stage\_Op\_Amp\_Ex\_Output\_Range.ms10, to verify the calculated output voltage range, we swept the input voltage from -2 mV to 2 mV (we used a small input voltage due to high

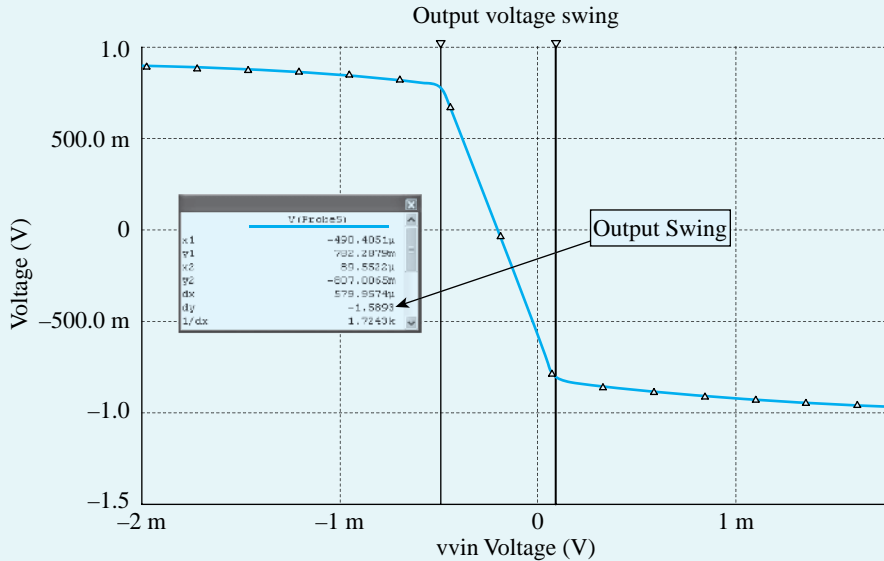
Example MS.8.1 *continued*


Figure B.86 Output-voltage range of the two-stage CMOS op amp.

gain). As can be seen from Fig. B.86, the output level changes from  $-0.795$  V to  $0.784$  V, a rather symmetrical range. Therefore, the simulation results confirm our hand-analysis calculations.

**Input Offset Voltage** Although, theoretically, there should be no systematic offset, we do observe an output offset voltage  $V_o$ . As defined by Eq. 7.102, the input offset voltage,  $V_{os}$ , can be obtained as

$$V_{os} = \frac{V_o}{A_v}$$

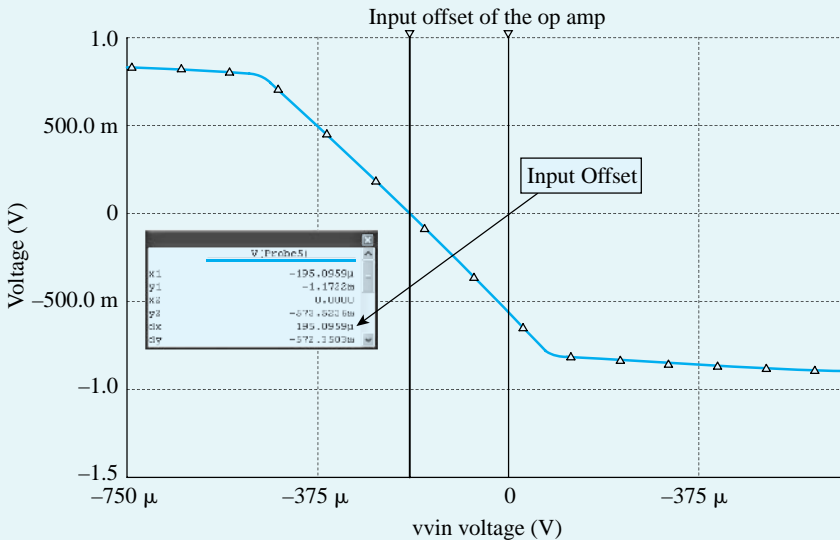


Figure B.87 Input offset voltage of the two-stage CMOS op amp.

Equivalently, if we apply a voltage  $-V_{os}$  between the input terminals of the differential amplifier, the output voltage should be reduced to zero. This equivalency can be verified using the simulation tool (Ch8\_Two\_Stage\_Op\_Amp\_Ex\_Output\_Range.ms10). When both the input terminals are grounded, the probe at the output reads the dc voltage 0.574 V. Also, when we apply the voltage  $V_{os} = (0.574/3145) \approx 183 \mu\text{V}$ , between the input terminals, the output voltage is reduced to zero (Fig. B.87). Hence, the op amp has an input offset voltage of  $V_{os} = 195 \mu\text{V}$ , which approximately corresponds to an output offset voltage of  $V_o = 0.574 \text{ V}$ .

### Example MS.9.1

#### Frequency Response of the Discrete CS Amplifier

In this example, we will investigate the frequency response of the CS amplifier of Example MS.5.1. By using Multisim to perform “ac analysis” on the designed CS amplifier, we are able to measure the midband gain  $A_M$  and the 3-dB frequencies  $f_L$  and  $f_H$ , and to plot the output-voltage magnitude (in dB) versus frequency. Figure B.88 shows the schematic capture of the CS amplifier.

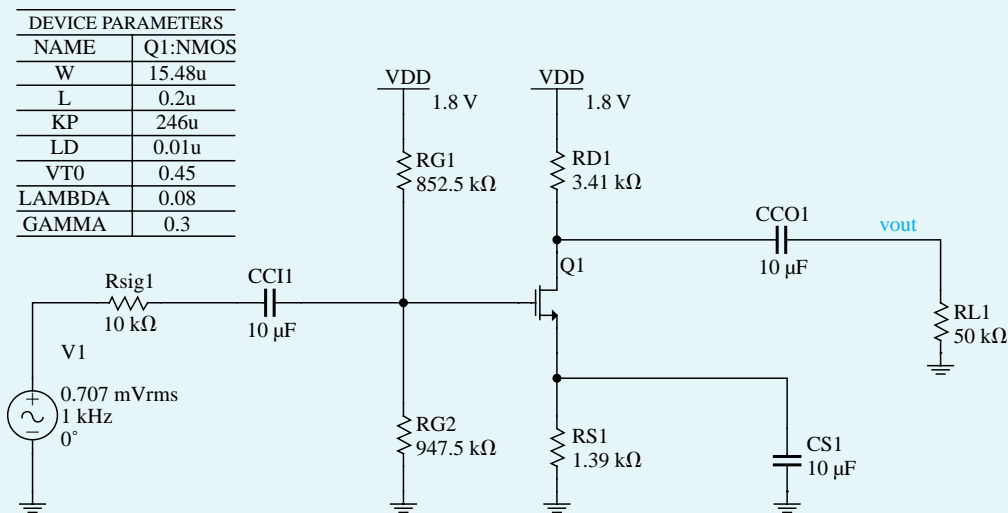


**Figure B.88** Schematic capture of discrete CS amplifier.

#### Hand Analysis

**Midband Gain** The midband gain of this CS amplifier can be determined using Eq. (8.9) as follows:

$$A_M = \frac{R_{in}}{R_{in} + R_{sig}} [g_m(R_D || R_L)]$$

$$R_{in} = (R_{G1} || R_{G2}) = 852.5 \times 10^3 \parallel 947.5 \times 10^3 = 448.75 \times 10^3 \Omega$$

$$g_m = 3.33 \text{ mA/V}$$

$$A_M = \frac{448.75 \times 10^3}{448.75 \times 10^3 + 10 \times 10^3} [3.33 \times 10^{-3} (3.41 \times 10^3 \parallel 50 \times 10^3)] \approx 10 \text{ V/V}$$

**Example MS.9.1** *continued*

**Low-Frequency Poles and Zero** We know from Section 8.1.1 that the low-frequency poles are as follows:

$$f_{P1} = \frac{1}{2\pi \times C_{CI}(R_{\text{sig}} + R_{\text{in}})} = \frac{1}{2\pi \times 10 \times 10^{-6}[(10 \times 10^3) + 448.75 \times 10^3]} \\ f_{P1} = 0.0347 \text{ Hz}$$

$$f_{P2} = \frac{1}{2\pi \times C_{CO}(R_D + R_L)} = \frac{1}{2\pi \times 10 \times 10^{-6}(3.41 \times 10^3) + (50 \times 10^3)} \\ f_{P2} = 0.30 \text{ Hz}$$

$$f_{P3} = \frac{1}{2\pi \times C_S} \left( g_m + \frac{1}{R_S} \right) = \frac{1}{2\pi \times 10 \times 10^{-6}} \left[ (3.33 \times 10^{-3}) + \frac{1}{1.39 \times 10^3} \right] \\ f_{P3} = 64.4 \text{ Hz}$$

And the location of the real transmission zero is determined as

$$f_Z = \frac{1}{2\pi \times C_S R_S} = \frac{1}{2\pi \times (10 \times 10^{-6})(1.39 \times 10^3)} \\ f_Z = 11.45 \text{ Hz}$$

Upon observing the relative magnitude of each of the poles, we can conclude that  $f_{P3}$  will determine  $f_L$ , the lower 3-dB frequency of the amplifier gain,

$$f_L \approx f_{P3} \approx 11.45 \text{ Hz}$$

**High-Frequency Rolloff** The high-frequency rolloff of the amplifier gain is caused by the MOSFET internal capacitance. The typical values for 0.180  $\mu\text{m}$  CMOS technology are given in Table B.4. We know from Eq. (8.54) in Section 8.3.1 that

$$f_H = \frac{1}{2\pi \times C_{\text{in}} R'_{\text{sig}}} \\ R'_{\text{sig}} = 10 \times 10^3 \| 448.75 \times 10^3 = 9.78 \times 10^3 \\ C_{\text{in}} = W \{ C_{gs0} + C_{gd0}[1 + g_m(R_L \| R_L)] \}$$

Note that  $C_{gs0}$  and  $C_{gd0}$  are per-unit-width values provided in the models.

$$C_{\text{in}} = (15.48 \times 10^{-6}) \times (0.3665 \times 10^{-9}) \times [1 + 1 + 3.33 \times 10^{-3} (50 \times 10^3 \| 3.41 \times 10^{-3})] \\ C_{\text{in}} = 0.716 \text{ fF}$$

$$f_H = \frac{1}{2\pi \times 0.716 \times 10^{-15} \times 9.78 \times 10^3} \\ f_H \approx 191 \text{ MHz}$$

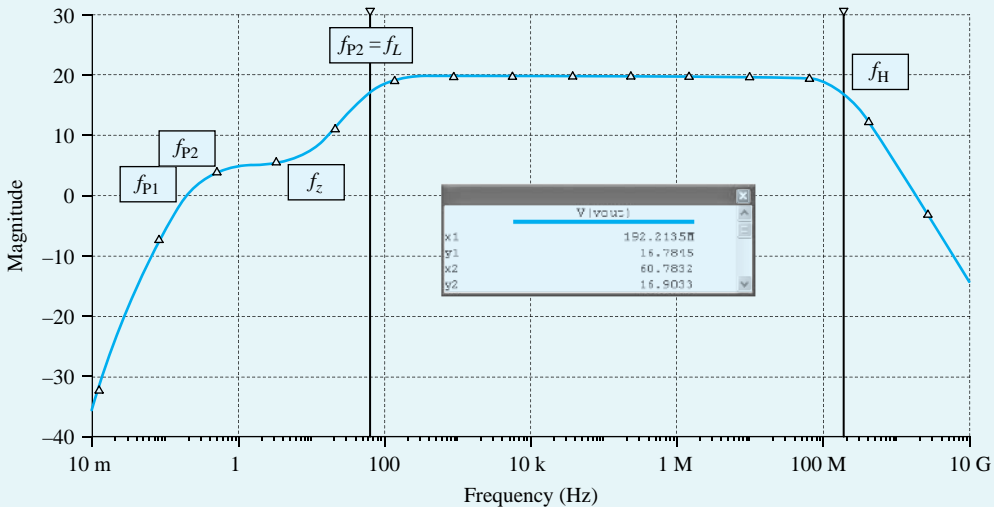
Now we can determine the bandwidth,  $BW$ , of the CS amplifier:

$$BW = f_H - f_L \\ BW \approx f_H = 191 \text{ MHz}$$

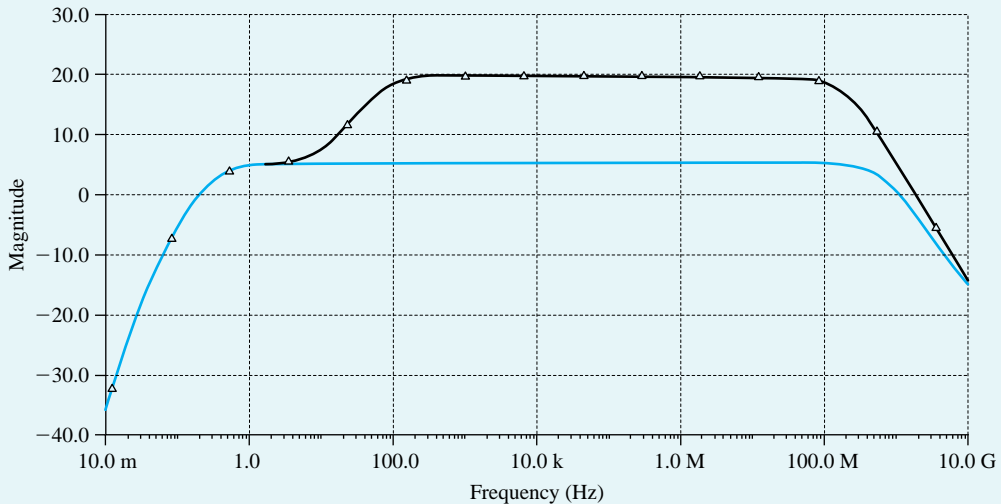
### Simulation

Figure B.89 shows the magnitude plot of the frequency response of this CS amplifier.

Based on the simulation results, the midband gain is  $A_M = 9.80 \text{ V/V}$ . Also,  $f_L = 60.8 \text{ Hz}$  and  $f_H = 192.2 \text{ MHz}$ , resulting in 3-dB bandwidth of  $BW = f_H - f_L = 192.2 \text{ MHz}$ . Figure B.89 further shows that



**Figure B.89** Frequency response of the CS amplifier.



**Figure B.90** Frequency response of the CS amplifier with  $C_s = 10 \mu\text{F}$  and  $C_o = 0$ .

(moving toward the left) the gain begins to fall off at about 300 Hz, but flattens out again at about 12.2 Hz. This flattening in the gain at low frequencies is due to a real transmission zero introduced in the transfer function of the amplifier by  $R_s$  together with  $C_s$ , with a frequency  $f_z = 1/2\pi R_s C_s = 11.45 \text{ Hz}$ . Students are encouraged to investigate this relationship by using the simulation tool to modify the values of  $R_s$  and  $C_s$  and observing the corresponding change in the zero frequency. Note this value of zero is typically between the break frequencies  $f_{P2}$  and  $f_{P3}$ . The simulation is set up in Ch9\_CS\_Amplifier\_Ex.ms10.

We can further verify this phenomenon by resimulating the CS amplifier with a  $C_s = 0$  (i.e., removing  $C_s$ ) in order to move  $f_z$  to infinity and remove its effect. The corresponding frequency response is plotted in Fig. B.90. As expected with  $C_s = 0$ , we do not observe any flattening in the low-frequency response of the amplifier. However, because the CS amplifier now includes a source resistor  $R_s$ , the value of  $A_M$  has dropped by a factor of 5.4. This factor is approximately equal to  $(1 + g_m R_s)$ , as expected from our

**Example MS.9.1** *continued*

study of the CS amplifier with a source-degeneration resistance. Note that the bandwidth  $BW$  has increased by approximately the same factor as the drop in gain  $A_M$ . As we learned in Chapter 9 in our study of negative feedback, the source-degeneration resistor  $R_s$  provides negative feedback, which allows us to trade off gain for a wider bandwidth.

**Example MS.9.2**

**The Frequency Response of CMOS CS Amplifier and the Folded-Cascode Amplifier**

In this example, we will investigate the frequency response of the CMOS CS amplifier and the folded-cascode amplifier studied in Examples MS.7.1 and MS.7.2. The circuit diagram of the CMOS CS amplifier is given in Fig. B.91.

By using Multisim to perform “ac analysis” on the designed CMOS CS amplifier, we are able to measure the midband gain  $A_M$  and the 3-dB frequency  $f_H$ , and to plot the output-voltage magnitude (in dB) versus frequency for two different cases of  $R_{\text{sig}}$  ( $100 \Omega$  and  $1 \text{ M}\Omega$ ), as shown in Fig. B.92.

Observe that  $f_H$  decreases when  $R_{\text{sig}}$  is increased. This is anticipated from our study of the high-frequency response of the CS amplifier. Specifically, as  $R_{\text{sig}}$  increases, the pole

$$f_{p,\text{in}} = \frac{1}{2\pi R_{\text{sig}} C_{\text{in}}}$$

formed at the amplifier input will have an increasingly significant effect on the overall frequency response of the amplifier. As a result, the effective time constant  $\tau_H$  increases and  $f_H$  decreases. When  $R_{\text{sig}}$  becomes very large, as it is when  $R_{\text{sig}} = 1 \text{ M}\Omega$ , a dominant pole is formed by  $R_{\text{sig}}$  and  $C_{\text{in}}$ . This results in

$$f_H \approx f_{p,\text{in}}$$

To estimate  $f_{p,\text{in}}$ , we need to calculate the input capacitance  $C_{\text{in}}$  of the amplifier. Using Miller’s theorem, we have

$$C_{\text{in}} = C_{gs1} + C_{gd1}(1 + g_m R'_L)$$

where

$$R'_L = r_{o1} \parallel r_{o2}$$

The value of  $C_{\text{in}}$  can be calculated by using the overlap capacitances  $C_{gs,ov1}$  and gate-to-channel  $C_{gs}$  and  $C_{gd,ov1}$  as follows:

$$C_{gs,ov1} = m_1 W_1 C_{GSO} = (5 \times 0.48 \times 10^{-6}) \times (0.3665 \times 10^{-9}) = 0.880 \text{ fF}$$

$$C_{gd,ov1} = m_1 W_1 C_{GDO} = (5 \times 0.48 \times 10^{-6}) \times (0.3665 \times 10^{-9}) = 0.880 \text{ fF}$$

For  $C_{gs}$ , we write

$$C_{gs\_channel} = \frac{2}{3} m_1 W_1 L C_{ox} = \frac{2}{3} \left[ (5 \times 0.48 \times 10^{-6}) \times (0.18 \times 10^{-6}) \left( \frac{3.9 \times 8.85 \times 10^{-12}}{4.08 \times 10^{-9}} \right) \right]$$

$$C_{gs\_channel} = 2.48 \text{ fF}$$

$$C_{gs} = 2.48 \text{ fF} + 0.880 \text{ fF} = 3.36 \text{ fF}$$

This results in  $C_{\text{in}} = 45.78 \text{ fF}$  when  $|G_v| = 50 \text{ V/V}$ . Accordingly,

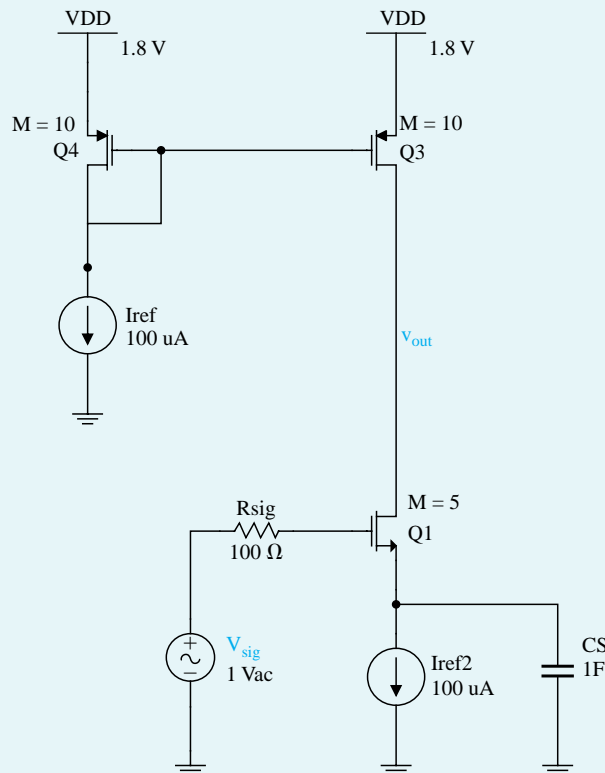
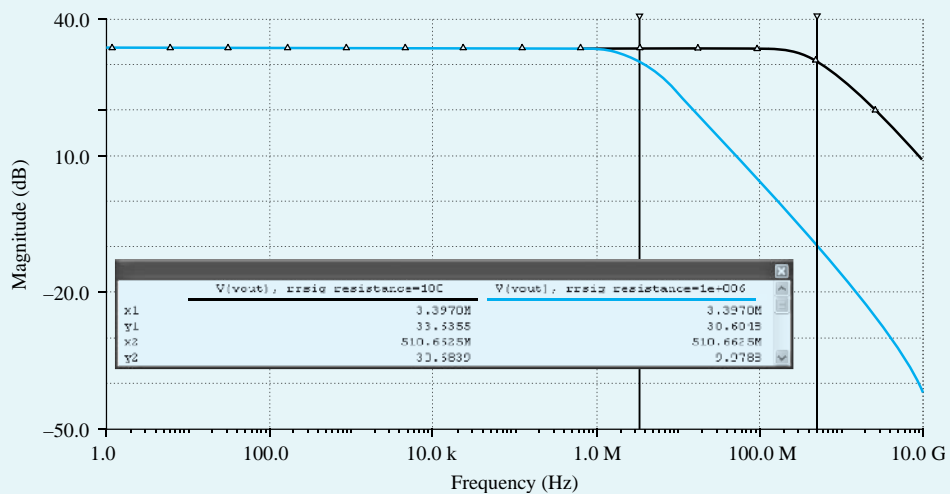
$$f_H \approx \frac{1}{2\pi} \frac{1}{1 \times 10^6 \times 43.3 \times 10^{-15}} = 3.48 \text{ MHz}$$

which is close to the value computed by Multisim (i.e.,  $f_H = 3.66 \text{ MHz}$ ).

NMOS	
V <sub>tn</sub>	0.5 V
V <sub>An</sub>	12.5V
k <sub>n'</sub>	246.2uA/V <sup>2</sup>
I <sub>REF</sub>	0.1mA
L	0.2 um
W	0.48 um

PMOS	
V <sub>tp</sub>	-0.5 V
V <sub>Ap</sub>	9V
k <sub>p'</sub>	-86.1 uA/V <sup>2</sup>
I <sub>REF</sub>	0.1mA
L	0.2 um
W	0.64 um

**Figure B.91** Schematic capture of the CMOS CS amplifier.**Figure B.92** Frequency response of the CMOS CS amplifier with  $R_{\text{sig}} = 100 \Omega$  and  $R_{\text{sig}} = 1 \text{ M}\Omega$ .

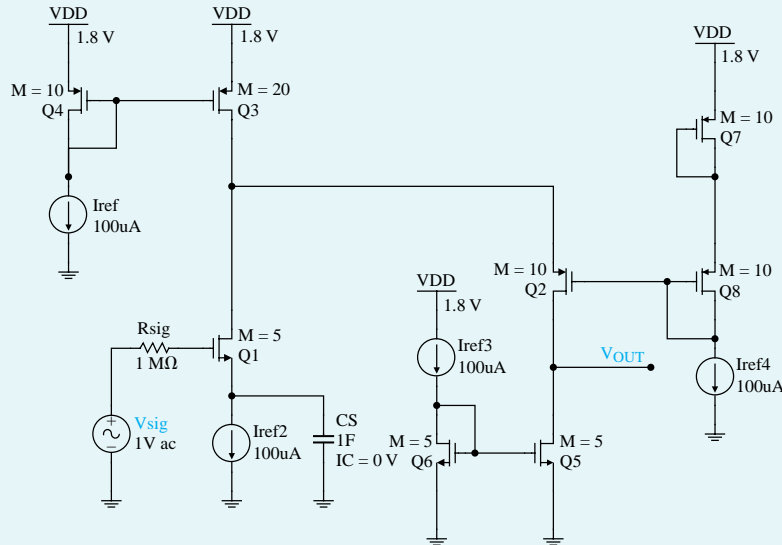
**Example MS.9.2 continued**

**The Folded-Cascode Amplifier** Next, we will investigate the frequency response of the folded-cascode amplifier and compare its performance with that of the CS amplifier. Figure B.93 shows the circuit diagram of the folded-cascode amplifier.

NMOS	
V <sub>tn</sub>	0.5 V
V <sub>An</sub>	12.5 V
k <sub>n</sub> '	246.2 $\mu$ A/V <sup>2</sup>
I <sub>REF</sub>	0.1 mA
L	0.2 $\mu$ m
W	0.48 $\mu$ m

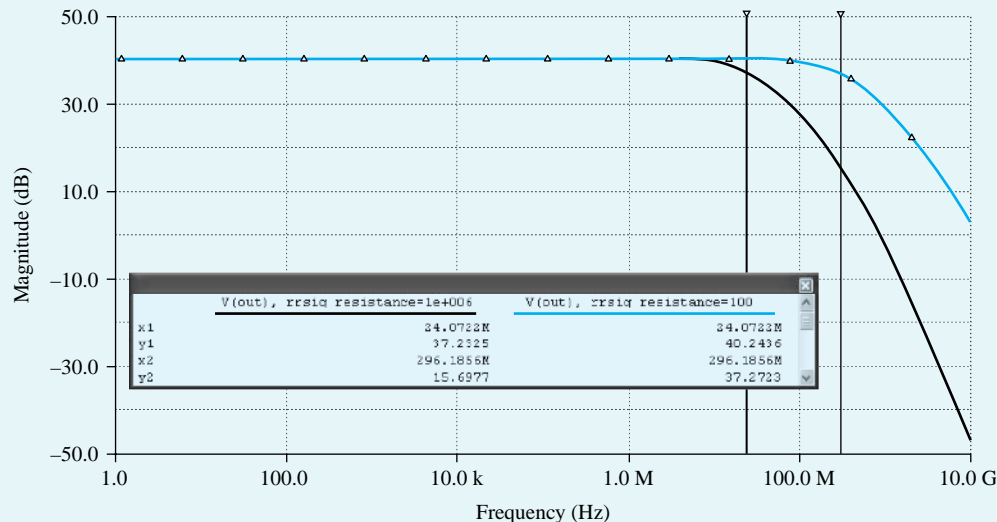
  

PMOS	
V <sub>tp</sub>	-0.5 V
V <sub>Ap</sub>	9 V
k <sub>p</sub> '	-86.1 $\mu$ A/V <sup>2</sup>
I <sub>REF</sub>	0.1 mA
L	0.2 $\mu$ m
W	0.64 $\mu$ m



**Figure B.93** Schematic capture of the Folded-Cascode amplifier.

Figure B.94 shows the frequency response of the folded-cascode amplifier as simulated by Multisim for the cases of  $R_{\text{sig}} = 100\Omega$  and  $1 \text{ M}\Omega$ . The corresponding values of the 3-dB frequency  $f_H$  of the amplifier are given in Table B.24.



**Figure B.94** Frequency response of the folded-cascode amplifier with  $R_{\text{sig}} = 100 \Omega$  and  $R_{\text{sig}} = 1 \text{ M}\Omega$ .

**Table B.24** Dependence of  $f_H$  for the Designed Amplifiers

$R_{sig}$	$f_H$	
	CS Amplifier	Folded-Cascode Amplifier
100 $\Omega$	510.7 MHz	296.2 MHz
1 M $\Omega$	3.39 MHz	24.0 MHz

First, note that for the designed folded-cascode amplifier,  $R_{out} = 125 \text{ k}\Omega$  and  $|G_v| = 100 \text{ V/V}$ . Thus,  $R_{out}$  and  $G_v$  are larger than those of the CS amplifier (by a factor of 2). Note that these calculations can be found in Examples MS.7.1 and MS.7.2.

Also, observe that when  $R_{sig}$  is small,  $f_H$  of the folded-cascode amplifier is lower than that of the CS amplifier by a factor of about 1.8, approximately equal to the factor by which the gain is increased. This is because when  $R_{sig}$  is small, the frequency response of both amplifiers is dominated by the pole formed at the output node, that is,

$$f_H \approx f_{p,out} = \frac{1}{2\pi R_{out} C_{out}}$$

Now the output resistance of the folded-cascode amplifier is larger than that of the CS amplifier, while their output capacitances are approximately equal. Therefore, the folded-cascode amplifier has a lower  $f_H$  in this case.

On the other hand, when  $R_{sig}$  is large,  $f_H$  of the folded-cascode amplifier is much higher than that of the CS amplifier. This is because in this case, the effect of the pole at  $f_{p,in}$  on the overall frequency response of the amplifier becomes dominant. Since, owing to the Miller effect,  $C_{in}$  of the CS amplifier is much larger than that of the folded-cascode amplifier, its  $f_H$  is much lower.

To confirm this point, observe that  $C_{in}$  of the folded-cascode amplifier can be estimated by replacing  $R'_L$  in the equation used to compute  $C_{in}$  for the CS amplifier, with the total resistance  $R_{d1}$ , between the drain of  $Q_1$  and ground. Here,

$$R_{d1} = r_{o1} \parallel r_{o3} \parallel R_{in2}$$

where  $R_{in2}$  is the input resistance of the common-gate transistor  $Q_2$  and can be obtained using an approximation of the relationship found for input resistance of the common-gate amplifier:

$$R_{in2} \approx \frac{r_{o2} + r_{o5}}{g_{m2} r_{o2}}$$

Thus,

$$R_{d1} \approx r_{o1} \parallel r_{o3} \parallel \frac{r_{o2} + r_{o5}}{g_{m2} r_{o2}} = \frac{2}{g_{m2}}$$

Therefore,  $R_{d1}$  is much smaller than  $R'_L$  (in the CS amplifier  $\approx r_{o1} \parallel r_{o3}$ ). Hence,  $C_{in}$  of the designed folded-cascode amplifier is indeed much smaller than that of the CS amplifier because the  $(1 + g_m R')$  multiplier is smaller for the folded-cascode device. This confirms that the folded-cascode amplifier is much less impacted by the Miller effect and, therefore, can achieve a much higher  $f_H$  when  $R_{sig}$  is large.

The midband gain of the folded-cascode amplifier can be significantly increased by replacing the current mirror  $Q_5-Q_6$  with a current mirror having a larger output resistance, such as the cascode current mirror in Fig. 6.32, whose output resistance is approximately  $g_m r_o^2$ . In this case, however,  $R_{in2}$  and, hence,  $R_{d1}$  increase, causing an increased Miller effect and a corresponding reduction in  $f_H$ .

Finally, it is interesting to observe that the frequency response of the folded-cascode amplifier shown in Fig. B.94 drops beyond  $f_H$  at approximately -20 dB/decade when  $R_{sig} = 100 \Omega$  and at approximately -40 dB/decade when  $R_{sig} = 1 \text{ M}\Omega$ . This is because when  $R_{sig}$  is small, the frequency response is dominated by the pole at  $f_{p,out}$ . However, when  $R_{sig}$  is increased,  $f_{p,in}$  is moved closer to  $f_{p,out}$ , and both poles contribute to the gain falloff.

## Example MS.10.1

## A Two-Stage CMOS Op Amp with Series-Shunt Feedback

In this example, we will investigate the effect of applying a series-shunt feedback to the two-stage CMOS op amp whose schematic capture is shown in Fig. B.95.

The first stage is a differential pair  $Q_1$ - $Q_2$  (which is actively loaded with the current mirror formed by  $Q_3$  and  $Q_4$ ) with bias current supplied by a current mirror formed by  $Q_8$  and  $Q_5$ , which utilizes the reference bias current  $I_{\text{REF}}$ . The second stage consists of  $Q_6$ , which is a common-drain amplifier actively loaded with a current source load (transistor  $Q_7$ ).

For the implementation of this CMOS op amp, we will use a  $0.18\text{-}\mu\text{m}$  CMOS technology for the MOSFETs and typical SPICE level-1 model parameters for this technology, including the intrinsic

NMOS	
Vtn	0.5 V
VAn	12.5V
kn'	246.2uA/V^2
L	0.2 um
W	0.48 um
PMOS	
Vtp	-0.5 V
VAp	9V
kp'	-86.1 $\mu$ A/V^2
L	0.2 um
W	0.64 um

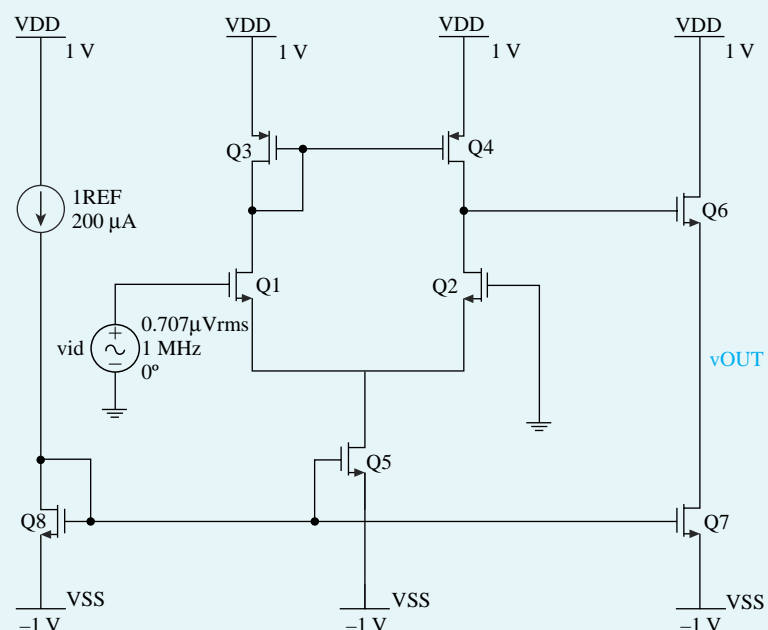


**Figure B.95** Schematic capture of the two-stage CMOS op amp.

capacitance values. The targeted specifications are an unloaded dc open-loop voltage gain  $|A_v| = 50 \text{ V/V}$ , and closed-loop voltage gain  $|A_f| = 10 \text{ V/V}$ , with each of transistors  $Q_1$ ,  $Q_2$ ,  $Q_3$ , and  $Q_4$  biased at a drain current of  $100 \mu\text{A}$ .

To achieve the targeted specifications, a biasing current  $I_{\text{REF}} = 200 \mu\text{A}$  is used, and the transistors  $Q_5$ ,  $Q_6$ ,  $Q_7$ , and  $Q_8$  will be sized to conduct drain currents of  $200 \mu\text{A}$ . The dc open-loop voltage gain for this amplifier is the product of the voltage gains of the two stages. Since the gain of the second stage (source follower) is approximately  $1 \text{ V/V}$ , the first stage must be designed to provide the full voltage gain of  $50 \text{ V/V}$  to achieve the specified open-loop voltage gain.

The amplifier specifications are summarized in Table B.25.

**Table B.25** Two-Stage CMOS Op-Amp Specifications

Parameters	Value
$I_{(Q1, Q2, Q3, \text{ and } Q4)}$	100 $\mu\text{A}$
$I_{(Q5, Q6, Q7, \text{ and } Q8)}$	200 $\mu\text{A}$
$ A_1 $	50 V/V
$ A_2 $	1 V/V
$ A_f $	10 V/V
$V_{DD}$	1 V
$V_{SS}$	-1 V

### Hand Design

**Design of the Two-Stage Op Amp** The first stage of this CMOS op amp is identical to the first stage of the op amp we designed in Example MS.8.1, to which the reader is referred. Also, transistors  $Q_6$  and  $Q_7$  are sized to provide the bias current of 200  $\mu\text{A}$  in the second stage.

As a result, using unit-size NMOS transistors with  $W_n/L_n = 0.48 \mu\text{m}/0.20 \mu\text{m}$ , and unit-size PMOS transistors with  $W_p/L_p = 0.64 \mu\text{m}/0.20 \mu\text{m}$ , the corresponding multiplicative factor  $m$  for each transistor can be calculated as found in Example MS.8.1 (with the difference here that  $Q_6$  and  $Q_7$  have the same dimensions). Table B.26 summarizes the relevant information and the calculated  $m$  values for the transistor.

**Table B.26** Transistor Sizes

Transistor	$I_D$ ( $\mu\text{A}$ )	$m$
1	100	6
2	100	6
3	100	14
4	100	14
5	200	13
6	200	13
7	200	13
8	200	13

**Design of the Feedback Network** First we need to determine the value of the feedback factor  $\beta$  for this series-shunt feedback amplifier. The  $\beta$  network can be implemented using a voltage divider, as shown in Fig. B.96. The resistor values are chosen large enough (in comparison to the output resistance of the designed two-stage op amp) to minimize the effect of loading. Therefore, effectively,

$$A \approx A_v$$

where  $A$  is the open-loop gain of the amplifier (with loading). Now we can calculate the required feedback factor,  $\beta$ , as follows:

$$|A_f| = \frac{A_v}{1 + A_v \beta} = \frac{50}{1 + 50\beta} = 10 \text{V/V}$$

$$\beta = 0.08$$

**Example MS.10.1** *continued*

The resistor values of this voltage divider are selected to provide voltage divisions of 0.08 ( $R_1 = 92 \text{ k}\Omega$  and  $R_2 = 8\text{k}\Omega$ ).

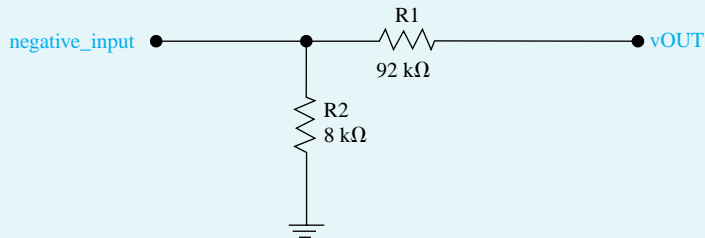


**Figure B.96**  $\beta$  Network.

### Simulation

Now we will simulate our designed circuit to verify our hand design and study the effect of feedback on the dc-gain, bandwidth, and output resistance of the amplifier.

**Verifying  $A_v$**  The schematic capture of the two-stage CMOS amplifier is in Fig. B.95. We can verify the dc voltage gain of this amplifier by performing frequency-response analysis as set up in Ch10\_OpAmp\_Ex\_Av.ms10.

As can be seen from Fig. B.97,  $|A_v| = 35.0 \text{ dB} \approx 56.2 \text{ V/V}$ , which is close to the targeted specification.

**Verifying A** The schematic capture of the A-circuit is given in Fig. B98.

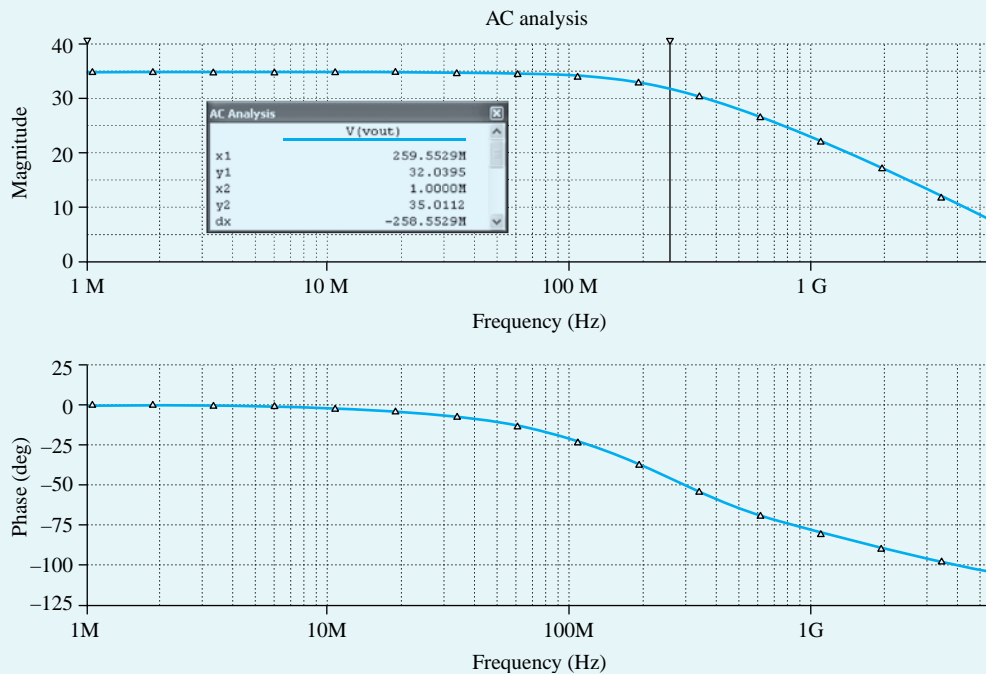


**Figure B.97** Frequency response of the two-stage CMOS op-amp amplifier.

NMOS	
Vtn	0.5 V
VAn	12.5V
kn'	246.2 $\mu$ A/V <sup>2</sup>
L	0.2 um
W	0.48 um
PMOS	
Vtp	-0.5 V
VAp	9V
kp'	-86.1 uA/V <sup>2</sup>
L	0.2 um
W	0.64 um

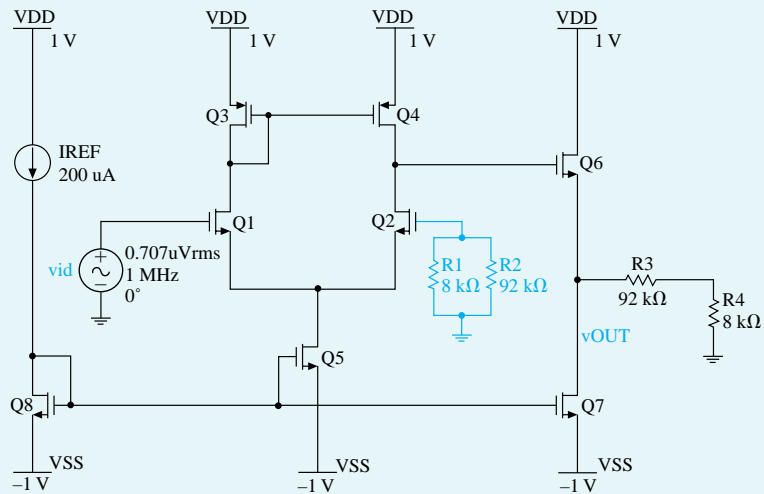


Figure B.98 Schematic capture of the A circuit.

We can verify the open-loop voltage gain of this circuit by performing a frequency-response analysis as set up in Ch10\_OpAmp\_Ex\_A.ms10. As can be seen from Fig. B.99,  $|A| = 34.9 \text{ dB} \approx 55.6 \text{ V/V}$ , which is close to the value of  $A_v$ . This supports our assumption of  $A \approx A_v$ .

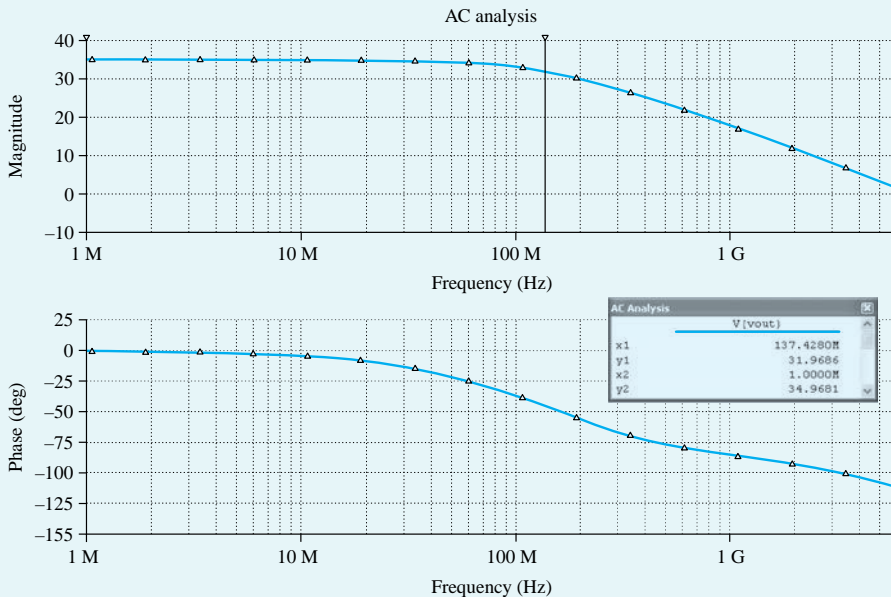
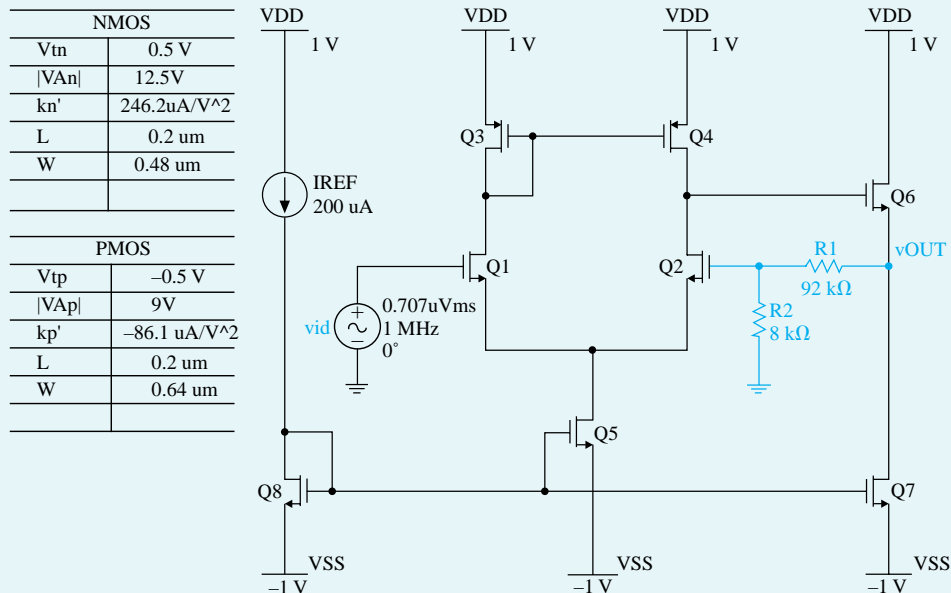


Figure B.99 Schematic capture of the A- circuit.

**Verifying  $A_f$**  The schematic capture of the closed-loop circuit is given in Fig. B.100. As can be seen from this schematic, the  $\beta$ -network establishes a series connection at the input and a shunt connection at the output of the original two-stage CMOS op amp.

**Example MS.10.1** *continued*

We can verify the closed-loop voltage gain by performing a frequency-response analysis as set up in Ch10\_OpAmp\_Ex\_Af.ms10. As can be seen from Fig. B.101,  $|A_f| = 20.2 \text{ dB} \approx 10.2 \text{ V/V}$ , which is close to the targeted specification for  $A_f$ .



**Figure B.100** Schematic capture of the closed-loop circuit.

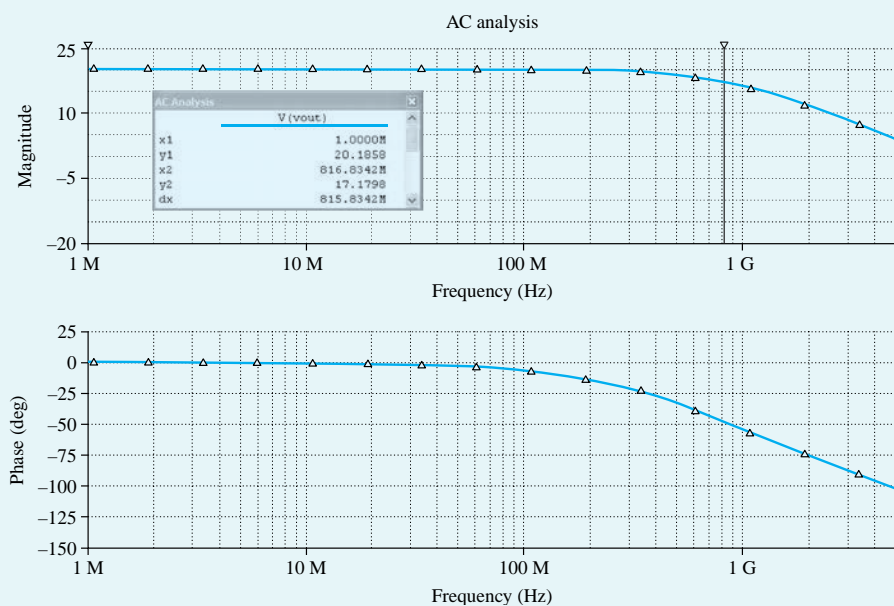


**Figure B.101** Frequency response of the closed-loop circuit.

**Investigating the Effect of Feedback** In addition to the frequency-response analysis, which provided information on the dc voltage gain and the 3-dB bandwidth, we used Multisim to find the output resistances of the open-loop and closed-loop circuits (as set up in Ch10\_OpAmp\_Ex\_A.ms10 and Ch10\_OpAmp\_Ex\_Af.ms10). Table B.27 summarizes our findings for open-loop ( $A$  circuit) and closed-loop circuits.

**Table B.27** Effect of Feedback on Gain, 3-dB Bandwidth, and Output Resistor

Circuit	Gain (V/V)	3-dB Bandwidth (MHz)	$R_{\text{out}}$ ( $\Omega$ )
Open loop	55.6	137	492.6
Closed loop	10.2	816	89.3

It can be seen from Table B.27 that the series-shunt feedback connection causes the dc voltage gain and the output resistance of the circuit to decrease by a factor of 5.5, while the 3-dB bandwidth increases by approximately the same factor. This factor is equal to  $1 + A\beta$ , the amount of the feedback. This is as expected and corresponds to what we learned in Chapter 9.

## Example MS.11.1

### Class B Bipolar Output Stage

In this example, we will design a class B output stage to deliver an average power of 20 W to an 8- $\Omega$  load. The schematic capture of a class B output stage implemented using BJTs is shown in Fig. B.102. We then will investigate various characteristics of the designed circuit such as crossover distortion and power-conversion efficiency. For this design, we are to select  $V_{CC}$  about 5 V greater than the peak output voltage in order to avoid transistor saturation and signal distortion.

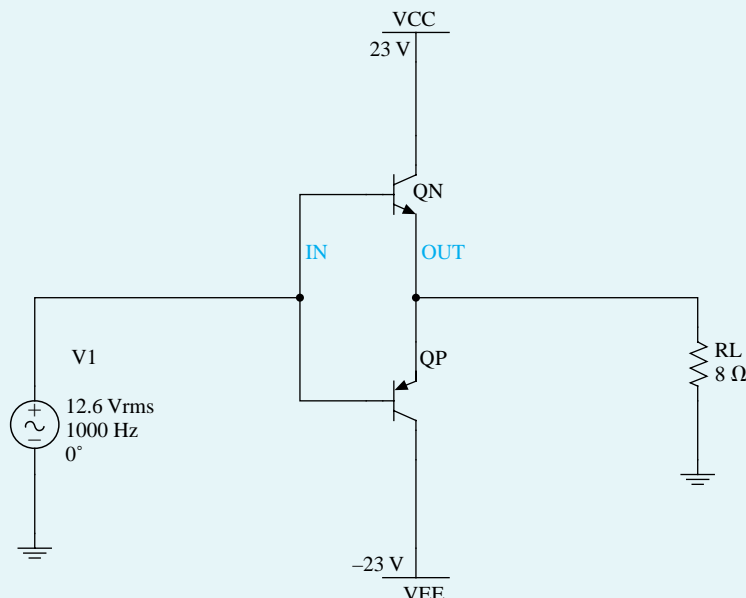


**Figure B.102** Schematic capture of class B output stage.

**Example MS.11.1** *continued*

The circuit specifications are summarized in Table B.28.

**Table B.28** Class B Output Stage Specifications

Specification	Value
$P_L$	20 W
$R_L$	$8\Omega$
$V_{cc}$	$\hat{V} + 5$ V

### Hand Design

We know from Eq. (13.12) that

$$P_L = \frac{1}{2} \frac{\hat{V}^2}{R_L}$$

Thus

$$\begin{aligned} V &= \sqrt{2P_L R_L} = \sqrt{2 \times 20 \times 8} \\ V &= 17.9 \text{ V} \end{aligned}$$

which leads to  $V_{cc} = 23$  V.

The peak current drawn from the supply will be

$$\begin{aligned} I_o &= \frac{\hat{V}}{R_L} = \frac{17.9}{8} \\ I_o &= 2.24 \text{ A} \end{aligned}$$

Now we can use Eq. (13.13) to calculate the average power drawn from each of the supplies

$$\begin{aligned} P_{S+} &= P_{S-} = \frac{1}{\pi} \frac{\hat{V}}{R_L} V_{cc} = \frac{1}{\pi} \times 2.24 \times 23 \\ P_{S+} &= P_{S-} = 16.4 \text{ W} \\ P_S &= P_{S+} + P_{S-} = 16.4 + 16.4 = 32.8 \text{ W} \end{aligned}$$

Therefore, the power-conversion efficiency,  $\eta$ , is

$$\eta = \frac{P_L}{P_S} \times 100\% = \frac{17.9}{32.8} \times 100\% = 61\%$$

Now we can utilize Eq. (13.22) to calculate the maximum power dissipated in each of the transistors as

$$\begin{aligned} P_{DNmax} &= P_{DPmax} = \frac{V_{cc}^2}{\pi^2 R_L} = \frac{(23)^2}{\pi^2 \times 8} \\ P_{DNmax} &= P_{DPmax} = 6.7 \text{ W} \end{aligned}$$

### Simulation

Next, we use Multisim to verify the operation of the class B output stage designed above. For simulation purposes, we will use discrete-power transistors MJE243 and MJE253 (from ON Semiconductor), which are rated for a maximum continuous collector current  $I_{Cmax} = 4$  A and a maximum collector-emitter voltage  $V_{CEmax}$  of 100 V.

**Load Power  $P_L$**  To measure the amount of power delivered to the load, we will utilize Transient Analysis in Multisim as set up in Ch11\_Class\_B\_Ex.ms10. The transient analysis simulation is performed over the interval 0 ms to 2 ms, and the waveforms of the voltage at the output node and the output current are plotted in Fig. B.103.

As can be seen in Fig. B.103, the peak voltage amplitude is approximately 16.9 V and the peak current amplitude is 2.1 A. Upon a closer look at the current and voltage waveforms, we can observe that both exhibit crossover distortion. The bottom graph in Fig. B.103 shows the instantaneous and the

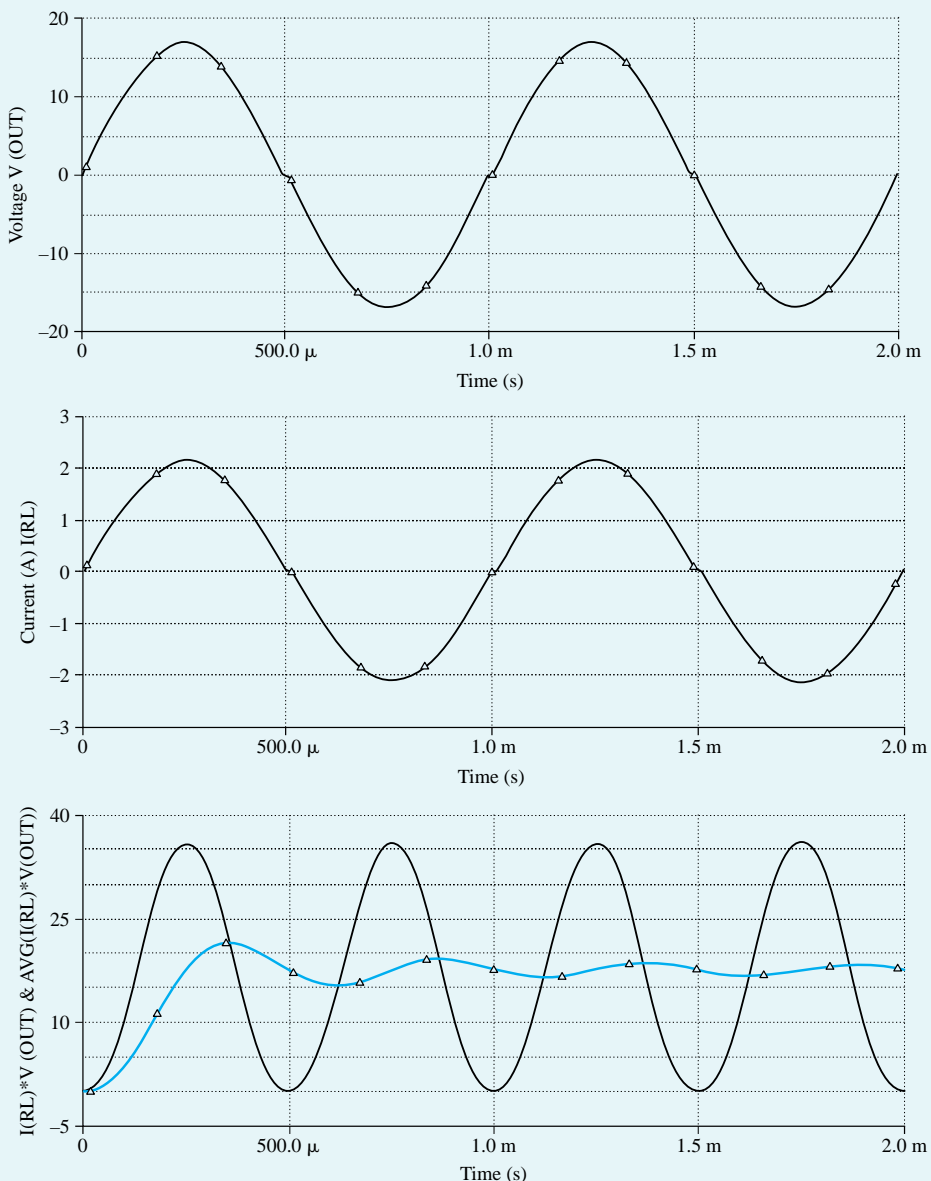


**Figure B.103** Load voltage, current, and instantaneous and average load power.

**Example MS.11.1** *continued*

average power dissipated in the load resistance. These waveforms were obtained by multiplying the current and voltage waveforms, and by taking the running average for the average power,  $P_L$ . The transient behavior of average power eventually settles into a quasiconstant steady-state value of 17.6 W.

**Supply Power,  $P_s$**  Similarly, we can plot instantaneous voltage and current at the  $V_{CC}$  and  $V_{EE}$  nodes to measure the value of  $P_s$ . Figure B.104 shows the voltage, current, instantaneous, and average power for  $+V_{CC}$ . We can plot these quantities for  $-V_{EE}$  as well. However, owing to symmetry, we do not need to generate plots for the negative voltage supply. The average power provided by  $+V_{CC}$ ,  $P_{s+}$ , is 15 W. Therefore, the total power provided by both voltage supplies is 30 W.

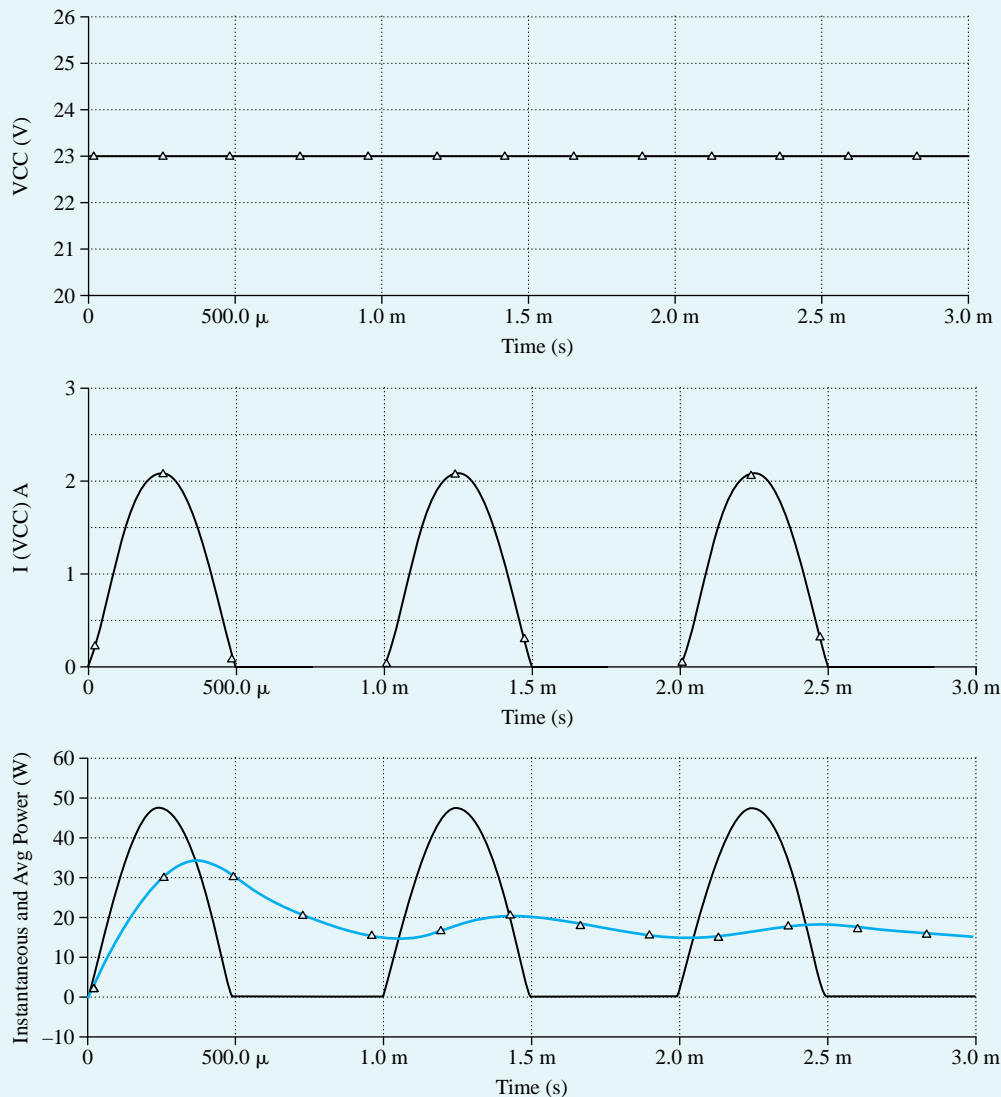


**Figure B.104** Supply voltage, current, and instantaneous and average supply power.

**Power-Conversion Efficiency,  $\eta$**  Now we can calculate the power-conversion efficiency of the simulated circuit as follows.

$$\eta = \frac{P_L}{P_S} \times 100\% = \frac{17.6}{30} \times 100\% = 58.6\%$$

**Transistor Power Dissipation,  $P_D$**  Figure B.103 shows voltage, current, instantaneous and average power plots for  $Q_p$  only. A similar plot can be obtained for  $Q_n$  to measure the power dissipated in the *npn* device. As expected, the voltage waveform is a sinusoid, and the current waveform consists of half-sinusoids. The waveform of instantaneous power is rather unusual. It indicates the presence of some distortion as a result of driving the transistors rather hard. This can be verified by reducing the amplitude of the input signal. Students are encouraged to investigate this point. The average power dissipated in  $Q_p$ , as measured from Fig. B.105, is approximately 6 W. Therefore, the total power dissipated in the transistors is 12 W.

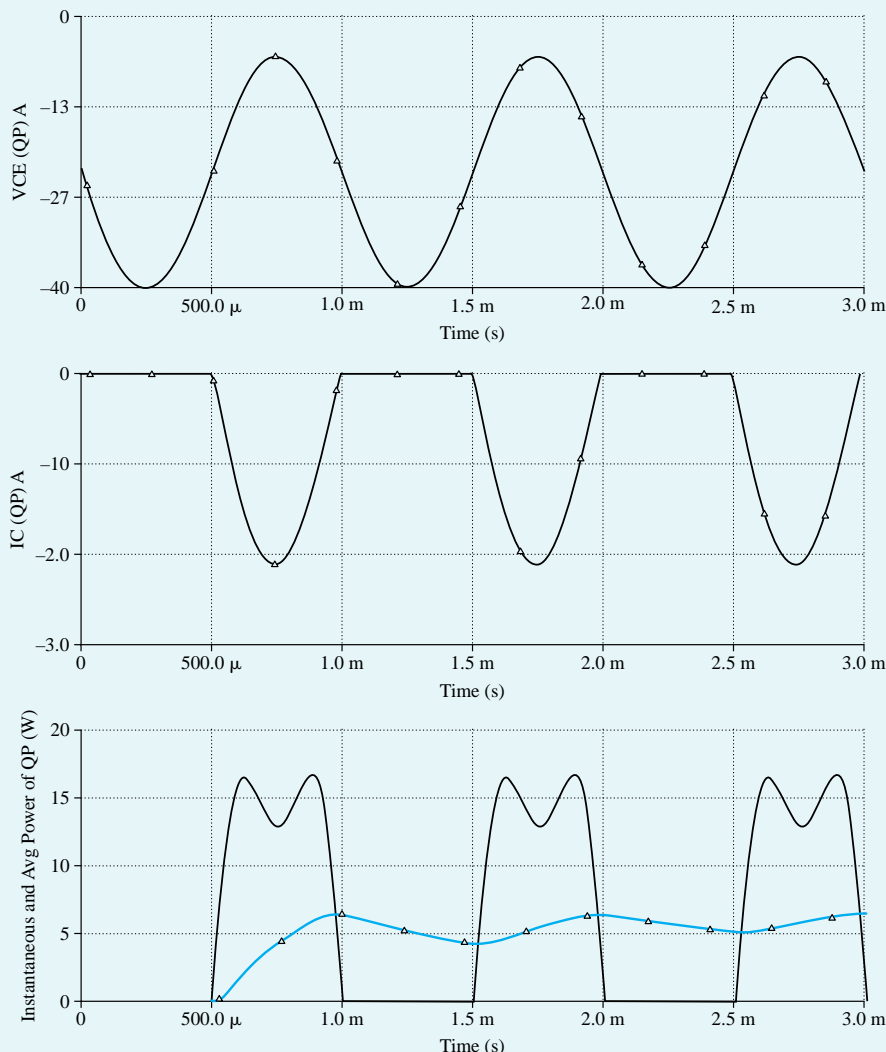


**Figure B.105** Voltage, current, and instantaneous and average power for  $Q_p$ .

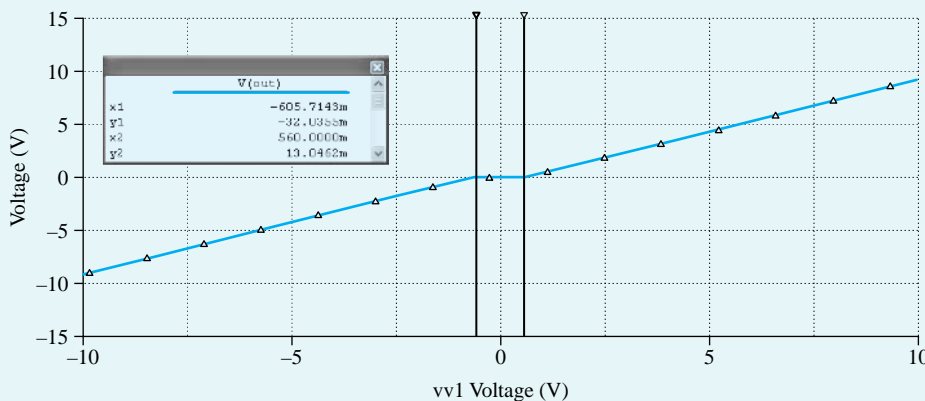
**Example MS.11.1** *continued*

The simulation results and hand-design calculations are summarized in Table B.29. Observe that the values are quite close, which verifies our design of the class B output stage.

**Table B.29** Summary of Simulation and Hand-Design Results

Measurement	Hand Design	Simulated	Error %
$P_L$	17.9 W	17.6 W	1.7
$P_S$	32.8 W	30 W	8.5
$P_D$	13.4 W	12 W	10.4
$n$	61%	58.6%	3.9

**Crossover Distortion** We can further investigate the crossover distortion of this circuit by utilizing the voltage transfer characteristics (VTC) curve of the class B output stage. The plot is obtained through a dc sweep analysis in Multisim where  $v_{IN}$  is swept over the range  $-10 \text{ V}$  to  $10 \text{ V}$  in  $1.0\text{-mV}$  increments. From the resulting VTC curve, shown in Fig. B.106, we can see that the dead band extends from  $-0.605 \text{ V}$  to  $0.56 \text{ V}$ . The effect of crossover distortion can be quantified by performing a Fourier analysis on the output voltage in Multisim.

**Figure B.106** VTC of class B output stage.

**Total Harmonic Distortion (THD)** This analysis decomposes the waveform generated via transient analysis into its Fourier-series components. Furthermore, Multisim computes the THD of the output waveform, and the results are shown in Fig. B.107.

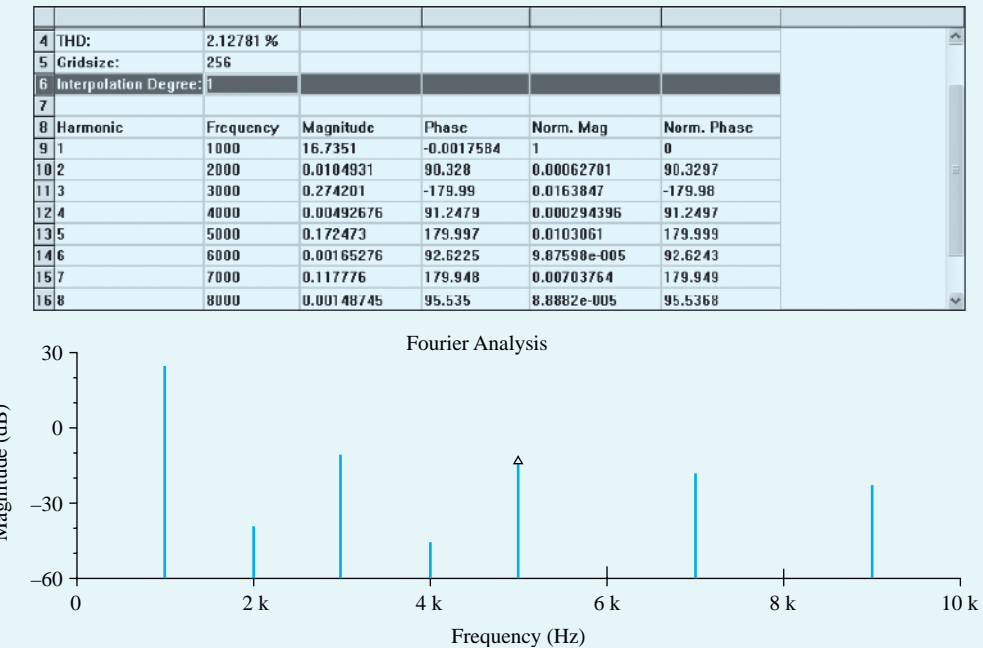


**Figure B.107** Fourier-series components of the output voltage and class B output stage THD.

From the Fourier analysis, we note that the waveform is rather rich in odd harmonics and that the resulting THD is 2.13%, which is rather high.

### Example MS.12.1

#### A Two-Stage CMOS Op Amp with Frequency Compensation

In this example, we will use Multisim to aid in designing the frequency compensation of the two-stage CMOS circuit whose schematic is shown in Fig. B.108. Multisim will then be employed to determine the frequency response and the slew rate of the op amp. We will assume a 0.5- $\mu$ m CMOS technology for the MOSFETs and use typical SPICE level-1 model parameters for this technology.

The op-amp circuit in Fig. B.108 is designed using a reference current  $I_{REF} = 90 \mu\text{A}$ , a supply voltage  $V_{DD} = 3.3 \text{ V}$ , and a load capacitor  $C_L = 1 \text{ pF}$ . Unit-size transistors with  $W/L = 1.25\mu\text{m}/0.6\mu\text{m}$  are used for both the NMOS and PMOS devices. The transistors are sized for an overdrive voltage  $V_{ov} = 0.3 \text{ V}$ . The corresponding multiplicative factors are shown in Fig. B.108.

In Multisim, the common-mode input voltage  $V_{CM}$  of the op-amp circuit is set to  $V_{DD}/2 = 1.65 \text{ V}$ , and DC Operating Point Analysis is performed to determine the dc bias conditions. Using the values found from the simulation results for the small-signal parameters of the MOSFETs, we obtain

$$G_{m1} = 0.333 \text{ mA/V}$$

$$G_{m2} = 0.650 \text{ mA/V}$$

$$C_1 = 26.5 \text{ fF}$$

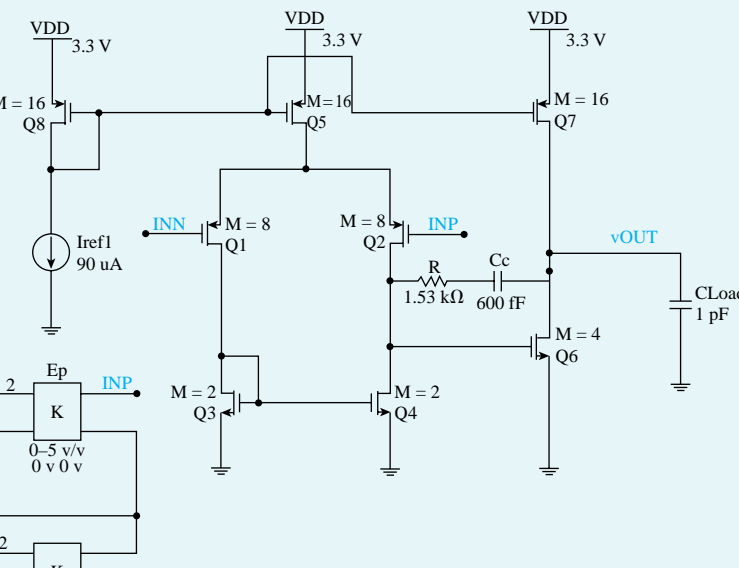
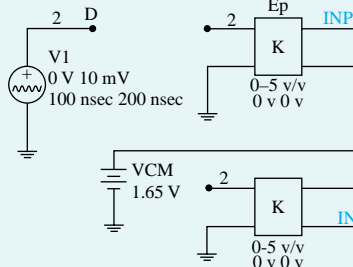
$$C_2 = 1.04 \text{ pF}$$

**Example MS.12.1** *continued*

NMOS	
Vtn	0.7 V
LAMBDA	0.1
kn'	246.2 uA/V^2
IREF	0.09 mA
L	0.6 um
W	1.25 um

PMOS	
Vtp	-0.7 V
LAMBDA	0.2
kp'	-86.1 uA/V^2
IREF	0.09 mA
L	0.6 um
W	1.25 um



**Figure B.108** Schematic capture of the two-stage CMOS op amp.

using Eqs. (10.7), (10.14), (10.25), and (10.26) respectively. Recall that  $G_{m1}$  and  $G_{m2}$  are the transconductances of, respectively, the first and second stages of the op amp. Capacitors  $C_1$  and  $C_2$  represent the total capacitance to ground at the output nodes of, respectively, the first and second stage of the op amp.

Then, using Eq. (10.28), the frequency of the second, nondominant, pole can be found as

$$f_{P2} \approx \frac{G_{m2}}{2\pi C_2} = 97.2 \text{ MHz}$$

To place the transmission zero, given by Eq. (10.38), at infinite frequency, we select

$$R = \frac{1}{G_{m2}} = 1.53 \text{ k}\Omega$$

Now, using Eq. (10.37), the phase margin of the op amp can be expressed as

$$\text{PM} = 90^\circ - \tan^{-1}\left(\frac{f_t}{f_{P2}}\right)$$

where  $f_t$  is the unity-gain frequency, given in Eq. (10.31):

$$f_t = \frac{G_{m1}}{2\pi C_C}$$

Using the above two equations we determine that compensation capacitors of  $C_C = 0.78 \text{ pF}$  and  $C_C = 2 \text{ pF}$  are required to achieve phase margins of  $\text{PM} = 55^\circ$  and  $\text{PM} = 75^\circ$ , respectively.

Next, an ac-analysis simulation is performed in Multisim to compute the frequency response of the op amp and to verify the foregoing design values (as set up in Ch12\_Two\_Stage\_CMOS\_OpAmp\_Ex\_Freq-Resp.ms10). It

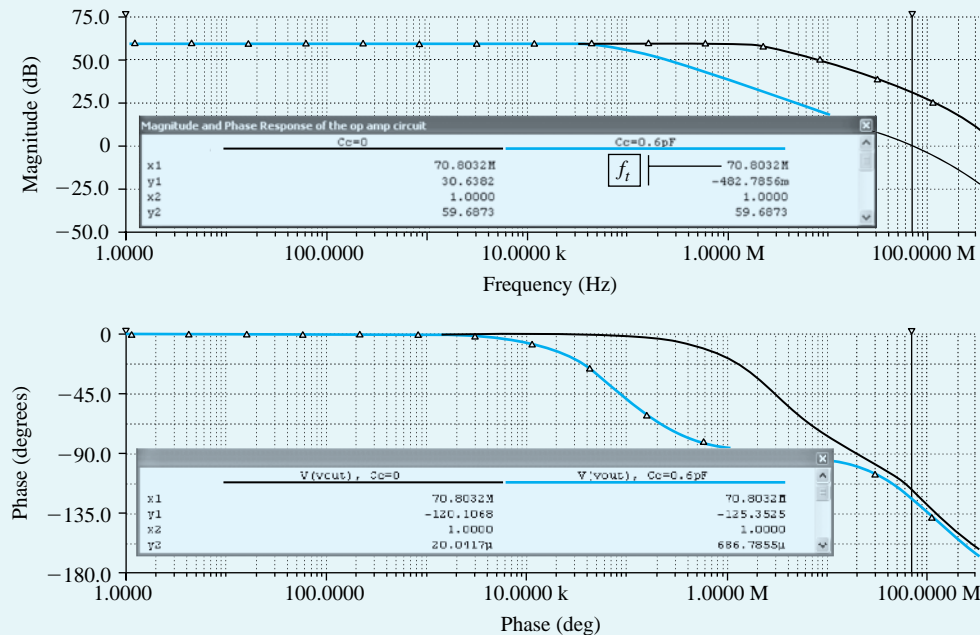


**Figure B.109** Magnitude and phase response of the op-amp circuit with  $R = 1.53 \text{ k}\Omega$ ,  $C_c = 0$  (no frequency compensation), and  $C_c = 1.8 \text{ pF}$  ( $PM = 75^\circ$ ).

was found that, with  $R = 1.53 \text{ k}\Omega$ , we needed  $C_c = 0.6 \text{ pF}$  and  $C_c = 1.8 \text{ pF}$  to set  $PM = 55^\circ$  and  $PM = 75^\circ$ , respectively. We note that these values are reasonably close to those predicted by hand analysis. The corresponding frequency responses for the compensated op amps are plotted in Figs. B.109 and B.110. For comparison, we also show the frequency response of the uncompensated op amp ( $C_c = 0$ ). Observe that the unity-gain frequency  $f_t$  drops from 70.8 MHz to 26.4 MHz as  $C_c$  is increased to improve  $PM$ .

Rather than increasing the compensation capacitor  $C_c$  to improve the phase margin, the value of the series resistor  $R$  can be increased: for a given  $C_c$ , increasing  $R$  above  $1/G_{m2}$  places the transmission zero at a negative real-axis location (Eq. 10.38), where the phase it introduces adds to the phase margin. Thus,  $PM$  can be improved without affecting  $f_t$ . To verify this point, we set  $C_c$  to 0.6 pF and simulate the op-amp circuit in Multisim for the cases of  $R = 1.53 \text{ k}\Omega$  and  $R = 3.2 \text{ k}\Omega$ . The corresponding frequency response is plotted in Fig. B.111. Observe that  $f_t$  is approximately independent of  $R$ . However, by increasing  $R$ , we can improve  $PM$  from  $55^\circ$  to  $75^\circ$ .

Increasing the  $PM$  is desirable because it reduces the overshoot in the step response of the op amp. To verify this point, we simulate in Multisim the step response of the op amp for  $PM = 55^\circ$  and  $PM = 75^\circ$ . To do that, we connect the op amp in a unity-gain configuration, apply a small (10-mV) pulse signal at the input with very short (1-ps) rise and fall times to emulate a step input, perform a transient analysis simulation (as set up in Ch12\_Two\_Stage\_CMOS\_OpAmp\_Ex\_Small-Signal.ms10), and plot the output voltage as shown in Fig. B.112. Observe that the overshoot in the step response drops from 15% to 1.4% when the phase margin is increased from  $55^\circ$  to  $75^\circ$ .

We conclude this example by computing  $SR$ , the slew rate of the op amp. From Eq. (10.40), we have

$$SR = 2\pi f_t V_{OV} = \frac{G_{m1}}{C_c} V_{OV} = 166.5 \text{ V}/\mu\text{s}$$

**Example MS.12.1** *continued*

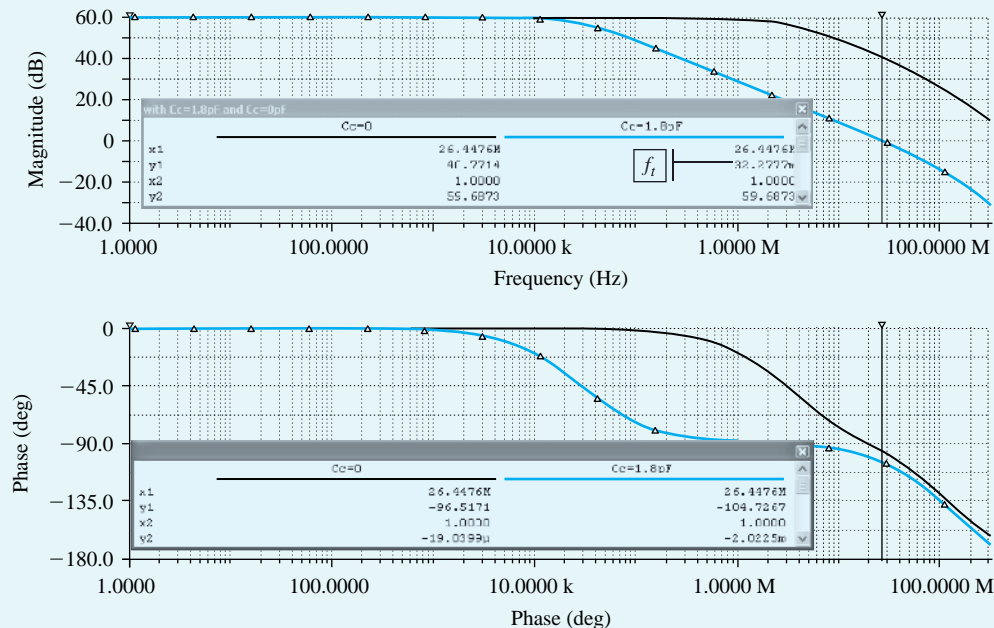


**Figure B.110** Magnitude and phase response of the op-amp circuit with  $R = 1.53 \text{ k}\Omega$ ,  $C_c = 0$  (no frequency compensation), and  $C_C = 1.8 \text{ pF}$  ( $PM = 75^\circ$ ).

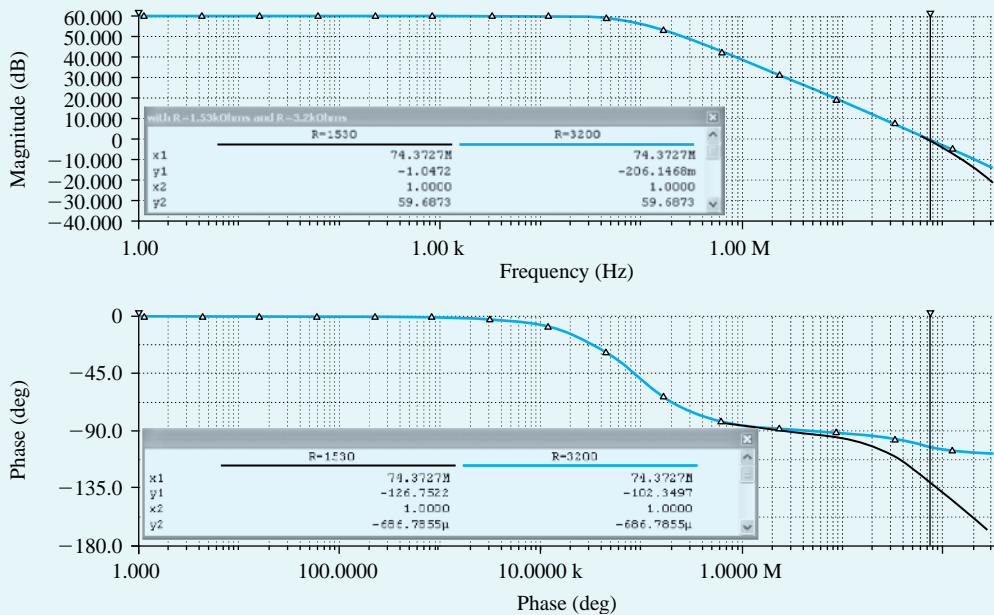


**Figure B.111** Magnitude and phase response of the op amp circuit with  $C_c = 0.6 \text{ pF}$ ,  $R = 1.53 \text{ k}\Omega$  ( $PM = 55^\circ$ ), and  $R = 3.2 \text{ k}\Omega$  ( $PM = 75^\circ$ ).

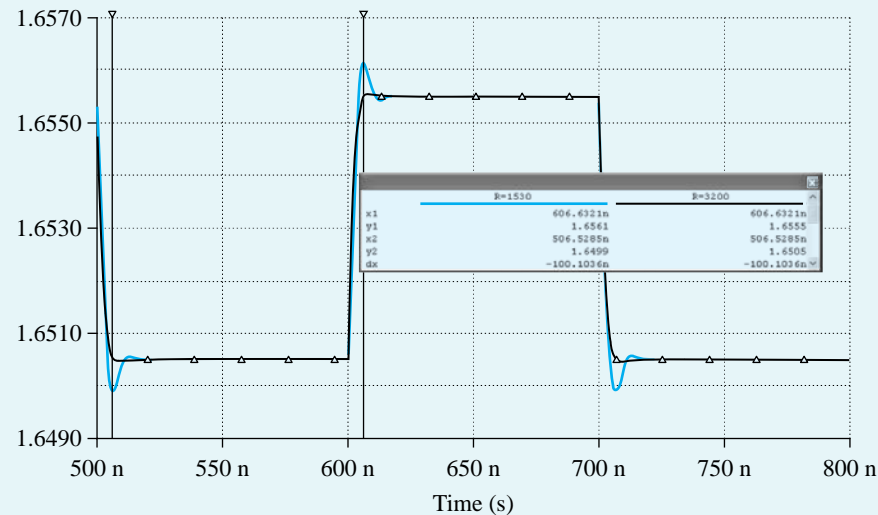


**Figure B.112** Small-signal step response (for a 10-mV step input) if the op-amp circuit is connected in a unity-gain configuration:  $PM = 55^\circ$  ( $C_C = 0.6 \text{ pF}$ ,  $R = 1.53 \text{ k}\Omega$ ) and  $PM = 75^\circ$  ( $C_C = 0.6 \text{ pF}$ ,  $R = 3.2 \text{ k}\Omega$ ).

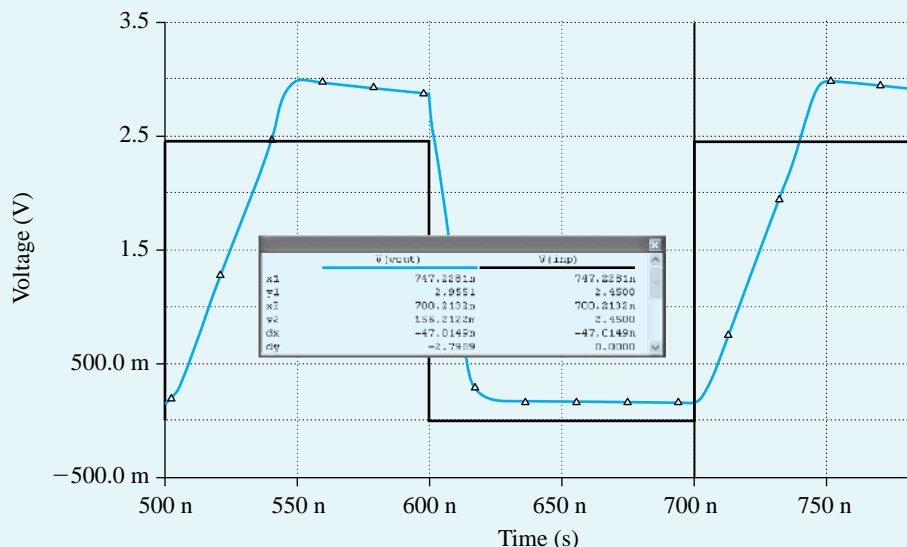


**Figure B.113** Large-signal step response (for a 2.2-V step input) if the op-amp circuit is connected in a unity-gain configuration. The slope of the rising and falling edges of the output waveform correspond to the slew rate of the op amp.

when  $C_C = 0.6 \text{ pF}$ . Next, to determine SR using Multisim, we again connect the op amp in a unity-gain configuration and perform a transient analysis simulation (as set up in Ch12\_Two\_Stage\_CMOS\_OpAmp\_Ex\_Large-Signal.ms10). However, we now apply a large pulse signal (2.2 V) at the input to cause slew-rate limiting at the output. The corresponding output voltage waveform is plotted in Fig. B.113. The slope of the slew-rate-limited output waveform corresponds to the slew rate of the op amp and is found to be  $SR = 160 \text{ V}/\mu\text{s}$  and  $60 \text{ V}/\mu\text{s}$  for the negative- and positive-going output, respectively. These results, with the

**Example MS.12.1** *continued*

unequal values of  $SR$  in the two directions, differ from those predicted by the simple model for the slew-rate limiting of the two-stage op-amp circuit. The difference can perhaps be said to be a result of transistor  $Q_4$  entering the triode region and its output current (which is sourced through  $C_c$ ) being correspondingly reduced. Of course, the availability of Multisim should enable the reader to explore this point further.

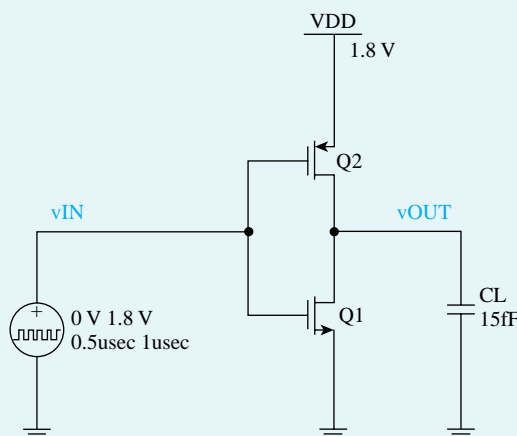
**Example MS.13.1****The CMOS Inverter**

In this example, we will use Multisim to design a CMOS inverter whose schematic capture is shown in Fig. B.114. We will assume a 0.18- $\mu\text{m}$  CMOS technology for the MOSFETs and use typical SPICE level-1 model parameters for this technology, including the intrinsic capacitance values. This model does not take into account the short-channel effects for this technology. Also, the load capacitance is assumed to be dominated by the extrinsic component  $C_{\text{ext}}$  (resulting from the wiring and the input capacitance of the driven gates), where the value used in this example is 15 fF. We will begin with an approximate hand-analysis design. We will then use Multisim to verify that the designed circuit meets the specifications. The targeted specification for this inverter is a high-to-low propagation delay ( $t_{PHL}$ ) of less than 45 ps. Once designed, the other characteristics of this inverter such as low-to-high propagation delay ( $t_{PLH}$ ), noise margins, and threshold voltage will be investigated.

The inverter specifications are summarized in Table B.30.

**Table B.30** CMOS Inverter Specifications

Parameters	Value
$t_{PHL}$	45 ps
$C_L$	15 fF
$V_{DD}$	1.8 V

**Figure B.114** Schematic capture of the CMOS inverter.

## Hand Design

For the design of this inverter we choose  $L = 0.2 \mu\text{m}$ , so we have  $L_{\text{eff}} = 0.180 \mu\text{m}$ . As mentioned earlier, to minimize area, all channels are usually made equal to the minimum length permitted by the given technology. To meet the specified  $t_{PHL}$ , we need to size  $(W/L_{\text{eff}})_n$  carefully. Once sized,  $(W/L_{\text{eff}})_p = 2(W/L_{\text{eff}})_n$  is chosen, which is a compromise between area, noise margins, and  $t_{PLH}$ .

The value of  $t_{PHL}$  can be estimated using Eq. (14.64) as

$$t_{PHL} = \frac{\alpha_n C}{k'_n \left( \frac{W}{L_{\text{eff}}} \right) V_{DD}} = \frac{15 \times 10^{-15} \alpha_n}{246.2 \times 10^{-6} \left( \frac{W}{L_{\text{eff}}} \right) 1.8}$$

where  $\alpha_n$  is a factor determined by the relative values of  $V_i$  and  $V_{DD}$  ( $V_m/V_{DD} = 0.5/1.8 = 0.278$ ):

$$\alpha_n = \frac{2}{7/4^{-3}(V_m/V_{DD}) + (V_{in}/V_{DD})^2} = 2.01$$

Based on the above equations, the specified  $t_{PHL}$  can be achieved by selecting the ratio  $(W/L_{\text{eff}})_n = 1.5$  and consequently  $(W/L_{\text{eff}})_p = 3$ . Table B.31 summarizes the relevant sizing information for each transistor. The third column of this table shows the transconductance parameter values for each transistor (which are typical values for 0.18- $\mu\text{m}$  CMOS technology).

**Table B.31** Transistor Sizes

Transistor	$W (\mu\text{m})$	$L_{\text{eff}} (\mu\text{m})$	$k' (\mu\text{A}/\text{V}^2)$
NMOS	0.27	0.18	246.2
PMOS	0.54	0.18	86.1

Note that for the selected width values, the intrinsic capacitances  $C_{gd1}$  and  $C_{gd2}$  are insignificant in comparison to the load capacitance. This confirms our initial assumption that in our hand calculations of delay, we could neglect  $C_{gd1}$  and  $C_{gd2}$  (which vary proportionally with width).

## Simulation

**Verifying Propagation Delay** To investigate the dynamic operation of the inverter and to verify that the design meets the specified  $t_{PHL}$ , we apply an ideal pulse signal at the input and perform a transient analysis, as set up in Ch13\_CMOS\_Inverter\_tPHL\_Ex.ms10. Then, we plot the input and output waveforms as shown in Fig. B.115. Based on the simulated response,  $t_{PHL} = 40.5 \text{ ps}$  (as indicated in Fig. B.115). Similarly, we obtain  $t_{PLH} = 60.3 \text{ ps}$ , resulting in the inverter propagation delay ( $t_p$ ) of 50.4 ps. Therefore, the specified high-to-low propagation delay specification is met, and  $t_p$  takes a reasonable value.

**Voltage Transfer Characteristic (VTC)** To compute both the VTC of the inverter and its supply current at various values of the input voltage  $V_{in}$ , we apply a dc voltage source at the input and perform a dc sweep with  $V_{in}$  swept over the range 0 to  $V_{DD}$ , as set up in Ch13\_CMOS\_Inverter\_VTC\_Ex.ms10. The resulting VTC is plotted in Fig. B.116. Note that the slope of the VTC in the switching region (where the NMOS and PMOS devices are both in saturation) is not infinite as predicted from the simple theory presented earlier. Rather, the nonzero value of  $\lambda$  causes the inverter gain to be finite. The two points on the VTC at which the inverter gain is unity (i.e., the VTC slope is  $-1 \text{ V/V}$ ) and that determine  $V_{IL}$  and  $V_{IH}$  are indicated in Fig. B.116. The corresponding noise margins are  $NM_L = 0.76 \text{ V}$  and  $NM_H = 0.81 \text{ V}$ . Note that the design provides high tolerance to noise, since noise margins are reasonably high ( $NM_L$  and  $NM_H$  are 42% and 45% of the supply voltage). This implies that the inverter would provide the correct logic output for an input noise variation of up to approximately 40% of the  $V_{DD}$ .

**Example MS.13.1** *continued*

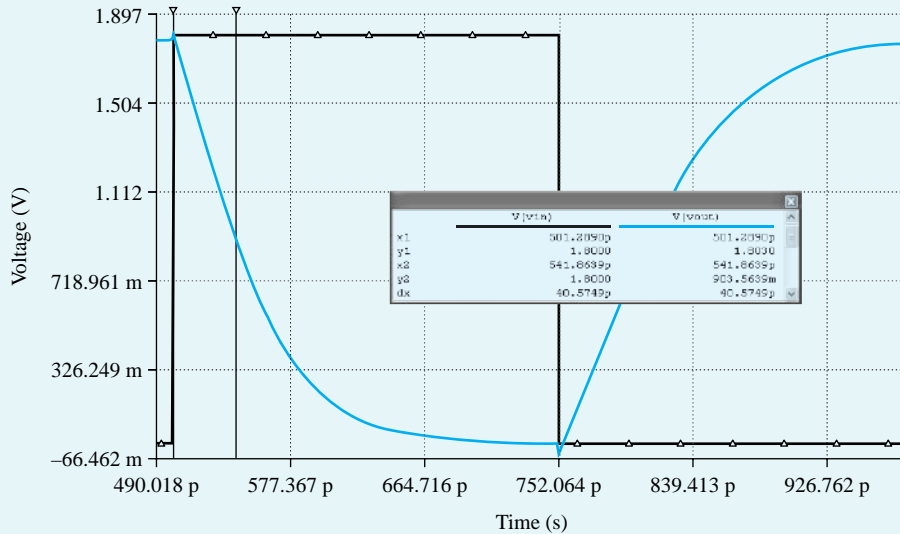


**Figure B.115** Time domain response of the CMOS inverter to measure  $t_{PHL}$ .

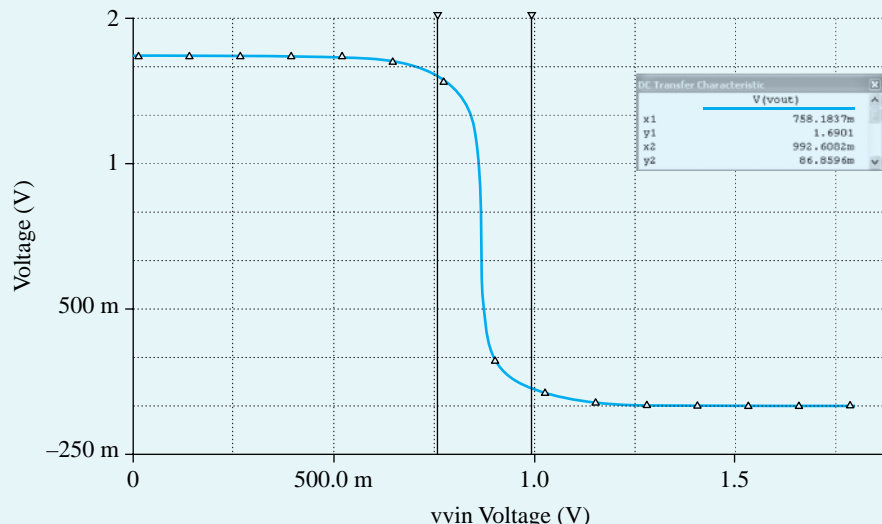


**Figure B.116** Output voltage versus input voltage for the inverter (to measure low and high noise margins  $NM_L$  and  $NM_H$ ).

The threshold voltage  $V_M$  of the CMOS inverter is defined as the input voltage  $v_{IN}$  that results in an identical switching output voltage  $v_{OUT}$ , that is,

$$V_M = v_{IN}|v_{OUT} = v_{IN}$$

Thus, as shown in Fig. B.117,  $V_M$  is at the intersection of the VTC with the straight line corresponding to  $v_{OUT} = v_{IN}$ . This line can be simply generated by plotting  $v_{IN}$  on the vertical axis, in addition to  $v_{OUT}$ . Note that  $V_M = 0.87$  V, which is very close to the desired value of  $V_{DD}/2 = 0.9$  V, as desired.

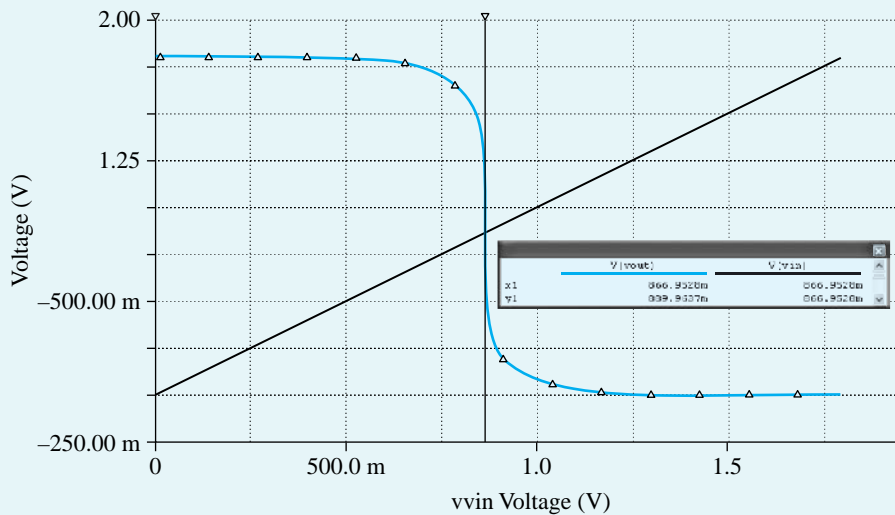


**Figure B.117** Output voltage versus input voltage for the inverter (to the threshold voltage measure  $V_{th}$ ).

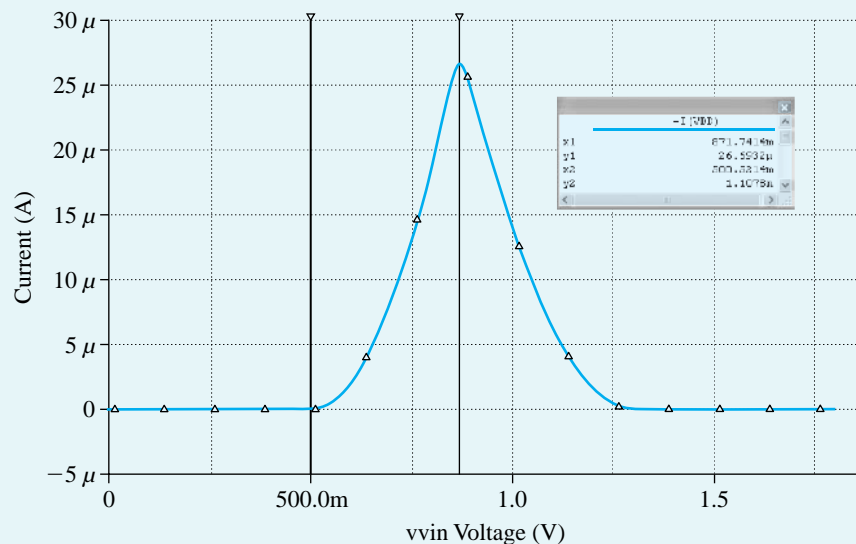


**Figure B.118** Supply current versus input voltage for the inverter.

Finally, the supply current is plotted versus input voltage in Fig. B.118. Observe that in the transition region, where the inverter is switching, the current is no longer zero. Specifically, the peak current occurs at the inverter threshold voltage.

## APPENDIX C

# TWO-PORT NETWORK PARAMETERS

### Introduction

At various points throughout the text, we make use of some of the different possible ways to characterize linear two-port networks. A summary of this topic is presented in this appendix.

### C.1 Characterization of Linear Two-Port Networks

A two-port network (Fig. C.1) has four port variables:  $V_1$ ,  $I_1$ ,  $V_2$ , and  $I_2$ . If the two-port network is linear, we can use two of the variables as excitation variables and the other two as response variables. For instance, the network can be excited by a voltage  $V_1$  at port 1 and a voltage  $V_2$  at port 2, and the two currents,  $I_1$  and  $I_2$ , can be measured to represent the network response. In this case,  $V_1$  and  $V_2$  are independent variables and  $I_1$  and  $I_2$  are dependent variables, and the network operation can be described by the two equations

$$I_1 = y_{11}V_1 + y_{12}V_2 \quad (\text{C.1})$$

$$I_2 = y_{21}V_1 + y_{22}V_2 \quad (\text{C.2})$$

Here, the four parameters  $y_{11}$ ,  $y_{12}$ ,  $y_{21}$ , and  $y_{22}$  are admittances, and their values completely characterize the linear two-port network.

Depending on which two of the four port variables are used to represent the network excitation, a different set of equations (and a correspondingly different set of parameters) is obtained for characterizing the network. We shall present the four parameter sets commonly used in electronics.

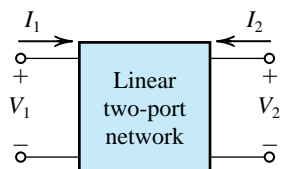


**Figure C.1** The reference directions of the four port variables in a linear two-port network.

### C.1.1 $y$ Parameters

The short-circuit admittance (or  $y$ -parameter) characterization is based on exciting the network by  $V_1$  and  $V_2$ , as shown in Fig. C.2(a). The describing equations are Eqs. (C.1) and (C.2). The four admittance parameters can be defined according to their roles in Eqs. (C.1) and (C.2).

Specifically, from Eq. (C.1) we see that  $y_{11}$  is defined as

$$y_{11} = \left. \frac{I_1}{V_1} \right|_{V_2=0}. \quad (\text{C.3})$$

Thus  $y_{11}$  is the input admittance at port 1 with port 2 short-circuited. This definition is illustrated in Fig. C.2(b), which also provides a conceptual method for measuring the input short-circuit admittance  $y_{11}$ .

The definition of  $y_{12}$  can be obtained from Eq. (C.1) as

$$y_{12} = \left. \frac{I_1}{V_2} \right|_{V_1=0}. \quad (\text{C.4})$$

Thus  $y_{12}$  represents transmission from port 2 to port 1. Since in amplifiers, port 1 represents the input port and port 2 the output port,  $y_{12}$  represents internal *feedback* in the network. Figure C.2(c) illustrates the definition of and the method for measuring  $y_{12}$ .

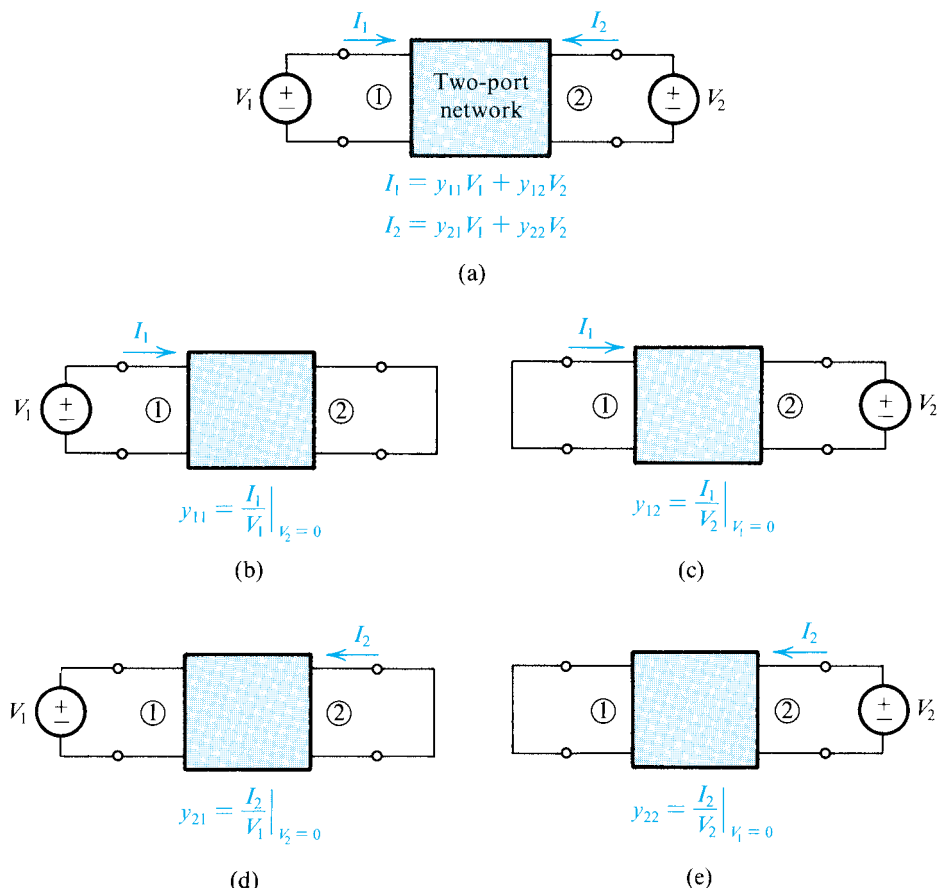


**Figure C.2** Definition of and conceptual measurement circuits for the  $y$  parameters.

The definition of  $y_{21}$  can be obtained from Eq. (C.2) as

$$y_{21} = \left. \frac{I_2}{V_1} \right|_{V_2=0} \quad (\text{C.5})$$

Thus  $y_{21}$  represents transmission from port 1 to port 2. If port 1 is the input port and port 2 the output port of an amplifier, then  $y_{21}$  provides a measure of the forward gain or transmission. Figure C.2(d) illustrates the definition of and the method for measuring  $y_{21}$ .

The parameter  $y_{22}$  can be defined, based on Eq. (C.2), as

$$y_{22} = \left. \frac{I_2}{V_2} \right|_{V_1=0} \quad (\text{C.6})$$

Thus  $y_{22}$  is the admittance looking into port 2 while port 1 is short-circuited. For amplifiers,  $y_{22}$  is the output short-circuit admittance. Figure C.2(e) illustrates the definition of and the method for measuring  $y_{22}$ .

### C.1.2 z Parameters

The open-circuit impedance (or  $z$ -parameter) characterization of two-port networks is based on exciting the network by  $I_1$  and  $I_2$ , as shown in Fig. C.3(a). The describing equations are

$$V_1 = z_{11}I_1 + z_{12}I_2 \quad (\text{C.7})$$

$$V_2 = z_{21}I_1 + z_{22}I_2 \quad (\text{C.8})$$

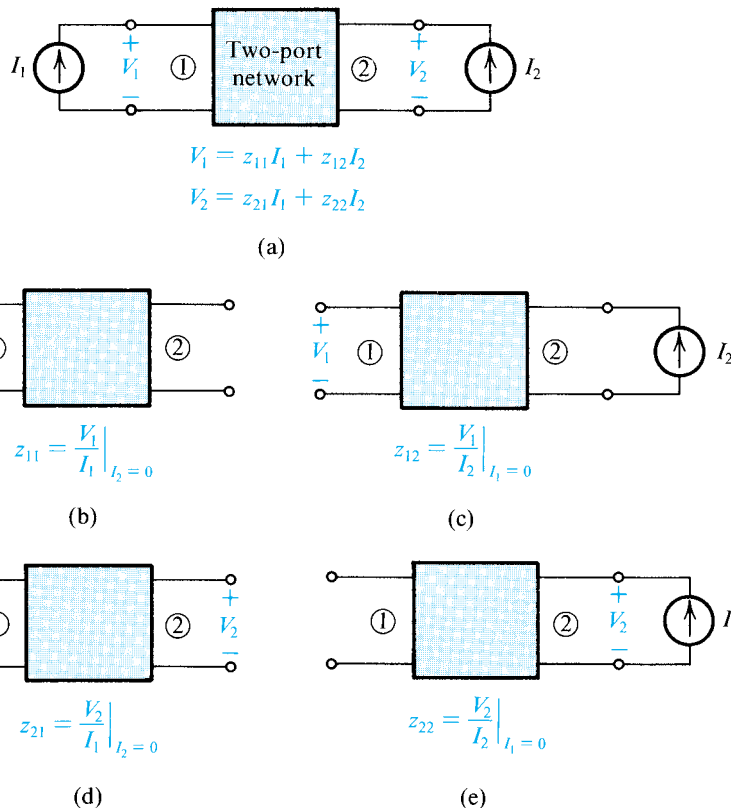


**Figure C.3** Definition of and conceptual measurement circuits for the  $z$  parameters.

## C-4 Appendix C Two-Port Network Parameters

Owing to the duality between the  $z$ - and  $y$ -parameter characterizations, we shall not give a detailed discussion of  $z$  parameters. The definition and the method of measuring each of the four  $z$  parameters are given in Fig. C.3.

### C.1.3 $h$ Parameters

The hybrid (or  $h$ -parameter) characterization of two-port networks is based on exciting the network by  $I_1$  and  $V_2$ , as shown in Fig. C.4(a) (note the reason behind the name *hybrid*). The describing equations are

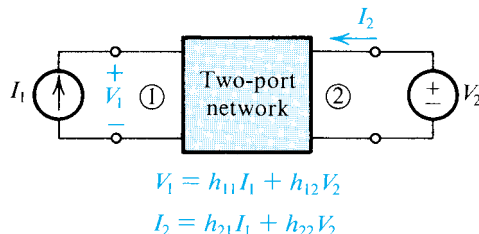
$$V_1 = h_{11}I_1 + h_{12}V_2 \quad (\text{C.9})$$

$$I_2 = h_{21}I_1 + h_{22}V_2 \quad (\text{C.10})$$

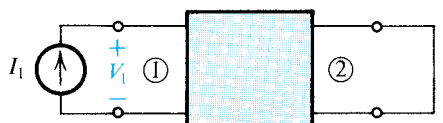
from which the definition of the four  $h$  parameters can be obtained as

$$h_{11} = \left. \frac{V_1}{I_1} \right|_{V_2=0} \quad h_{21} = \left. \frac{I_2}{I_1} \right|_{V_2=0}$$

$$h_{12} = \left. \frac{V_1}{V_2} \right|_{I_1=0} \quad h_{22} = \left. \frac{I_2}{V_2} \right|_{I_1=0}$$

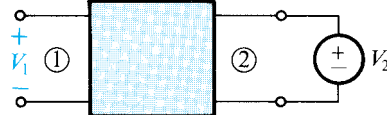


(a)



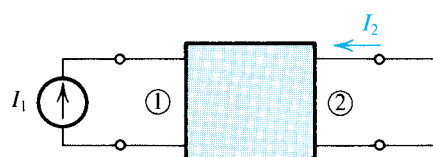
$$h_{11} = \left. \frac{V_1}{I_1} \right|_{V_2=0}$$

(b)



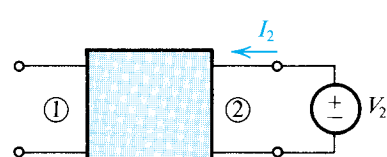
$$h_{12} = \left. \frac{V_1}{V_2} \right|_{I_1=0}$$

(c)



$$h_{21} = \left. \frac{I_2}{I_1} \right|_{V_2=0}$$

(d)



$$h_{22} = \left. \frac{I_2}{V_2} \right|_{I_1=0}$$

(e)

**Figure C.4** Definition of and conceptual measurement circuits for the  $h$  parameters.

Thus,  $h_{11}$  is the input impedance at port 1 with port 2 short-circuited. The parameter  $h_{12}$  represents the reverse or feedback voltage ratio of the network, measured with the input port open-circuited. The forward-transmission parameter  $h_{21}$  represents the current gain of the network with the output port short-circuited; for this reason,  $h_{21}$  is called the *short-circuit current gain*. Finally,  $h_{22}$  is the output admittance with the input port open-circuited.

The definitions and conceptual measuring setups of the  $h$  parameters are given in Fig. C.4.

### C.1.4 $g$ Parameters

The inverse-hybrid (or  $g$ -parameter) characterization of two-port networks is based on excitation of the network by  $V_1$  and  $I_2$ , as shown in Fig. C.5(a). The describing equations are

$$I_1 = g_{11}V_1 + g_{12}I_2 \quad (\text{C.11})$$

$$V_2 = g_{21}V_1 + g_{22}I_2 \quad (\text{C.12})$$

The definitions and conceptual measuring setups are given in Fig. C.5.

### C.1.5 Equivalent-Circuit Representation

A two-port network can be represented by an equivalent circuit based on the set of parameters used for its characterization. Figure C.6 shows four possible equivalent circuits corresponding

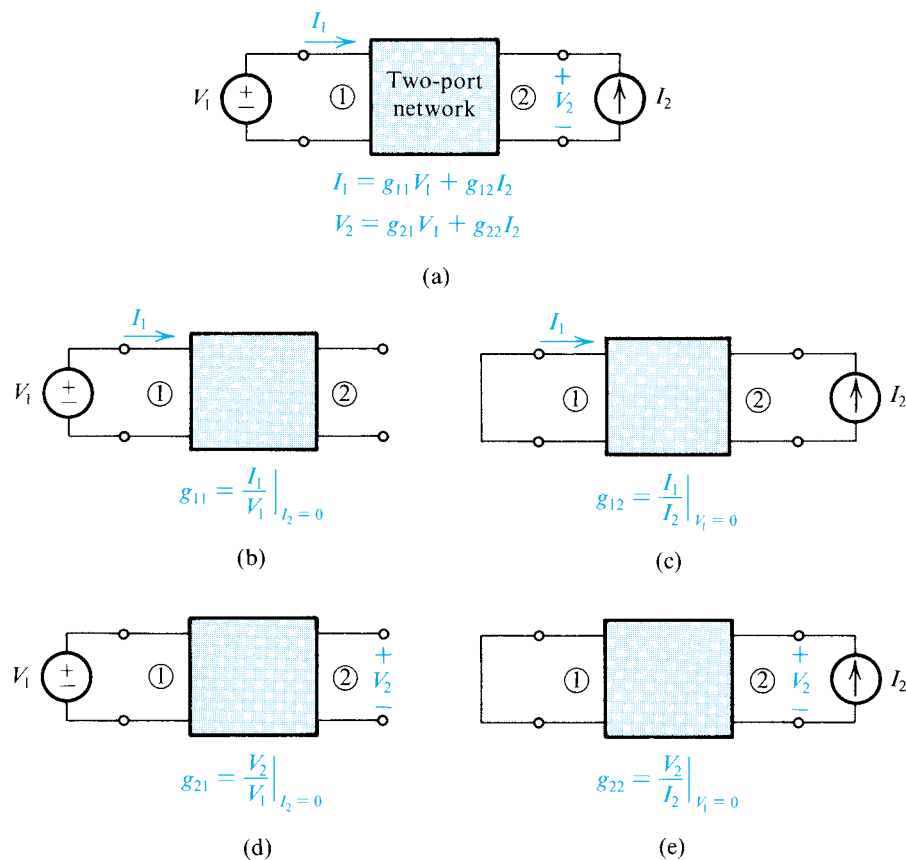


**Figure C.5** Definition of and conceptual measurement circuits for the  $g$  parameters.

## C-6 Appendix C Two-Port Network Parameters

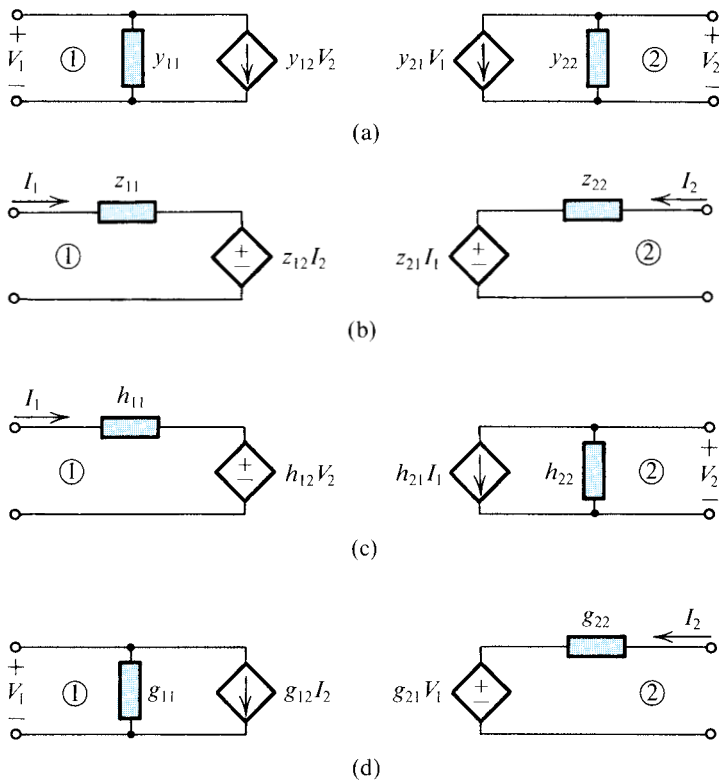


**Figure C.6** Equivalent circuits for two-port networks in terms of (a)  $y$ , (b)  $z$ , (c)  $h$ , and (d)  $g$  parameters.

to the four parameter types just discussed. Each of these equivalent circuits is a direct pictorial representation of the corresponding two equations describing the network in terms of the particular parameter set.

Finally, it should be mentioned that other parameter sets exist for characterizing two-port networks, but these are not discussed or used in this book.

### EXERCISE

- C.1** Figure EC.1 shows the small-signal, equivalent-circuit model of a transistor. Calculate the values of the  $h$  parameters.

**Ans.**  $h_{11} \approx 2.6 \text{ k}\Omega$ ;  $h_{12} \approx 2.5 \times 10^{-4}$ ;  $h_{21} \approx 100$ ;  $h_{22} \approx 2 \times 10^{-5} \Omega$

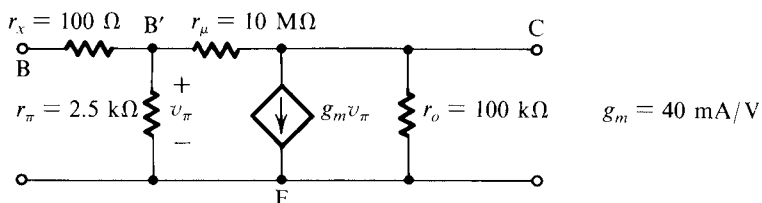


**Figure EC.1**

## PROBLEMS

**C.1** (a) An amplifier characterized by the  $h$ -parameter equivalent circuit of Fig. C.6(c) is fed with a source having a voltage  $V_s$  and a resistance  $R_s$ , and is loaded in a resistance  $R_L$ . Show that its voltage gain is given by

$$\frac{V_2}{V_s} = \frac{-h_{21}}{(h_{11} + R_s)(h_{22} + 1/R_L) - h_{12}h_{21}}$$

(b) Use the expression derived in (a) to find the voltage gain of the transistor in Exercise C.1 for  $R_s = 1\text{ k}\Omega$  and  $R_L = 10\text{ k}\Omega$

**C.2** The terminal properties of a two-port network are measured with the following results: With the output short-circuited and an input current of 0.01 mA, the output current is 1.0 mA and the input voltage is 26 mV. With the input open-circuited and a voltage of 10 V applied to the output,

the current in the output is 0.2 mA and the voltage measured at the input is 2.5 mV. Find values for the  $h$  parameters of this network.

**C.3** Figure PC.3 shows the high-frequency equivalent circuit of a BJT. (For simplicity,  $r_x$  has been omitted.) Find the  $y$  parameters.

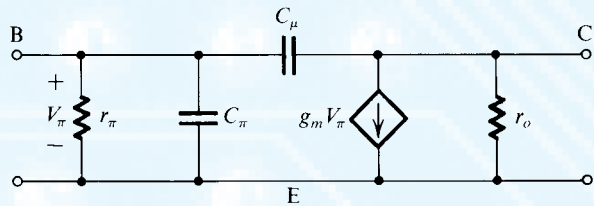


Figure PC.3

## APPENDIX D

# SOME USEFUL NETWORK THEOREMS

### Introduction

In this appendix we review three network theorems that are useful in simplifying the analysis of electronic circuits: Thévenin's theorem, Norton's theorem, and the source-absorption theorem.

### D.1 Thévenin's Theorem

Thévenin's theorem is used to represent a part of a network by a voltage source  $V_t$  and a series impedance  $Z_t$ , as shown in Fig. D.1. Figure D.1(a) shows a network divided into two parts, A and B. In Fig. D.1(b), part A of the network has been replaced by its Thévenin equivalent: a voltage source  $V_t$  and a series impedance  $Z_t$ . Figure D.1(c) illustrates how  $V_t$  is to be determined: Simply open-circuit the two terminals of network A and measure (or calculate) the voltage that appears between these two terminals. To determine  $Z_t$ , we reduce all external (i.e., independent) sources in network A to zero by short-circuiting voltage sources and open-circuiting current sources. The impedance  $Z_t$  will be equal to the input impedance of network A after this reduction has been performed, as illustrated in Fig. D.1(d).

### D.2 Norton's Theorem

Norton's theorem is the *dual* of Thévenin's theorem. It is used to represent a part of a network by a current source  $I_n$  and a parallel impedance  $Z_n$ , as shown in Fig. D.2. Figure D.2(a) shows a network divided into two parts, A and B. In Fig. D.2(b), part A has been replaced by its Norton's equivalent: a current source  $I_n$  and a parallel impedance  $Z_n$ . The Norton's current source  $I_n$  can be measured (or calculated) as shown in Fig. D.2(c). The terminals of the network being reduced (network A) are shorted, and the current  $I_n$  will be equal simply to the short-circuit current. To determine the impedance  $Z_n$ , we first reduce the external excitation in network A to zero: That is, we short-circuit independent voltage sources and open-circuit independent current sources. The impedance  $Z_n$  will be equal to the input impedance of network A after this source-elimination process has taken place. Thus the Norton impedance  $Z_n$  is equal to the Thévenin impedance  $Z_t$ . Finally, note that  $I_n = V_t/Z$ , where  $Z = Z_n = Z_t$ .

## D-2 Appendix D Some Useful Network Theorems

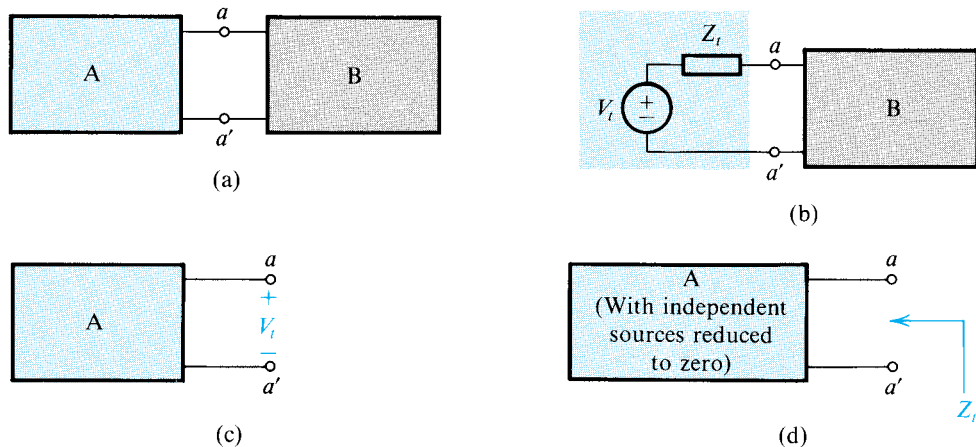


**Figure D.1** Thévenin's theorem.

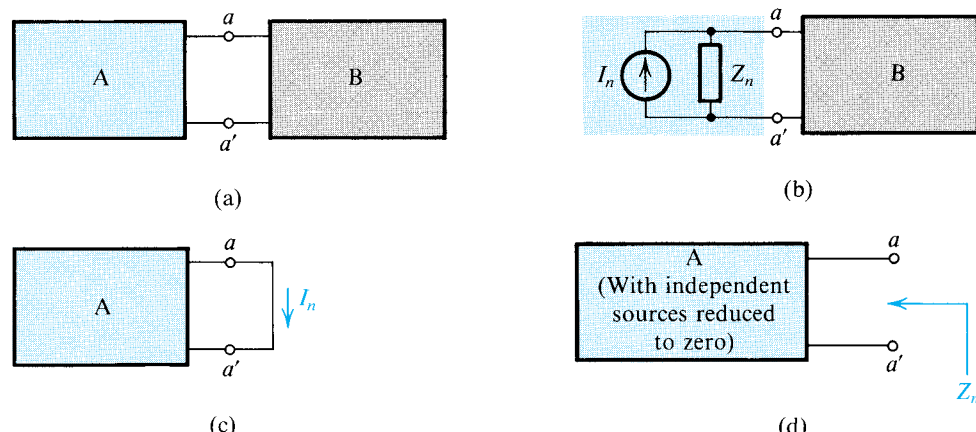


**Figure D.2** Norton's theorem.

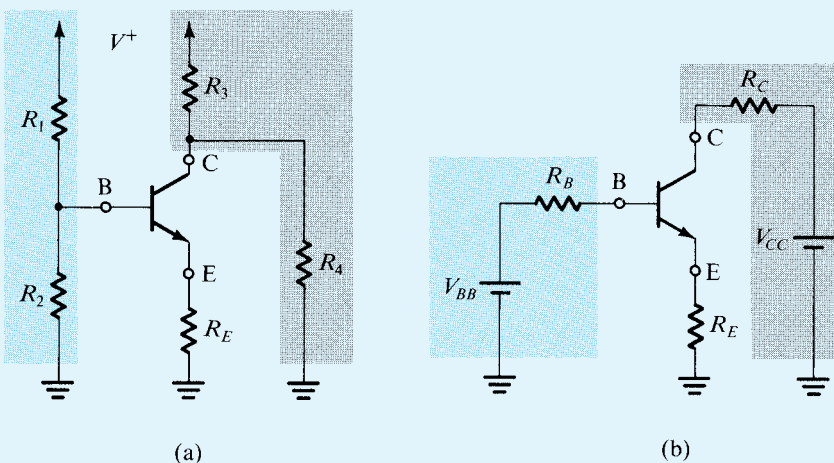
### Example D.1

Figure D.3(a) shows a bipolar junction transistor circuit. The transistor is a three-terminal device with the terminals labeled E (emitter), B (base), and C (collector). As shown, the base is connected to the dc power supply  $V^+$  via the voltage divider composed of  $R_1$  and  $R_2$ . The collector is connected to the dc supply  $V^+$  through  $R_3$  and to ground through  $R_4$ . To simplify the analysis, we wish to apply Thévenin's theorem to reduce the circuit.

#### Solution

Thévenin's theorem can be used at the base side to reduce the network composed of  $V^+$ ,  $R_1$ , and  $R_2$  to a dc voltage source  $V_{BB}$ ,

$$V_{BB} = V^+ \frac{R_2}{R_1 + R_2}$$



**Figure D.3** Thévenin's theorem applied to simplify the circuit of (a) to that in (b). (See Example D.1.)

and a resistance  $R_B$ ,

$$R_B = R_1 \parallel R_2$$

where  $\parallel$  denotes “in parallel with.” At the collector side, Thévenin’s theorem can be applied to reduce the network composed of  $V^+$ ,  $R_3$ , and  $R_4$  to a dc voltage source  $V_{CC}$ ,

$$V_{CC} = V^+ \frac{R_4}{R_3 + R_4}$$

and a resistance  $R_C$ ,

$$R_C = R_3 \parallel R_4$$

The reduced circuit is shown in Fig. D.3(b).

## D.3 Source-Absorption Theorem

Consider the situation shown in Fig. D.4. In the course of analyzing a network, we find a controlled current source  $I_x$  appearing between two nodes whose voltage difference is the controlling voltage  $V_x$ . That is,  $I_x = g_m V_x$  where  $g_m$  is a conductance. We can replace this controlled source by an impedance  $Z_x = V_x / I_x = 1/g_m$ , as shown in Fig. D.4, because the current drawn by this impedance will be equal to the current of the controlled source that we have replaced.

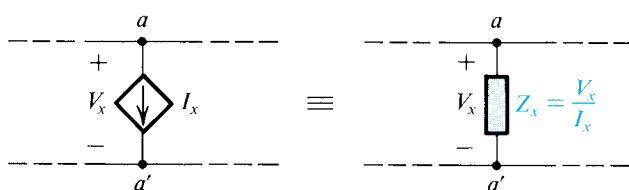


**Figure D.4** The source-absorption theorem.

**Example D.2**

Figure D.5(a) shows the small-signal, equivalent-circuit model of a transistor. We want to find the resistance  $R_{in}$  “looking into” the emitter terminal E—that is, the resistance between the emitter and ground—with the base B and collector C grounded.

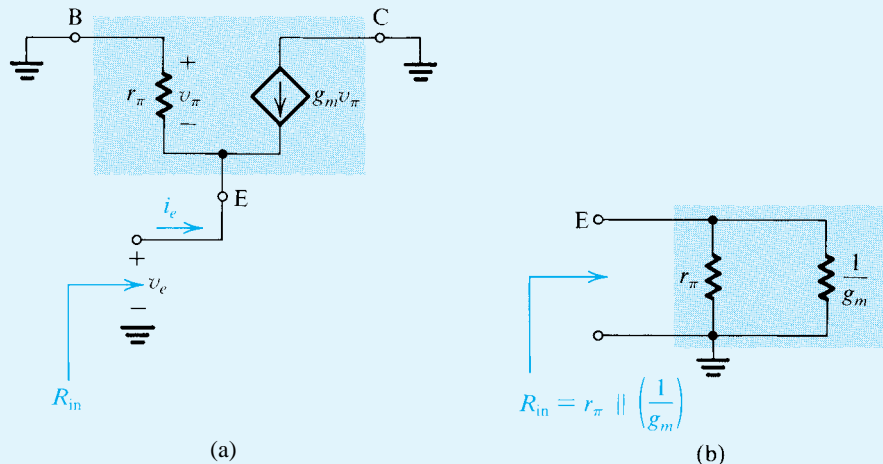


**Figure D.5** Circuit for Example D.2.

**Solution**

From Fig. D.5(a), we see that the voltage  $v_{\pi}$  will be equal to  $-v_e$ . Thus, looking between E and ground, we see a resistance  $r_{\pi}$  in parallel with a current source drawing a current  $g_m v_e$  away from terminal E. The latter source can be replaced by a resistance  $(1/g_m)$ , resulting in the input resistance  $R_{in}$  given by

$$R_{in} = r_{\pi} \parallel (1/g_m)$$

as illustrated in Fig. D.5(b).

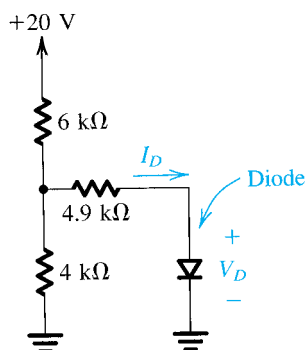
**EXERCISES**

- D.1** A source is measured and found to have a 10-V open-circuit voltage and to provide 1 mA into a short circuit. Calculate its Thévenin and Norton equivalent source parameters.

**Ans.**  $V_t = 10$  V;  $Z_t = Z_n = 10$  k $\Omega$ ;  $I_n = 1$  mA

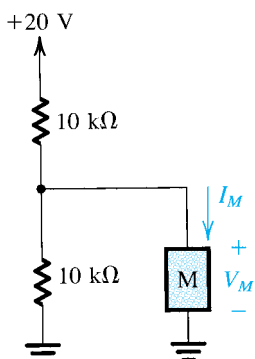
- D.2** In the circuit shown in Fig. ED.2, the diode has a voltage drop  $V_D \approx 0.7$  V. Use Thévenin’s theorem to simplify the circuit and hence calculate the diode current  $I_D$ .

**Ans.** 1 mA

**Figure ED.2**

- D.3** The two-terminal device M in the circuit of Fig. ED.3 has a current  $I_M \approx 1 \text{ mA}$  independent of the voltage  $V_M$  across it. Use Norton's theorem to simplify the circuit and hence calculate the voltage  $V_M$ .

**Ans.** 5 V

**Figure ED.3**

## PROBLEMS

- D.1** Consider the Thévenin equivalent circuit characterized by  $V_t$  and  $Z_t$ . Find the open-circuit voltage  $V_{oc}$  and the short-circuit current  $I_{sD}$  (i.e., the current that flows when the terminals are shorted together). Express  $Z_t$  in terms of  $V_{oc}$  and  $I_{sD}$ .

- D.2** Repeat Problem D.1 for a Norton equivalent circuit characterized by  $I_n$  and  $Z_n$ .

- D.3** A voltage divider consists of a 9-kΩ resistor connected to +10 V and a resistor of 1 kΩ connected to ground. What is the Thévenin equivalent of this voltage divider? What output voltage results if it is loaded with 1 kΩ? Calculate this two ways: directly and using your Thévenin equivalent.

## D-6 Appendix D Some Useful Network Theorems

**D.4** Find the output voltage and output resistance of the circuit shown in Fig. PD.4 by considering a succession of Thévenin equivalent circuits.

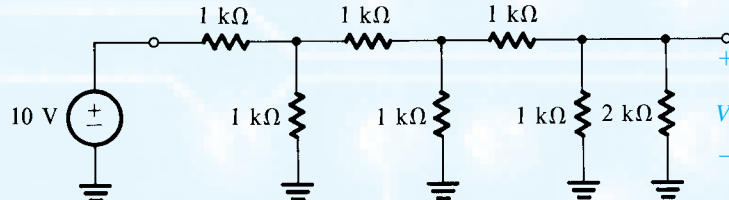


Figure PD.4

**D.5** Repeat Example D.2 with a resistance  $R_B$  connected between B and ground in Fig. D.5 (i.e., rather than directly grounding the base B as indicated in Fig. D.5).

**D.6** Figure PD.6(a) shows the circuit symbol of a device known as the *p*-channel junction field-effect transistor (JFET). As indicated, the JFET has three terminals. When the gate terminal G is connected to the source terminal S, the two-terminal device shown in Fig. PD.6(b) is obtained. Its  $i$ - $v$  characteristic is given by

$$\begin{aligned} i &= I_{DSS} \left[ 2 \frac{v}{V_P} - \left( \frac{v}{V_P} \right)^2 \right] && \text{for } v \leq V_P \\ i &= I_{DSS} && \text{for } v \geq V_P \end{aligned}$$

where  $I_{DSS}$  and  $V_P$  are positive constants for the particular JFET. Now consider the circuit shown in Fig. PD.6(c) and let  $V_P = 2$  V and  $I_{DSS} = 2$  mA. For  $V^+ = 10$  V show that the JFET is operating in the constant-current mode and find the voltage across it. What is the minimum value of  $V^+$  for which this mode of operation is maintained? For  $V^+ = 2$  V find the values of  $I$  and  $V$ .

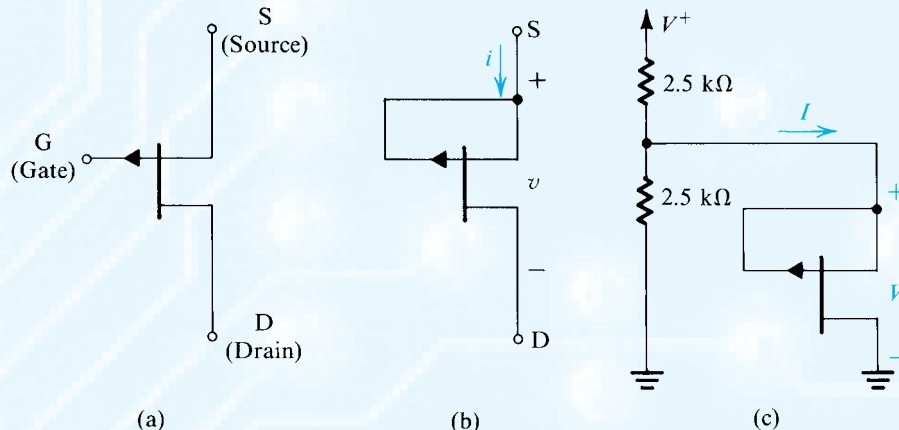


Figure PD.6

## APPENDIX E

# SINGLE-TIME-CONSTANT CIRCUITS

### Introduction

Single-time-constant (STC) circuits are those circuits that are composed of or can be reduced to one reactive component (inductance or capacitance) and one resistance. An STC circuit formed of an inductance  $L$  and a resistance  $R$  has a time constant  $\tau = L/R$ . The time constant  $\tau$  of an STC circuit composed of a capacitance  $C$  and a resistance  $R$  is given by  $\tau = CR$ .

Although STC circuits are quite simple, they play an important role in the design and analysis of linear and digital circuits. For instance, the analysis of an amplifier circuit can usually be reduced to the analysis of one or more STC circuits. For this reason, we will review in this appendix the process of evaluating the response of STC circuits to sinusoidal and other input signals such as step and pulse waveforms. The latter signal waveforms are encountered in some amplifier applications but are more important in switching circuits, including digital circuits.

### E.1 Evaluating the Time Constant

The first step in the analysis of an STC circuit is to evaluate its time constant  $\tau$ .

#### Example E.1

Reduce the circuit in Fig. E.1(a) to an STC circuit, and find its time constant.

#### Solution

The reduction process is illustrated in Fig. E.1 and consists of repeated applications of Thévenin's theorem. From the final circuit (Fig. E.1c), we obtain the time constant as

$$\tau = C \{ R_4 \parallel [R_3 + (R_1 \parallel R_2)] \}$$

#### E.1.1 Rapid Evaluation of $\tau$

In many instances, it will be important to be able to evaluate rapidly the time constant  $\tau$  of a given STC circuit. A simple method for accomplishing this goal consists first of reducing the excitation to zero; that is, if the excitation is by a voltage source, short it, and if by a current

## E-2 Appendix E Single-Time-Constant Circuits

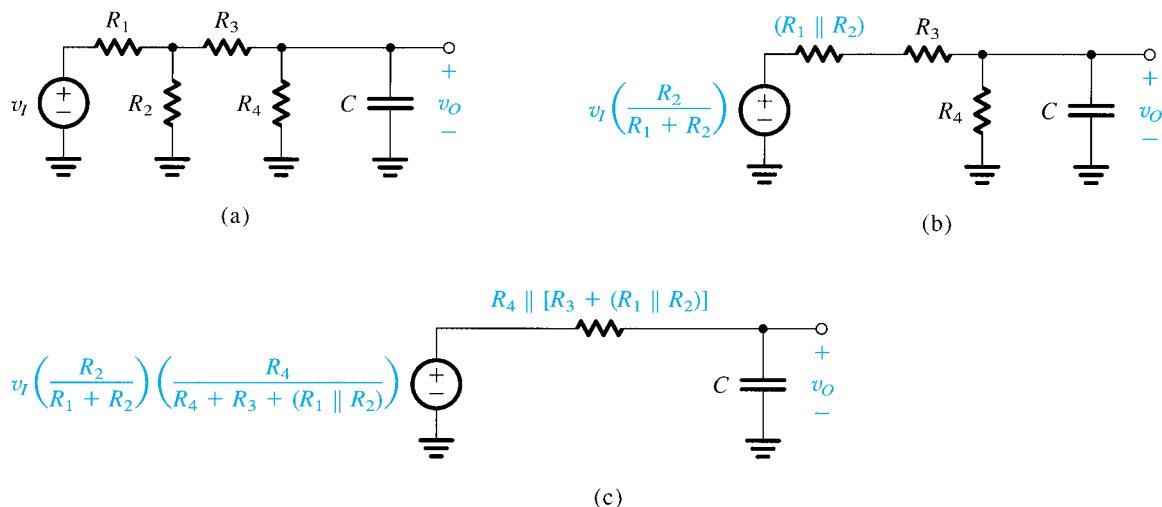


**Figure E.1** The reduction of the circuit in (a) to the STC circuit in (c) through the repeated application of Thévenin’s theorem.

source, open it. Then, if the circuit has one reactive component and a number of resistances, “grab hold” of the two terminals of the reactive component (capacitance or inductance) and find the equivalent resistance  $R_{\text{eq}}$  seen by the component. The time constant is then either  $L/R_{\text{eq}}$  or  $CR_{\text{eq}}$ . As an example, in the circuit of Fig. E.1(a), we find that the capacitor  $C$  “sees” a resistance  $R_4$  in parallel with the series combination of  $R_3$  and  $R_2$  in parallel with  $R_1$ . Thus

$$R_{\text{eq}} = R_4 \parallel [R_3 + (R_2 \parallel R_1)]$$

and the time constant is  $CR_{\text{eq}}$ .

In some cases it may be found that the circuit has one resistance and a number of capacitances or inductances. In such a case, the procedure should be inverted; that is, “grab hold” of the resistance terminals and find the equivalent capacitance  $C_{\text{eq}}$ , or equivalent inductance  $L_{\text{eq}}$ , seen by this resistance. The time constant is then found as  $C_{\text{eq}}R$  or  $L_{\text{eq}}/R$ . This is illustrated in Example E.2.

### Example E.2

Find the time constant of the circuit in Fig. E.2.

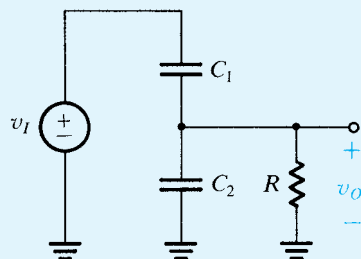


**Figure E.2** Circuit for Example E.2.

**Solution**

After reducing the excitation to zero by short-circuiting the voltage source, we see that the resistance  $R$  “sees” an equivalent capacitance  $C_1 + C_2$ . Thus, the time constant  $\tau$  is given by

$$\tau = (C_1 + C_2)R$$

Finally, in some cases an STC circuit has more than one resistance and more than one capacitance (or more than one inductance). Such cases require some initial work to simplify the circuit, as illustrated by Example E.3.

**Example E.3**

Here we show that the response of the circuit in Fig. E.3(a) can be obtained using the method of analysis of STC circuits.

**Solution**

The analysis steps are illustrated in Fig. E.3. In Fig. E.3(b) we show the circuit excited by two separate but equal voltage sources. The reader should convince himself or herself of the equivalence of the circuits in Fig. E.3(a) and E.3(b). The “trick” employed to obtain the arrangement in Fig. E.3(b) is a very useful one.

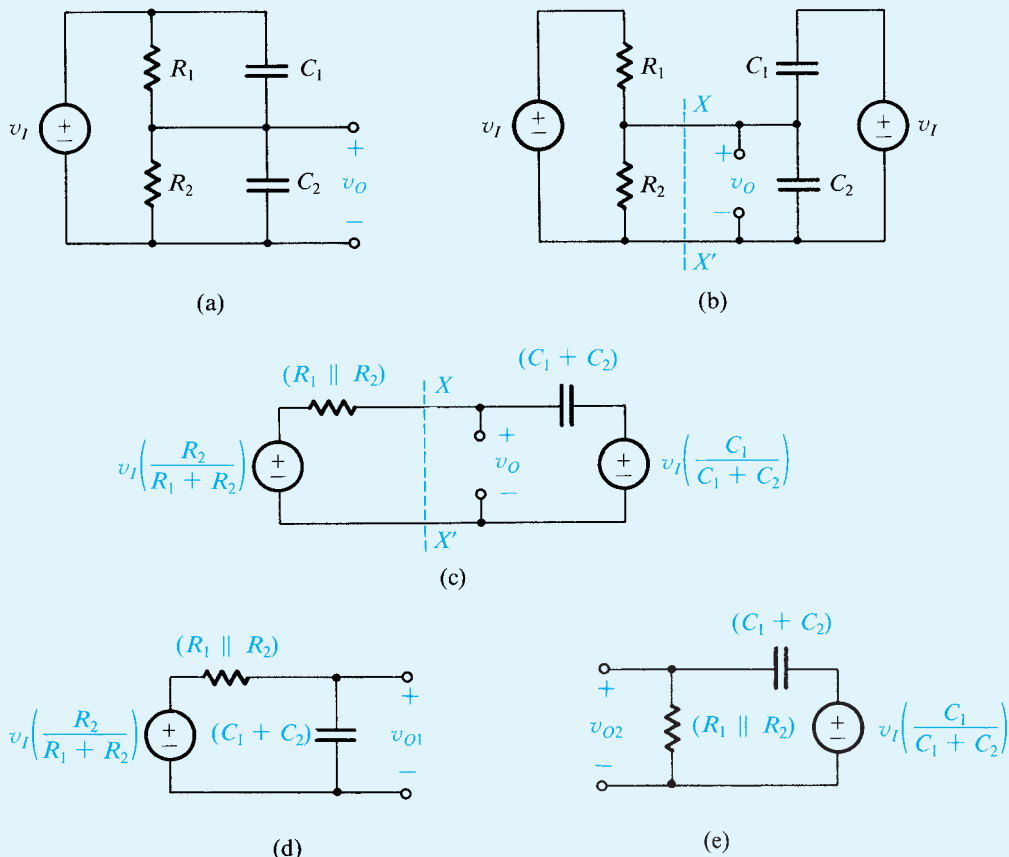


**Figure E.3** The response of the circuit in (a) can be found by superposition, that is, by summing the responses of the circuits in (d) and (e).

**Example E.3** *continued*

Application of Thévenin's theorem to the circuit to the left of the line  $XX'$  and then to the circuit to the right of that line results in the circuit of Fig. E.3(c). Since this is a linear circuit, the response may be obtained using the principle of superposition. Specifically, the output voltage  $v_O$  will be the sum of the two components  $v_{O1}$  and  $v_{O2}$ . The first component,  $v_{O1}$ , is the output due to the left-hand-side voltage source with the other voltage source reduced to zero. The circuit for calculating  $v_{O1}$  is shown in Fig. E.3(d). It is an STC circuit with a time constant given by

$$\tau = (C_1 + C_2)(R_1 \parallel R_2)$$

Similarly, the second component  $v_{O2}$  is the output obtained with the left-hand-side voltage source reduced to zero. It can be calculated from the circuit of Fig. E.3(e), which is an STC circuit with the same time constant  $\tau$ .

Finally, it should be observed that the fact that the circuit is an STC one can also be ascertained by setting the independent source  $v_I$  in Fig. E.3(a) to zero. Also, the time constant is then immediately obvious.

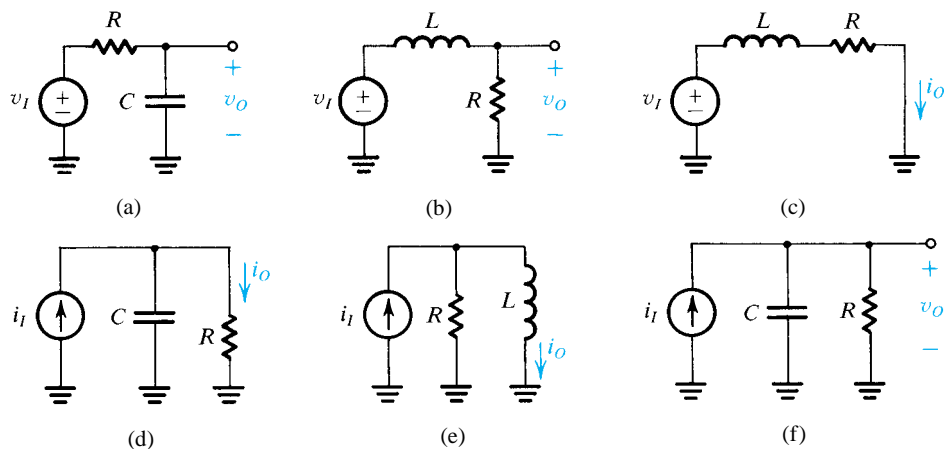
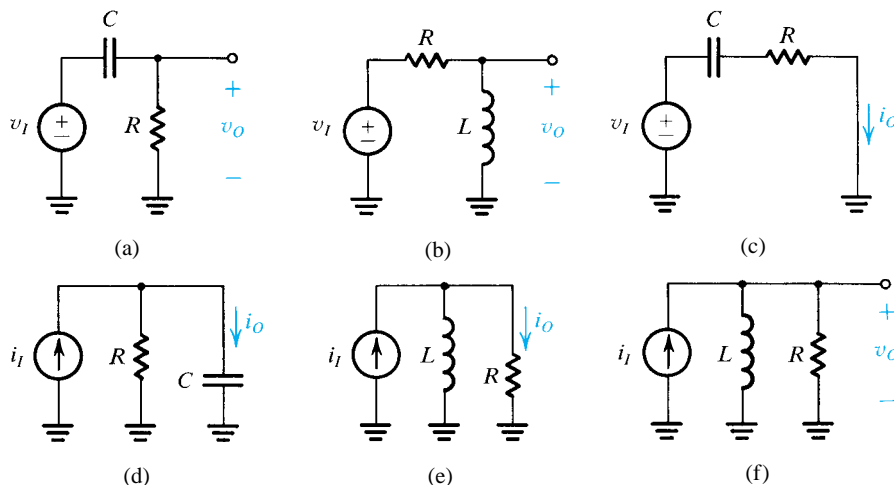
## E.2 Classification of STC Circuits

STC circuits can be classified into two categories, *low-pass* (LP) and *high-pass* (HP) types, with each category displaying distinctly different signal responses. The task of finding whether an STC circuit is of LP or HP type may be accomplished in a number of ways, the simplest of which uses the frequency domain response. Specifically, low-pass circuits pass dc (i.e., signals with zero frequency) and attenuate high frequencies, with the transmission being zero at  $\omega = \infty$ . Thus, we can test for the circuit type either at  $\omega = 0$  or at  $\omega = \infty$ . At  $\omega = 0$  capacitors should be replaced by open circuits ( $1/j\omega C = \infty$ ) and inductors should be replaced by short circuits ( $j\omega L = 0$ ). Then if the output is zero, the circuit is of the high-pass type, while if the output is finite, the circuit is of the low-pass type. Alternatively, we may test at  $\omega = \infty$  by replacing capacitors with short circuits ( $1/j\omega C = 0$ ) and inductors with open circuits ( $j\omega L = \infty$ ). Then if the output is finite, the circuit is of the HP type, whereas if the output is zero, the circuit is of the LP type. In Table E.1, which provides a summary of these results, s.c. stands for short circuit and o.c. for open circuit.

Figure E.4 shows examples of low-pass STC circuits, and Fig. E.5 shows examples of high-pass STC circuits. For each circuit we have indicated the input and output variables of interest. Note that a given circuit can be of either category, depending on the input and output variables. The reader is urged to verify, using the rules of Table E.1, that the circuits of Figs. E.4 and E.5 are correctly classified.

**Table E.1** Rules for Finding the Type of STC Circuit

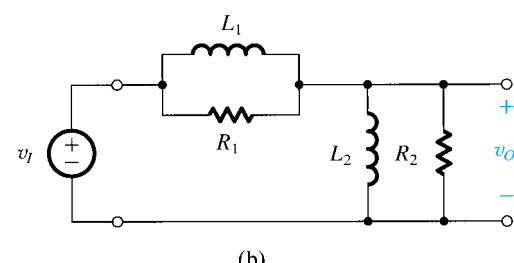
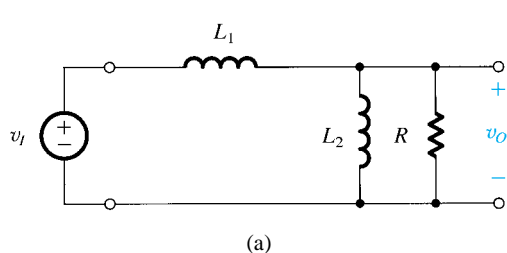
Test at	Replace	Circuit is LP if	Circuit is HP if
$\omega = 0$	$C$ by o.c. $L$ by s.c.	output is finite	output is zero
$\omega = \infty$	$C$ by s.c. $L$ by o.c.	output is zero	output is finite

**Figure E.4** STC circuits of the low-pass type.**Figure E.5** STC circuits of the high-pass type.

## EXERCISES

**E.1** Find the time constants for the circuits shown in Fig. EE.1.

$$\text{Ans. (a)} \frac{(L_1 \parallel L_2)}{R}; \text{ (b)} \frac{(L_1 \parallel L_2)}{(R_1 \parallel R_2)}$$

**Figure EE.1**

- E.2** Classify the following circuits as STC high-pass or low-pass: Fig. E.4(a) with output  $i_O$  in  $C$  to ground; Fig. E.4(b) with output  $i_O$  in  $R$  to ground; Fig. E.4(d) with output  $i_O$  in  $C$  to ground; Fig. E.4(e) with output  $i_O$  in  $R$  to ground; Fig. E.5(b) with output  $i_O$  in  $L$  to ground; and Fig. E.5(d) with output  $v_O$  across  $C$ .

**Ans.** HP; LP; HP; HP; LP; LP

## E.3 Frequency Response of STC Circuits

### E.3.1 Low-Pass Circuits

The transfer function  $T(s)$  of an STC low-pass circuit can always be written in the form

$$T(s) = \frac{K}{1 + (s/\omega_0)} \quad (\text{E.1})$$

which, for physical frequencies, where  $s = j\omega$ , becomes

$$T(j\omega) = \frac{K}{1 + j(\omega/\omega_0)} \quad (\text{E.2})$$

where  $K$  is the magnitude of the transfer function at  $\omega = 0$  (dc) and  $\omega_0$  is defined by

$$\omega_0 = 1/\tau$$

with  $\tau$  being the time constant. Thus the magnitude response is given by

$$|T(j\omega)| = \frac{K}{\sqrt{1 + (\omega/\omega_0)^2}} \quad (\text{E.3})$$

and the phase response is given by

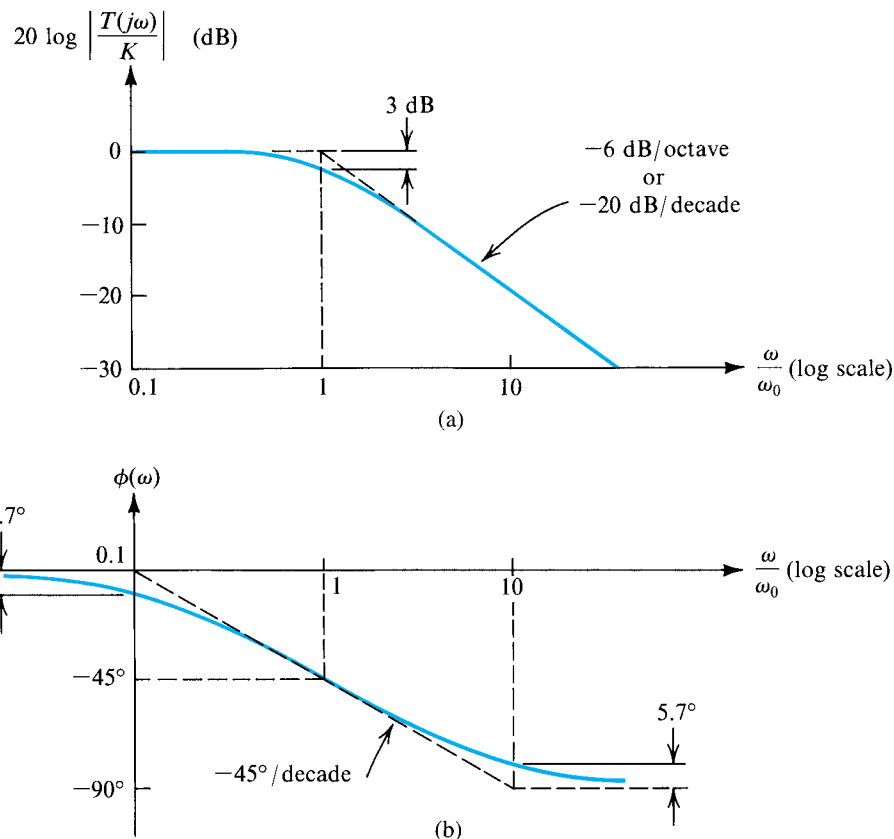
$$\phi(\omega) = -\tan^{-1}(\omega/\omega_0) \quad (\text{E.4})$$

Figure E.6 sketches the magnitude and phase responses for an STC low-pass circuit. The magnitude response shown in Fig. E.6(a) is simply a graph of the function in Eq. (E.3). The magnitude is normalized with respect to the dc gain  $K$  and is expressed in decibels; that is, the plot is for  $20 \log|T(j\omega)/K|$ , with a logarithmic scale used for the frequency axis. Furthermore, the frequency variable has been normalized with respect to  $\omega_0$ . As shown, the magnitude curve is closely defined by two straight-line asymptotes. The low-frequency asymptote is a horizontal straight line at 0 dB. To find the slope of the high-frequency asymptote, consider Eq. (E.3) and let  $\omega/\omega_0 \gg 1$ , resulting in

$$|T(j\omega)| \approx K \frac{\omega_0}{\omega}$$

It follows that if  $\omega$  doubles in value, the magnitude is halved. On a logarithmic frequency axis, doublings of  $\omega$  represent equally spaced points, with each interval called an *octave*. Halving the magnitude function corresponds to a 6-dB reduction in transmission ( $20 \log 0.5 = -6$  dB). Thus the slope of the high-frequency asymptote is  $-6$  dB/octave. This can be equivalently expressed as  $-20$  dB/decade, where “decade” indicates an increase in frequency by a factor of 10.

The two straight-line asymptotes of the magnitude-response curve meet at the “corner frequency” or “break frequency”  $\omega_0$ . The difference between the actual magnitude-response curve



**Figure E.6** (a) Magnitude and (b) phase response of STC circuits of the low-pass type.

and the asymptotic response is largest at the corner frequency, where its value is 3 dB. To verify that this value is correct, simply substitute  $\omega = \omega_0$  in Eq. (E.3) to obtain

$$|T(j\omega_0)| = K/\sqrt{2}$$

Thus at  $\omega = \omega_0$ , the gain drops by a factor of  $\sqrt{2}$  relative to the dc gain, which corresponds to a 3-dB reduction in gain. The corner frequency  $\omega_0$  is appropriately referred to as the 3-dB frequency.

Similar to the magnitude response, the phase-response curve, shown in Fig. E.6(b), is closely defined by straight-line asymptotes. Note that at the corner frequency the phase is  $-45^\circ$ , and that for  $\omega \gg \omega_0$  the phase approaches  $-90^\circ$ . Also note that the  $-45^\circ/\text{decade}$  straight line approximates the phase function, with a maximum error of  $5.7^\circ$ , over the frequency range  $0.1\omega_0$  to  $10\omega_0$ .

### Example E.4

Consider the circuit shown in Fig. E.7(a), where an ideal voltage amplifier of gain  $\mu = -100$  has a small (10-pF) capacitance connected in its feedback path. The amplifier is fed by a voltage source having a source resistance of  $100 \text{ k}\Omega$ . Show that the frequency response  $V_o/V_s$  of this amplifier is equivalent to that of an STC circuit, and sketch the magnitude response.

**Example E.4** continued

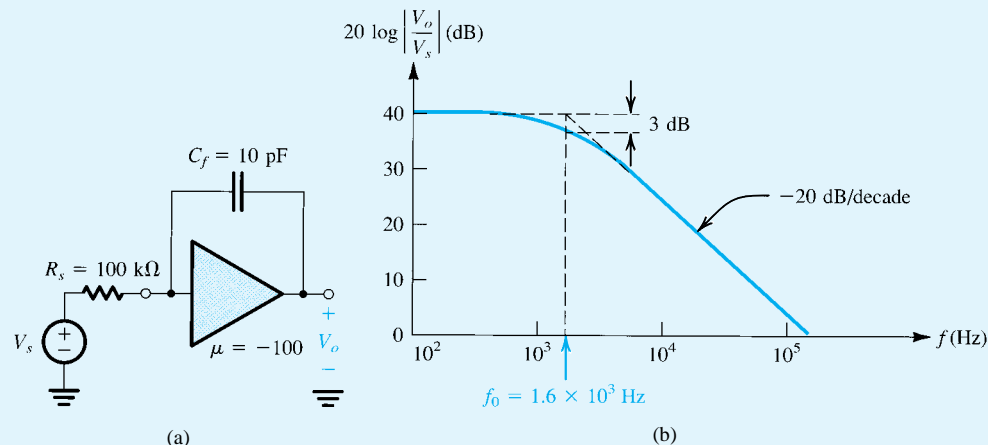


**Figure E.7** (a) An amplifier circuit and (b) a sketch of the magnitude of its transfer function.

### Solution

Direct analysis of the circuit in Fig. E.7(a) results in the transfer function

$$\frac{V_o}{V_s} = \frac{\mu}{1 + sRC_f(-\mu + 1)}$$

which can be seen to be that of a low-pass STC circuit with a dc gain  $\mu = -100$  (or, equivalently, 40 dB) and a time constant  $\tau = RC_f(-\mu + 1) = 100 \times 10^3 \times 10 \times 10^{-12} \times 101 \approx 10^{-4}$  s, which corresponds to a frequency  $\omega_0 = 1/\tau = 10^4$  rad/s. The magnitude response is sketched in Fig. E.7(b).

### E.3.2 High-Pass Circuits

The transfer function  $T(s)$  of an STC high-pass circuit can always be expressed in the form

$$T(s) = \frac{Ks}{s + \omega_0} \quad (\text{E.5})$$

which for physical frequencies  $s = j\omega$  becomes

$$T(j\omega) = \frac{K}{1 - j\omega_0/\omega} \quad (\text{E.6})$$

where  $K$  denotes the gain as  $s$  or  $\omega$  approaches infinity and  $\omega_0$  is the inverse of the time constant  $\tau$ ,

$$\omega_0 = 1/\tau$$

The magnitude response

$$|T(j\omega)| = \frac{K}{\sqrt{1 + (\omega_0/\omega)^2}} \quad (\text{E.7})$$

and the phase response

$$\phi(\omega) = \tan^{-1}(\omega_0/\omega) \quad (\text{E.8})$$

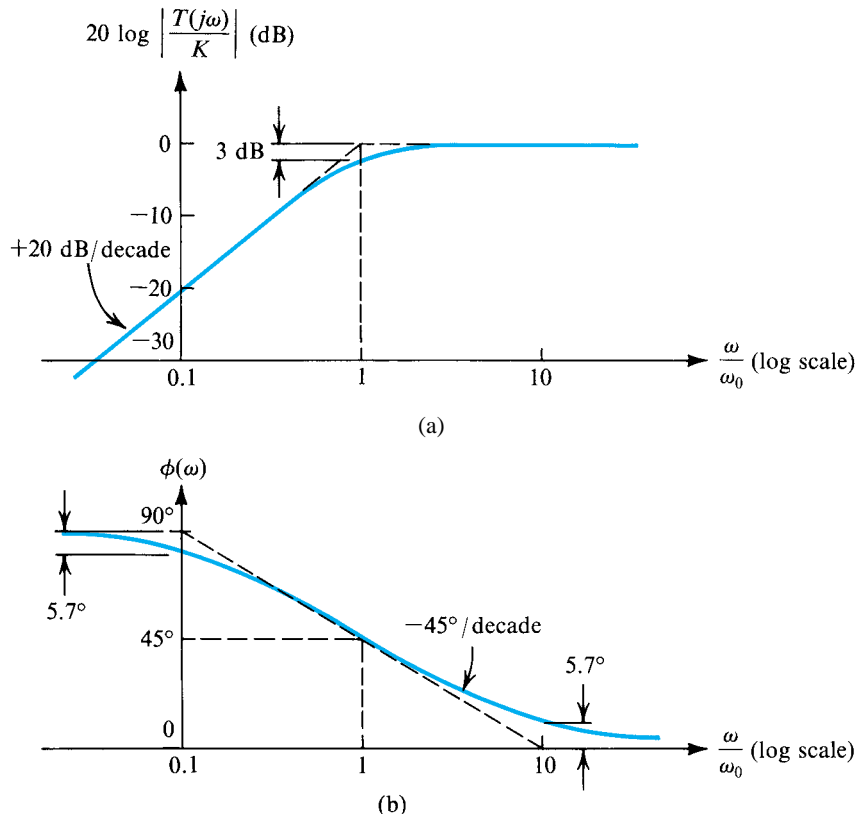


**Figure E.8** (a) Magnitude and (b) phase response of STC circuits of the high-pass type.

are sketched in Fig. E.8. As in the low-pass case, the magnitude and phase curves are well defined by straight-line asymptotes. Because of the similarity (or, more appropriately, duality) with the low-pass case, no further explanation will be given.

### EXERCISES

- E.3** Find the dc transmission, the corner frequency  $f_0$ , and the transmission at  $f = 2$  MHz for the low-pass STC circuit shown in Fig. EE.3.

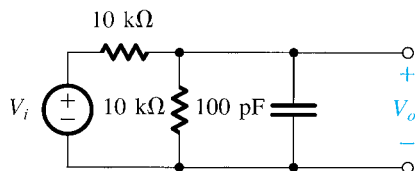


**Figure EE.3**

**Ans.**  $-6 \text{ dB}$ ;  $318 \text{ kHz}$ ;  $-22 \text{ dB}$

- E.4** Find the transfer function  $T(s)$  of the circuit in Fig. E.2. What type of STC network is it?

$$\text{Ans. } T(s) = \frac{C_1}{C_1 + C_2} \frac{s}{s + [1/(C_1 + C_2)R]}; \text{ HP}$$

- E.5** For the situation discussed in Exercise E.4, if  $R = 10 \text{ k}\Omega$ , find the capacitor values that result in the circuit having a high-frequency transmission of 0.5 V/V and a corner frequency  $\omega_0 = 10 \text{ rad/s}$ .

**Ans.**  $C_1 = C_2 = 5 \mu\text{F}$

- E.6** Find the high-frequency gain, the 3-dB frequency  $f_0$ , and the gain at  $f = 1 \text{ Hz}$  of the capacitively coupled amplifier shown in Fig. EE.6. Assume the voltage amplifier to be ideal.

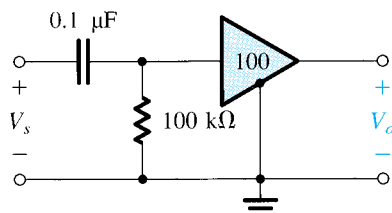


**Figure EE.6**

**Ans.** 40 dB; 15.9 Hz; 16 dB

## E.4 Step Response of STC Circuits

In this section we consider the response of STC circuits to the step-function signal shown in Fig. E.9. Knowledge of the step response enables rapid evaluation of the response to other switching-signal waveforms, such as pulses and square waves.

### E.4.1 Low-Pass Circuits

In response to an input step signal of height  $S$ , a low-pass STC circuit (with a dc gain  $K = 1$ ) produces the waveform shown in Fig. E.10. Note that while the input rises from 0 to  $S$  at  $t = 0$ , the output does not respond immediately to this transient and simply begins to rise exponentially toward the *final* dc value of the input,  $S$ . In the long term—that is, for  $t \gg \tau$ —the output approaches the dc value  $S$ , a manifestation of the fact that low-pass circuits faithfully pass dc.

The equation of the output waveform can be obtained from the expression

$$y(t) = Y_\infty - (Y_\infty - Y_{0+})e^{-t/\tau} \quad (\text{E.9})$$

where  $Y_\infty$  denotes the *final* value or the value toward which the output is heading and  $Y_{0+}$  denotes the value of the output immediately after  $t = 0$ . This equation states that *the output at any time  $t$  is equal to the difference between the final value  $Y_\infty$  and a gap that has an initial value of  $Y_\infty - Y_{0+}$  and is “shrinking” exponentially*. In our case,  $Y_\infty = S$  and  $Y_{0+} = 0$ ; thus,

$$y(t) = S(1 - e^{-t/\tau}) \quad (\text{E.10})$$

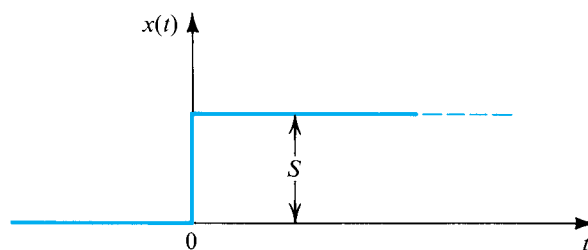


**Figure E.9** A step-function signal of height  $S$ .  
©2010 Oxford University Press, Inc.  
Reprinting or distribution, electronically or otherwise, without the express written consent of Oxford University Press, Inc. is prohibited.

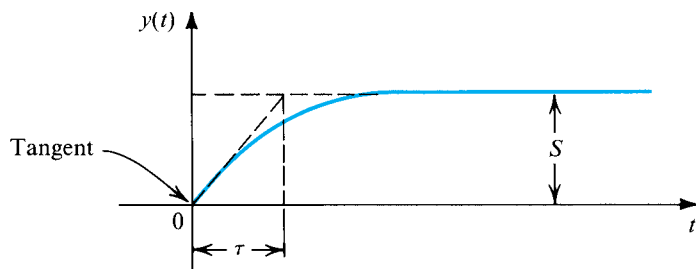


**Figure E.10** The output  $y(t)$  of a low-pass STC circuit excited by a step of height  $S$ .

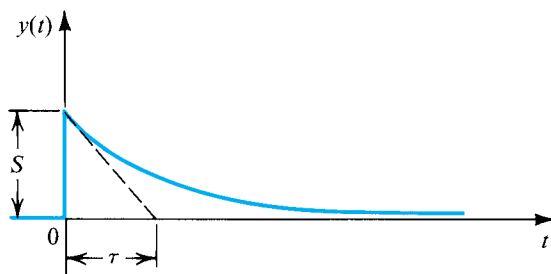


**Figure E.11** The output  $y(t)$  of a high-pass STC circuit excited by a step of height  $S$ .

The reader's attention is drawn to the slope of the tangent to  $y(t)$  at  $t = 0$ , which is indicated in Fig. E.10.

## E.4.2 High-Pass Circuits

The response of an STC high-pass circuit (with a high-frequency gain  $K = 1$ ) to an input step of height  $S$  is shown in Fig. E.11. The high-pass circuit faithfully transmits the transient part of the input signal (the step change) but blocks the dc. Thus the output at  $t = 0$  follows the input,

$$Y_{0+} = S$$

and then it decays toward zero,

$$Y_\infty = 0$$

Substituting for  $Y_{0+}$  and  $Y_\infty$  in Eq. (E.9) results in the output  $y(t)$ ,

$$y(t) = Se^{-t/\tau} \quad (\text{E.11})$$

The reader's attention is drawn to the slope of the tangent to  $y(t)$  at  $t = 0$ , indicated in Fig. E.11.

### Example E.5

This example is a continuation of the problem considered in Example E.3. For an input  $v_i$  that is a 10-V step, find the condition under which the output  $v_O$  is a perfect step.

#### Solution

Following the analysis in Example E.3, which is illustrated in Fig. E.3, we have

$$v_{O1} = k_r[10(1 - e^{-t/\tau})]$$

**Example E.5** *continued*

where

$$k_r \equiv \frac{R_2}{R_1 + R_2}$$

and

$$v_{O2} = k_c(10e^{-t/\tau})$$

where

$$k_c \equiv \frac{C_1}{C_1 + C_2}$$

and

$$\tau = (C_1 + C_2)(R_1 \parallel R_2)$$

Thus

$$\begin{aligned} v_O &= v_{O1} + v_{O2} \\ &= 10k_r + 10e^{-t/\tau}(k_c - k_r) \end{aligned}$$

It follows that the output can be made a perfect step of height  $10k_r$  volts if we arrange that

$$k_c = k_r$$

that is, if the resistive voltage divider ratio is made equal to the capacitive voltage divider ratio.

This example illustrates an important technique, namely, that of the “compensated attenuator.” An application of this technique is found in the design of the oscilloscope probe. The oscilloscope probe problem is investigated in Problem E.3.

**EXERCISES**

- E.7** For the circuit of Fig. E.4(f), find  $v_O$  if  $i_I$  is a 3-mA step,  $R = 1 \text{ k}\Omega$ , and  $C = 100 \text{ pF}$ .

**Ans.**  $3(1 - e^{-10^7 t})$

- E.8** In the circuit of Fig. E.5(f), find  $v_O(t)$  if  $i_I$  is a 2-mA step,  $R = 2 \text{ k}\Omega$ , and  $L = 10 \mu\text{H}$ .

**Ans.**  $4e^{-2 \times 10^8 t}$

- E.9** The amplifier circuit of Fig. EE.6 is fed with a signal source that delivers a 20-mV step. If the source resistance is  $100 \text{ k}\Omega$ , find the time constant  $\tau$  and  $v_O(t)$ .

**Ans.**  $\tau = 2 \times 10^{-2} \text{ s}; v_O(t) = 1 \times e^{-50t}$

- E.10** For the circuit in Fig. E.2 with  $C_1 = C_2 = 0.5 \mu\text{F}$ ,  $R = 1 \text{ M}\Omega$ , find  $v_O(t)$  if  $v_I(t)$  is a 10-V step.

**Ans.**  $5e^{-t}$

- E.11** Show that the area under the exponential of Fig. E.11 is equal to that of the rectangle of height  $S$  and width  $\tau$ .

## E.5 Pulse Response of STC Circuits

Figure E.12 shows a pulse signal whose height is  $P$  and whose width is  $T$ . We wish to find the response of STC circuits to input signals of this form. Note at the outset that a pulse can be considered as the sum of two steps: a positive one of height  $P$  occurring at  $t = 0$  and a negative one of height  $P$  occurring at  $t = T$ . Thus, the response of a linear circuit to the pulse signal can be obtained by summing the responses to the two step signals.

### E.5.1 Low-Pass Circuits

Figure E.13(a) shows the response of a low-pass STC circuit (having unity dc gain) to an input pulse of the form shown in Fig. E.12. In this case, we have assumed that the time constant  $\tau$  is in the same range as the pulse width  $T$ . As shown, the LP circuit does not respond immediately to the step change at the leading edge of the pulse; rather, the output starts to rise exponentially toward a final value of  $P$ . This exponential rise, however, will be stopped at time  $t = T$ , that is, at the trailing edge of the pulse when the input undergoes a negative step change. Again, the output will respond by starting an exponential decay toward the final value of the input, which is zero. Finally, note that the area under the output waveform will be equal to the area under the input pulse waveform, since the LP circuit faithfully passes dc.

A low-pass effect usually occurs when a pulse signal from one part of an electronic system is connected to another. The low-pass circuit in this case is formed by the output resistance (Thévenin's equivalent resistance) of the system part from which the signal originates and the input capacitance of the system part to which the signal is fed. This unavoidable low-pass filter will cause distortion—of the type shown in Fig. E.13(a)—of the pulse signal. In a well-designed system such distortion is kept to a low value by arranging that the time constant  $\tau$  be much smaller than the pulse width  $T$ . In this case, the result will be a slight rounding of the pulse edges, as shown in Fig. E.13(b). Note, however, that the edges are still exponential.

The distortion of a pulse signal by a parasitic (i.e., unwanted) low-pass circuit is measured by its *rise time* and *fall time*. The rise time is conventionally defined as the time taken by the amplitude to increase from 10% to 90% of the final value. Similarly, the fall time is the time during which the pulse amplitude falls from 90% to 10% of the maximum value. These definitions are illustrated in Fig. E.13(b). By use of the exponential equations of the rising and falling edges of the output waveform, it can be easily shown that

$$t_r = t_f \approx 2.2\tau \quad (\text{E.12})$$

which can be also expressed in terms of  $f_0 = \omega_0/2\pi = 1/2\pi\tau$  as

$$t_r = t_f \approx \frac{0.35}{f_0} \quad (\text{E.13})$$

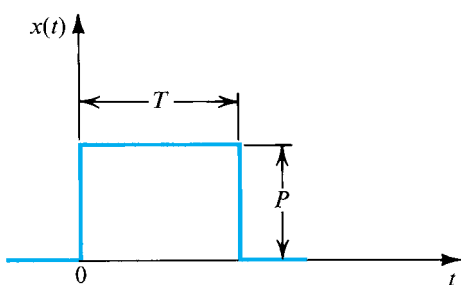


**Figure E.12** A pulse signal with height  $P$  and width  $T$ .

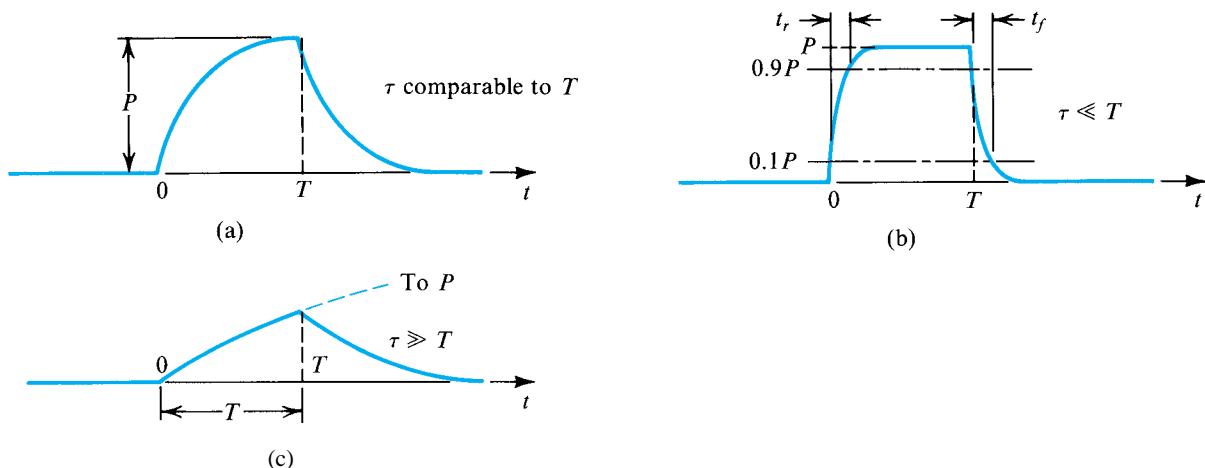


**Figure E.13** Pulse responses of three STC low-pass circuits.

Finally, we note that the effect of the parasitic low-pass circuits that are always present in a system is to “slow down” the operation of the system: To keep the signal distortion within acceptable limits, one has to use a relatively long pulse width (for a given low-pass time constant).

The other extreme case—namely, when  $\tau$  is much larger than  $T$ , is illustrated in Fig. E.13(c). As shown, the output waveform rises exponentially toward the level  $P$ . However, since  $\tau \gg T$ , the value reached at  $t = T$  will be much smaller than  $P$ . At  $t = T$ , the output waveform starts its exponential decay toward zero. Note that in this case the output waveform bears little resemblance to the input pulse. Also note that because  $\tau \gg T$ , the portion of the exponential curve from  $t = 0$  to  $t = T$  is almost linear. Since the slope of this linear curve is proportional to the height of the input pulse, we see that the output waveform approximates the time integral of the input pulse. That is, a low-pass network with a large time constant approximates the operation of an *integrator*.

### E.5.2 High-Pass Circuits

Figure E.14(a) shows the output of an STC HP circuit (with unity high-frequency gain) excited by the input pulse of Fig. E.12, assuming that  $\tau$  and  $T$  are comparable in value. As shown, the step transition at the leading edge of the input pulse is faithfully reproduced at the output of the HP circuit. However, since the HP circuit blocks dc, the output waveform immediately starts an exponential decay toward zero. This decay process is stopped at  $t = T$ , when the negative step transition of the input occurs and the HP circuit faithfully reproduces it. Thus, at  $t = T$  the output waveform exhibits an *undershoot*. Then it starts an exponential decay toward zero. Finally, note that the area of the output waveform above the zero axis will be equal to that below the axis for a total average area of zero, consistent with the fact that HP circuits block dc.

In many applications, an STC high-pass circuit is used to couple a pulse from one part of a system to another part. In such an application, it is necessary to keep the distortion in the pulse shape as small as possible. This can be accomplished by selecting the time constant  $\tau$  to be much longer than the pulse width  $T$ . If this is indeed the case, the loss in amplitude during the pulse period  $T$  will be very small, as shown in Fig. E.14(b). Nevertheless, the output waveform still swings negatively, and the area under the negative portion will be equal to that under the positive portion.

Consider the waveform in Fig. E.14(b). Since  $\tau$  is much larger than  $T$ , it follows that the portion of the exponential curve from  $t = 0$  to  $t = T$  will be almost linear and that its slope will be

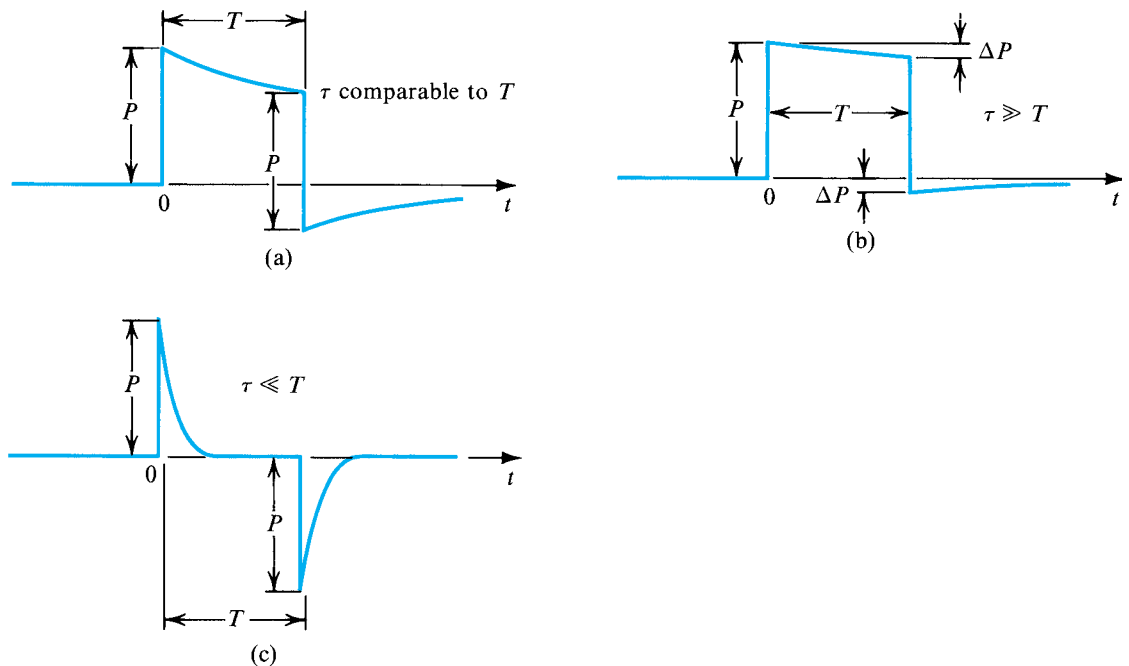


**Figure E.14** Pulse responses of three STC high-pass circuits.

equal to the slope of the exponential curve at  $t = 0$ , which is  $P/\tau$ . We can use this value of the slope to determine the loss in amplitude  $\Delta P$  as

$$\Delta P \approx \frac{P}{\tau} T \quad (\text{E.14})$$

The distortion effect of the high-pass circuit on the input pulse is usually specified in terms of the per-unit or percentage loss in pulse height. This quantity is taken as an indication of the “sag” in the output pulse,

$$\text{Percentage sag} \equiv \frac{\Delta P}{P} \times 100 \quad (\text{E.15})$$

Thus

$$\text{Percentage sag} = \frac{T}{\tau} \times 100 \quad (\text{E.16})$$

Finally, note that the magnitude of the undershoot at  $t = T$  is equal to  $\Delta P$ .

The other extreme case—namely,  $\tau \ll T$ —is illustrated in Fig. E.14(c). In this case, the exponential decay is quite rapid, resulting in the output becoming almost zero shortly beyond the leading edge of the pulse. At the trailing edge of the pulse, the output swings negatively by an amount almost equal to the pulse height  $P$ . Then the waveform decays rapidly to zero. As seen from Fig. E.14(c), the output waveform bears no resemblance to the input pulse. It consists of two spikes: a positive one at the leading edge and a negative one at the trailing edge. Note that the output waveform is approximately equal to the time derivative of the input pulse. That is, for  $\tau \ll T$ , an STC high-pass circuit approximates a *differentiator*. However, the resulting differentiator is not an ideal one; an ideal differentiator would produce two impulses. Nevertheless, high-pass STC circuits with short time constants are employed in some applications to produce sharp pulses or spikes at the transitions of an input waveform.

## EXERCISES

**E.12** Find the rise and fall times of a 1- $\mu$ s pulse after it has passed through a low-pass RC circuit with a corner frequency of 10 MHz.

**Ans.** 35 ns

**E.13** Consider the pulse response of a low-pass STC circuit, as shown in Fig. E.13(c). If  $\tau = 100T$ , find the output voltage at  $t = T$ . Also, find the difference in the slope of the rising portion of the output waveform at  $t = 0$  and  $t = T$  (expressed as a percentage of the slope at  $t = 0$ ).

**Ans.** 0.01P; 1%

**E.14** The output of an amplifier stage is connected to the input of another stage via a capacitance  $C$ . If the first stage has an output resistance of 10 k $\Omega$ , and the second stage has an input resistance of 40 k $\Omega$ , find the minimum value of  $C$  such that a 10- $\mu$ s pulse exhibits less than 1% sag.

**Ans.** 0.02  $\mu$ F

**E.15** A high-pass STC circuit with a time constant of 100  $\mu$ s is excited by a pulse of 1-V height and 100- $\mu$ s width. Calculate the value of the undershoot in the output waveform.

**Ans.** 0.632 V

## PROBLEMS

**E.1** Consider the circuit of Fig. E.3(a) and the equivalent shown in (d) and (e). There, the output,  $v_O = v_{O1} + v_{O2}$ , is the sum of outputs of a low-pass and a high-pass circuit, each with the time constant  $\tau = (C_1 + C_2)(R_1 \parallel R_2)$ . What is the condition that makes the contribution of the low-pass circuit at zero frequency equal to the contribution of the high-pass circuit at infinite frequency? Show that this condition can be expressed as  $C_1R_1 = C_2R_2$ . If this condition applies, sketch  $|V_o/V_i|$  versus frequency for the case  $R_1 = R_2$ .

**E.2** Use the voltage divider rule to find the transfer function  $V_o(s)/V_i(s)$  of the circuit in Fig. E.3(a). Show that the transfer function can be made independent of frequency if the condition  $C_1R_1 = C_2R_2$  applies. Under this condition the circuit is called a *compensated attenuator*. Find the transmission of the compensated attenuator in terms of  $R_1$  and  $R_2$ .

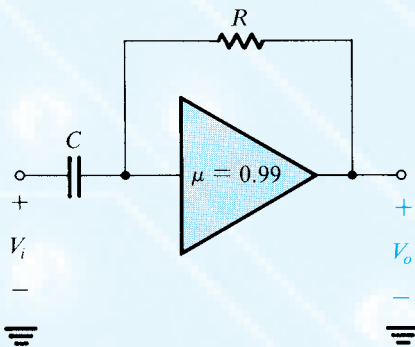
**\*\*DE.3** The circuit of Fig. E.3(a) is used as a compensated attenuator (see Problems E.1 and E.2) for an oscilloscope probe. The objective is to reduce the signal voltage applied to the input amplifier of the oscilloscope, with the signal attenuation independent of frequency. The probe itself includes  $R_1$  and  $C_1$ , while  $R_2$  and  $C_2$  model the oscilloscope input circuit. For an oscilloscope having an input resistance of 1 M $\Omega$  and an input capacitance of 30 pF,

design a compensated “10-to-1 probe”—that is, a probe that attenuates the input signal by a factor of 10. Find the input impedance of the probe when connected to the oscilloscope, which is the impedance seen by  $v_L$  in Fig. E.3(a). Show that this impedance is 10 times higher than that of the oscilloscope itself. This is the great advantage of the 10:1 probe.

**E.4** In the circuits of Figs. E.4 and E.5, let  $L = 10$  mH,  $C = 0.01$   $\mu$ F, and  $R = 1$  k $\Omega$ . At what frequency does a phase angle of 45° occur?

**\*E.5** Consider a voltage amplifier with an open-circuit voltage gain  $A_{vo} = -100$  V/V,  $R_o = 0$ ,  $R_i = 10$  k $\Omega$  and an input capacitance  $C_i$  (in parallel with  $R_i$ ) of 10 pF. The amplifier has a feedback capacitance (a capacitance connected between output and input)  $C_f = 1$  pF. The amplifier is fed with a voltage source  $V_s$  having a resistance  $R_s = 10$  k $\Omega$ . Find the amplifier transfer function  $V_o(s)/V_s(s)$  and sketch its magnitude response versus frequency (dB vs. frequency) on a log axis.

**E.6** For the circuit in Fig. PE.6, assume the voltage amplifier to be ideal. Derive the transfer function  $V_o(s)/V_i(s)$ . What type of STC response is this? For  $C = 0.01$   $\mu$ F and  $R = 100$  k $\Omega$ , find the corner frequency.

**Figure PE.6**

**E.7** For the circuits of Figs. E.4(b) and E.5(b), find  $v_O(t)$  if  $v_I$  is a 10-V step,  $R = 1 \text{ k}\Omega$  and  $L = 1 \text{ mH}$ .

**E.8** Consider the exponential response of an STC low-pass circuit to a 10-V step input. In terms of the time constant  $\tau$ , find the time taken for the output to reach 5 V, 9 V, 9.9 V, and 9.99 V.

**E.9** The high-frequency response of an oscilloscope is specified to be like that of an STC LP circuit with a 100-MHz corner frequency. If this oscilloscope is used to display an ideal step waveform, what rise time (10% to 90%) would you expect to observe?

**E.10** An oscilloscope whose step response is like that of a low-pass STC circuit has a rise time of  $t_s$  seconds. If an input signal having a rise time of  $t_w$  seconds is displayed, the waveform seen will have a rise time  $t_d$  seconds, which can be found using the empirical formula  $t_d = \sqrt{t_s^2 + t_w^2}$ . If  $t_s = 35 \text{ ns}$ , what is the 3-dB frequency of the oscilloscope? What is the

observed rise time for a waveform rising in 100 ns, 35 ns, and 10 ns? What is the actual rise time of a waveform whose displayed rise time is 49.5 ns?

**E.11** A pulse of 10-ms width and 10-V amplitude is transmitted through a system characterized as having an STC high-pass response with a corner frequency of 10 Hz. What undershoot would you expect?

**E.12** An RC differentiator having a time constant  $\tau$  is used to implement a short-pulse detector. When a long pulse with  $T \gg \tau$  is fed to the circuit, the positive and negative peak outputs are of equal magnitude. At what pulse width does the negative output peak differ from the positive one by 10%?

**E.13** A high-pass STC circuit with a time constant of 1 ms is excited by a pulse of 10-V height and 1-ms width. Calculate the value of the undershoot in the output waveform. If an undershoot of 1 V or less is required, what is the time constant necessary?

**E.14** A capacitor  $C$  is used to couple the output of an amplifier stage to the input of the next stage. If the first stage has an output resistance of  $2 \text{ k}\Omega$  and the second stage has an input resistance of  $3 \text{ k}\Omega$  find the value of  $C$  so that a 1-ms pulse exhibits less than 1% sag. What is the associated 3-dB frequency?

**DE.15** An RC differentiator is used to convert a step voltage change  $V$  to a single pulse for a digital-logic application. The logic circuit that the differentiator drives distinguishes signals above  $V/2$  as “high” and below  $V/2$  as “low.” What must the time constant of the circuit be to convert a step input into a pulse that will be interpreted as “high” for  $10 \mu\text{s}$ ?

**DE.16** Consider the circuit in Fig. E.7(a) with  $\mu = -100$ ,  $C_f = 100 \text{ pF}$ , and the amplifier being ideal. Find the value of  $R$  so that the gain  $|V_o/V_s|$  has a 3-dB frequency of 1 kHz.

## APPENDIX F

# *s*-DOMAIN ANALYSIS: POLES, ZEROS, AND BODE PLOTS

In analyzing the frequency response of an amplifier, most of the work involves finding the amplifier voltage gain as a function of the complex frequency  $s$ . In this  $s$ -domain analysis, a capacitance  $C$  is replaced by an admittance  $sC$ , or equivalently an impedance  $1/sC$ , and an inductance  $L$  is replaced by an impedance  $sL$ . Then, using usual circuit-analysis techniques, one derives the voltage transfer function  $T(s) \equiv V_o(s)/V_i(s)$ .

### EXERCISE

- F.1 Find the voltage transfer function  $T(s) \equiv V_o(s)/V_i(s)$  for the STC network shown in Fig. EF.1.

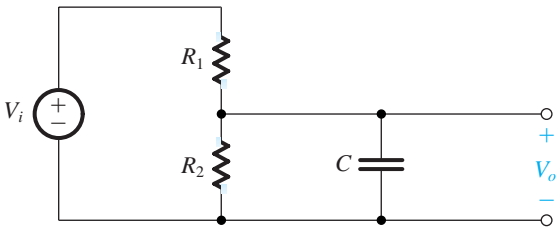


Figure EF.1

**Ans.**  $T(s) = \frac{1/CR_1}{s + 1/C(R_1 \parallel R_2)}$

Once the transfer function  $T(s)$  is obtained, it can be evaluated for **physical frequencies** by replacing  $s$  by  $j\omega$ . The resulting transfer function  $T(j\omega)$  is in general a complex quantity whose magnitude gives the magnitude response (or transmission) and whose angle gives the phase response of the amplifier.

In many cases it will not be necessary to substitute  $s = j\omega$  and evaluate  $T(j\omega)$ ; rather, the form of  $T(s)$  will reveal many useful facts about the circuit performance. In general, for all

the circuits dealt with in this book,  $T(s)$  can be expressed in the form

$$T(s) = \frac{a_m s^m + a_{m-1} s^{m-1} + \cdots + a_0}{s^n + b_{n-1} s^{n-1} + \cdots + b_0} \quad (\text{F.1})$$

where the coefficients  $a$  and  $b$  are real numbers, and the order  $m$  of the numerator is smaller than or equal to the order  $n$  of the denominator; the latter is called the **order of the network**. Furthermore, for a **stable circuit**—that is, one that does not generate signals on its own—the denominator coefficients should be such that *the roots of the denominator polynomial all have negative real parts*. The problem of amplifier stability is studied in Chapter 10.

## F.1 Poles and Zeros

An alternate form for expressing  $T(s)$  is

$$T(s) = a_m \frac{(s - Z_1)(s - Z_2) \cdots (s - Z_m)}{(s - P_1)(s - P_2) \cdots (s - P_n)} \quad (\text{F.2})$$

where  $a_m$  is a multiplicative constant (the coefficient of  $s^m$  in the numerator),  $Z_1, Z_2, \dots, Z_m$  are the roots of the numerator polynomial, and  $P_1, P_2, \dots, P_n$  are the roots of the denominator polynomial.  $Z_1, Z_2, \dots, Z_m$  are called the **transfer-function zeros** or **transmission zeros**, and  $P_1, P_2, \dots, P_n$  are the **transfer-function poles** or the **natural modes** of the network. A transfer function is completely specified in terms of its poles and zeros together with the value of the multiplicative constant.

The poles and zeros can be either real or complex numbers. However, since the  $a$  and  $b$  coefficients are real numbers, the complex poles (or zeros) must occur in **conjugate pairs**. That is, if  $5 + j\beta$  is a zero, then  $5 - j\beta$  also must be a zero. A zero that is purely imaginary ( $\pm j\omega_Z$ ) causes the transfer function  $T(j\omega)$  to be exactly zero at  $\omega = \omega_Z$ . This is because the numerator will have the factors  $(s + j\omega_Z)(s - j\omega_Z) = (s^2 + \omega_Z^2)$ , which for physical frequencies becomes  $(-\omega^2 + \omega_Z^2)$ , and thus the transfer fraction will be exactly zero at  $\omega = \omega_Z$ . Thus the “trap” one places at the input of a television set is a circuit that has a transmission zero at the particular interfering frequency. Real zeros, on the other hand, do not produce transmission nulls. Finally, note that for values of  $s$  much greater than all the poles and zeros, the transfer function in Eq. (F.1) becomes  $T(s) \approx a_m / s^{n-m}$ . Thus the transfer function has  $(n - m)$  zeros at  $s = \infty$ .

## F.2 First-Order Functions

Many of the transfer functions encountered in this book have real poles and zeros and can therefore be written as the product of first-order transfer functions of the general form

$$T(s) = \frac{a_1 s + a_0}{s + \omega_0} \quad (\text{F.3})$$

where  $-\omega_0$  is the location of the real pole. The quantity  $\omega_0$ , called the **pole frequency**, is equal to the inverse of the time constant of this single-time-constant (STC) network (see Appendix E). The constants  $a_0$  and  $a_1$  determine the type of STC network. Specifically, we

studied in Chapter 1 two types of STC networks, low pass and high pass. For the low-pass first-order network we have

$$T(s) = \frac{a_0}{s + \omega_0} \quad (\text{F.4})$$

In this case the dc gain is  $a_0/\omega_0$ , and  $\omega_0$  is the corner or 3-dB frequency. Note that this transfer function has one zero at  $s = \infty$ . On the other hand, the first-order high-pass transfer function has a zero at dc and can be written as

$$T(s) = \frac{a_1 s}{s + \omega_0} \quad (\text{F.5})$$

At this point the reader is strongly urged to review the material on STC networks and their frequency and pulse responses in Appendix E. Of specific interest are the plots of the magnitude and phase responses of the two special kinds of STC networks. Such plots can be employed to generate the magnitude and phase plots of a high-order transfer function, as explained below.

### F.3 Bode Plots

A simple technique exists for obtaining an approximate plot of the magnitude and phase of a transfer function given its poles and zeros. The technique is particularly useful in the case of real poles and zeros. The method was developed by H. Bode, and the resulting diagrams are called **Bode plots**.

A transfer function of the form depicted in Eq. (F.2) consists of a product of factors of the form  $s + a$ , where such a factor appears on top if it corresponds to a zero and on the bottom if it corresponds to a pole. It follows that the magnitude response in decibels of the network can be obtained by summing together terms of the form  $20 \log_{10} \sqrt{a^2 + \omega^2}$ , and the phase response can be obtained by summing terms of the form  $\tan^{-1}(\omega/a)$ . In both cases the terms corresponding to poles are summed with negative signs. For convenience we can extract the constant  $a$  and write the typical magnitude term in the form  $20 \log \sqrt{1 + (\omega/a)^2}$ . On a plot of decibels versus log frequency this term gives rise to the curve and straight-line asymptotes shown in Fig. F.1. Here the low-frequency asymptote is a horizontal straight line

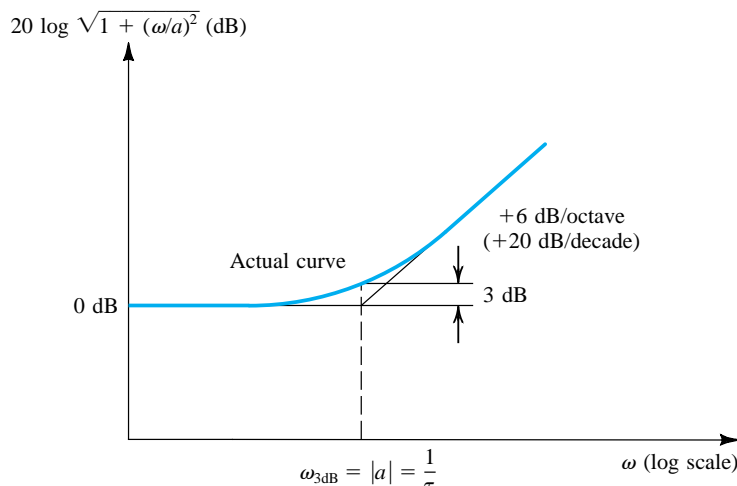


**Figure F.1** Bode plot for the typical magnitude term. The curve shown applies for the case of a zero. For a pole, the high-frequency asymptote should be drawn with a  $-6\text{-dB/octave}$  slope.

at 0-dB level and the high-frequency asymptote is a straight line with a slope of 6 dB/octave or, equivalently, 20 dB/decade. The two asymptotes meet at the frequency  $\omega = |a|$ , which is called the **corner frequency**. As indicated, the actual magnitude plot differs slightly from the value given by the asymptotes; the maximum difference is 3 dB and occurs at the corner frequency.

For  $a = 0$ —that is, a pole or a zero at  $s = 0$ —the plot is simply a straight line of 6 dB/octave slope intersecting the 0-dB line at  $\omega = 1$ .

In summary, to obtain the Bode plot for the magnitude of a transfer function, the asymptotic plot for each pole and zero is first drawn. The slope of the high-frequency asymptote of the curve corresponding to a zero is +20 dB/decade, while that for a pole is -20 dB/decade. The various plots are then added together, and the overall curve is shifted vertically by an amount determined by the multiplicative constant of the transfer function.

### Example F.1

An amplifier has the voltage transfer function

$$T(s) = \frac{10s}{(1+s/10^2)(1+s/10^5)}$$

Find the poles and zeros and sketch the magnitude of the gain versus frequency. Find approximate values for the gain at  $\omega = 10$ ,  $10^3$ , and  $10^6$  rad/s.

#### Solution

The zeros are as follows: one at  $s = 0$  and one at  $s = \infty$ . The poles are as follows: one at  $s = -10^2$  rad/s and one at  $s = -10^5$  rad/s.

Figure F.2 shows the asymptotic Bode plots of the different factors of the transfer function. Curve 1, which is a straight line intersecting the  $\omega$ -axis at 1 rad/s and having a +20 dB/decade slope, corresponds to the  $s$  term (that is, the zero at  $s = 0$ ) in the numerator. The pole at  $s = -10^2$  results in curve 2, which consists of two asymptotes intersecting at  $\omega = 10^2$ . Similarly, the pole at  $s = -10^5$  is represented by curve 3, where the intersection of the asymptotes is at  $\omega = 10^5$ . Finally, curve 4 represents the multiplicative constant of value 10.

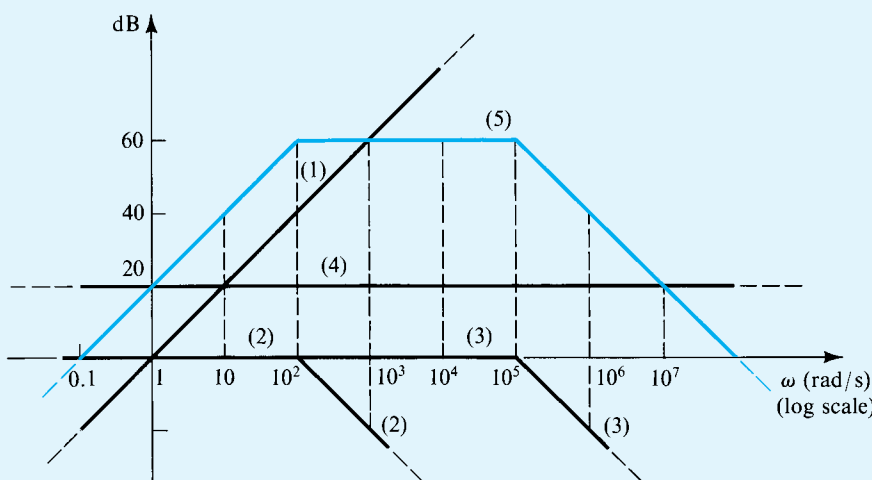


**Figure F.2** Bode plots for Example F.1.

Adding the four curves results in the asymptotic Bode diagram of the amplifier gain (curve 5). Note that since the two poles are widely separated, the gain will be very close to  $10^3$  (60 dB) over the frequency range  $10^2$  to  $10^5$  rad/s. At the two corner frequencies ( $10^2$  and  $10^5$  rad/s) the gain will be approximately 3 dB below the maximum of 60 dB. At the three specific frequencies, the values of the gain as obtained from the Bode plot and from exact evaluation of the transfer function are as follows:

$\omega$	Approximate Gain	Exact Gain
$10$	40 dB	39.96 dB
$10^3$	60 dB	59.96 dB
$10^6$	40 dB	39.96 dB

We next consider the Bode phase plot. Figure F.3 shows a plot of the typical phase term  $\tan^{-1}(\omega/a)$ , assuming that  $a$  is negative. Also shown is an asymptotic straight-line approximation of the arctan function. The asymptotic plot consists of three straight lines. The first is horizontal at  $\phi = 0$  and extends up to  $\omega = 0.1|a|$ . The second line has a slope of  $-45^\circ/\text{decade}$  and extends from  $\omega = 0.1|a|$  to  $\omega = 10|a|$ . The third line has a zero slope and a level of  $\phi = -90^\circ$ . The complete phase response can be obtained by summing the asymptotic Bode plots of the phase of all poles and zeros.

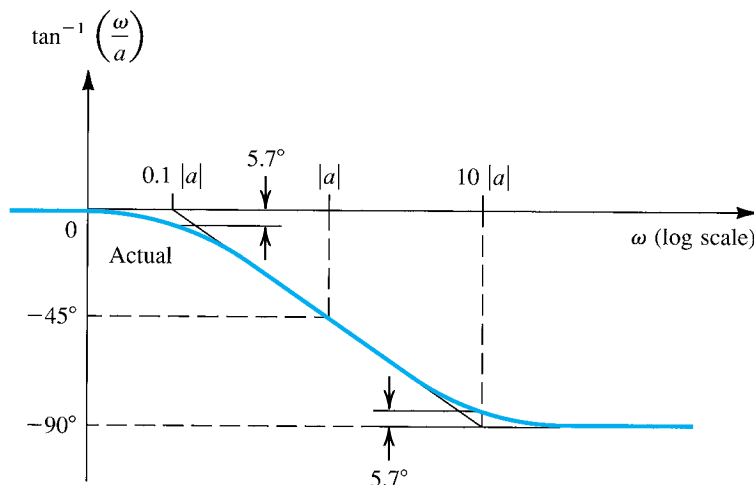


**Figure F.3** Bode plot of the typical phase term  $\tan^{-1}(\omega/a)$  when  $a$  is negative.

### Example F.2

Find the Bode plot for the phase of the transfer function of the amplifier considered in Example F.1.

#### Solution

The zero at  $s = 0$  gives rise to a constant  $+90^\circ$  phase function represented by curve 1 in Fig. F.4. The pole at  $s = -10^2$  gives rise to the phase function

$$\phi_1 = -\tan^{-1} \frac{\omega}{10^2}$$

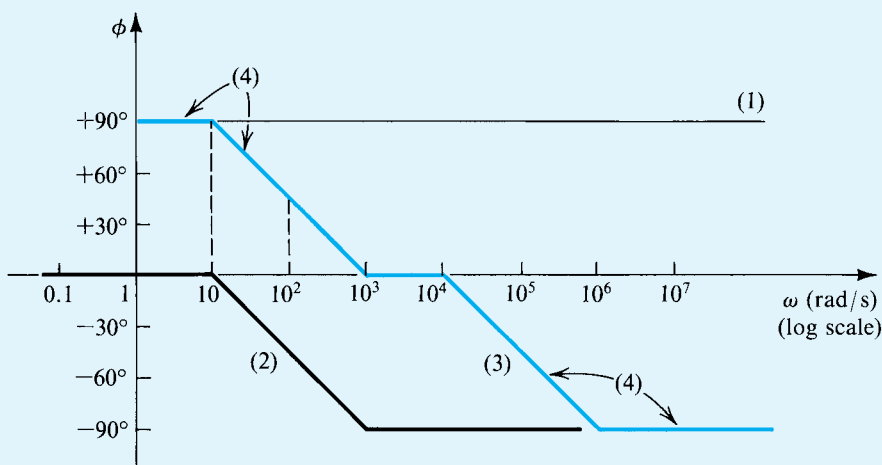


**Figure F.4** Phase plots for Example F.2.

(the leading minus sign is due to the fact that this singularity is a pole). The asymptotic plot for this function is given by curve 2 in Fig. F.4. Similarly, the pole at  $s = -10^5$  gives rise to the phase function

$$\phi_2 = -\tan^{-1} \frac{\omega}{10^5}$$

whose asymptotic plot is given by curve 3. The overall phase response (curve 4) is obtained by direct summation of the three plots. We see that at 100 rad/s, the amplifier phase leads by 45° and at  $10^5$  rad/s the phase lags by 45°.

## F.4 An Important Remark

For constructing Bode plots, it is most convenient to express the transfer-function factors in the form  $(1 + s/a)$ . The material of Figs. F.1 and F.2 and of the preceding two examples is then directly applicable.

## PROBLEMS

- F.1** Find the transfer function  $T(s) = V_o(s)/V_i(s)$  of the circuit in Fig. PF.1. Is this an STC network? If so, of what type? For  $C_1 = C_2 = 0.5 \mu\text{F}$  and  $R = 100 \text{ k}\Omega$ , find the location of the pole(s) and zero(s), and sketch Bode plots for the magnitude response and the phase response.

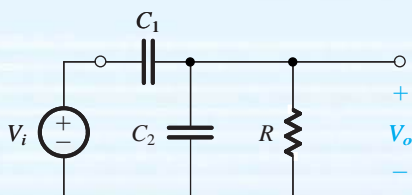


**Figure PF.1**

**D\*F.2** (a) Find the voltage transfer function  $T(s) = V_o(s)/V_i(s)$ , for the STC network shown in Fig. PF.2.

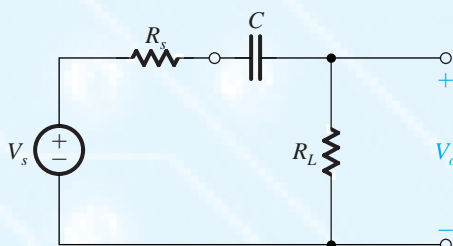


Figure PF.2

(b) In this circuit, capacitor  $C$  is used to couple the signal source  $V_s$  having a resistance  $R_s$  to a load  $R_L$ . For  $R_s = 10 \text{ k}\Omega$ , design the circuit, specifying the values of  $R_L$  and  $C$  to only one significant digit to meet the following requirements:

- (i) The load resistance should be as small as possible.
- (ii) The output signal should be at least 70% of the input at high frequencies.
- (iii) The output should be at least 10% of the input at 10 Hz.

**F.3** Two STC RC circuits, each with a pole at 100 rad/s and a maximum gain of unity, are connected in cascade with an intervening unity-gain buffer that ensures that they function separately. Characterize the possible combinations (of low-pass and high-pass circuits) by providing (i) the relevant transfer functions, (ii) the voltage gain at 10 rad/s, (iii) the voltage gain at 100 rad/s, and (iv) the voltage gain at 1000 rad/s.

**F.4** Design the transfer function in Eq. (F.5) by specifying  $a_1$  and  $\omega_0$  so that the gain is 10 V/V at high frequencies and 1 V/V at 10 Hz.

**F.5** An amplifier has a low-pass STC frequency response. The magnitude of the gain is 20 dB at dc and 0 dB at 100 kHz. What is the corner frequency? At what frequency is the gain 19 dB? At what frequency is the phase  $-6^\circ$ ?

**F.6** A transfer function has poles at  $(-5)$ ,  $(-7 + j10)$ , and  $(-20)$ , and a zero at  $(-1 - j20)$ . Since this function represents

an actual physical circuit, where must other poles and zeros be found?

**F.7** An amplifier has a voltage transfer function  $T(s) = 10^6 s / (s + 10)(s + 10^3)$ . Convert this to the form convenient for constructing Bode plots [that is, place the denominator factors in the form  $(1 + s/a)$ ]. Provide a Bode plot for the magnitude response, and use it to find approximate values for the amplifier gain at  $1, 10, 10^2, 10^3, 10^4$ , and  $10^5$  rad/s. What would the actual gain be at 10 rad/s? At  $10^3$  rad/s?

**F.8** Find the Bode phase plot of the transfer function of the amplifier considered in Problem F.7. Estimate the phase angle at  $1, 10, 10^2, 10^3, 10^4$ , and  $10^5$  rad/s. For comparison, calculate the actual phase at  $1, 10$ , and  $100$  rad/s.

**F.9** A transfer function has the following zeros and poles: one zero at  $s = 0$  and one zero at  $s = \infty$ ; one pole at  $s = -100$  and one pole at  $s = -10^6$ . The magnitude of the transfer function at  $\omega = 10^4$  rad/s is 100. Find the transfer function  $T(s)$  and sketch a Bode plot for its magnitude.

**F.10** Sketch Bode plots for the magnitude and phase of the transfer function

$$T(s) = \frac{10^4(1 + s/10^5)}{(1 + s/10^3)(1 + s/10^4)}$$

From your sketches, determine approximate values for the magnitude and phase at  $\omega = 10^6$  rad/s. What are the exact values determined from the transfer function?

**F.11** A particular amplifier has a voltage transfer function  $T(s) = 10s^2 / (1 + s/10)(1 + s/100)(1 + s/10^6)$ . Find the poles and zeros. Sketch the magnitude of the gain in dB versus frequency on a logarithmic scale. Estimate the gain at  $10^0, 10^3, 10^5$ , and  $10^7$  rad/s.

**F.12** A direct-coupled differential amplifier has a differential gain of 100 V/V with poles at  $10^6$  and  $10^8$  rad/s, and a common-mode gain of  $10^{-3}$  V/V with a zero at  $10^4$  rad/s and a pole at  $10^8$  rad/s. Sketch the Bode magnitude plots for the differential gain, the common-mode gain, and the CMRR. What is the CMRR at  $10^7$  rad/s? (Hint: Division of magnitudes corresponds to subtraction of logarithms.)

## APPENDIX G

# BIBLIOGRAPHY

### HISTORY OF ELECTRONICS

- L. Berlin, *The Man Behind the Microchip: Robert Noyce and the Invention of Silicon Valley*, New York: Oxford University Press, 2005.
- T.R. Reid, *The Chip*, New York: Random House, 2001.
- J.N. Shurkin, *Broken Genius: The Rise and Fall of William Shockley, Creator of the Electronic Age*, New York, Macmillan, 2008.
- J. Williams, editor, *Analog Circuit Design: Art, Science, and Personalities*, Boston: Butterworth-Heinemann, 1991.
- IEEE Solid-State Circuits Magazine*, and its predecessor, *IEEE Solid-State Circuits Newsletter*, published quarterly by the IEEE Solid-State Circuits Society.

### GENERAL TEXTBOOKS ON ELECTRONIC CIRCUITS

- E.F. Angelo Jr., *Electronics: BJTs, FETs, and Microcircuits*, New York: McGraw-Hill, 1969.
- S.B. Burns and P.R. Bond, *Principles of Electronic Circuits*, St. Paul: West, 1987.
- M.S. Ghausi, *Electronic Devices and Circuits: Discrete and Integrated*, New York: Holt, Rinehart and Winston, 1985.
- P.E. Gray and C.L. Searle, *Electronic Principles*, New York: Wiley, 1969.
- A.R. Hambley, *Electronics*, 2nd ed., Upper Saddle River, NJ: Prentice-Hall, 1999.
- W.H. Hayt and G.W. Neudeck, *Electronic Circuit Analysis and Design*, 2nd ed., Boston: Houghton Mifflin Co., 1984.
- C.A. Holt, *Electronic Circuits*, New York: Wiley, 1978.
- M.N. Horenstein, *Microelectronic Circuits and Devices*, 2nd ed., Englewood Cliffs, NJ: Prentice-Hall, 1995.
- R.T. Howe and C.G. Sodini, *Microelectronics—An Integrated Approach*, Englewood Cliffs, NJ: Prentice-Hall, 1997.
- R.C. Jaeger and T.N. Blalock, *Microelectronic Circuit Design*, 3rd ed., New York: McGraw-Hill, 2008.
- N.R. Malik, *Electronic Circuits: Analysis, Simulation, and Design*, Englewood Cliffs, NJ: Prentice-Hall, 1995.

J. Millman and A. Grabel, *Microelectronics*, 2nd ed., New York: McGraw-Hill, 1987.

D.A. Neamen, *Electronic Circuit Analysis and Design*, 3rd ed., New York: McGraw-Hill, 2007.

M.H. Rashid, *Microelectronic Circuits: Analysis and Design*, Boston: PWS, 1999.

B. Ravazi, *Fundamentals of Microelectronics*, Hoboken, NJ: Wiley, 2008.

D.L. Schilling and C. Belowe, *Electronic Circuits*, 2nd ed., New York: McGraw-Hill, 1979.

R.A. Spencer and M.S. Ghausi, *Introduction to Electronic Circuit Design*, Upper Saddle River, NJ: Pearson Education Inc. (Prentice-Hall), 2003.

### CIRCUIT AND SYSTEM ANALYSIS

L.S. Bobrow, *Elementary Linear Circuit Analysis*, 2nd ed., New York: Holt, Rinehart and Winston, 1987.

A.M. Davis, *Linear Circuit Analysis*, Boston, PWS Publishing Company, 1998.

S.S. Haykin, *Active Network Theory*, Reading, MA: Addison-Wesley, 1970.

W.H. Hayt, G.E. Kemmerly, and S.M. Durbin, *Engineering Circuit Analysis*, 6th ed., New York: McGraw-Hill, 2003.

D. Irwin, *Basic Engineering Circuit Analysis*, 7th ed., New York: Wiley, 2001.

B.P. Lathi, *Linear Systems and Signals*, New York: Oxford University Press, 1992.

J.W. Nilsson and S. Riedel, *Electronic Circuits*, 7th ed., Upper Saddle River, NJ: Prentice-Hall, 2005.

### DEVICES AND IC FABRICATION

R.S.C. Cobbold, *Theory and Applications of Field Effect Transistors*, New York: Wiley, 1969.

I. Getreu, *Modeling the Bipolar Transistor*, Beaverton, OR: Tektronix, Inc., 1976.

R.S. Muller and T.I. Kamins, *Device Electronics for Integrated Circuits*, 3rd ed., New York: Wiley, 2003.

J.D. Plummer, M.D. Deal, and P.B. Griffin, *Silicon VLSI Technology*, Upper Saddle River, NJ: Prentice-Hall, 2000.

D.L. Pulfrey and N.G. Tarr, *Introduction to Microelectronic Devices*, Englewood Cliffs, NJ: Prentice-Hall, 1989.

## G-2 Appendix G Bibliography

- C.L. Searle, A.R. Boothroyd, E.J. Angelo, Jr., P.E. Gray, and D.O. Pederson, *Elementary Circuit Properties of Transistors*, Vol. 3 of the SEEC Series, New York: Wiley, 1964.
- B.G. Streetman and S. Banerjee, *Solid-State Electronic Devices*, 5th ed., Upper Saddle River, NJ: Prentice-Hall, 2000.
- Y. Tsividis, *Operation and Modeling of the MOS Transistor*, 2nd ed., New York: Oxford University Press, 1999.
- ### OPERATIONAL AMPLIFIERS
- G.B. Clayton, *Experimenting with Operational Amplifiers*, London: Macmillan, 1975.
- G.B. Clayton, *Operational Amplifiers*, 2nd ed., London: Newnes-Butterworths, 1979.
- S. Franco, *Design with Operational Amplifiers and Analog Integrated Circuits*, 3rd ed., New York: McGraw-Hill, 2001.
- J.G. Graeme, G.E. Tobey, and L.P. Huelsman, *Operational Amplifiers: Design and Applications*, New York: McGraw-Hill, 1971.
- W. Jung, *IC Op Amp Cookbook*, Indianapolis: Howard Sams, 1974.
- E.J. Kennedy, *Operational Amplifier Circuits: Theory and Applications*, New York: Holt, Rinehart and Winston, 1988.
- J.K. Roberge, *Operational Amplifiers: Theory and Practice*, New York: Wiley, 1975.
- J.L. Smith, *Modern Operational Circuit Design*, New York: Wiley-Interscience, 1971.
- J.V. Wait, L.P. Huelsman, and G.A. Korn, *Introduction to Operational Amplifiers: Theory and Applications*, New York: McGraw-Hill, 1975.
- ### ANALOG CIRCUITS
- P.E. Allen and D.R. Holberg, *CMOS Analog Circuit Design*, 2nd ed., New York: Oxford University Press, 2002.
- K. Bult, *Transistor-Level Analog IC Design*. Notes for a short course organized by Mead, Ecole Polytechnique Fédéral de Lausanne, 2002.
- M.J. Fonderic and J.H. Huisings, *Design of Low-Voltage Bipolar Operational Amplifiers*, Boston: Kluwer Academic Publishers, 1993.
- R.L. Geiger, P.E. Allen, and N.R. Strader, *VLSI Design Techniques for Analog and Digital Circuits*, New York: McGraw-Hill, 1990.
- P.R. Gray, P.J. Hurst, S.H. Lewis, and R.G. Meyer, *Analysis and Design of Analog Integrated Circuits*, 5th ed., Hoboken, NJ: Wiley, 2008.
- A.B. Grebene, *Bipolar and MOS Analog Integrated Circuit Design*, New York: Wiley, 1984.
- R. Gregorian and G.C. Temes, *Analog MOS Integrated Circuits for Signal Processing*, New York: Wiley, 1986.
- J.H. Huisings, *Operational Amplifiers*, Boston: Kluwer Academic Publishers, 2001.
- IEEE Journal of Solid-State Circuits*, a monthly publication of the IEEE.
- D.A. Johns and K. Martin, *Analog Integrated Circuit Design*, New York: Wiley, 1997.
- K. Laker and W. Sansen, *Design for Analog Integrated Circuits and Systems*, New York: McGraw-Hill, 1999.
- H.S. Lee, "Analog Design," Chapter 8 in *BiCMOS Technology and Applications*, A.R. Alvarez, editor, Boston: Kluwer Academic Publishers, 1989.
- National Semiconductor Corporation, *Audio/Radio Handbook*, Santa Clara, CA: National Semiconductor Corporation, 1980.
- B. Razavi, *Design of Analog CMOS Integrated Circuits*, New York: McGraw-Hill, 2001.
- J.K. Roberge, *Operational Amplifiers: Theory and Practice*, New York: Wiley, 1975.
- S. Rosenstark, *Feedback Amplifier Principles*, New York: Macmillan, 1986.
- W.M.C. Sansen, *Analog Design Essentials*, Dordrecht, The Netherlands: Springer, 2006.
- A.S. Sedra and G.W. Roberts, "Current Conveyor Theory and Practice," Chapter 3 in *Analogue IC Design: The Current-Mode Approach*, C. Toumazou, F.J. Lidger, and D.G. Haigh, editors, London: Peter Peregrinus, 1990.
- R. Severns, editor, *MOSPOWER Applications Handbook*, Santa Clara, CA: Siliconix, 1984.
- Texas Instruments, Inc., *Power Transistor and TTL Integrated-Circuit Applications*, New York: McGraw-Hill, 1977.
- S. Soclof, *Applications of Analog Integrated Circuits*, Englewood Cliffs, NJ: Prentice-Hall, 1985.
- J.M. Steininger, "Understanding wideband MOS transistors," *IEEE Circuits and Devices*, Vol. 6, No. 3, pp. 26–31, May 1990.
- ### DIGITAL CIRCUITS
- A.R. Alvarez, editor, *BiCMOS Technology and Applications*, 2nd ed., Boston: Kluwer Academic Publishers, 1993.
- S.H.K Embabi, A. Bellaour, and M.I. Elmasry, *Digital BiCMOS Integrated Circuit Design*, Boston: Kluwer, 1993.
- M.I. Elmasry, editor, *Digital MOS Integrated Circuits*, New York: IEEE Press, 1981. Also, *Digital MOS Integrated Circuits II*, 1992.
- D.A. Hodges, H.G. Jackson, and R.A. Saleh, *Analysis and Design of Digital Integrated Circuits*, 3rd ed., New York: McGraw-Hill, 2004.
- IEEE Journal of Solid-State Circuits*, a monthly publication of the IEEE.
- S.M. Kang and Y. Leblebici, *CMOS Digital Integrated Circuits*, 3rd ed., New York: McGraw-Hill, 2003.
- R. Littauer, *Pulse Electronics*, New York: McGraw-Hill, 1965.
- K. Martin, *Digital Integrated Circuit Design*, New York: Oxford University Press, 2000.
- J. Millman and H. Taub, *Pulse, Digital, and Switching Waveforms*, New York: McGraw-Hill, 1965.
- Motorola, *MECL Device Data*, Phoenix, AZ: Motorola Semiconductor Products, Inc., 1989.
- Motorola, *MECL System Design Handbook*, Phoenix, AZ: Motorola Semiconductor Products, Inc., 1988.

- J.M. Rabaey, *Digital Integrated Circuits*, Englewood Cliffs, NJ: Prentice-Hall, 1996. Note: A 2nd ed., with A. Chandrakasan and B. Nikolic, also appeared in 2003.
- L. Strauss, *Wave Generation and Shaping*, 2nd ed., New York: McGraw-Hill, 1970.
- H. Taub and D. Schilling, *Digital Integrated Electronics*, New York: McGraw-Hill, 1977.
- N. Weste and K. Eshraghian, *Principles of CMOS VLSI Design*, Reading, MA: Addison-Wesley, 1985 and 1993.

### FILTERS AND TUNED AMPLIFIERS

- P.E. Allen and E. Sanchez-Sinencio, *Switched-Capacitor Circuits*, New York: Van Nostrand Reinhold, 1984.
- K.K. Clarke and D.T. Hess, *Communication Circuits: Analysis and Design*, Ch. 6, Reading, MA: Addison Wesley, 1971.
- G. Daryanani, *Principles of Active Network Synthesis and Design*, New York: Wiley, 1976.
- R. Gregorian and G.C. Temes, *Analog MOS Integrated Circuits for Signal Processing*, New York: Wiley-Interscience, 1986.
- C. Ouslis and A. Sedra, "Designing custom filters," *IEEE Circuits and Devices*, May 1995, pp. 29–37.
- S.K. Mitra and C.F. Kurth, editors, *Miniatirized and Integrated Filters*, New York: Wiley-Interscience, 1989.
- R. Schaumann, M.S. Ghausi, and K.R. Laker, *Design of Analog Filters*, Englewood Cliffs, NJ: Prentice-Hall, 1990.

- R. Schaumann, M. Soderstand, and K. Laker, editors, *Modern Active Filter Design*, New York: IEEE Press, 1981.
- R. Schaumann and M.E. Van Valkenburg, *Design of Analog Filters*, New York: Oxford University Press, 2001.

- A.S. Sedra, "Switched-capacitor filter synthesis," in *MOS VLSI Circuits for Telecommunications*, Y. Tsividis and P. Antognetti, editors, Englewood Cliffs, NJ: Prentice-Hall, 1985.

- A.S. Sedra and P.O. Brackett, *Filter Theory and Design: Active and Passive*, Portland, OR: Matrix, 1978.

- M.E. Van Valkenburg, *Analog Filter Design*, New York: Holt, Rinehart and Winston, 1981.

- A.I. Zverev, *Handbook of Filter Synthesis*, New York: Wiley, 1967.

### SPICE

- M.E. Herniter, *Schematic Capture with Cadence PSpice*, 2nd ed., Upper Saddle River, NJ: Prentice-Hall, 2003.
- G. Massobrio and P. Antognetti, *Semiconductor Device Modeling with SPICE*, 2nd ed., New York: McGraw-Hill, 1993.
- G.W. Roberts and A.S. Sedra, *SPICE*, New York: Oxford University Press, 1992 and 1997.
- J.A. Svoboda, *PSpice for Linear Circuits*, New York: Wiley, 2002.
- P.W. Tuinenga, *SPICE: A Guide to Circuit Simulation & Analysis Using PSpice*, 2nd ed., Englewood Cliffs, NJ: Prentice-Hall, 1992.